Propriétés structurales et dynamiques des sulfates d'alcalins

Roman Shakhovoy

UNIVERSITÉ D'ORLÉANS

***ÉCOLE DOCTORALE** (ENERGIE, MATERIAUX, SCIENCES DE LA TERRE ET DE L'UNIVERS)*

Conditions Extrêmes et Matériaux: Haute Température et Irradiation (CEMHTI)

THÈSE

Présentée par:

Roman SHAKHOVOY

soutenue le : **29 septembre 2015**

pour obtenir le grade de : **Docteur de l'université d'Orléans**

Discipline/ Spécialité : Physique des matériaux

Structural Properties and Dynamics of Alkali Sulfates

THÈSE dirigée par:

Catherine Bessada	Directrice de Recherche, CEMHTI, CNRS, Orléans

RAPPORTEURS:

Jean-Pierre KORB	Directeur de Recherche, PMC, Polytechnique, Palaiseau
Laurent Le Polles	Maitre de Conference HDR, SCR, Rennes

JURY:

Catherine Bessada	Directrice de Recherche, CEMHTI, CNRS, Orléans, Président du jury
John Hanna	Directeur de Recherche, Dept of Physics, Warwick, UK
Thibault Charpentier	Ingénieur Chercheur, IRAMIS, CEA Saclay
Jean-Pierre KORB	Directeur de Recherche,PMC, Polytechnique, Palaiseau
Laurent Le Polles	Maitre de Conference HDR, SCR, Rennes

Mathematics is boundless and it is impossible to know it satisfactorily.

Therefore, it is better to do physics.

L.D. Landau (1908-1968)

Introduction

Durant les 30 dernières années, des efforts considérables ont été menés en sciences de matériaux autour de l'étude de matériaux conducteurs solides superioniques. Ils combinent une conductivité ionique élevée et une bonne résistance mécanique, et trouvent ainsi un large domaine d'applications dans les piles à combustibles, les capteurs, les supercondensateurs ou les batteries, etc... [1].

Les sulfates d'alcalins, conducteurs superioniques sont référencés comme des électrolytes solides à base de Li_2SO_4 (Li_2SO_4, $LiNaSO_4$, $LiKSO_4$, etc.) appartenant à la famille des conducteurs ioniques $LiMSO_4$ (M = Na, K, Rb, NH_4, Ag). Les diagrammes de phase des systèmes Li_2SO_4–Na_2SO_4, Li_2SO_4–Ag_2SO_4, Li_2SO_4–K_2SO_4, et Li_2SO_4–$ZnSO_4$ indiquent l'existence de plusieurs phases conductrices à haute température : $LiNaSO_4$ (bcc), $LiAgSO_4$ (bcc), et $Li_4Zn(SO_4)_3$ (réseau non-cubique), avec des conductivités pouvant atteindre 1 $Ohm^{-1}cm^{-1}$ à 600°C.

Les sulfates doubles d'alcalins à haute conductivité ionique ($LiNaSO_4$, $LiKSO_4$) sont étudiés plus particulièrement dans cette thèse, les sulfates moins conducteurs, comme $LiRbSO_4$ et $LiCsSO_4$, seront aussi abordés dans ce travail, l'idée étant de mieux comprendre les mécanismes de transport dans ces cristaux.

Les deux membres de la famille des sulfates d'alcalins doubles, $LiNaSO_4$ (LNS) et $LiKSO_4$ (LKS) méritent une attention particulière de par leurs propriétés de conduction. Ils sont de plus peu sensibles à l'humidité à l'inverse de beaucoup d'autres sulfates à base de lithium (comme Li_2SO_4) [2]. Les monocristaux de LNS et LKS peuvent être préparés simplement à partir d'une solution aqueuse des sulfates d'alcalins correspondants.
Ces propriétés en font des bons candidats pour des applications dans le domaine des batteries solides, des piles à combustibles ou des batteries de stockage [3].

L'évolution en température de la conductivité ionique dans LNS et LKS (Fig. i) indique des valeurs tout à fait intéressantes: pour LKS, entre 708K et la température de fusion à 950K (phase *II*) la conductivité augmente de 10^{-2} jusqu'à 10^{2} $Ohm^{-1}cm^{-1}$. Pour LNS, dans la phase haute température, au-dessus de 788 K la conductivité est plus élevée que dans LKS mais le domaine de température concernée par ces valeurs reste très restreint et la température de transition assez élevée comparée aux températures visées pour des batteries thermiques (670-870 K) [2] par exemple. Néanmoins les caractéristiques attendues pour ce type d'applications seraient une conductivité ionique autour de 0.1 $Ohm^{-1}cm^{-1}$ dans la phase

conductrice alors qu'au-dessous de 340 K, l'électrolyte devrait avoir une conductivité négligeable pour éviter la décharge « spontanée » de la batterie.

Aujourd'hui LNS et LKS ont été testés uniquement dans des cellules prototypes entre 770-870 K [2]. Malgré ces différentes limitations, il est intéressant de bien comprendre les mécanismes mis en jeu dans ces systèmes que ce soit pour des applications à venir ou dans un intérêt purement académique comme nous le montrerons dans ce travail.

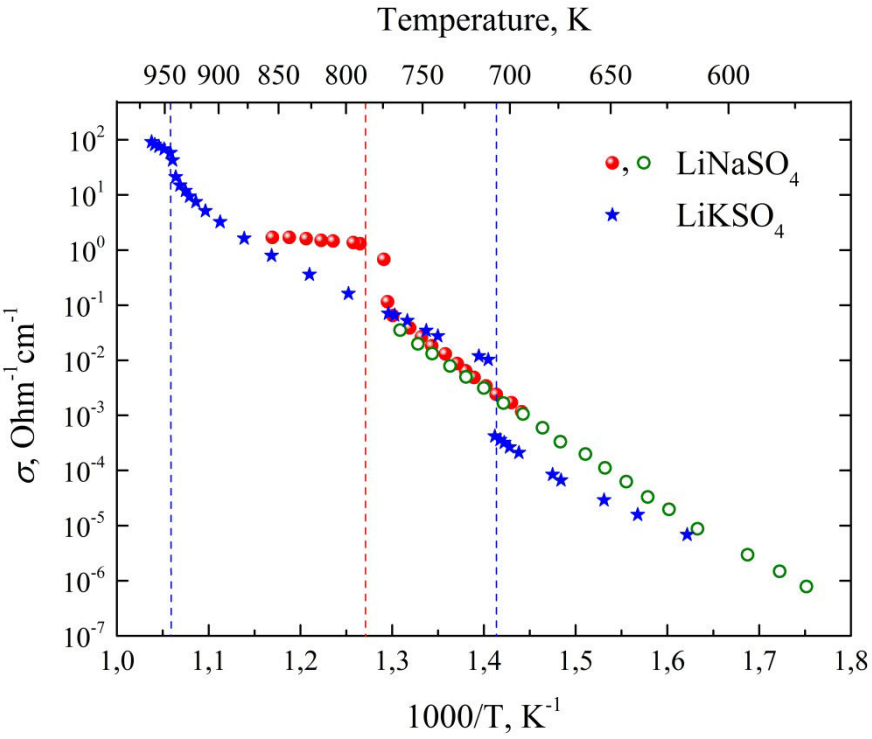

Fig. i. Dépendance en température de la conductivité ionique d.c. de monocristal de $LiNaSO_4$ (points verts) [4], de la poudre $LiNaSO_4$ (points rouges) [5], et dans le monocristal de $LiKSO_4$ perpendiculaire à l'axe *c*-axis (étoiles bleues) [6]. Les lignes bleues en pointillés indiquent les températures de transition dans $LiKSO_4$ (708 et 943 K), la ligne rouge en pointillé indique la température de transition de phase dans $LiNaSO_4$ (788 K).

Les sulfates LNS et LKS sont en effet caractérisés en plus d'un sous réseau cationique "quasi-liquide" par un désordre rotationnel des groupements sulfates avec un couplage entre les rotations des anions SO_4^{2-} et la diffusion des cations. La présence de tels mouvements corrélés a souvent été décrit par un mécanisme d'engrenage, "paddle-wheel"ou "cog-wheel", les atomes d'oxygène des ions sulfates « pousseraient » les cations dans des sites interstitiels voisins, ou dans des lacunes et une telle 'assistance' augmenterait la conductivité ionique[7-9]. Pendant plus d'un demi-siècle, depuis la découverte d'une conductivité superionique dans

LNS, de nombreux articles ont été publiés sur sa structure et ses propriétés dynamiques. Il a été montré que la transition de phase était complétement réversible avec des effets d'hystérésis très faibles et une enthalpie de fusion $\Delta H_f = 4.1\,\mathrm{kJ\,mol^{-1}}$ anormalement faible comparée à l'enthalpie de la transition solide-solide, $\Delta H_{tr} = 20.8\,\mathrm{kJ\,mol^{-1}}$ [10]. Cette « anomalie » a été attribuée à la dynamique et à la réorientation du tétraèdre SO_4 dans le cristal LNS.

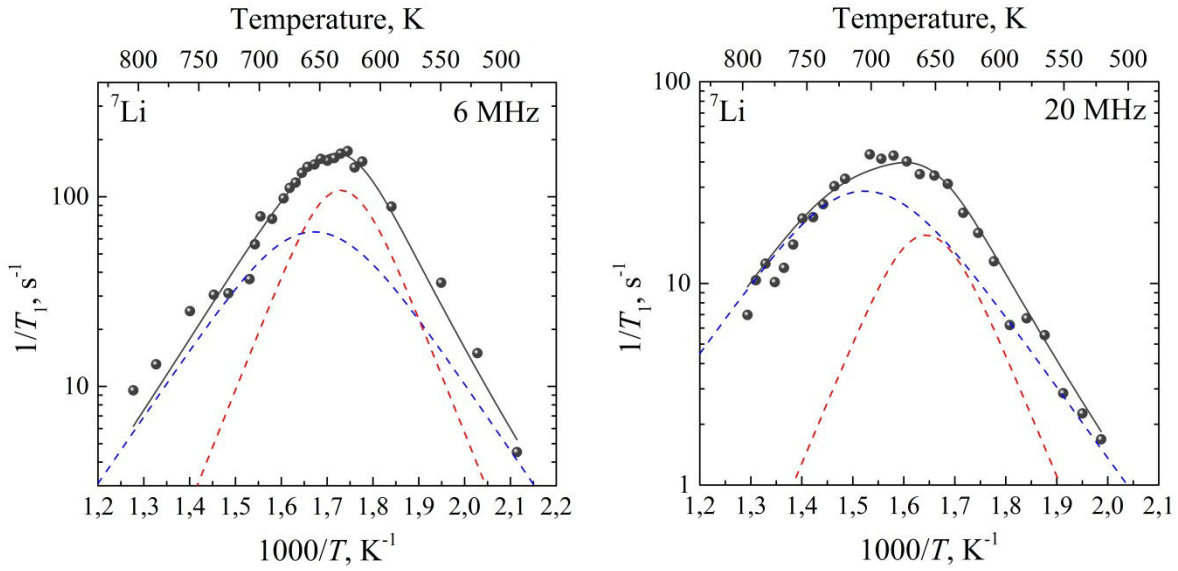

Fig. ii. Dépendance en température des temps de relaxation spin-réseau de ^{7}Li dans $LiNaSO_4$ à deux champs différents $\nu(^7\mathrm{Li})$ = 6 MHz (à gauche) et 20 MHz (à droite) [11]. Les contributions BPP sont reportées en pointillés rouges (^{7}Li) et bleus (^{23}Na), respectivement. Les énergies d'activation sont estimées à $E_a^{\mathrm{Li}} = 0.7\,\mathrm{eV}$ and $E_a^{\mathrm{Na}} = 1.2\,\mathrm{eV}$.

Kanashiro *et al*. [11] ont publié des mesures de T_1 du ^{7}Li à différents champs magnétiques et ont montré que l'évolution en température de la vitesse de relaxation dans le monocristal de LNS ne pouvait pas être décrite par un simple modèle BPP, mais qu'il fallait tenir compte d'une fonction de densité spectrale avec au moins deux temps de corrélation.

D'autre part, il a été montré que le désordre réorientationnel des groupements SO_4^{2-} ainsi que la mobilité cationique démarraient bien avant la transition de phase α-β [12, 13], mais que les réorientations à basse température n'avaient qu'un effet très faible sur la diffusion des ions Li^+ [13], dans la phase β (< 788 K).

Dans ce travail, nous avons cherché à caractériser l'ensemble de la dynamique sur toute la gamme de température en utilisant la potentialité des outils RMN à notre disposition :

depuis les mesures de T_1, l'évolution des largeurs de raies et les mesures de coefficients d'autodiffusion en température. En parallèle à la description de la mobilité des cations Li^+ et Na^+, nous avons montré expérimentalement comment sonder les réorientations des SO_4^{2-} à partir de la dépendance en température de l'éclatement quadripolaire du ^{7}Li, ν_Q, dans le cristal de LNS.

Pour $LiKNO_3$, malgré de nombreuses approches expérimentales et théoriques, certaines conclusions sont toujours controversées et une vision claire et définitive du diagramme de phase n'est toujours pas disponible. Néanmoins, les structures des deux polymorphes de $LiKSO_4$ sont bien établies pour la phase à haute température (phase *I*, $T > 943$ K) et la phase à température ambiante (phase *III*, 203 K < T < 708 K), tandis que les structures de la structure de la phase intermédiaire et des phases au-dessous de 203 K ne sont toujours pas validées. M. Pimenta *et al*. [6] ont montré qu'au-dessous de 653 K et au-dessus de 708 K la conductivité ionique dans le monocristal de LKS (le long de l'axe *c*) suivait une loi d'Arrhenius. Pour les composes "faiblement conducteurs", $LiRbSO_4$ et $LiCsSO_4$ (et leurs solutions solides) beaucoup d'études ont été menées pour leurs propriétés ferroélectriques et leurs diagrammes de phase [14-19], mais la question de leur mobilité ionique n'a jamais été prise en compte.

Il reste donc un certain nombre questions non résolues autour de la mobilité ionique dans les sulfates d'alcalins. De plus du fait de l'évolution rapide des techniques expérimentales et de leurs potentialités notamment pour la spectroscopie RMN, et ses développements à haute température pour la mesure des coefficients d'autodiffusion par RMN à gradients de champs pulsés [20], nous avons pu réexaminer les différentes approches et tenté de répondre à ces questions en mettant à profit l'ensemble de ces outils RMN pour suivre in situ en température les différentes étapes de la mobilité ionique dans les sulfates d'alcalins.

***

Dans le premier chapitre de la thèse, "***Elements of NMR relaxation theory***", nous avons choisi de décrire quelques éléments de théorie RMN pour les noyaux quadripolaires dans les solides. En effet, dans les sulfates d'alcalins, les différents atomes étudiés sont tous quadripolaires, comme dans le cas de $LiNaSO_4$ et les isotopes ^{7}Li, ^{23}Na, ^{33}S, avec un spin $I = 3/2$, ^{6}Li avec un spin $I = 1$, et ^{17}O, avec un spin $I = 5/2$. Dans le cadre de cette étude principalement focalisée sur l'approche de la mobilité ionique dans les phases cristallines, une

attention particulière a été naturellement portée sur les mesures et l'interprétation des temps de relaxation spin réseau.

Le second chapitre, "***Theory and measurements of diffusion in solids***", est consacré à l'étude de la diffusion et de l'autodiffusion dans les solides. La première partie du chapitre donne les éléments théoriques pour décrire les processus de diffusion, et dans la deuxième partie nous décrivons les méthodes de mesures utilisées, notamment la RMN à Gradients de champs pulsés.

Le chapitre 3 traite des aspects expérimentaux des mesures RMN à haute température (HT) et des différentes optimisations effectuées au cours de ce travail pour contrôler au mieux la température et sa mesure au niveau de l'échantillon.

Enfin dans le chapitre 4 "***Experimental study of alkali sulfates",*** nous présentons les résultats expérimentaux obtenus dans les différents sulfates d'alcalins avec une attention particulière sur le composé $LiNaSO_4$ qui montre une dynamique ionique la plus intéressante, et une approche comparée de la mobilité du lithium dans les sulfates « doubles » avec des cations plus gros, (K^+, Rb^+, and Cs^+).

Table of contents

Acknowledgements

I am grateful to all staff of CEMHTI, who worked with me during last three years. First, I would like to express my gratitude to my scientific advisor, Catherine Bessada, for her willingness to help me in any small question. Be it some formula in my “new theory” or administrative problem in the university, she always knew what to do and helped me to acquire again a confidence in myself. I am grateful to Aydar Rakhmatullin and Vincent Sarou-Kanian for an invaluable aid in the experimental part of my thesis. In addition, I would like to thank Michaël Deschamps, Pierre Florian, and Franck Fayon for their answers on my endless questions.

I am particularly grateful to my advisor in Russia, Yury Yuzyuk, who acquainted me with Catherine and helped me to find a PhD position in CEMHTI. I also would like to thank Vladimir Shirokov for valuable comments.

Introduction

I.1 Superionics and their classifications

The last 25-30 years considerable efforts of theorists and experimentalists in the field of material science are aimed at solid ionic conductors with liquid-like ionic conductivity. Such second-class (ionic) conductors are referred to as *solid electrolytes*, *superionic conductors* or *fast ionic conductors*. They combine high ionic conductivity and mechanical strength and, due to this, find wide applications in fuel cells, sensors, supercapacitors, batteries, etc. In fact, a number of researches increases in the field of power engineering, machine industry, electronics for the newest current sources with high capacity, energy, and power density. An analysis of the passive electronic components industry shows that one of the most promising electronic devices of the nearest future are supercapacitors, whereas lithium batteries are considered as the most promising active elements [1].

Application prospects of solid electrolyte-based devices are determined by understanding of their physicochemical properties and by ability to modify these properties in a controlled manner. Therefore, a detailed study of electronic structure and transport properties as well is required. The rapid development of computer technology and specialized softwares for material science significantly expanded capabilities of solid state physics and chemistry methods in the study of electronic structure of solids and even their transport properties. Nevertheless, experimental methods, particularly traditional techniques such as ionic conductivity, self-diffusion and NMR relaxation measurements play still a decisive role in this field.

In general, under normal conditions the ion transport in both crystalline and amorphous solids is insignificant; at room temperature, the ionic conductivity σ in usual solids does not surpass $10^{-10} - 10^{-12}$ $Ohm^{-1}cm^{-1}$ [21]. Since the ionic conductivity has thermally activated nature, σ increases with temperature, but even near the melting point it rarely surpasses 10^{-3} $Ohm^{-1}cm^{-1}$. However, anomalously high conductivity of solid electrolytes occurs far below the melting point. Thus, solid electrolytes combine the properties of liquids and solids.

For the first time, high ionic conductivity in solids was found in silver sulfide by Faraday (1833) [22]. It was shown that it exhibits conductivity comparable to metals in the high-temperature range, but, in contrast to metals, loses its conductivity upon cooling down. One year later, a considerable increase of the ionic conductivity was found in lead fluoride at

723 K. Nowadays, this effect observed in crystals with fluorite-type structure is referred to as Faraday (diffuse) transition. It was also recognized later that the generation of a counter voltage (polarization by chemical precipitation) during the passage of a current is a characteristic feature of electrolytic conductivity of solids, and this led to the discovery of an increasing number of solid conductors of a second class.

High value of the ionic conductivity in solid electrolytes is generally caused by a disordering of one or more crystalline sub-lattices. Obviously, this could be realized only in solids with extremely weak covalent bonds. Other prerequisites for existing of fast ionic conductivity in a solid are as follows: 1) the number of energetically equivalent crystallographic positions should exceed the actual number of ions; 2) energy barriers for ionic jumps should be quite small (in comparison with kT); 3) conducting channels should exist in the structure, otherwise, only local motions of ions could be fast.

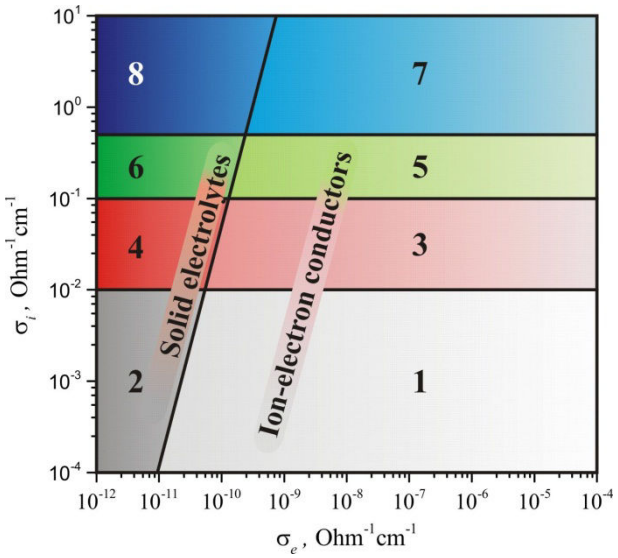

Fig. 1. A general classification of ionic conductors: 2,4,6 – known solid electrolytes, i.e. materials with $\sigma_i >> \sigma_e$; 1,3,5 – ion-electron conductors; 3,4 – superionic conductors; 5,6 – advanced superionic conductors; 7,8 – hypothetic advanced superionic conductors with $\Delta E \approx kT \approx 0.03$ eV (300 K) [1].

Other significant feature of the fast ionic conductors is that the concentration of point defects in their structure is much higher than the concentration of charge carriers (interstitial atoms or vacancies) in usual ionic conductors. Unfortunately, there is still no reliable method to measure the actual concentration of defects in solid electrolytes; therefore, one usually assumes that all ions of the disordered sub-lattice participate to the charge transport. In different solid electrolytes the conductivity is provided by single-, double-, and triply-charged cations (Ag^+, Cu^+, Li^+, Na^+, K^+, Rb^+, Cs^+, Ca^{2+}, Zn^{2+}, Mg^{2+}, Al^{3+}, Ce^{3+}, Eu^{3+}), and by anions (

F^-, Cl^-, Br^-, O^{2-}) [21]. There are also materials, where diffusion of two different ions occurs, e.g. Li^+ and Na^+ in $LiNaSO_4$.

The enhancement of the conductivity in solid electrolytes is commonly accompanied by a phase transition; above the phase transition temperature, ion diffusion is characterized by the same values of preexponential factor and activation energy as for diffusion in liquids. It was suggested by O'Keefe [23, 24] to classify ionic solids by the type of transition to the conducting state. According to this classification, ionic solids could be divided into three classes. The Class I includes *normal salts* ($PbCl_2$, $MgCl_2$, $CaBr_2$, etc.); in these materials the ionic conductivity increases only after the melting. In solids of the Class II a first order phase transition to the conducting state occurs; this phase transition is accompanied by a value of the latent heat close to the fusion heat of normal salts. The Class II includes CuBr, CuI, AgI, Ag_2S, Li_2SO_4, $LiNaSO_4$, YF_3, $BaCl_2$, $SrBr_2$, etc. There is also a number of salts (Na_2S, Li_4SiO_4, CaF_2, SrF_2, PbF_2, LaF_3, etc.), in which the non-conducting–conducting transformation is not a first order transition as in Class II solids but is spread out over a substantial temperature range. Such salts are classified as Class III.

In Refs. [1, 25] the classification of ionic conductors in terms of (σ_i, σ_e)-diagram was suggested (σ_i and σ_e are the ionic and electronic conductivity, respectively) (Fig. 1). According to this classification, solid electrolytes include materials with $\sigma_i >> \sigma_e$ (regions 2, 4, and 6 on the diagram). Materials, satisfying this condition but possessing also high electronic conductivity are referred to ion-electron conductors (regions 1, 3, 5). Examples for such materials are $Ag_{2+x}S$, $Ce_{2-x}O$, $YBa_2Cu_3O_{6+x}$ [26]. Materials with ionic conductivity $\sigma_i > 10^{-1}$ $Ohm^{-1}cm^{-1}$ ($E_a \approx 0.1$ eV) at room temperature are called advanced superionic conductors (regions 5, 6). The well-known advanced superionic conductors are α-AgI, α-$RbAg_4I_5$, $CsAg_4Br_{3-x}I_{2+x}$, $Rb_4Cu_{16}I_7Cl_{13}$ and some others [25]. Finally, regions 7 and 8 correspond to hypothetic (not yet discovered) advanced superionic conductors with $E_a \approx kT \approx 0.03$ eV at room temperature. Such value of activation energy should provide $\sigma_i = 2$ $Ohm^{-1}cm^{-1}$ for Ag^{2+} mobile ions and $\sigma_i = 8(20)$ $Ohm^{-1}cm^{-1}$ for small Li^+ (H^+) mobile ions.

Sometimes, the value of the activation energy (and of the pre-exponential factor as well) is a better criterion for characterization of fast ionic conductors than the ionic conductivity itself. It should be noted that in complex solid electrolytes the conducting ions are distributed non-uniformly over crystallographically nonequivalent sites characterizing by

potential barriers of different heights. However, one can introduce the average value of the activation energy, which is usually small relative to that of ordinary solids.

I.2 Sulfate superionics

Sulfate superionic conductors also referred to as Li_2SO_4-based solid electrolytes (Li_2SO_4, $LiNaSO_4$, $LiKSO_4$, etc.) belong to a distinct family of fast ionic conductors with general formula $LiMSO_4$ (M = Na, K, Rb, NH_4, Ag). These compounds exhibit successive structural phase transitions, ferroelectricity (albeit weakly pronounced), and interesting properties of ionic conductivity. The first study of lithium sulfate has been carried out in 1921 [27], when it was reported that solid Li_2SO_4 shows a drastic increase of the electrical conductivity when the temperature is approaching 580°C. However, this did not attract much attention until after it had been determined that the structure of the high-temperature phase was fcc for Li_2SO_4 and bcc for $LiNaSO_4$ [28, 29] and that the electrical conductivity of both these phases was of the same magnitude as that of the fused state [29].

Table 1. Transport properties of some sulfate fast ionic conductors at 873 K [21].

Phase	σ, $Ohm^{-1}cm^{-1}$	E_σ, eV	Ion	D, 10^{-9} m^2/s	E_D
Li_2SO_4, fcc	1.07	0.43	Li^+	1.59	0.34
			SO_4^{-2}	~0.0002	0.22
$LiNaSO_4$, bcc	1.25	0.44	Li^+	1.00	0.63
			Na^+	0.93	0.64
$LiAgSO_4$, bcc	1.52*	0.40	Li^+	1.03	0.52
			Ag^+	1.00	0.52
$Li_{1.33}Zn_{0.33}SO_4$	1	0.36	Li^+	1.30	0.19
			Zn^{+2}	0.14	0.22
AgI, bcc	2.69*	0.11	Ag^+		0.12

Asterisk denotes extrapolated values; E_σ and E_D stand for activation energies of conductivity and diffusion, respectively; D is a diffusion coefficient.

Phase diagrams of systems Li_2SO_4–Na_2SO_4, Li_2SO_4–Ag_2SO_4, Li_2SO_4–K_2SO_4, and Li_2SO_4–$ZnSO_4$ indicate the existence of several high-temperature conducting phases: $LiNaSO_4$ (bcc lattice), $LiAgSO_4$ (bcc lattice), and $Li_4Zn(SO_4)_3$ (non-cubic lattice). The double sulfate $LiKSO_4$, in turn, has hexagonal symmetry in the high-temperature modification.

Mentioned phases are of the most interest as solid electrolytes, since their conductivity reaches 1 $Ohm^{-1}cm^{-1}$ (at 600°C). It should be noted that along with high ionic conductivity, these sulfates possess also ferroelectric, ferroelastic and other related properties.

Table 2. Phase transition temperatures (T_{tr}) and enthalpies (ΔH_{tr}); melting temperatures (T_m) and enthalpies (ΔH_m) for different compounds [7, 21].

Phase	T_{tr}, K	ΔH_{tr}, eV	T_m, K	ΔH_m, eV
Li_2SO_4, fcc	850	0.258	1133	0.094
$LiNaSO_4$, bcc	788	0.257	888	Small
$LiAgSO_4$, bcc	710	-	845	0.036
$Li_{1.33}Zn_{0.33}SO_4$	755	0.263	852	Small
AgI, bcc	420	0.65	828	0.52

Comparison of some Li_2SO_4-based solid electrolytes with silver iodide (other well-known superionic conductor) is given in Tables 1 and 2. It is worth noting that in sulfates phase transition enthalpies are much higher than melting enthalpies, whereas in AgI these values are quite close. Let us note also that below the melting temperature the conductivity of AgI is slightly increased, whereas in sulfates the conductivity is decreased after the solidification: at 22% in Li_2SO_4, at 8% in $LiNaSO_4$, and at 5% in $LiAgSO_4$ [4, 30].

Double alkali sulfates with high ionic conductivity ($LiNaSO_4$, $LiKSO_4$) are the main subject of the present thesis. However, the low-conducting sulfates, $LiRbSO_4$ and $LiCsSO_4$, are also considered here. The main goal of the research is a detailed study of diffusion mechanisms in such crystals. In addition, we consider some related properties, such as phase transition kinetics, orientational disorder of sulfate groups, features of the high-temperature sintering, etc. It should be noted that we are focused mainly on temperatures below the phase transition to the superionic state. In fact, many of the properties typical for solid electrolytes (high value of the ionic conductivity, rotational disorder of molecular groups) appear in $LiNaSO_4$ and $LiKSO_4$ far below the transition temperature; therefore, better understanding of transport properties in given crystal requires consideration of low-temperature modifications.

I.3 Why does double alkali sulfate family deserve attention?

The two main members of the double alkali sulfate family, $LiNaSO_4$ (LNS) and $LiKSO_4$ (LKS) deserve a special attention, since both of these compounds have an extensive field of possible applications. Moreover, LNS and LKS are insensitive to the moisture unlike

a number of other lithium compounds (including Li_2SO_4) possessing high ionic conductivity [2]. Moreover, LNS and LKS single crystals are comparatively inexpensive and could be easily prepared from the water solution of corresponding alkali sulfates. These properties make these compounds a good candidate for application in solid-state batteries, fuel cells, and reserve batteries. The most promising application of LNS and LKS is a solid electrolyte in reserve batteries for military equipment (e.g. missiles) [3]. In reserve batteries, the electrolyte is stored in an inactive state and then is deliberately activated. In thermal reserve batteries, activation of the electrolyte could occur due to its melting or phase transition to the state with a high ionic conductivity. Unlike other reserve batteries, which require movement of electrolyte to activate them, the design of thermal batteries is mechanically simple and reliability is extremely high.

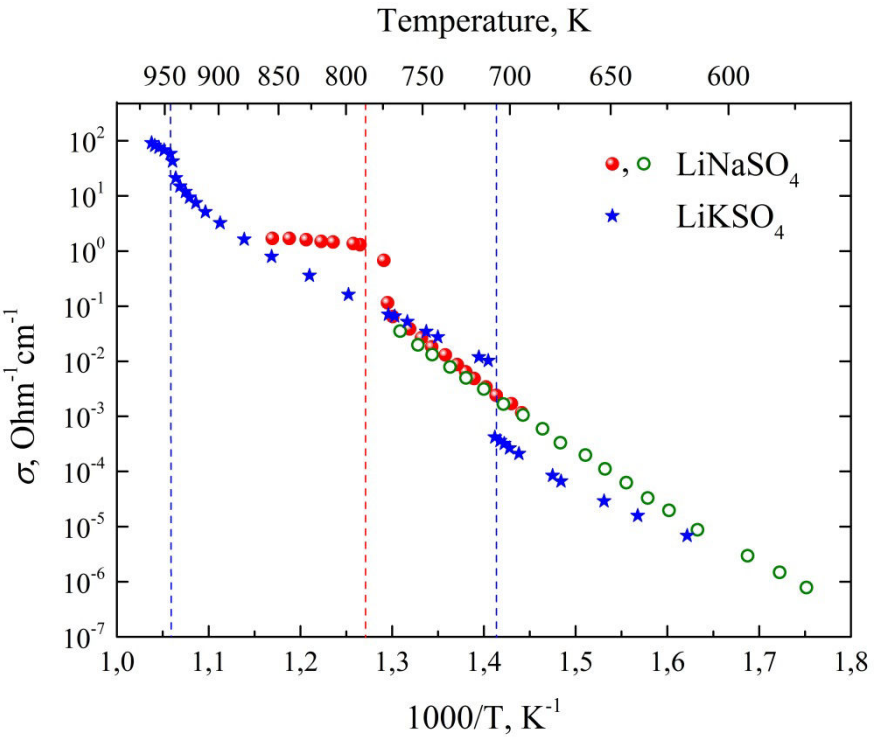

Fig. 2. Temperature dependences of the d.c. ionic conductivity in $LiNaSO_4$ single crystal (green empty dots) [4], in $LiNaSO_4$ powder (red filled dots) [5], and in $LiKSO_4$ single crystal perpendicular to the *c*-axis (blue stars) [6]. Blue dashed lines indicate phase transition temperatures in $LiKSO_4$ (708 and 943 K), whereas red dashed line indicates the phase transition temperature in $LiNaSO_4$ (788 K).

In the working temperature range of thermal batteries, 670-870 K [2], the ionic conductivity should be around 0.1 $Ohm^{-1}cm^{-1}$, whereas below 340 K the electrolyte has to have negligible conductivity to avoid self-discharge of the battery. Temperature dependences of the ionic conductivity in LNS and LKS are presented in Fig. 2. One can see that the

conductivity of LKS almost satisfies this requirement: in the 708-870 K temperature range (phase *II*) it grows steadily from 10^{-2} up to 10^{0} $Ohm^{-1}cm^{-1}$. The conductivity of LNS above 788 K (α-modification) is higher than in $LiKSO_4$; however, the temperature of the phase transition is still a little too high and the operating temperature range rather narrow. Unfortunately, LNS and LKS are not still widely used in batteries, although prototype cells with, e.g., Li_2SO_4-Na_2SO_4 compounds have already been used between 770-870 K [2].

Other field of possible applications of LNS is a design of fuel cells with proton conducting electrolytes, which does not require very high operating temperatures (900-1000°C) typically needed for solid oxide fuel cells. Thus, Feng *et al*. [31] developed a method to measure the proton conductivity of LNS under fuel cell conditions. Unfortunately, it was shown that the major portion of the ionic conductivity of α-LNS is due to Li^+ and Na^+ ion transport, and proton conductivity accounts for only 5-10% of total ion conductivity. It explains the poor performance of hydrocarbon conversion fuel cells using LNS as the electrolyte.

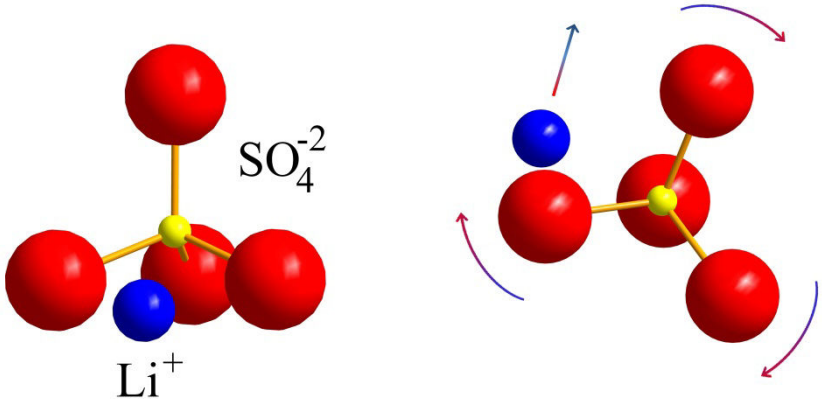

Fig. 3. Schematic representation of the paddle-wheel mechanism [5].

Despite of mentioned difficulties, LNS and LKS have not to be discounted, since the development of new current sources could make new demands to solid electrolytes. It is possible that LNS or LKS will satisfy these new demands and will find their niche.

In addition to their possible applications, both of these compounds are of interest from the academic point of view as model objects. In fact, along with "quasi-liquid" cationic sub-lattice, LNS and LKS have considerable rotational disorder of sulfate groups, and the coupling between rotational motions of SO_4 anions and cations occurs. The existence of these correlated motions led to the concept of a "paddle-wheel" or "cog-wheel" mechanism, according to which oxygen atoms push cations into neighboring interstices and/or vacancies,

and such "assistance" increases the ionic conductivity [7-9] (Fig. 3). Paddle-wheel mechanism considers the radii of cations of little importance for their diffusion rates in contrast to a so-called "percolation" mechanism [32-34], which emphasizes the role of cation radii and mass on the diffusion coefficients and favors the idea that the diffusion of cation is enhanced by the lattice expansion and/or incorporation of ion vacancies by guest ion presence. A dispute of authors upholding different views on the mechanism of the ionic motion in the LNS was resolved by Karlsson and McGreevy in 1995 [35]. Using neutron diffraction measurements and reverse Monte Carlo modeling they have reported that the ionic conductivity in Li_2SO_4 and $LiNaSO_4$ is a combination of both paddle-wheel and percolation mechanisms. Thus, it was noted that Na^+ ions always diffuse due to "paddle-wheel" mechanism because of its big radius (ionic radii of Na^+ and Li^+ ions are 0.97 Å and 0.68 Å, respectively [36]), whereas Li^+ ions can move differently. If Li^+ occupies $(\frac{1}{2},0,\frac{1}{4})$ site of the cubic cell, there is no correlation between its subsequent jump and the rotation of the neighboring SO_4 group that corresponds to percolation-type motion; from $(\frac{1}{4},0,0)$ positions, Li^+ ions move due to paddle-wheel.

1.4 Previous studies of double alkali sulfates: are there unresolved questions?

For more than half a century since the fast ionic conductivity was revealed in LNS, dozens of articles about its structure and properties were published. Features of the trigonal-to-cubic phase transition in LNS were studied in detail by Freiheit *et al* [10]. It was shown that the phase transition is completely reversible and hysteresis effects are very small in comparison to other first order phase transitions, i.e. only low kinetic barriers exist. The enthalpy of fusion, $\Delta H_f = 4.1\,\mathrm{kJ\,mol^{-1}}$, was found to be anomalously low compared to the enthalpy of the solid-solid transition, $\Delta H_{tr} = 20.8\,\mathrm{kJ\,mol^{-1}}$ [10]. The origin of this anomaly has been attributed to the dynamic and the reorientation of sulfate tetrahedral group in the LNS crystal. Such rotational disordering is typical of a plastic crystal; therefore, high-temperature phase of LNS is often referred to as a rotator phase [37]. The *α-β* transformation corresponds also to paraelastic-ferroelastic phase transition, i.e. a spontaneous strain occurs in the *β*-modification of LNS, where the evolution of rotational disorder of the sulfate groups plays the role of an order parameter [10, 38]. It was also noted by Freiheit *et al*. [10] that the

α-β phase transition is accompanied by a volume change of 6% (Fig. 4); however, the α- and β-form bear a close structural relationship [10, 38].

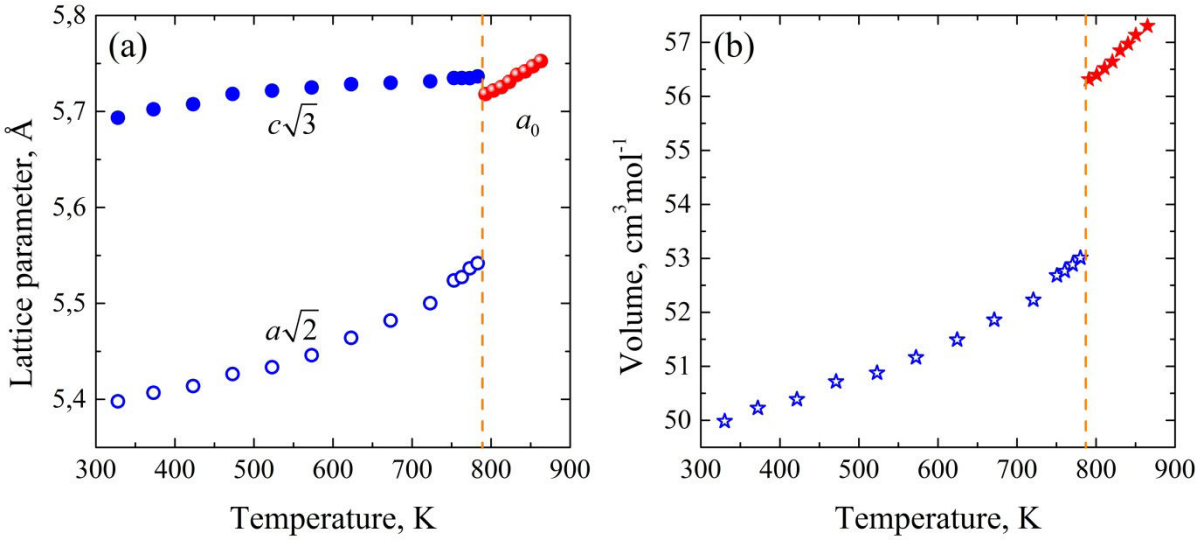

Fig. 4. (a) Variation of the scaled trigonal unit cell parameters ($a\sqrt{2}$, $c\sqrt{3}$) and the cubic unit cell parameter a_0 in $LiNaSO_4$ with temperature; (b) temperature dependence of the molar volume in $LiNaSO_4$. Dashed line indicates the phase transition temperature.

Features of the ionic mobility were studied by means of NMR relaxation [11, 39], NMR line width analysis [40], IR and Raman study [13, 41-44], ionic conductivity [4, 5, 31, 45] and diffusion [36] measurements. Massiot *et al*. [40] carried out ^{7}Li and ^{23}Na NMR line width analysis as well as spin-lattice relaxation measurements in a wide temperature range (295-940 K), and activation energies for Li^+ and Na^+ motion below the phase transition were estimated to be 0.86 and 1.54 eV, respectively. Thereby, it was revealed that both cations exhibit significant translational disorder far below the phase transition point. Kanashiro *et al*. [11] performed the spin-lattice relaxation measurements of ^{7}Li nuclei and revealed that the temperature evolution of the ^{7}Li spin-lattice relaxation rate in LNS single crystal at different magnetic fields could not be described by a single BPP curve, but the spectral density function with at least two correlation times has to be used (Fig. 5), i.e. diffusivity of both cationic sub-lattices was confirmed. The authors estimated activation energies for Li^+ and Na^+ motion below 788 K to be 0.7 and 1.20 eV, respectively.

Rotational disorder of the SO_4 anions in the LNS has been studied by inelastic and quasi-elastic neutron scattering [46], and by optical (IR and Raman) spectroscopy [12, 13, 43]. It was noted that the SO_4 orientational disorder as well as cationic mobility occurs also

well below the α-β phase transition [12, 13]. However, the low-temperature reorientations have only weak effect on the behavior of the Li^+ ions [13], i.e. there is no strong coupling between the cationic diffusion and the SO_4 reorientational jumps in the β-phase (below 788 K).

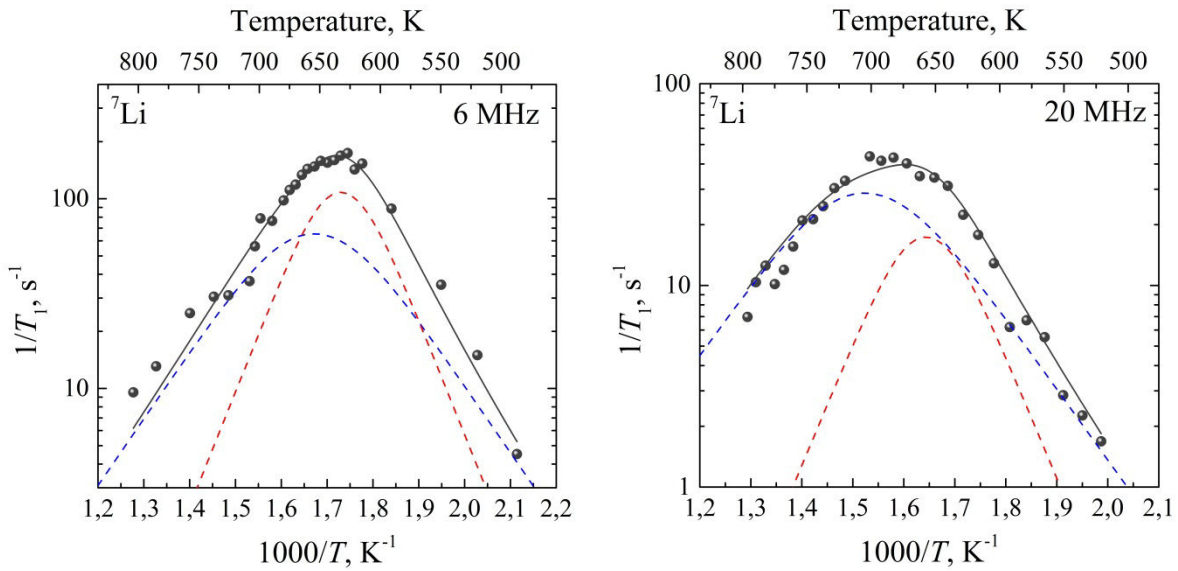

Fig. 5. Temperature dependences of ^{7}Li spin-lattice relaxation in $LiNaSO_4$ in two different magnetic fields with Larmor frequencies of ^{7}Li nuclei to be 6 MHz (on the left) and 20 MHz (on the right) [11]. An asymmetry of the $1/T_1$ curves was assumed to be due to simultaneous diffusion of two cationic sub-lattices: Li^+ and Na^+. The BPP contributions of Li and Na motion to relaxation are shown by red and blue dashed curves, respectively. Activation energies for ionic jumps were found to be $E_a^{Li} = 0.7\,\text{eV}$ and $E_a^{Na} = 1.2\,\text{eV}$.

As for LKS, the first publication (1890) on this compound described a phase transition at high temperature giving rise to a multi-domain structure [47]; seventeen years later Nacken [48] determined this transition temperature value as 708 K. Since then a great number of scientific works have been dedicated to this compound. The phase transition at 708 K was investigated by several experimental techniques, including double reflection [49], differential thermal analysis [50], measurement of thermal expansion coefficient, d.c. conductivity [6, 51], pyroelectric current and dielectric constants [51], X-ray diffraction study [52, 53], and Raman scattering [54]. The phase transition at 943 K was detected by differential thermal analysis [50] and by X-ray diffraction [55]. The most extensive study on lithium conductivity was carried out by Pimenta *et al*. [6] It was revealed that below 653 K and above 708 K the ionic conductivity of the LKS single crystal (along the *c*-axis) obeyed an Arrhenius law with activation energies 1.8 and 1.65 eV in phases *III* and *II*, respectively (Fig. 2).

Despite of plenty of experimental and theoretical studies devoted to alkali sulfates, some features of their structure and ionic dynamics are not clear or even have not been yet studied. Thus, only the structures of two modifications of LKS are now well established: the high-temperature modification (phase *I*, $T > 943$ K) and the room temperature modification (phase *III*, $203\ \text{K} < T < 708\ \text{K}$), whereas the structures of the intermediate phase and the phases below 203 K are still the subject of a dispute. Ionic mobility in LKS has been studied by conductivity measurements, i.e. in terms of the long-range transport, whereas NMR study of ionic mobility in LKS, which allows probing short-range local motions, has not been carried out.

A number of features of the LNS properties also have not been yet studied. Among such "gaps" are: 1) the temperature evolution of ^{7}Li and ^{23}Na self-diffusion coefficients below 788 K, 2) the kinetics of the *α-β* phase transition, 3) motional narrowing of the NMR line in the *β*-LNS, and some other features. Other question, which is still open, is the reorientational dynamics of SO_4 groups, particularly, the value of the activation energy of reorientational jumps in the *β*-phase. It is shown in the experimental part of this thesis, how to probe the SO_4 reorientations using temperature dependence of the ^{7}Li quadrupolar splitting, ν_Q, in the LNS single crystal.

Finally, the "low-conducting members" of the sulfate family, namely, $LiRbSO_4$ and $LiCsSO_4$ (and their solid solutions) have been extensively studied as ferroelectric compounds with interesting phase diagrams [14-19], whereas features of their ionic mobility has not been considered at all.

Thereby, the question embedded into the title of the present section is essentially positive. There are a number of unresolved problems in regard to ionic mobility in double alkali sulfates. It should be noted that if there were not such "gaps", the development of more advanced experimental techniques, which allow exploring "well-known" phenomena in more detail provides another reason to study these systems. One of these advanced experimental methods is the high-temperature pulsed field gradient (PFG) NMR technique [20], developed recently in CEMHTI, Orléans, which allows expanding the temperature range of self-diffusion measurements up to 1700 K. Some new applications of NMR spectroscopy for kinetics measurements have been developed in the scope of the present work to study the kinetics of the *α-β* phase transition in $LiNaSO_4$ (see chapter 4).

I.5 Synopsis

In the present work, nuclear magnetic resonance (NMR) is the principal method of investigation. Different methods of NMR allow investigating different types of motion in a broad range of characteristic times and so NMR plays an important role in the research of solids. There are a huge amount of NMR techniques, and theoretical aspects of them are developed nowadays into vast areas of science, so it is just impossible to write about all of them (even in brief) and to deal with their theoretical background. Therefore, we have decided to focus our attention only on some aspects of NMR relaxation theory of quadrupolar nuclei. The reason of such choice is caused by the fact that sulfates of alkali metals, which are the subject of the present work, consist of atoms containing quadrupolar nuclei. Thus, e.g. lithium-sodium sulfate $LiNaSO_4$ contains isotopes ^{7}Li, ^{23}Na, ^{33}S, having spin $I = 3/2$, isotope ^{6}Li with spin $I = 1$, and isotope ^{17}O, possessing spin $I = 5/2$.

In the first chapter of the thesis, "***Elements of NMR relaxation theory for quadrupolar nuclei***", we consider some aspects of NMR theory for quadrupolar nuclei in solids. As the present work is devoted mainly to the investigation of the ionic mobility in crystals, a great attention is naturally paid to measurements and interpretations of spin-lattice relaxation in the laboratory and in the rotating frames.

The second chapter, "***Theory and measurements of diffusion in solids***", is devoted to the problem of diffusion (and self-diffusion) in solids. The first section of this chapter gives a theoretical description of the diffusion processes, whereas the second one considers methods of measurements of a (self)diffusion coefficient. We focus there predominantly on principles of the PFG NMR. It is shown, how different types of echo (Hahn echo and stimulated echo) could be used in the experiment on diffusion.

Chapter 3, "***High temperature NMR***", considers experimental aspects of NMR measurements at high temperatures (HT). General features of HT NMR, particularly the question of temperature calibration, are considered in detail.

Finally, in chapter 4, "***Experimental study of alkali sulfates***", we present experimental results on ionic mobility in double alkali sulfates. Most attention has been paid to $LiNaSO_4$ as to the most interesting (in terms of the ion dynamics) compound among other double sulfates; however, lithium mobility in other double alkali sulfates with bigger cations (K^+, Rb^+, and Cs^+) is also considered.

In chapter 4, we presented measurements of the α-β phase transition kinetics in LNS, which have been carried out for the first time, thanks to the developed of a new NMR

technique, which is based on the difference of spin-lattice relaxation times in the two phases. Measurements of ^{7}Li and ^{23}Na self-diffusion coefficients in $LiNaSO_4$ as well as "traditional" measurements, such as spin-lattice relaxation and line width analysis, are also presented in the final chapter.

High-temperature NMR study of other relative compounds is also presented in chapter 4. The line width analysis and $T_{1\rho}$ measurements have been carried out for all of them. It should be noted that lithium mobility in $LiRbSO_4$ and $LiCsSO_4$ has been studied for the first time.

Along with a pure experimental study, some novel theoretical approaches have been also proposed. Thus, for the treatment of experimental data on LNS, we have obtained an expression for the dipolar correlation function characterizing the fluctuations of the Hamiltonian under uncorrelated diffusion of two cationic sub-lattices. A corresponding formula, which could be used for fitting of the two-step temperature dependencies of the NMR line width, has been deduced. The influence of the SO_4 reorientational jumps on the quadrupolar interactions of ^{7}Li nuclei was treated by a jump reorientational model, which has not been previously applied to sulfates. In addition, DFT calculations of NMR parameters in some compouns have been also carried out using a CASTEP code.

Chapter 1. Elements of NMR relaxation theory for quadrupolar nuclei

1.1 Quadrupolar Hamiltonian

1.1.1 Classical quadrupole moment of a nucleus

Assumption that an atomic nucleus is a spherical object with uniformly distributed positive charge is, in the general case, incorrect. In fact, if nuclei were ideal uniformly charged balls, then the electrostatic interaction of nuclei with surrounding electrons always would be equal to zero. However, it is known from the experiment that such interaction is nonzero in case of nuclei with the spin $I > 1/2$, moreover, *quadrupolar interactions* often play a major role in relaxation processes. It is experimentally proven that the dipole moment of nuclei is always zero [56]; therefore, an interaction of nuclei with the electric field is associated with electric moments of higher orders. As multipole moments of orders more than four play negligible role in nuclear magnetism, nuclei with the spin $I > 1/2$ are called *quadrupolar nuclei.*

Let us consider a nucleus as a system of point charges located in the small region of space. Let us put the origin of coordinates somewhere in the interior of the nucleus. It is obvious that in this case radius vectors of nucleons are much less than radius vectors of electrons, which could create the electric field. Thus, external (with respect to the nucleus) field potential $\varphi(\mathbf{r})$ at the site of the nucleon may be taken equal to the value of the potential in the origin of coordinates φ_0.

The energy of nucleons' interaction with the electric field could be written in the form of a classical sum:

$$U = \sum_a e_a \varphi(\mathbf{r}_a), \tag{1}$$

where e_a is a charge of the nucleon (for neutrons it equals to zero, and for protons it equals in absolute value to the elementary electronic charge), and $\mathbf{r}_a$ is its radius vector. Energy U can be developed as series in $\mathbf{r}_a$:

$$U = U^{(0)} + U^{(1)} + U^{(2)} + \ldots \tag{2}$$

The first term of the series,

$$U^{(0)} = \varphi_0 \cdot \sum_a e_a, \tag{3}$$

corresponds to an approximation, when all charges are situated in the same point. The second term of the series has the following form:

$$U^{(1)} = (\operatorname{grad}\varphi)_0 \sum_a e_a \mathbf{r}_a. \tag{4}$$

Introducing the field strength in the origin of coordinates, $\mathbf{E}_0 = -(\operatorname{grad}\varphi)_0$, and the dipole moment of the system, $\mathbf{d} = \sum_a e_a \mathbf{r}_a$, we have

$$U^{(1)} = -\mathbf{d}\mathbf{E}_0. \tag{5}$$

As it was mentioned above, the dipole moment of nuclei always equals to zero; therefore, $U^{(1)} = 0$. Finally, the third term of the series equals to

$$U^{(2)} = \frac{1}{2}\sum_{i,j}\sum_a e_a x_i^{(a)} x_j^{(a)} \frac{\partial^2 \varphi_0}{\partial x_i \partial x_j}. \tag{6}$$

Here x_i ranges over *x, y, z*.

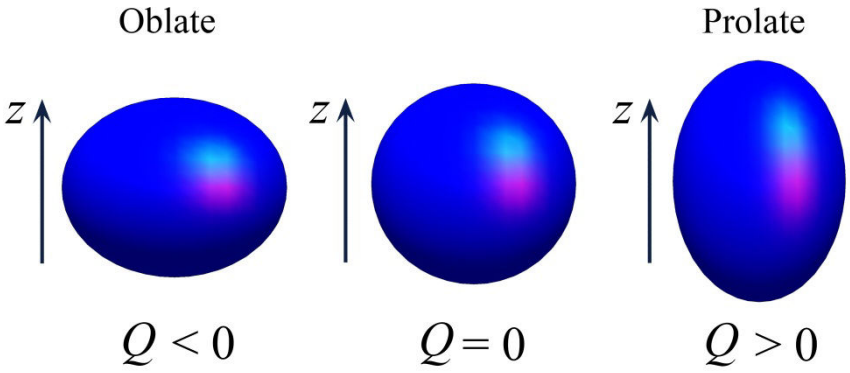

Fig. 6. Shapes of nucleus with different quadrupole moments.

Electric field potential φ satisfies the Laplace equation

$$\Delta\varphi \equiv \delta_{ij} \frac{\partial^2 \varphi}{\partial x_i \partial x_j} = 0, \tag{7}$$

where δ_{ij} is the Kronecker symbol. This implies that we can rewrite Eq. 6 in the following form:

$$U^{(2)} = \frac{1}{2}\sum_{i,j} \frac{\partial^2 \varphi_0}{\partial x_i \partial x_j} \sum_a e_a \left(x_i^{(a)} x_j^{(a)} - \frac{1}{3}\delta_{ij} r_a^2 \right), \tag{8}$$

or as

$$U^{(2)} = \frac{1}{6}\sum_{i,j} V_{ij} Q_{ij}, \tag{9}$$

where

$$Q_{ij} = \sum_a e_a \left(3x_i^{(a)} x_j^{(a)} - \delta_{ij} r_a^2\right) \tag{10}$$

is the *tensor of the quadrupole moment* of a nucleus, and

$$V_{ij} = \frac{\partial^2 \varphi_0}{\partial x_i \partial x_j} \tag{11}$$

is the *electric field gradient* (EFG) *tensor*.

It follows from Eq. 10 that the second rank tensor of the quadrupole moment is *symmetric* and *traceless*, consequently, Q_{ij} contains only five independent components. Any second rank tensor could be reduced to principle axes. If we assume that a nucleus is symmetric with respect to the rotation around some axis (*z*-axis), i.e. corresponds to the ellipsoid of revolution, then all of its three principal values are coupled by following way:

$$Q_{XX} = Q_{YY} = -\frac{1}{2} Q_{ZZ}. \tag{12}$$

The magnitude Q_{ZZ}/e is called the *quadrupole moment* of the nucleus (one designates it as *Q*). Using formula

$$eQ = Q_{ZZ} = \sum_a e_a \left(3z_a^2 - \delta_{ij} r_a^2\right), \tag{13}$$

one can see that the quadrupole moment of the nucleus defines the deviation of its shape from a sphere. If $Q > 0$, then the nucleus corresponds to the ellipsoid of revolution elongated along the *z*-axis; if $Q < 0$, the nucleus is oblate (Fig. 6). The measuring unit of *Q* is barn (1 barn equals to 10^{-28} m^2).

1.1.2 Quantum-mechanical formulation

Substituting tensor Q_{ij} by corresponding quantum-mechanical operator we shall obtain in Eq. 9 an expression for the quadrupolar Hamiltonian $\mathcal{H}_Q$. However, operator Q_{ij} in the form of Eq. 10 is very inconvenient for application, since it is expressed as the sum of nucleons. In such approach, the nucleus has to be regarded as a many-particle system. To turn aside this difficulty, we have to take into account that only nuclei in the ground state are investigated in NMR, i.e. only spatial reorientations of nuclei are of interest. Transition between eigenstates of nucleus is associated with the change of angular momentum *I*, i.e.

these transitions lead to the change of nuclear spin. In NMR nuclear spin is conserved, therefore we are interested only in those matrix elements of operator Q_{ij}, which are diagonal with respect to *I*. Using Wigner-Eckart theorem, one can show that [57]:

$$\left\langle I\,m\right|\sum_a e_a\left(3x_i^{(a)}x_j^{(a)}-\delta_{ij}r_a^2\right)\left|I\,m'\right\rangle = C\left\langle I\,m\right|\frac{3}{2}\left(I_iI_j+I_jI_i\right)-\delta_{ij}I^2\left|I\,m'\right\rangle. \tag{14}$$

Here m designates eigenstates of z component of the angular momentum, ranging over $2I+1$ values. Coefficient *C* is the same for all values of m, m', *i*, and *j*, therefore it could be expressed in terms of any matrix element in Eq. 14. It is convenient to do this for matrix element with $m=m'=I$ and $i=j=z$:

$$\left\langle I\,I\right|\sum_a e_a\left(3z_a^2-r_a^2\right)\left|I\,I\right\rangle = C\left\langle I\,I\right|3I_z^2-I^2\left|I\,I\right\rangle = CI\left(2I-1\right). \tag{15}$$

Left-hand term in Eq. 15 equals to *eQ*, therefore we have:

$$C=\frac{eQ}{I\left(2I-1\right)}. \tag{16}$$

Equation 14 allows carrying out the transition from many-particle problem to the consideration of a nucleus as a single particle with the spin *I*. In a new formulation, the quadrupolar Hamiltonian could be written in the following form:

$$\mathcal{H}_Q=\frac{eQ}{6I\left(2I-1\right)\hbar}\sum_{i,j}V_{ij}\left[\frac{3}{2}\left(I_iI_j+I_jI_i\right)-\delta_{ij}I^2\right]. \tag{17}$$

In the principle axis system (PAS) of tensor V_{ij} (let us designate this system by upper-case letters *XYZ*) the quadrupolar Hamiltonian takes the form

$$\mathcal{H}_Q^{\mathrm{PAS}}=\frac{eQ}{2I\left(2I-1\right)\hbar}\left\{V_{ZZ}I_Z^2+V_{XX}I_X^2+V_{YY}I_Y^2\right\}. \tag{18}$$

It is convenient to rewrite the Hamiltonian $\mathcal{H}_Q^{\mathrm{PAS}}$ in terms of operators I_Z, $I^+=I_X+iI_Y$, and $I^-=I_X-iI_Y$. Introducing following designations:

$$V_{ZZ}=eq,\ \frac{V_{XX}-V_{YY}}{V_{ZZ}}=\eta, \tag{19}$$

one can obtain:

$$\mathcal{H}_Q^{\mathrm{PAS}}=\frac{e^2qQ}{4I\left(2I-1\right)\hbar}\left\{3I_Z^2-I\left(I+1\right)+\frac{1}{2}\eta\left[\left(I^+\right)^2+\left(I^-\right)^2\right]\right\}. \tag{20}$$

The magnitude being before the curly brackets could be rewritten as follows:

$$\frac{e^2qQ}{4I(2I-1)\hbar}=\frac{1}{6}\chi_Q, \tag{21}$$

where

$$\chi_Q=\frac{3e^2qQ}{2I(2I-1)\hbar}=\frac{3\pi}{I(2I-1)}C_Q. \tag{22}$$

The magnitude

$$C_Q=\frac{e^2qQ}{h} \tag{23}$$

is called *quadrupolar coupling constant*; it is a measure of the strength of the quadrupolar interaction. The *asymmetry parameter* η, in turn, is a measure of the deviation of the EFG from an axial symmetry.

1.1.3 Spherical tensors

It is convenient to rewrite the Hamiltonian $\mathcal{H}_Q$ in terms of *spherical tensors* (*irreducible tensor operators*). A spherical tensor is a magnitude $T_l^{(m)}$, which transforms under the rotation of the coordinate system according to the following formula:

$$T_l^{(m)R}=\sum_n T_l^{(n)}\mathcal{D}_{nm}^l(\Omega),\quad n=l,l-1,...,-l, \tag{24}$$

where $T_l^{(m)R}$ is a spherical tensor in the rotated frame, and $\mathcal{D}(\Omega)$ is the rotation operator (so-called Wigner rotation matrix), matrix elements of which could be written in the following form:

$$\mathcal{D}_{mn}^l(\Omega)=e^{-im\alpha}d_{mn}^l(\beta)e^{-in\gamma}. \tag{25}$$

Here $\Omega=\{\alpha\beta\gamma\}$ is a set of Euler angles, and functions $d_{mn}^l(\beta)$ are tabulated elsewhere [58].

Using components of the second rank Cartesian tensor V_{ij} one can built linear combinations, which will transform according to Eq. 24. Such combinations could be written as follows [59]:

$$\begin{gathered}F_0^{(0)}=V^0,\\ F_1^{(0)}=V_{xy}^a,\quad F_1^{(\pm1)}=\pm\frac{1}{\sqrt{2}}\left(V_{yz}^a\mp iV_{xz}^a\right),\\ F_2^{(0)}=\sqrt{\frac{3}{2}}V_{zz}^s,\quad F_2^{(\pm1)}=\mp\left(V_{xz}^s\pm iV_{yz}^s\right),\quad F_2^{(\pm2)}=\frac{1}{2}\left(V_{xx}^s-V_{yy}^s\pm 2iV_{xy}^s\right).\end{gathered} \tag{26}$$

In terms of spin operators, spherical tensors (in this case, tensor operators) could be written as [60]:

$$T_0^{(0)} = \mathbf{1},$$

$$T_0^{(1)} = I_z,\ T_1^{(\pm 1)} = \mp\frac{1}{\sqrt{2}} I_{\pm}, \tag{27}$$

$$T_2^{(0)} = \frac{1}{\sqrt{6}}\left\{3I_z^2 - I(I+1)\right\},\ T_2^{(\pm 1)} = \mp\frac{1}{2}\left[I_z, I^{\pm}\right]_+,\ T_2^{(\pm 2)} = \frac{1}{2}\left(I^{\pm}\right)^2,$$

where brackets $[...]_+$ denote the anticommutator.

It should be noted that spherical tensors built of elements V_{ij} differ substantially from tensors built of spin operators. The fact is that the tensor $\mathbf{V}$ operates in the real three-dimensional space, whereas the spin tensor operates in the space spanned by basic functions of angular momentum operator, and dimensionality of its basis can be more than three. To express this difference explicitly we designate spin spherical tensors by letter *T*, and tensors built of elements V_{ij} – by letter *F*.

1.1.4 Spherical tensor representation of the quadrupolar Hamiltonian

It follows from Eq. 17 that the quadrupolar Hamiltonian can be represented in the form of a product of two Cartesian tensors: EFG tensor $\mathbf{V}$ and tensor $\mathbf{U}$ formed of pair products of the spin operators:

$$\mathcal{H}_Q = \mathbf{UV}. \tag{28}$$

It easy to show that a product of two Cartesian tensors could be written in the following form [59]:

$$\mathbf{UV} = 3U^0V^0 + \sum_{i,j=x,y,z}\left(U_{ij}^a V_{ij}^a + U_{ij}^s V_{ij}^s\right). \tag{29}$$

As the tensor $\mathbf{V}$ is traceless and symmetric, i.e. $V^0 = 0$ and $\mathbf{V}^a = \mathbf{0}$, the quadrupolar Hamiltonian could be written as

$$\mathcal{H}_Q = \sum_{i,j=x,y,z} U_{ij}^s V_{ij}^s. \tag{30}$$

One can see from Eq. 26 and Eq. 27 that elements of a symmetric Cartesian tensor could be arranged to build tensors $T_2^{(m)}$; therefore, it is clear that the quadrupolar Hamiltonian could be written in the form of pair products of second order spherical tensors.

Let us return to Eq. 17. Using the approach, which was used to rewrite it in the form of Eq. 20, one can obtain:

$$\mathcal{H}_Q = \Lambda_Q \sqrt{\frac{3}{2}} V_{zz} \frac{1}{\sqrt{6}} \left[3I_z^2 - I(I+1) \right] + \Lambda_Q \left(V_{xz} - iV_{yz} \right) \frac{1}{2} \left(I_z I^+ + I^+ I_z \right) +$$
$$+ \Lambda_Q \left(V_{xz} + iV_{yz} \right) \frac{1}{2} \left(I_z I^- + I^- I_z \right) + \Lambda_Q \frac{1}{2} \left(V_{xx} - V_{yy} - 2iV_{xy} \right) \frac{1}{2} \left(I^+ \right)^2 + \quad (31)$$
$$+ \Lambda_Q \frac{1}{2} \left(V_{xx} - V_{yy} + 2iV_{xy} \right) \frac{1}{2} \left(I^- \right)^2 .$$

Introducing spherical tensors via Eq. 12 one can write the quadrupolar Hamiltonian in the form of the series:

$$\mathcal{H}_Q = \Lambda_Q \sum_{m=-2}^{2} (-1)^m F_2^{(-m)} T_2^{(m)}, \quad (32)$$

where

$$F_2^{(0)} = \sqrt{\frac{3}{2}} V_{zz},$$
$$F_2^{(\pm 1)} = \mp \left(V_{xz} \pm iV_{yz} \right),$$
$$F_2^{(\pm 2)} = \frac{1}{2} \left(V_{xx} - V_{yy} \mp 2iV_{xy} \right), \quad (33)$$
$$\Lambda_Q = \frac{eQ}{2I(2I-1)\hbar},$$

and

$$T_2^{(0)} = \frac{1}{\sqrt{6}} \left\{ 3I_z^2 - I(I+1) \right\},$$
$$T_2^{(\pm 1)} = \mp \frac{1}{2} \left\{ I_z I^\pm + I^\pm I_z \right\}, \quad (34)$$
$$T_2^{(\pm 2)} = \frac{1}{2} \left(I^\pm \right)^2 .$$

One can see from Eq. 33 and Eq. 34 that

$$F_l^{(-m)} = (-1)^m F_l^{(m)*}, \quad T_l^{(-m)} = (-1)^m T_l^{(m)\dagger}. \quad (35)$$

1.1.5 Quadrupolar Hamiltonian in the laboratory system

It should be noted that Eq. 33 and Eq. 34 are valid in any coordinate frame. We can use this fact to find the expression for the quadrupolar Hamiltonian in the laboratory system. First, let us write the expression for the tensor V_{ij} in this system. To do this it is necessary to rotate it from the system associated with the crystal (PAS). Let us write the rotation matrix in terms of Euler angles [58]:

$$\mathbf{R}_\Omega = \mathbf{R}_z(\alpha)\mathbf{R}_y(\beta)\mathbf{R}_z(\gamma) = \begin{pmatrix} c_\alpha c_\beta c_\gamma - s_\alpha s_\gamma & -c_\alpha c_\beta s_\gamma - s_\alpha c_\gamma & c_\alpha s_\beta \\ s_\alpha c_\beta c_\gamma + c_\alpha s_\gamma & -s_\alpha c_\beta s_\gamma + c_\alpha c_\gamma & s_\alpha s_\beta \\ -s_\beta c_\gamma & s_\beta s_\gamma & c_\beta \end{pmatrix}, \tag{36}$$

where $c_\theta \equiv \cos\theta$, $s_\theta \equiv \sin\theta$. New tensor $\mathbf{V}^{\text{lab}}$ could be found by the use of the following formula:

$$\mathbf{V}^{\text{lab}} = \mathbf{R}_\Omega^{-1}\mathbf{V}^{\text{PAS}}\mathbf{R}_\Omega. \tag{37}$$

One can build tensors $F^{(m)}$ by means of Eq. 33, using elements of derived tensor $\mathbf{V}^{\text{lab}}$:

$$\begin{aligned} F_2^{(0)} &= \frac{\sqrt{6}}{4}V_{ZZ}\left(3\cos^2\beta - 1 + \eta\sin^2\beta\cos 2\alpha\right), \\ F_2^{(\pm 1)} &= \pm\frac{1}{4}V_{ZZ}e^{\mp i\gamma}\left\{3\sin 2\beta - \eta\left[\sin 2\beta\cos 2\alpha \mp i2\sin\beta\sin 2\alpha\right]\right\}, \\ F_2^{(\pm 2)} &= \frac{1}{4}V_{ZZ}e^{\mp i2\gamma}\left\{3\sin^2\beta + \eta\left[\left(1+\cos^2\beta\right)\cos 2\alpha \mp i2\cos\beta\sin 2\alpha\right]\right\}. \end{aligned} \tag{38}$$

The Hamiltonian $\mathcal{H}_Q$ in the laboratory system will have the following form:

$$\begin{aligned} \mathcal{H}_Q = \frac{eQ}{4I(2I-1)\hbar}\Bigg\{ & \frac{\sqrt{6}}{3}F_2^{(0)}\left[3I_z^2 - I(I+1)\right] + F_2^{(-1)}\left(I_zI^+ + I^+I_z\right) - \\ & -F_2^{(1)}\left(I_zI^- + I^-I_z\right) + F_2^{(-2)}\left(I^+\right)^2 + F_2^{(2)}\left(I^-\right)^2 \Bigg\}, \end{aligned} \tag{39}$$

where tensors $F_2^{(m)}$ are defined by Eq. 38.

1.1.6 The first- and the second-order quadrupolar interactions

As one can see from Eq. 39, the quadrupolar Hamiltonian contains operators $I^\pm$; therefore, most of the problems related to the spin dynamics will be complicated by the nondiagonality of $\mathcal{H}_Q$. To get the "nondiagonality" out the stationary perturbation theory is used, where $\mathcal{H}_Q$ is regarded as a small correction to the Zeeman Hamiltonian $\mathcal{H}_Z = \omega_L I_z$. Let us find first- and second-order corrections.

It is known from the stationary perturbation theory [61] that the zero-order correction is determined by eigenvalues of the operator $\mathcal{H}_Z$, e.

$$\omega_m^{(0)} = -m\omega_L. \tag{40}$$

The first-order correction is determined by diagonal elements of the matrix of perturbation operator, specified in the basis of $\mathcal{H}_Z$. In our case,

$$\omega_m^{(1)} = \left(\mathcal{H}_Q\right)_{mm}. \tag{41}$$

As $I_z|m\rangle = m|m\rangle$, it follows from Eq. 39 that

$$\omega_m^{(1)} = \frac{eQ}{4I(2I-1)\hbar}\frac{\sqrt{6}}{3}F_2^{(0)}\left[3m^2 - I(I+1)\right] \tag{42}$$

or in the operator form

$$\mathcal{H}_Q^{(1)} = \frac{eQ}{4I(2I-1)\hbar}\frac{\sqrt{6}}{3}F_2^{(0)}\left[3I_z^2 - I(I+1)\right] = \frac{1}{\sqrt{6}}\omega_Q^{(1)}T_2^{(0)}, \tag{43}$$

where

$$\omega_Q^{(1)} = \frac{1}{2}\chi_Q\left(3\cos^2\beta - 1 + \eta\sin^2\beta\cos 2\alpha\right) \tag{44}$$

The second-order correction is determined by nondiagonal matrix elements of the operator $\mathcal{H}_Q$:

$$\omega_m^{(2)} = \sum_n{}' \frac{\left|\left(\mathcal{H}_Q\right)_{nm}\right|^2}{\omega_m^{(0)} - \omega_n^{(0)}}; \tag{45}$$

the prime above the sum means that the summation takes under the condition $m \neq n$. Taking into account that $\omega_m^{(0)} - \omega_n^{(0)} = -\omega_L(m-n)$, one can write for $\omega_m^{(2)}$:

$$\omega_m^{(2)} = -\frac{1}{\omega_L}\sum_n{}' \frac{\left|\left(\mathcal{H}_Q\right)_{nm}\right|^2}{m-n}. \tag{46}$$

Required non-diagonal elements are determined by operators $I_zI^+ + I^+I_z$, $I_zI^- + I^-I_z$, $\left(I^+\right)^2$, and $\left(I^-\right)^2$. Recalling that

$$\begin{aligned} I^+|m\rangle &= \left[I(I+1) - m(m+1)\right]^{1/2}|m+1\rangle, \\ I^-|m\rangle &= \left[I(I+1) - m(m-1)\right]^{1/2}|m-1\rangle, \end{aligned} \tag{47}$$

we can write general expressions for non-diagonal elements

$$\begin{aligned} \langle m+1|I_zI^+ + I^+I_z|m\rangle &= (2m+1)\left[I(I+1) - m(m+1)\right]^{1/2}, \\ \langle m-1|I_zI^- + I^-I_z|m\rangle &= (2m-1)\left[I(I+1) - m(m-1)\right]^{1/2}, \\ \langle m+2|I^+I^+|m\rangle &= \left[I(I+1) - m(m+1)\right]^{1/2}\left[I(I+1) - (m+1)(m+2)\right]^{1/2}, \\ \langle m-2|I^+I^+|m\rangle &= \left[I(I+1) - m(m-1)\right]^{1/2}\left[I(I+1) - (m-1)(m-2)\right]^{1/2}. \end{aligned} \tag{48}$$

Taking into account that

$$\left|F_2^{(m)}\right|^2 = F_2^{(m)}F_2^{(m)*}, \quad F_2^{(m)*} = (-1)^m F_2^{(-m)}, \tag{49}$$

we have

$$\left|F_2^{(1)}\right|^2 = \left|F_2^{(-1)}\right|^2 = -F_2^{(1)}F_2^{(-1)},$$
$$\left|F_2^{(2)}\right|^2 = \left|F_2^{(-2)}\right|^2 = F_2^{(2)}F_2^{(-2)}. \tag{50}$$

Using Eqs. 39, 46-48, we shall obtain for the second-order correction the following expression

$$\omega_m^{(2)} = -\frac{1}{\omega_L}\left[\frac{eQ}{4I(2I-1)\hbar}\right]^2 \left\{2F_2^{(1)}F_2^{(-1)}m\left[4I(I+1)-8m^2-1\right]+ \right.$$
$$\left. +2F_2^{(2)}F_2^{(-2)}m\left[2I(I+1)-2m^2-1\right]\right\}. \tag{51}$$

Now let us consider nuclei with half-integer spin. In this case, as one can see from Eqs. 40, 42, and 51, the spectrum of a single crystal, where angles $\alpha, \beta,$ and γ are fixed, splits into $2I$ lines. The frequency of the central line (transition $-1/2 \leftrightarrow 1/2$) is determined by the following expression:

$$\omega^{\mathrm{CT}} = \omega_{-\frac{1}{2}} - \omega_{\frac{1}{2}} = \left(\omega_{-\frac{1}{2}}^{(0)} - \omega_{\frac{1}{2}}^{(0)}\right) + \left(\omega_{-\frac{1}{2}}^{(1)} - \omega_{\frac{1}{2}}^{(1)}\right) + \left(\omega_{-\frac{1}{2}}^{(2)} - \omega_{\frac{1}{2}}^{(2)}\right) =$$
$$= \underbrace{\omega_L}_{0^{\text{th}}\text{ order}} +$$
$$+ \underbrace{2\frac{1}{\omega_L}\left[\frac{eQ}{4I(2I-1)\hbar}\right]^2 \left\{F_2^{(1)}F_2^{(-1)}\left[4I(I+1)-3\right] + F_2^{(2)}F_2^{(-2)}\left[2I(I+1)-\frac{3}{2}\right]\right\}}_{2^{\text{nd}}\text{ order}}. \tag{52}$$

One can see from Eq. 52 that the first-order quadrupolar interaction has no influence on the position of the central line; this is the consequence of the fact that $\omega_m^{(1)}$ is an even function of m. Frequencies of external transitions for $I = 3/2$ are determined by

$$\omega_{1,2}^{\mathrm{ET}} = \pm\left(\omega_{\pm\frac{1}{2}}^{(0)} - \omega_{\pm\frac{3}{2}}^{(0)}\right) \pm \left(\omega_{\pm\frac{1}{2}}^{(1)} - \omega_{\pm\frac{3}{2}}^{(1)}\right) \pm \left(\omega_{\pm\frac{1}{2}}^{(2)} - \omega_{\pm\frac{3}{2}}^{(2)}\right) =$$
$$= \underbrace{\omega_L}_{0^{\text{th}}\text{ order}} \underbrace{\mp\frac{1}{\sqrt{6}}\frac{eQ}{\hbar}F_2^{(0)}}_{1^{\text{st}}\text{ order}} \underbrace{-\left(\frac{eQ}{\hbar}\right)^2 F_2^{(1)}F_2^{(-1)}}_{2^{\text{nd}}\text{ order}}. \tag{53}$$

Thus, the interaction of the quadrupolar moment of nuclei with EFG splits an NMR spectrum of a single crystal into $2I$ lines with frequencies determined by Eq. 52 and Eq. 53. It is interesting to note that the second-order correction changes the position of the central line as well as the frequencies of external transitions, but does not change the "distance" between satellites; this is the consequence of the fact that $\omega_m^{(1)}$ is an odd function of m.

Found expressions for $\omega_m^{(1)}$ and $\omega_m^{(2)}$ contain the Euler angles. It is worth noting that finding of these angles is often accompanied by a muddle, which is caused by the ambiguous

definition of Euler angles, by the use of the right-handed or left-handed coordinate systems, by the ambiguity (degeneracy) of rotation matrices, etc. Therefore, sometimes it is more convenient to express the Hamiltonian in the laboratory system or in the coordinate system related to the crystal. In this case, one has to find corrections of the perturbation theory using the Hamiltonian defined by Eq. 17:

Let us confine our consideration to the first order correction. It was mentioned above that it is defined by the diagonal elements of the quadrupolar Hamiltonian, e., by the operators I_x^2, I_y^2 and I_z^2. Matrix elements of the operator I_z^2 could be determined as follows: $\langle m|I_z^2|m\rangle = m^2$; expressions for the diagonal elements of the operators I_x^2, I_y^2 could be found using the rule of matrix multiplication:

$$\langle m|I_{x,y}^2|m\rangle = \langle m|I_{x,y}|m+1\rangle\langle m+1|I_{x,y}|m\rangle + \langle m|I_{x,y}|m-1\rangle\langle m-1|I_{x,y}|m\rangle. \tag{54}$$

It is known from the theory of the angular momentum [61] that

$$\begin{aligned}\langle m|I_x|m-1\rangle &= \langle m-1|I_x|m\rangle = \frac{1}{2}\sqrt{(I+m)(I-m+1)},\\ \langle m|I_y|m-1\rangle &= -\langle m-1|I_y|m\rangle = -\frac{i}{2}\sqrt{(I+m)(I-m+1)},\end{aligned} \tag{55}$$

so we shall obtain from Eq. 54 and Eq. 55:

$$\begin{aligned}\langle m|I_x^2|m\rangle = \langle m|I_y^2|m\rangle &= \frac{1}{4}(I+m-1)(I-m) + \frac{1}{4}(I+m)(I-m+1) =\\ &= \frac{1}{2}\left[-m^2 + I(I+1)\right].\end{aligned} \tag{56}$$

Thus, we have the following expression for $\mathcal{H}_Q^{(1)}$:

$$\mathcal{H}_Q^{(1)} = \frac{eQ}{2I(2I-1)\hbar}\left\{V_{zz}I_z^2 + \frac{1}{2}\left(V_{xx}+V_{yy}\right)\left[-I_z^2 + I(I+1)\right]\right\}. \tag{57}$$

Ab initio calculations of the NMR parameters are usually carried out in terms of tensor V_{ij} in the coordinate system related to the crystal. Substituting calculated tensor elements into Eq. 57 one will obtain the first order quadrupolar Hamiltonian and, consequently, the frequencies of the spectral lines. The rotation of the crystal in the laboratory frame could be reduced to the transformation (rotation) of the tensor V_{ij}.

1.2 Quadrupolar relaxation in solids

1.2.1 Phenomenological equation of spin-lattice relaxation

If system, containing equivalent nuclei of spin *I*, is put into an external magnetic field B_0, then the degeneracy of the spin energy will be removed, and the energy of each spin will be split into $2I+1$ equidistant levels. The "distance" between these levels (in terms of frequency) will be equal to γB_0, where γ is a gyromagnetic ratio. If we assume that the magnetic field arises suddenly, then, immediately Zeeman levels will be occupied by the same numbers of spins. To return to Boltzmann distribution, an irreversible process, so-called *magnetic relaxation*, occurs. In the course of time, which could be characterized by the magnitude T_1 (so-called *longitudinal* or *spin-lattice relaxation time*), the system will reach an equilibrium state.

If the *z*-axis is oriented along the external magnetic field, the equilibration of the longitudinal magnetization, in most cases, will satisfy the following phenomenological equation:

$$\frac{d\left(M_z - M_0\right)}{dt} = -\frac{1}{T_1}\left(M_z - M_0\right), \tag{58}$$

where M_z is the value of the longitudinal magnetization at time *t*, and M_0 is its equilibrium value.

A spin-lattice relaxation process could be interpreted as an energy exchange between the spin system and "the lattice" (the lattice is a common name of the spins' environment). The heat capacity of the lattice is assumed to be infinite, i.e. one supposes the lattice to be always in the equilibrium state, irrespective of the amount of energy imparted to it from the spin system. In its nature, the magnetic relaxation is caused by thermal motion of atoms, which is associated with the fluctuations of local magnetic as well as electric fields. In fact, the spectrum of the fluctuating field always contains the Fourier components with the frequencies being equal to the transition frequency between the levels of the spin system. Such varying local fields cause transitions between spin levels, and the equilibration occurs.

Since the motion of molecules causes the magnetic relaxation, measurement of T_1 at different temperatures allows studying the molecular dynamics in liquids, solids, or even in gases. The spin-lattice relaxation is most sensitive to the fluctuations with frequencies close to

ω_L; therefore, the T_1 measurements are usually used as a probe for molecular motions of the frequency $\sim 10^7 - 10^8$ Hz.

1.2.2 Measurement of spin-lattice relaxation

The usual technique for measuring T_1 is called *inversion recovery*. The pulse sequence is given by Fig. 7a and consists of two radiofrequency pulses separated by an interval τ, which varies during the experiment. A $(180°)_x$ pulse generates an inverted population distribution. Then the populations relax back towards thermal equilibrium during the interval τ and their progress is monitored by the $(90°)_x$ pulse, which converts the population difference into coherences, including the observable $p = -1$ quantum coherence (p denotes a coherence order), which induces an NMR signal (case $I = 1/2$) [56]:

$$s(\tau, t) = A(\tau) e^{i\omega_0 t} e^{-t/T_2^*}, \tag{59}$$

where T_2^* is the characteristic time of the free induction decay, whereas

$$A(\tau) = \frac{1}{2}\mathbb{B}\left(1 - 2e^{-\tau/T_1}\right) \tag{60}$$

and $\mathbb{B} = \hbar\gamma B_0 / kT$ is the Boltzmann factor. Thus, the amplitude of the signal $A(\tau)$ reflects the history of the longitudinal magnetization. The spectral peak amplitude is negative for small values of τ, but goes through zero and becomes positive for large values of τ.

It should be noted that for each value of τ the pulse sequence and data acquisition are normally repeated many times, adding the signals together in order to enhance the signal at the expense of the noise. Each repetition of the pulse sequence is separated by an interval τ_{wait}, during which the spins return to a reproducible thermal equilibrium state. For this to be satisfied, the waiting interval τ_{wait}, plus the signal acquisition period, must be several times the relaxation time constant, i.e. $\tau_{\text{wait}} = nT_1$, where $n = 5..7$.

Spin-lattice relaxation of quadrupole nuclei in solid dielectrics is governed by two mechanisms: 1) the lattice mechanism responsible for relaxation in “perfect” samples and 2) the impurity mechanism associated with the presence of impurity paramagnetic ions, radiation-induced centers, etc. The overall process of spin-lattice relaxation is characterized by the rate

$$\frac{1}{T_1^{\Sigma}} = \frac{1}{T_1^{lat}} + \frac{1}{T_1^{imp}}, \tag{61}$$

where T_1^{lat} and T_1^{imp} are the lattice and impurity components, respectively.

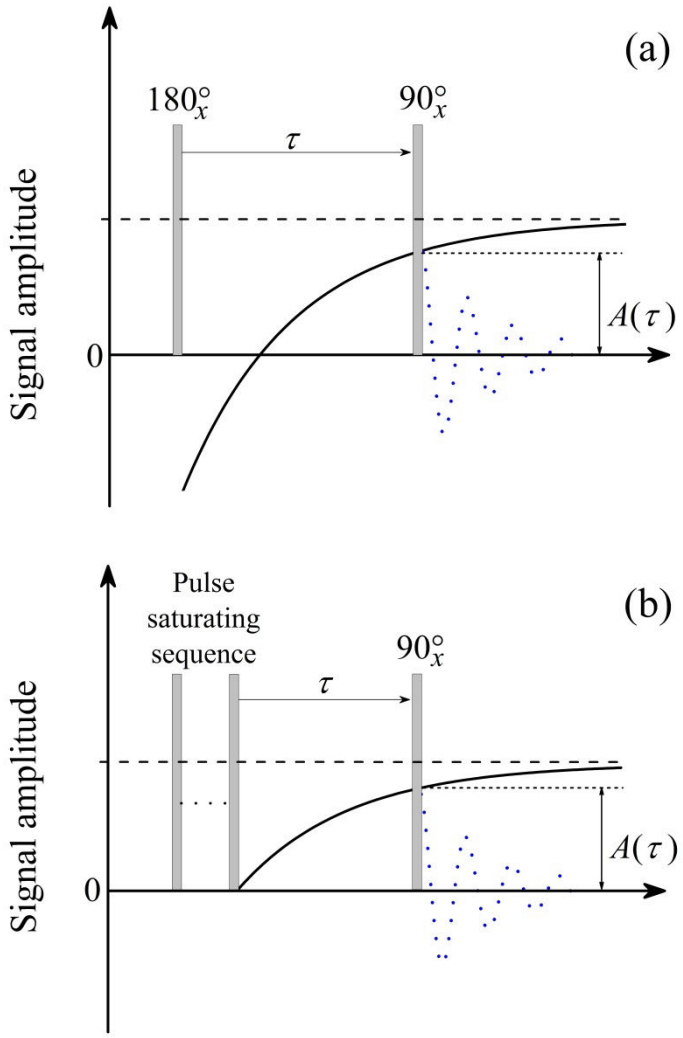

Fig. 7. Inversion recovery (a) and saturation recovery (b) pulse sequences. Solid line denotes a longitudinal magnetization recovery.

The former mechanism of spin-lattice relaxation in perfect crystals predominantly occurs through the modulation of the internuclear separation in the crystal lattice by thermal vibrations and, consequently, through changes in the electric-field gradient at a nucleus. Since the density of phonon states at frequencies close to the Larmor frequency is relatively low, Raman processes involving all phonons of the spectrum more efficiently manifest themselves in spin-lattice relaxation.

In ionic conductors, crystal ideality is broken not only due to the anharmonicity of lattice vibrations, but also by disordering of the cation and anion sub-lattices due to cation diffusion. In this case, relaxation is governed mainly by transaltional diffusion (of course, if concentration of paramagnetic impurities is negligible).

Unlike the lattice component, the impurity component T_1^{imp} characterizes the degree of perfection of a particular sample rather than the structure of the material. A theoretical evaluation of the impurity contribution is substantially complicated by the presence of undetectable paramagnetic centers, by the complex dependence of the spin relaxation rate of paramagnetic centers on temperature and concentration, etc. [62]

Note that it is impossible to separate the two contributions to spin-lattice relaxation by means of inversion recovery technique. Therefore, quadrupolar relaxation rate in solids is measured by special method based on suppressing the impurity contribution to nuclear spin-lattice relaxation through additional stationary saturation of the NMR line (see Fig. 7b). If the spin-lattice relaxation time is measured in the course of the nuclear magnetization recovery after complete saturation of the NMR line by a sequence of radiofrequency pulses (the so-called *saturation-recovery* method), the impurity relaxation makes a contribution to spin-lattice relaxation under the following condition [62]:

$$\varepsilon_{loc} > \langle \varepsilon \rangle, \tag{62}$$

where ε_{loc} is reciprocal of the local spin temperature in the vicinity of the impurity and $\langle \varepsilon \rangle$ is reciprocal of the mean spin temperature in other regions of the sample. Strong additional stationary acoustical, magnetic, or electric saturation of the NMR line can result in local overheating of the nuclear spin system in the vicinity of defects to $\varepsilon_{loc} = 0$, whereas $\langle \varepsilon \rangle$ becomes equal to a certain steady-state value $\langle \varepsilon \rangle > 0$. Thus, in the case when the regions near defects are overheated, Eq. 62 becomes invalid and the impurity contribution to spin-lattice relaxation is suppressed.

1.2.3 Master equation for the density matrix

Phenomenological equation of the spin-lattice relaxation, Eq. 58, does not contain information concerning the molecular motion. To find the relation between molecular dynamics and relaxation one has to use the density matrix formalism.

Time evolution of the density matrix is determined by the *von Neumann equation*:

$$\frac{d\sigma}{dt} = -i[\mathcal{H}, \sigma], \tag{63a}$$

where σ is the density matrix operator, $\mathcal{H}$ is the total Hamiltonian of the spin system, and square brackets designate a commutator (as above, the Hamiltonian is written in terms of frequency). If we want to describe relaxation, the time-dependent part of the total Hamiltonian associated with the fluctuations of the local fields has to be taken into account. Thus, the total

Hamiltonian could be written as follows: $\mathcal{H} = \mathcal{H}_0 + \mathcal{H}_1(t)$, where $\mathcal{H}_0 = \mathcal{H}_Z + \overline{\mathcal{H}_1}$, and $\overline{\mathcal{H}_1}$ is a non-averaged part of the fluctuating Hamiltonian. The term $\overline{\mathcal{H}_1}$ always exists in solids; it could correspond to residual dipolar or quadrupolar interaction. In liquids, this term often tends to zero. However, we shall assume that $\overline{\mathcal{H}_1} = 0$, since this term does not affect the spin-lattice relaxation. The von Neumann equation could be written now as follows:

$$\frac{d\sigma}{dt} = -i\left[\mathcal{H}_0 + \mathcal{H}_1(t), \sigma\right]. \tag{63b}$$

It should be noted that this equation is written in the laboratory system, and it is convenient to rewrite it in the interaction representation [63]. In this representation, the equation of motion will have the following form:

$$\frac{d\tilde{\sigma}}{dt} = -i\left[\tilde{\mathcal{H}}_1(t), \tilde{\sigma}\right], \tag{64}$$

where

$$\tilde{\sigma} = e^{i\mathcal{H}_0 t}\sigma e^{-i\mathcal{H}_0 t}, \quad \tilde{\mathcal{H}}_1 = e^{i\mathcal{H}_0 t}\mathcal{H}_1 e^{-i\mathcal{H}_0 t}. \tag{65}$$

After integration of Eq. 64 we have

$$\tilde{\sigma}(t) = \tilde{\sigma}(0) - i\int_0^t \left[\tilde{\mathcal{H}}_1(t'), \tilde{\sigma}(t')\right]dt'. \tag{66}$$

This integral equation can be solved by method of successive approximations (iteration method). Introducing new variable $\tau = t - t'$ we obtain for the second approximation

$$\frac{d\tilde{\sigma}}{dt} = -i\left[\tilde{\mathcal{H}}_1(t), \tilde{\sigma}(0)\right] - \int_0^t \left[\tilde{\mathcal{H}}_1(t), \left[\tilde{\mathcal{H}}_1(t-\tau), \tilde{\sigma}(0)\right]\right]d\tau. \tag{67}$$

The observable behavior of the system will be described by the ensemble-averaged value $\langle\tilde{\sigma}\rangle$. It is obvious that if the random function equiprobably takes positive and negative values, then its average value equals to zero; therefore, $\langle\mathcal{H}_1(t)\rangle = 0$. Thus, the first term in the right hand side of Eq. 67 disappears. One can show [64] that, under certain conditions, $\tilde{\sigma}(0)$ could be substituted by $\tilde{\sigma}(t)$. Hereby, omitting angle brackets at $\tilde{\sigma}(t)$, we can write the following equation:

$$\frac{d\tilde{\sigma}}{dt} = -\int_0^\infty \left\langle\left[\tilde{\mathcal{H}}_1(t), \left[\tilde{\mathcal{H}}_1(t-\tau), \tilde{\sigma}(t)\right]\right]\right\rangle d\tau. \tag{68}$$

It should be noted that the upper limit of integration was substituted by infinity. In fact, the main contribution to the integral $\int_0^t \left\langle \tilde{\mathcal{H}}_1(t)\tilde{\mathcal{H}}_1(t-\tau)\right\rangle d\tau$ is given by values of τ, which satisfy the inequality $\tau \le \tau_c$, where τ_c is a *correlation time* of fluctuations (see below). The contribution of members, satisfying the condition $\tau >> \tau_c$, is negligible; therefore one can spread the upper limit up to infinity. Equation 68 is called *master equation* for the density operator and is often referred to as a *weak-collision approximation*.

It is convenient to rewrite this equation in terms of spherical tensors. Before doing this, let us introduce some definitions.

1.2.4 Definition of the spectral density function

Let a stationary random function $F(t)$ with zero average value exist. Stationarity of this function means that it is invariant by the choice of the time origin. The function $G(\tau) = \left\langle F(t)F^*(t+\tau)\right\rangle$ is referred to as *autocorrelation function* of the random function $F(t)$, and because of its stationarity is time-independent (the asterisk means a complex conjugation). If there is a symmetry between the future and the past, then $G(-\tau) = G^*(\tau) = G(\tau)$, i.e. the autocorrelation function is even and real function of τ. It is obvious that under big values of τ values the function $F(t)$ cease to correlate; therefore, $G(\tau)$ equals to zero when $\tau \to \infty$.

Fourier transform

$$J(\omega) = 2\int_0^\infty G(\tau)\cos(\omega\tau)d\tau = \int_{-\infty}^{\infty} G(\tau)e^{-i\omega\tau}d\tau \qquad (69)$$

is referred to as *spectral density function*. Similarly, one can introduce a *cross correlation function* for two different random functions F_a and F_b

$$G_{ab}(\tau) = \left\langle F_a(t)F_b^*(t+\tau)\right\rangle \qquad (70)$$

and corresponding spectral densities.

1.2.5 Master equation for the density operator in terms of spherical tensors

The random Hamiltonian $\mathcal{H}_1(t)$ could be developed as a series in spherical tensors. Let us restrict our consideration only by the quadrupolar interaction, whose Hamiltonian is expressed in terms of the second rank spherical tensors:

$$\mathcal{H}_1(t) = \Lambda_Q \sum_{m=-2}^{2} (-1)^m F_2^{(-m)}(t) T_2^{(m)}, \tag{71}$$

where $F_2^{(m)}(t)$ are random functions, and $T_2^{(m)}$ are tensor operators acting on spin variables of the system. It is easy to show that, in the rotating frame, the following equality is valid (in the case under consideration, transition to the rotating frame coincides with the transition to the interaction representation):

$$\tilde{T}_2^{(m)} = T_2^{(m)} e^{im\omega_L t}; \tag{72}$$

therefore,

$$\tilde{\mathcal{H}}_1(t) = \Lambda_Q \sum_{m=-2}^{2} (-1)^m F_2^{(-m)}(t) T_2^{(m)} e^{im\omega_L t}. \tag{73}$$

Let us substitute Eq. 73 into Eq. 68:

$$\begin{aligned} \frac{d\tilde{\sigma}}{dt} = -\Lambda_Q^2 \sum_{m'=-2}^{2} \sum_{m=-2}^{2} \int_0^{\infty} (-1)^{m'+m} \left\langle F_2^{(-m')}(t) F_2^{(-m)}(t-\tau) \right\rangle e^{-im\omega_L \tau} d\tau \times \\ \times \left[T_2^{(m')}, \left[T_2^{(m)}, \tilde{\sigma}(t) \right] \right] e^{i(m'+m)\omega_L t}. \end{aligned} \tag{74}$$

Terms of Eq. 74 proportional to $e^{i(m'+m)\omega_L t}$ with $m' \neq m \neq 0$ vary rapidly in time; thereby, they are averaged to zero during the characteristic time of relaxation ($\tau \sim \tau_c$), if $(m'+m)\omega_L >> \tau_c^{-1}$. In this case, only terms with $m' = -m$ give the contribution to relaxation. Thus, one can write

$$\frac{d\tilde{\sigma}}{dt} = -\Lambda_Q^2 \sum_{m=-2}^{2} \int_0^{\infty} \left\langle F_2^{(m)}(t) F_2^{(-m)}(t-\tau) \right\rangle e^{-im\omega_L \tau} d\tau \left[T_2^{(-m)}, \left[T_2^{(m)}, \tilde{\sigma}(t) \right] \right]. \tag{75}$$

Taking into account that $F_2^{(-m)} = (-1)^m F_2^{*(m)}$ we shall obtain for the integral in Eq. 75:

$$\begin{aligned} \int_0^{\infty} \left\langle F_2^{(m)}(t) F_2^{(-m)}(t-\tau) \right\rangle e^{-im\omega_L \tau} d\tau = (-1)^m \int_0^{\infty} \left\langle F_2^{(m)}(t) F_2^{*(m)}(t-\tau) \right\rangle e^{-im\omega_L \tau} d\tau = \\ = (-1)^m \frac{1}{2} J_m(m\omega_L) + i(-1)^{m+1} \int_0^{\infty} G_m(\tau) \sin(m\omega_L \tau) d\tau. \end{aligned} \tag{76}$$

where $J_m(m\omega_L)$ are spectral densities, and $G_m(\tau)$ are corresponding correlation functions. One can show that the imaginary term leads to the shift of the energy of the spin system; this

shift could be included into the main Hamiltonian $\mathcal{H}_0$, therefore we can drop it [64]. As a result, we have the equation

$$\frac{d\tilde{\sigma}}{dt} = -\frac{1}{2}\Lambda_Q^2 \sum_{m=-2}^{2} (-1)^m J_m(m\omega_L)\left[T_2^{(-m)},\left[T_2^{(m)},\tilde{\sigma}(t)\right]\right]. \tag{77}$$

It should be noted that the Hamiltonian expansion, specified by Eq. 71, corresponds to the semi-classical approximation, since the influence of the lattice is specified by "classical" functions $F^{(m)}(t)$, whose spectral densities $J_m(m\omega_L)$ given by Eq. 76 obey the following obvious condition:

$$J_m(m\omega_L) = J_{-m}(-m\omega_L). \tag{78}$$

However, when using pure quantum mechanical approach, functions $F^{(m)}(t)$ have to be substituted by the corresponding operators, and Eq. 78 will take the following form [64]:

$$J_m(m\omega_L) = \exp\left(-\frac{\hbar m\omega_L}{kT}\right) J_{-m}(-m\omega_L). \tag{79}$$

Equation 79 coincides with Eq. 78 only when $T \to \infty$; therefore, the perturbative solution given by Eq. 77 is only valid for infinite temperature. However, it could be shown [64] that the weak-collision approximation can also be applied if $\tilde{\sigma}$ is interpreted as the difference between $\tilde{\sigma}$ and the equilibrium density operator

$$\tilde{\sigma}^{eq} = \sigma^{eq} = \frac{\exp(-\hbar\mathcal{H}_0 / kT)}{\mathrm{Sp}\{\exp(-\hbar\mathcal{H}_0 / kT)\}}. \tag{80}$$

Thereby,

$$\frac{d}{dt}\left(\tilde{\sigma}(t) - \sigma^{eq}\right) = -\frac{1}{2}\Lambda_Q^2 \sum_{m=-2}^{2} (-1)^m J_m(m\omega_L)\left[T_2^{(-m)},\left[T_2^{(m)},\tilde{\sigma}(t) - \sigma^{eq}\right]\right]. \tag{81}$$

The following solution of the problem could be executed by different ways. In the first approach, which was developed by Abragam [64], one has to try to rewrite Eq. 81 in the form of the macroscopic differential equation (Eq. 58); if it is possible, then the formula for the spin-lattice relaxation rate is obtained automatically. This approach is limited by the cases of dipolar relaxation and quadrupolar relaxation of spins $I = 1$; for higher spins this method doesn't work. However, Abragam's approach could be generalized by the introduction of fictitious spin-1/2 operators [65], using which one can always reduce the master equation to the form of Eq. 58.

The second approach is based on the introduction of the so-called relaxation supermatrix. This approach as well as the formalism of the fictitious spin-1/2 operators implies the transition to the Liouville space.

1.2.6 Multi-exponential spin-lattice relaxation in I=3/2 systems

Using the relaxation supermatrix technique one can show [66] that recovery of the longitudinal magnetization of $I = 3/2$ system after the saturation-recovery pulse sequence is determined as follows:

$$M_z(\tau) = M_z^{eq}\left[1 - \frac{4}{5}\exp(R_2^{(0)}\tau) - \frac{1}{5}\exp(R_1^{(0)}\tau)\right], \tag{82}$$

where the spin-lattice relaxation rates $R_2^{(0)}$ and $R_1^{(0)}$ are defined as

$$R_1^{(0)} = -\Lambda_Q^2 J_1, \quad R_2^{(0)} = -\Lambda_Q^2 J_2, \tag{83}$$

where Λ_Q is determined by Eq. 33, and J_m is a spectral density at frequency $m\omega_L$ defined by

$$J_m(m\omega_L) = \int_{-\infty}^{\infty} \left\langle F_2^{(m)}(t) F_2^{*(m)}(t-\tau)\right\rangle e^{-im\omega_L\tau} d\tau, \tag{84}$$

where the field gradient tensors $F_2^{(m)}$ are given by Eq. 34.

Note also that generally one can separate the contribution of the external transitions from the central transition. For example, in single crystal with magnetically identical spins, one can measure the intensity of the satellites separately from the intensity of the central line. It is easy to show using an approach of G. Jaccard *et al*. [66] that the time evolution of the external transition due to spin-lattice relaxation is monoexponential:

$$A^{\mathrm{ET}}(\tau) \sim \frac{3}{4}\mathbb{B}\left[1 - \exp(R_2^{(0)}\tau)\right], \tag{85}$$

while the central transition relaxes through two exponents

$$A^{\mathrm{CT}}(\tau) \sim \mathbb{B}\left[1 - \frac{1}{2}\exp(R_2^{(0)}\tau) - \frac{1}{2}\exp(R_1^{(0)}\tau)\right]. \tag{86}$$

Equation 82 yields very important result: unlike the $I \le 1$ system, whose relaxation is monoexponential and could be characterized by the single relaxation rate (Eq. 60), the $I = 3/2$ system relaxes through two exponents with two different relaxation rates. Let us desscribe the nature of such "multi-exponential" behavior.

The motion of surrounding charges produces at the nucleus position field-gradient components, which are function of time. Equation 31 shows that the resulting time-dependent quadrupolar Hamiltonian $\mathcal{H}_Q$, which couples nuclear spins to the surrounding lattice, can lead to transitions, in which the nucleus changes its quantum number *m* by $\Delta m = \pm 1$ or $\Delta m = \pm 2$. For clarity, let us write the Hamiltonian $\mathcal{H}_Q$ for $I = 3/2$ system in its explicit matrix form:

$$\mathcal{H}_Q(t) = \Lambda_Q \sqrt{3} \begin{pmatrix} F_2^{(0)}(t)/\sqrt{2} & F_2^{(-1)}(t) & F_2^{(+2)}(t) & 0 \\ -F_2^{(+1)}(t) & -F_2^{(0)}(t)/\sqrt{2} & 0 & F_2^{(+2)}(t) \\ F_2^{(-2)}(t) & 0 & -F_2^{(0)}(t)/\sqrt{2} & -F_2^{(-1)}(t) \\ 0 & F_2^{(-2)}(t) & F_2^{(+1)}(t) & F_2^{(0)}(t)/\sqrt{2} \end{pmatrix}. \tag{87}$$

Let examine how quadrupolar relaxation processes affect the behavior of the central line.

The first peculiarity to be noted is that, although one observes the absorption of radio-frequency power only in the –1/2↔1/2 transition, the quadrupolar Hamiltonian $\mathcal{H}_Q$ responsible for the relaxation induces transitions between all energy levels for which $\Delta m = \pm 1,\ \pm 2$ except between the levels 1/2 and –1/2, since $\langle \tfrac{1}{2} | \mathcal{H}_Q | \tfrac{1}{2} \rangle - \langle -\tfrac{1}{2} | \mathcal{H}_Q | -\tfrac{1}{2} \rangle = 0$. The nuclear relaxation, therefore, takes place in a roundabout way. Let *w* denote the transition probability per unit time for transitions –1/2↔1/2 induced by the applied radio-frequency field; let W_{mn} be the transition probability per unit time for the nuclear transition from state *m* to state *n* induced by the time-dependent Hamiltonian $\mathcal{H}_Q$ responsible for relaxation. The four equations determining the time dependence of the numbers N_m of nuclei in each of the four energy states *m* are then given by [67]

$$\frac{d}{dt} N_m = \sum_{n,m \neq n} \left[-N_m (W_{mn} + w_{mn}) + N_n (W_{nm} + w_{nm}) \right], \tag{88}$$

where $w_{mn} = 0$ except $w_{\frac{1}{2},-\frac{1}{2}} = w_{-\frac{1}{2},\frac{1}{2}} = w$.

As a first approximation, one can compute the transition probabilities arising from $\mathcal{H}_Q$ by regarding the four nuclear energy levels to be equally spaced by amount ω_L (in terms of frequency), where ω_L is the Larmor frequency. According to the Fermi's golden rule, the transition probability is $W_{mn} \sim \left| \langle n | \mathcal{H}_Q | m \rangle \right|^2$; it is obvious from Eq. 87 that the matrix elements are such that one can express the upward transition probabilities in the form

$$W_{\frac{1}{2},-\frac{1}{2}} = 0, \quad W_{\frac{3}{2},\frac{1}{2}} = W_{-\frac{1}{2},-\frac{3}{2}} \equiv W_1, \quad W_{\frac{3}{2},-\frac{1}{2}} = W_{\frac{1}{2},-\frac{3}{2}} \equiv W_2. \tag{89}$$

The quantities W_1 and W_2 thus defined represent transition probabilities between levels separated by ω_L and $2\omega_L$, respectively. From general principles of statistical mechanics (e.g., detailed balancing), one knows that W_{nm} is related to the inverse transition probability W_{mn} from a state of energy E_m to that of energy E_n by

$W_{nm}/W_{mn} = \exp\left[-(E_m - E_n)/kT\right]$. Since $\Delta = \hbar\omega_L/kT << 1$ one can then write the downward transition probabilities in the form

$$W_{-1/2,1/2} = 0, \quad W_{1/2,3/2} = W_{-3/2,-1/2} \equiv W_1(1+\Delta), \quad W_{-1/2,3/2} = W_{-3/2,1/2} \equiv W_2(1+\Delta). \tag{90}$$

Equations 88 could be reduced to two equations for the quantities

$$\begin{aligned} n_{1/2} &= N_{1/2} - N_{-1/2}, \\ n_{1/2} &= N_{3/2} - N_{-3/2}, \end{aligned} \tag{91}$$

namely

$$\begin{cases} \dot{n}_{1/2} = -n_{1/2}(W_1 + W_2 + 2w) + n_{3/2}(W_1 - W_2) + N\Delta(W_2 - 1/2\,W_2) \\ \dot{n}_{3/2} = -n_{1/2}(W_1 + W_2) + n_{1/2}(W_1 - W_2) + N\Delta(W_2 - 1/2\,W_2) \end{cases}. \tag{92}$$

Here we made use of the fact that the population of any level never departs appreciably from $N/4$, N being the total number of nuclei. In the absence of an external radio-frequency field $(w = 0)$, a transient measurement of the recovery of the population difference $n_{1/2}$ to its equilibrium value $n_{1/2}^{eq}$ would show the following dependence:

$$n_{1/2}(t) = n_{1/2}^{eq} + C_1 \exp(-2W_1 t) + C_2 \exp(-2W_2 t), \tag{93}$$

where C_1 and C_2 are constants depending on the initial condition. If the recovery of the population difference $n_{1/2}$ is measured via inversion recovery method, Eq. 93 coincides with Eq. 82 that indicates the equivalence of two approaches used for derivation of these equations. The following compliance is obvious:

$$R_1^{(0)} = -2W_1, \quad R_2^{(0)} = -2W_2, \tag{94}$$

where the relaxation rates are defined by Eq. 83.

To summarize the above, note once again that the relaxation process of the $I = 3/2$ system is characterized by the two relaxation rates corresponding to single-quantum, W_1, and double-quantum, W_2, transition probabilities. It should be noted that these probabilities are not equal, in general, not only do they involve different spin operators, but, more important, they involve different components of the fluctuating electric field gradient tensor. It is interesting that despite of the coupling of transitions between the energy states, relaxation of the external transitions is determined only by the single-quantum transition probability (see Eq. 85). This gives the means for finding W_1 and W_2 separately.

An explicit calculation of the nuclear relaxation time quite generally involves only a calculation of transition probabilities of the type W_1 and W_2 produced by the time-dependent quadrupolar Hamiltonian $\mathcal{H}_Q$. The field-gradient components $F_2^{(m)}$ (see Eq. 33) are functions of time because of the motion of charges. It follows from the Hamiltonian given by Eq. 32 that the Fourier components of $F_2^{(\pm 1)}$ near the nuclear frequency ω_L and components of $F_2^{(\pm 2)}$ near the frequency $2\omega_L$ are those effective in including the nuclear transition (characterized by probabilities W_1 and W_2) in which m changes by $\Delta m = \pm 1$ and by $\Delta m = \pm 2$ respectively. Thus, the following solution of the problem is reduced to the Fourier analysis of $F_2^{(m)}$.

1.2.7 Spin-lattice relaxation in the rotating frame

As we have just noted, spin-lattice relaxation is the most sensitive to the fluctuations occuring at frequencies close to ω_L. Since magnetic fields usually used in the relaxation experiment belong to the range 0.5–10 T, the Larmor frequency could take the values in the range $10^7 - 10^9$ MHz. Therefore, spin-lattice relaxation allows measuring the molecular dynamics with characteristic times being in the range $\tau_c \sim 10^{-9} - 10^{-7}$ s. Thus, slow molecular motion ($\tau_c \sim 10^{-2} - 10^{-3}$ s) is not available with this technique. For investigation of a slow molecular motion so-called *spin-lattice relaxation in the rotating frame* $T_{1\rho}$ is usually measured.

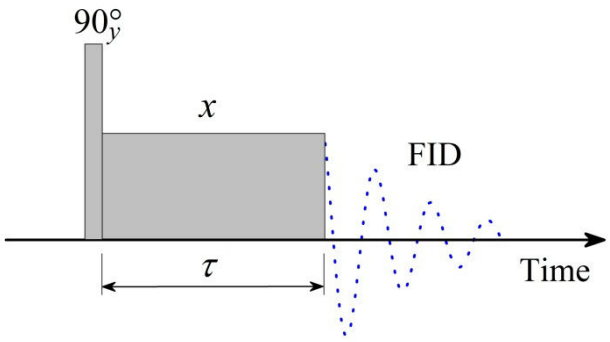

Fig. 8. Pulse sequence for measuring of $T_{1\rho}$.

Measurement of $T_{1\rho}$ is based on the locking of the transverse magnetization. A typical spin-locking pulse sequence is presented in Fig. 8. First, let us consider the effect of the spin-locking experiment on the $I = 1/2$ system.

The initial $(90°)_y$-pulse converts the initial longitudinal magnetization into transverse magnetization along the rotating frame x'-axis. The phase of the radiofrequency field is suddenly changed to $\varphi_p = 0$, so that the rotating frame radiofrequency field B_1 is also along the x'-axis, i.e. in the same direction as the transverse magnetization. If the radiofrequency field is large enough, then the transverse magnetization is unable to precess away from the x'-axis – it is said to be *spin-locked*. After a time τ, the locking field B_1 is turned off, releasing the transverse magnetization and allowing it to generate an NMR signal. Due to relaxation processes, the spin-locked magnetization decays exponentially to zero. The decay process may be followed by conducting a series of experiments with several values of the locking time τ. The time constant of the exponential decay is usually denoted $T_{1\rho}$, and is usually called the *spin lattice relaxation time constant in the rotating frame*.

In case of quadrupolar nuclei, spin-lattice relaxation in the rotating frame, similar to spin-lattice relaxation in the laboratory frame, shows non-exponentiality. Let us consider a $T_{1\rho}$ theory in detail.

The Hamiltonian of the system, in the presence of the radiofrequency field, could be written as

$$\mathcal{H} = \mathcal{H}_Z + \mathcal{H}_1(t) + \mathcal{H}_{\mathrm{RF}}(t), \tag{95}$$

where, as above, we assumed that non-averaged part of the fluctuating Hamiltonian $\overline{\mathcal{H}_1}$ equals to zero; $\mathcal{H}_{\mathrm{RF}}(t)$ is the Hamiltonian of the radiofrequency field oscillating with frequency $\omega = \omega_L$. In the rotating frame, the Hamiltonian is

$$\tilde{\mathcal{H}} = \tilde{\mathcal{H}}_1(t) + I_x \omega_{nut}, \tag{96}$$

where ω_{nut} is a nutation frequency. The von Neumann equation thus could be written as

$$\frac{d\tilde{\sigma}}{dt} = -i\left[\tilde{\mathcal{H}}_1(t) + I_x \omega_{nut}, \tilde{\sigma}\right]. \tag{97}$$

It should be noted that transition to the rotating frame does not correspond here to the interaction representation. The latter could be introduced by the following formula:

$$\tilde{\tilde{\sigma}} = e^{iI_x\omega_{nut}t}\tilde{\sigma}e^{-iI_x\omega_{nut}t}. \tag{98}$$

The von Neumann equation, in the interaction representation, has the following form:

$$\frac{d\tilde{\tilde{\sigma}}}{dt} = -i\left[\tilde{\tilde{\mathcal{H}}}_1(t), \tilde{\tilde{\sigma}}\right]. \tag{99}$$

This representation describes motion in the *doubly rotating frame*, i.e. in a frame rotating about B_1 which is rotating about B_0. Restricting ourselves by quadrupolar interactions one can substitute $\tilde{\tilde{\mathcal{H}}}_1(t)$ by its usual expansion in terms of spherical tensors (Eq. 73). Similar to Eq. 72, one can find for the second order normalized irreducible tensor operators in the doubly rotating frame the following relations:

$$\tilde{\tilde{\hat{T}}}_2^{(m)} = \sum_{n=-2}^{2} \hat{B}_n^{(m)} e^{i(m\omega_L + n\omega_{nut})t}, \tag{100}$$

where $\hat{T}_l^{(m)}$ are *normalized* irreducible spherical tensors, whose normalization is defined as follows:

$$\hat{T}_l^{(m)} = \frac{1}{l!}\left[\frac{(2l+1)(2I-l)!\,2^l\,(2l)!}{(2I+l+1)!}\right]^{1/2} T_l^{(m)}. \tag{101}$$

Operators $\hat{B}_n^{(m)}$, in turn, may be written as linear combinations of $\hat{T}_2^{(m)}$

$$\begin{gathered}
\hat{B}_{\pm1}^{(0)} = \hat{B}_0^{(\pm1)} = 0, \\
\hat{B}_0^{(0)} = -\frac{2}{\sqrt{6}}\hat{B}_0^{(\pm2)} = \frac{1}{4}\hat{T}_2^{(0)} - \frac{\sqrt{6}}{8}\left(T_2^{(2)} + T_2^{(-2)}\right), \\
\hat{B}_{\pm2}^{(0)} = \sqrt{6}\hat{B}_{\pm2}^{(2)} = \sqrt{6}\hat{B}_{\pm2}^{(-2)} = \frac{3}{8}\hat{T}_2^{(0)} \pm \frac{\sqrt{6}}{8}\left(\hat{T}_2^{(1)} + \hat{T}_2^{(-1)}\right) + \frac{\sqrt{6}}{16}\left(\hat{T}_2^{(2)} + \hat{T}_2^{(-2)}\right), \\
\hat{B}_{\pm1}^{(1)} = -\hat{B}_{\pm1}^{(-1)} = \frac{1}{4}\left(\hat{T}_2^{(1)} - \hat{T}_2^{(-1)}\right) \pm \frac{1}{4}\left(\hat{T}_2^{(2)} - \hat{T}_2^{(-2)}\right), \\
\hat{B}_{\pm2}^{(1)} = \hat{B}_{\pm2}^{(-1)} = \pm\frac{\sqrt{6}}{8}\hat{T}_2^{(0)} + \frac{1}{4}\left(\hat{T}_2^{(1)} + \hat{T}_2^{(-1)}\right) \pm \frac{1}{8}\left(\hat{T}_2^{(2)} + \hat{T}_2^{(-2)}\right), \\
\hat{B}_{\pm1}^{(2)} = \hat{B}_{\pm1}^{(-2)} = \mp\frac{1}{4}\left(\hat{T}_2^{(1)} - \hat{T}_2^{(-1)}\right) + \frac{1}{4}\left(\hat{T}_2^{(2)} - \hat{T}_2^{(-2)}\right).
\end{gathered} \tag{102}$$

So, we have for the quadrupolar Hamiltonian, in the doubly rotating frame:

$$\tilde{\tilde{\mathcal{H}}}_1(t) = \Lambda_Q \sum_{m=-2}^{2}\sum_{n=-2}^{2} (-1)^m F_2^{(m)} \hat{B}_n^{(m)} e^{i(m\omega_L + n\omega_{nut})t}. \tag{103}$$

Substituting Eq. 103 in to Eq. 99 we shall obtain

$$\begin{aligned}
\frac{d\tilde{\tilde{\sigma}}}{dt} = -\Lambda_Q^2 \sum_{m,m';n,n'} \int_0^\infty (-1)^{m'+m} \left\langle F_2^{(-m')}(t) F_2^{(-m)}(t-\tau)\right\rangle e^{-i(m\omega_L + n\omega_{nut})\tau} d\tau \times \\
\times\left[\hat{B}_{n'}^{(m')}, \left[\hat{B}_n^{(m)}, \tilde{\tilde{\sigma}}(t)\right]\right] e^{i\left[(m'+m)\omega_L + (n'+n)\omega_{nut}\right]t}.
\end{aligned} \tag{104}$$

Assuming that $(m'+m)\omega_L >> \tau_c$ as well as $(n'+n)\omega_{nut} >> \tau_c$, one can write

$$\frac{d\tilde{\tilde{\sigma}}}{dt} = -\frac{1}{2}\Lambda_Q^2 \sum_{m=-2}^{2}\sum_{n=-2}^{2} (-1)^m J_{mn}(m\omega_L + n\omega_{nut})\left[\hat{B}_{-n}^{(-m)}, \left[\hat{B}_n^{(m)}, \tilde{\tilde{\sigma}}(t)\right]\right], \tag{105}$$

where

$$J_{mn}(m\omega_L + n\omega_{nut}) = \int_{-\infty}^{\infty} \left\langle F_2^{(m)}(t) F_2^{*(m)}(t-\tau) \right\rangle e^{-i(m\omega_L + n\omega_{nut})\tau} d\tau. \tag{106}$$

Table 3.

Coefficients $c_n^{(m)}$ in Eq. 108.

n \ m	−2	−1	0	1	2
−2	1/4	1/2	$\sqrt{6}/4$	−1/2	1/4
−1	1/2	−1/2	0	1/2	−1/2
0	$\sqrt{6}/4$	0	−1/2	0	$\sqrt{6}/4$
1	−1/2	1/2	0	−1/2	1/2
2	1/4	−1/2	$\sqrt{6}/4$	1/2	1/4

It is helpful to make a further transformation to this equation given by

$$U' = \exp\left(i\pi/2\, I_y\right) U \exp\left(-i\pi/2\, I_y\right), \tag{107}$$

which corresponds to a rotation of $\pi/2$ about the *y* axis. The reason of this transformation is that it can be shown that the transformed operators $\hat{B}_n'^{(m)}$ are of the form

$$\hat{B}_n'^{(m)} = c_n^{(m)} \hat{T}_2^{(m)}, \tag{108}$$

where coefficients $c_n^{(m)}$ are listed in Table **3**.

Applying the transformation given by Eq. 107 to Eq. 105 and using Eq. 108 we obtain

$$\frac{d\tilde{\tilde{\sigma}}'}{dt} = -\frac{1}{2}\Lambda_Q^2 \sum_{m=-2}^{2} (-1)^m J_\rho^{(m)}(\omega_L, \omega_{nut}) \left[\hat{T}_2^{(-m)}, \left[\hat{T}_2^{(m)}, \tilde{\tilde{\sigma}}'(t) \right] \right], \tag{109}$$

where

$$J_\rho^{(m)}(\omega_L, \omega_{nut}) = \sum_{n=-2}^{2} \left(c_n^{(m)} \right)^2 J_{mn}(m\omega_L + n\omega_{nut}). \tag{110}$$

If $\omega_{nut} << \omega_L$, Eq. 110 reduces to

$$J_\rho^{(0)}(\omega_L,\omega_{nut})=\frac{1}{4}J_0(0)+\frac{3}{4}J_2(2\omega_L),$$
$$J_\rho^{(1)}(\omega_L,\omega_{nut})=\frac{1}{2}J_1(\omega_L)+\frac{1}{2}J_2(2\omega_L), \qquad (111)$$
$$J_\rho^{(2)}(\omega_L,\omega_{nut})=\frac{3}{8}J_0(2\omega_{nut})+\frac{1}{2}J_1(\omega_L)+\frac{1}{8}J_2(2\omega_L).$$

Equation 109 is identical in form to Eq. 77 if $J_m(m\omega_L)$ is replaced by $J_\rho^{(m)}(\omega_L,\omega_{nut})$. It means that the solution of Eq. 109 for $\tilde{\tilde{\sigma}}'$, the density operator in the doubly rotating frame for relaxation in the presence of $\mathcal{H}_{\mathrm{RF}}(t)$, can be simply deduced from the solution of Eq. 77 for $\tilde{\sigma}$, the density operator in the singly rotating frame for relaxation in the absence of $\mathcal{H}_{\mathrm{RF}}(t)$. In other words, corresponding results for relaxation in the rotating frame can be deduced from the theory of relaxation in the laboratory frame simply by replacing $J_m(m\omega_L)$ in the appropriate expressions by $J_\rho^{(m)}(\omega_L,\omega_{nut})$.

It is easy to show that relaxation of the magnetization along the field B_1 corresponds to longitudinal relaxation in the rotating frame:

$$\langle I_x\rangle=\mathrm{Tr}\{\tilde{\sigma}I_x\}=\mathrm{Tr}\{\tilde{\tilde{\sigma}}I_x\}=\mathrm{Tr}\{\tilde{\tilde{\sigma}}'I_z\}; \qquad (112)$$

therefore, similar to Eq. 82, one can write for relaxation of the locking magnetization in the rotating frame after the pulse sequence presented in Fig. 8:

$$M_{z\rho}(\tau)=\frac{1}{5}M_{z\rho}^0\left(4\exp(R_{2\rho}^{(0)}\tau)+\exp(R_{1\rho}^{(0)}\tau)\right), \qquad (113)$$

where

$$R_{1\rho}^{(0)}=-\Lambda_Q^2J_\rho^{(1)},\quad R_{2\rho}^{(0)}=-\Lambda_Q^2J_\rho^{(2)}, \qquad (114)$$

and spectral densities in the rotating frame $J_\rho^{(m)}(\omega_L,\omega_{nut})$ are defined by Eq. 111.

1.2.8 Correlation functions

First, let us introduce some definitions of a random functions theory. Let $y(t)$ be a random function of time; if a function $f(y)$ exists, then it is also a random function of time. Let the probability that at time t the function $y(t)$ takes a certain value denote as $p(y,t)$. Then the average value of $y(t)$ can be written as follows:

$$\langle y(t)\rangle=\int p(y,t)y(t)dy. \qquad (115)$$

The average value of $f(t)$ is

$$\langle f(t)\rangle = \int p(y,t) f(y) dy. \tag{116}$$

Different values of the function $y(t)$ at different moments of time could be correlated with each other. Let us introduce the conditional probability $P(y_1,t_1;y_2,t_2)$ of that the function $y(t)$ takes the value y_1 at time t_1, if it takes the value y_2 at time t_2. If the function $y(t)$ is invariant with respect to the change of the origin of time, then $P(y_1,t_1;y_2,t_2)$ depends only on the difference $t_2 - t_1 = \tau$. The probability $p(y,t)$, in this case, is time-independent function $p(y)$. The correlation between the values of the function $y(t)$ at times t_1 and t_2 is then defined by the correlation function

$$G(\tau) = \iint p(y_1) P(y_1, y_2, \tau) f(y_1) f^*(y_2) dy_1 dy_2. \tag{117}$$

Let us assume that the fluctuations of the field gradient tensor are caused by the relative motion of ions, i.e. by the self-diffusion process. In this case, the value of the function $F_2^{(m)}(t)$ at certain moment of time is determined by the value of the electric field potential $\varphi(r)$ produced by the moving ions at the site of a given nucleus. The electric field gradient at this nucleus is the sum of the gradients over all moving ions:

$$V_{ij} = \beta \sum_n \frac{\partial^2 \varphi_n}{\partial x_i \partial x_j}, \tag{118}$$

where the multiplication factor β is introduced to take into account the following effects:

Antishielding effect.

The electric field gradient, which affect the quadrupole moment of the nucleus and which is produced by all other ions, is usually referred to as the *local field gradient* V_{ij}^{loc}. The gradient V_{ij}^{loc} would be the sole source of interaction if the charge distribution of the ion, in which the nucleus lies, were spherically symmetric. However, the ion is distorted both by the quadrupolar field of the nucleus and by V_{ij}^{loc}; this distortion adds, in effect, a contribution κV_{ij}^{loc} to the total gradient V_{ij}, where κ is so-called *quadrupole antishielding factor*. The physical reason of the antishielding effect is the distortion of the electronic density of the ion due to the interaction with the quadrupole moment of the nucleus. In fact, to decrease their energy, electrons tend to move inward along the principle axis of the EFG tensor of the nucleus and outward at $90°$. This shift of the charge gives rise to a positive *electronic* quadrupole moment, i.e. to antishielding of *Q*.

Polarization and strain effects.

Ionic diffusion in the crystal is always accompanied by the creation of charged point defects. Each of such charged defects induces the polarization of the crystal, which also contributes to the local field gradient. Moreover, the point defect creates around itself the mechanical strain, which causes the additional electric field gradient.

All mentioned contributions are proportional to r^{-3}; this allows to introduce a common factor β, which contains contributions from antishielding, polarizing, and strain effects as well.

If the charge of the *n*-th ion is e_n, then the electric potential of its field in the point **r** is $\varphi(r) = e/r$. Substituting such $\varphi(r)$ in Eq. 118, we obtain

$$V_{ij} = \beta \sum_n e_n r_n^{-5} \left(3x_i^{(n)} x_j^{(n)} - \delta_{ij} r_n^2\right), \tag{119}$$

where δ_{ij} is the Kronecker symbol. Substituting Eq. 119 into the definition of the field gradient components $F_2^{(1)}$ and $F_2^{(2)}$ (Eq. 33), we have in a spherical coordinate system:

$$\begin{aligned} F_2^{(1)} &= -3\beta \sum_n e_n r_n^{-3} \cos\theta_n \sin\theta_n e^{i\varphi_n}, \\ F_2^{(2)} &= \frac{3}{2}\beta \sum_n e_n r_n^{-3} \sin^2\theta_n e^{2i\varphi_n}, \end{aligned} \tag{120}$$

where θ_n and φ_n are the polar angles of the position vector $\mathbf{r}_n$ of the *n*-th defect with respect to the *z*-axis. If the *N* diffusing charges move independently of each other, then it is sufficient to consider only one of them; correlation functions and spectral densities could be derived for this sole charge, and the result has to be just multiplied by *N*. Taking into account the form of well-tabulated spherical harmonics

$$\begin{aligned} Y_2^{(1)} &= -\sqrt{\frac{15}{8\pi}} \cos\theta \sin\theta e^{i\varphi}, \\ Y_2^{(2)} &= \frac{1}{2}\sqrt{\frac{15}{8\pi}} \sin^2\theta e^{2i\varphi}, \end{aligned} \tag{121}$$

one can write for the $F_2^{(1)}$ and $F_2^{(2)}$ components of the field gradient created by the sole charge

$$F_2^{(1,2)} = 3\beta e r^{-3} \sqrt{\frac{8\pi}{15}} Y_2^{(1,2)}. \tag{122}$$

As it was shown in the previous section, transition probabilities W_1 and W_2 could be expressed in terms of spectral densities of the functions $F_2^{(1)}$ and $F_2^{(2)}$ (combine Eq. 84, Eq. 83, and Eq. 94):

$$W_m = \frac{1}{2}\Lambda_Q^2 J_m = \frac{1}{2}\Lambda_Q^2 \int_{-\infty}^{\infty} \left\langle F_2^{(m)}(t) F_2^{*(m)}(t-\tau) \right\rangle e^{-im\omega_L \tau} d\tau, \tag{123}$$

where $m = 1, 2$. According to Eq. 117, the correlation function $G_m(\tau) = \left\langle F_2^{(m)}(t) F_2^{*(m)}(t-\tau) \right\rangle$ could be written as

$$G_m(\tau) = \iint p(\mathbf{r}_0) P(\mathbf{r}_0, \mathbf{r}, \tau) F_2^{(m)}(\mathbf{r}_0) F_2^{*(m)}(\mathbf{r}_1) d^3 r_0 d^3 r, \tag{124}$$

where $\mathbf{r}_0$ is the distance between two relatively moving ions at initial moment of time, and $\mathbf{r}$ is the distance between them after the time τ. The probability $p(\mathbf{r}_0)$ is *a priori* constant and equals to the inverse volume of the crystal V^{-1}. Thus, to find the autocorrelation functions of the components $F_2^{(m)}$, one needs to know the probability $P(\mathbf{r}_0, \mathbf{r}, \tau)$. In case of the latter is determined by the diffusion equation

$$\frac{\partial P(\mathbf{r}_0, \mathbf{r}, \tau)}{\partial \tau} = D \Delta P(\mathbf{r}_0, \mathbf{r}, \tau), \tag{125}$$

where D is the diffusion coefficient, and Δ is the Laplace operator. Solution of the diffusion equation with the initial condition $P(\mathbf{r}_0, \mathbf{r}, 0) = \delta(\mathbf{r} - \mathbf{r}_0)$ is well known:

$$P(\mathbf{r}_0, \mathbf{r}, \tau) = (8\pi D t)^{-3/2} \exp\left\{ -\frac{|\mathbf{r} - \mathbf{r}_0|^2}{8Dt} \right\}. \tag{126}$$

Thus, the autocorrelation function G_m could be written as follows:

$$G_m(\tau) = \frac{24\pi}{5} V^{-1} \beta^2 e^2 (8\pi D t)^{-3/2} \iint \exp\left\{ -\frac{|\mathbf{r} - \mathbf{r}_0|^2}{8Dt} \right\} \frac{Y_2^{(m)}}{r_0^3} \frac{Y_2^{*(m)}}{r^3} d^3 r_0 d^3 r. \tag{127}$$

Multiplying Eq. 127 by N and calculating the integral [64], we shall obtain

$$G_1(\tau) = G_2(\tau) = \frac{24\pi}{5d^3} n \beta^2 e^2 \int_0^{\infty} [J_{3/2}(u)]^2 \exp\left(-\frac{\tau}{\tau_c} u^2 \right) \frac{du}{u}, \tag{128}$$

where $\tau_c = d^2/2D$, d is the distance of the closest approach of two ions, $n = N/V$ is the concentration of defects, and $J_{3/2}(u)$ is the Bessel function. The corresponding spectral densities are

$$J_m(m\omega_L) = \frac{24\pi}{5}\beta^2 e^2 \frac{n}{dD}\int_0^\infty [J_{3/2}(u)]^2 \frac{udu}{u^4 + (m\omega_L)^2\tau_c^2}. \quad (129)$$

Correlation time τ_c characterizes a fluctuation rate of the local field. The magnitude $1/\tau_c$ corresponds to its fluctuation frequency, i.e. during τ_c the random function (in our case, $F_2^{(m)}(t)$) changes its sign. The relation between τ_c and the parameters of the system depends on the model chosen for the description of the system dynamics.

It is convenient to introduce the so-called *reduced* spectral densities $j(\omega) = J(\omega)/G(0)$. One can find from Eq. 128 that

$$G(0) = \frac{8\pi}{5d^3} n\beta^2 e^2; \quad (130)$$

therefore,

$$j_m(m\omega_L) = 6\tau_c \int_0^\infty [J_{3/2}(u)]^2 \frac{udu}{u^4 + (m\omega_L)^2\tau_c^2}. \quad (131)$$

Taking into account Eq. 123, we obtain for the $I = 3/2$ system

$$W_m = \frac{\pi}{15}\left(\frac{e^2Q}{\hbar}\right)^2 \beta^2 \frac{n}{dD}\int_0^\infty [J_{3/2}(u)]^2 \frac{udu}{u^4 + (m\omega_L)^2\tau_c^2}, \quad m = 1, 2. \quad (132)$$

It should be noted that the autocorrelation function $G(\tau)$ in the form of Eq. 127 assumes that the diffusion process could be described by the Fick's second law (Eq. 125). It means that both radial and angular parts of the ions' coordinates run through a continuous range of values. However, diffusing jumps of ions in a solid are characterized by the discrete values of the polar angles and distances. In this case, the integral in Eq. 124 has to be substituted by the corresponding sum, and the probability $P(\mathbf{r}_0, \mathbf{r}, \tau)$ could be found from the Smoluchowski equation. We shall consider the model of the ionic motion in solid between discrete lattice sites in the next chapter.

Functions given by Eq. 128 and Eq. 129 are quite complex, therefore, approximate functions are often used for the analysis of relaxation. Thus, the autocorrelation function is often taken in the simple exponential form

$$G(\tau) = G(0)e^{-|\tau|/\tau_c}, \quad (133)$$

Such choice of the correlation function for the analysis of magnetic relaxation is referred to as a *Bloembergen-Purcell-Pound* (BPP) *approximation*. In case of isotropic rotational diffusion, the precise form of the correlation function corresponds to Eq. 133; therefore, for spherical

molecules in liquids this approximation gives very good result. However, BBP model is a quite rough approximation for anisotropic translational diffusion of ions in solids; nevertheless, sometimes it could give satisfactory values for the correlation times of the ionic motion.

Taking into account Eq. 133, one can write for $G(\tau)$

$$G_m(\tau) = \left\langle \left| F_2^{(m)} \right|^2 \right\rangle e^{-|\tau|/\tau_c}, \tag{134}$$

where

$$\left\langle \left| F_2^{(m)} \right|^2 \right\rangle = V^{-1} \int_d^\infty \int_0^{2\pi} \int_0^\pi \left| F_2^{(m)} \right|^2 r^2 \sin\theta d\theta d\varphi dr. \tag{135}$$

Here, as above, d is the distance of the closest approach of two ions, and V is the volume of the crystal. Substituting $F_2^{(m)}$ from Eq. 122 into Eq. 135, one can obtain:

$$\left\langle \left| F_2^{(1)} \right|^2 \right\rangle = \left\langle \left| F_2^{(2)} \right|^2 \right\rangle = \frac{72\pi}{45} \frac{e^2\beta^2}{Va^3}, \tag{136}$$

hence we have for W_m

$$W_m = \frac{\pi}{45} \left(\frac{e^2 Q}{\hbar} \right)^2 \frac{n}{d^3} j(m\omega_L), \quad m = 1, 2, \tag{137}$$

where the reduced spectral density is

$$j(\omega) = \frac{2\tau_c}{1 + \omega^2 \tau_c^2}. \tag{138}$$

For the relaxation rates $R_1^{(0)}$ and $R_2^{(0)}$ we thus have

$$R_1^{(0)} = -2C \frac{2\tau_c}{1 + \omega_L^2 \tau_c^2}, \quad R_2^{(0)} = -2C \frac{2\tau_c}{1 + 4\omega_L^2 \tau_c^2}, \tag{139}$$

where

$$C = \frac{\pi}{45} \left(\frac{e^2 Q}{\hbar} \right)^2 \frac{n}{d^3}. \tag{140}$$

The constant C could be expressed in terms of more "familiar" quantities: quadrupolar coupling constant C_Q and asymmetry parameter η. To do this, one need to use the functions $F_2^{(m)}$ in the form of Eq. 38. Thus, for isotropic rotational diffusion one can obtain [66]

$$C = \frac{\pi^2}{10} C_Q^2 \left(1 + \frac{\eta^2}{3} \right), \tag{141}$$

and Eq. 139 will be still valid.

The BPP approximation assumes that the correlation function decays down to zero when increasing the time τ. In fact, molecular motions could be restricted in space, and nuclear interactions will not be averaged down to zero. In terms of the correlation function, it means that $G(\tau)$ has to be divided into two parts, one of which defines the residual correlations and other one corresponds to the decay. The simplest form of such correlation function was suggested by Lipari and Szabo within the scope of the *model-free approach* [68]. In terms of reduced correlation function $g(\tau) = G(\tau)/G(0)$, the model-free approach is defined as follows:

$$g(\tau) = S^2 + \left(1 - S^2\right) e^{-|\tau|/\tau_c}, \tag{142}$$

where *S* is a *generalized order parameter*, which is a measure of the averaging of the nuclear interactions by a given type of motion. Thus, if the internal motion is isotropic, then $S = 0$, i.e. a given interaction is averaged down to zero when increasing τ. On the other hand, if the motion is completely restricted, then $S = 1$. Spectral density of such correlation function is

$$j(\omega) = 2\pi S^2 \delta(\omega) + \left(1 - S^2\right) \frac{2\tau_c}{1 + \omega^2 \tau_c^2}, \tag{143}$$

where $\delta(\omega)$ is a Dirac delta-function. We shall use the spectral density given by Eq. 138 below, when considering the NMR line width analysis.

One can see from Eq. 139 that relaxation rates $R_1^{(0)}$ and $R_2^{(0)}$ obey the following relations: 1) at very fast motion, when $\omega_L \tau_c << 1$, they are equal, $R_1^{(0)} = R_2^{(0)}$; 2) at $\omega_L \tau_c >> 1$, i.e. in slow motional regime, $R_1^{(0)} = 4R_2^{(0)}$. Thus, the relaxation rates do not differ more than four times; in other words, the recovery of the magnetization due to spin-lattice relaxation does not differ considerably from single exponent. This allows introducing an "effective" relaxation rate T_{1Z}^{-1}. To derive it, let us refer to Eq. 82,

$$M_z(\tau) = M_z^{eq}\left[1 - \frac{4}{5}\exp(R_2^{(0)}\tau) - \frac{1}{5}\exp(R_1^{(0)}\tau)\right], \tag{82}$$

which determines the time evolution of the longitudinal magnetization measured via the saturation-recovery method by integrating of the whole resonance line. At small τ, one can expand the function $f(\tau) = 1/5\left[4\exp(R_2^{(0)}\tau) + \exp(R_1^{(0)}\tau)\right]$ in a series, restricting expansion by the two first terms. It gives

$$f(\tau) \approx 1 + \frac{4}{5}R_2^{(0)}\tau + \frac{1}{5}R_1^{(0)}\tau \approx \exp\left\{\left(\frac{4}{5}R_2^{(0)} + \frac{1}{5}R_1^{(0)}\right)\tau\right\} = \exp\left(-\frac{\tau}{T_{1Z}}\right), \tag{144}$$

where

$$\frac{1}{T_{1Z}} = -\frac{4}{5}R_3^{(0)} - \frac{1}{5}R_4^{(0)} = \frac{2}{5}C\left(\frac{2\tau_c}{1+\omega_L^2\tau_c^2} + \frac{8\tau_c}{1+4\omega_L^2\tau_c^2}\right). \tag{145}$$

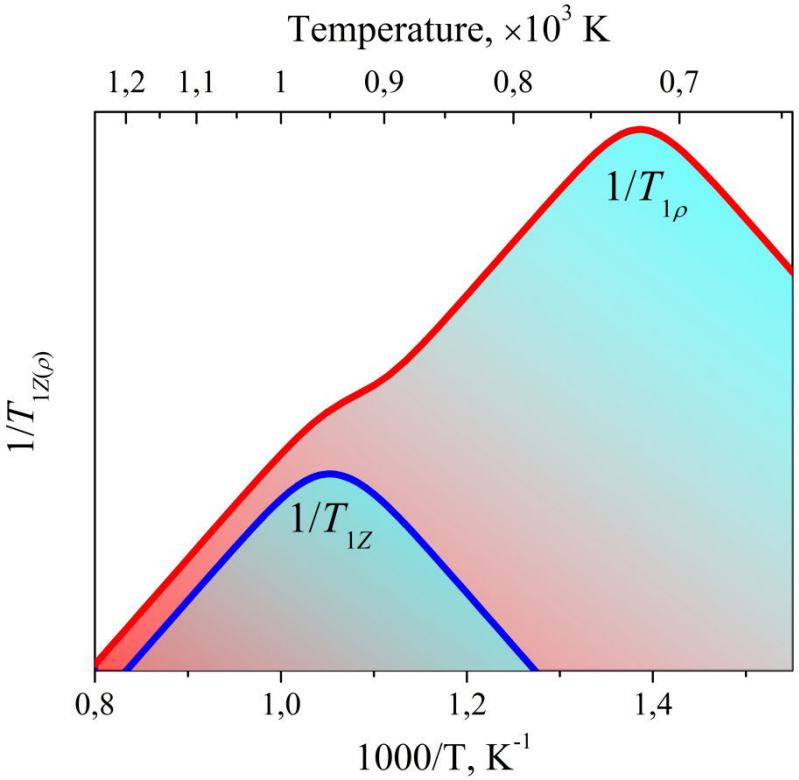

Fig. 9. Temperature evolution of longitudinal relaxation rates: in the laboratory frame, $1/T_{1\rho}$ (red line), and in the rotating frame, $1/T_{1Z}$ (blue line). Parameters of the system are taken to be:

$$E = 2\,\text{eV}\ ,\ \tau_0 = 10^{-19}\,\text{s}\ .$$

One can even extend Eq. 145 to the more general case [69]:

$$\frac{1}{T_{1Z}} = K_Q\left(\frac{\tau_c}{1+\omega_L^2\tau_c^2} + \frac{4\tau_c}{1+4\omega_L^2\tau_c^2}\right), \tag{146}$$

where

$$K_Q = \frac{3\pi^2}{10}\frac{2I+3}{I^2(2I-1)}\left(1+\frac{\eta^2}{3}\right)C_Q^2. \tag{147}$$

The relaxation rate defined by Eq. 146 is referred to as relaxation of the Zeeman order (subscript *Z* denotes this).

If only relaxation of the central transition could be measured in the experiment (Eq. 86), then one needs to convert the function $f^{\text{CT}}(t) = 1/2\left[\exp(R_3^{(0)}t) + \exp(R_4^{(0)}t)\right]$ as above:

$$f^{\mathrm{CT}}(t) \approx 1 + \frac{1}{2} R_1^{(0)} t + \frac{1}{2} R_2^{(0)} t \approx \exp\left\{ \frac{1}{2} \left(R_1^{(0)} + R_2^{(0)} \right) t \right\} = \exp\left(-\frac{\tau}{T_1^{\mathrm{CT}}} \right), \tag{148}$$

where

$$\frac{1}{T_1^{\mathrm{CT}}} = -\frac{1}{2} \left(R_1^{(0)} + R_2^{(0)} \right) = C \left(\frac{2\tau_c}{1+\omega_L^2 \tau_c^2} + \frac{2\tau_c}{1+4\omega_L^2 \tau_c^2} \right). \tag{149}$$

Using Eq. 111 one can extend Eq. 145 to the case of longitudinal relaxation in the rotating frame:

$$\frac{1}{T_{1\rho}} = \frac{2}{5} C \left(j_\rho^{(1)} + 4 j_\rho^{(2)} \right) = C \left(\frac{5\tau_c}{1+\omega_L^2 \tau_c^2} + \frac{2\tau_c}{1+4\omega_L^2 \tau_c^2} + \frac{3\tau_c}{1+4\omega_{nut}^2 \tau_c^2} \right). \tag{150}$$

Temperature evolution of the relaxation rate is determined by the time dependence of the correlation time τ_c. If an Arrhenius behavior of the correlation time is assumed, $\tau_c = \tau_0 e^{E/kT}$, a semi-logarithmic plot of $1/T_{1Z}$ (Eq. 145) together with $1/T_{1\rho}$ (Eq. 150) has the form presented in Fig. 9. Maxima of $1/T_{1Z}$ and $1/T_{1\rho}$ are observed at $\omega_L \tau_c \approx 0.62$ and $\omega_{nut} \tau_c = 0.5$, respectively, and one can see from Fig. 9 that they are significantly spaced in the temperature domain.

1.2.9 Non-exponential relaxation

In a wide class of various materials, dynamical process could be characterized by a continuous set of relaxation times T_i. Such situation often takes place in amorphous and crystalline semiconductors, insulators, polymers, disordered crystals and glasses. In this case, the time-domain relaxation data could not be fitted via simple exponential function, since relaxation will have non-exponential behavior. It should be noted that such non-exponentiality differs from the non-exponentiality of pure quadrupolar relaxation. In fact, the latter is caused by the existence of two different probabilities for single-quantum and double-quantum transitions between energy levels. The non-exponentiality in the case under consideration is caused by the disordering of the material structure and, as a result, by distribution of activation energies and correlation times characterizing a given type of dynamics.

If the system is characterized by the set of relaxation times, one can introduce the probability $\rho(T,\alpha,\beta,...)dT$ that the relaxation time T takes a certain value, where $\rho(T;\alpha,\beta,...)$ is referred to as *relaxation time probability density function*, where $\alpha,\beta,...$ are additional parameters which characterize the distribution of relaxation time *T*. Then the global relaxation of the system, i.e. the average relaxation function $f(t)$, could be considered as a

continuous sum of pure exponential decays with a particular probability distribution $\rho(T;\alpha,\beta,...)$ of T values:

$$\left\langle e^{-t/T} \right\rangle = \int_0^\infty e^{-t/T} \rho(T;\alpha,\beta,...)dT. \tag{151}$$

It was found that the relaxation responses obtained by different experimental techniques can be well characterized by a small class of fitting functions exhibiting asymptotically power-law properties [70]. The most popular function applied to fit the time-domain relaxation is the stretched-exponential function, known also as the *Kohlrausch-Williams-Watts function* (or just Kohlrausch function):

$$f_\beta(t) = \exp[-(t/T^*)^\beta], \tag{152}$$

where T^* is an effective relaxation time, and β is a stretching parameter, which characterizes the width of the probability distribution $\rho(T;\beta)$ of T values; for the Kohlrausch function, $0 < \beta < 1$. Thereby, Eq. 151 has to be rewritten as follows:

$$\exp[-(t/T^*)^\beta] = \int_0^\infty \exp(-t/T)\rho(T;\beta)dT, \tag{153}$$

where the probability distribution $\rho(T;\beta)$ depends on the value of the stretching parameter.

Introducing an effective relaxation rate $R^* = 1/T^*$, one can rewrite Eq. 152 in the following form:

$$f_\beta(t) = \exp[-(R^*t)^\beta]. \tag{154}$$

Equation 153 can now be written as follows:

$$\exp[-(R^*t)^\beta] = \int_0^\infty \exp(-sR^*t)P_\beta(s)ds, \tag{155}$$

where $s = R/R^*$, and $R = 1/T$. Probability density $P_\beta(s)$ obeys the usual condition:

$$\int_0^\infty P_\beta(s)ds = 1. \tag{156}$$

For $\beta = 1$, the stretched exponential function (Eq. 154) is a pure exponential with $R = R^*$ and hence the probability density $P_1(s)$ is a Dirac δ-function at $s = 1$. For general β, one can express $P_\beta(s)$ in the form of the following series [71]:

$$P_\beta(s) = \frac{1}{\pi}\sum_{n=1}^{\infty} \frac{(-1)^{n+1}\Gamma(n\beta+1)}{n!s^{n\beta+!}} \sin(n\pi\beta), \tag{157}$$

where $\Gamma(x)$ is the Gamma (factorial) function.

Let us give physical interpretation of R^* and β. The parameter R^* in the stretched exponential function is often referred to as some undefined "average" relaxation rate. However, one can show [71] that the average of R is infinite (in the absence of a high-*s* cutoff to $P_\beta(s)$), and the physical interpretation of R^* is that R is about equally likely to be less than R^* as it is to be greater (to within $\sim \pm 20\%$). The stretching parameter β is often cited as a measure of the width Δs of the distribution $P_\beta(s)$. However, a statistical definition of the width, such as the root mean square width $\Delta s = \sqrt{\langle s^2 \rangle - \langle s \rangle^2}$, is undefined for $P_\beta(s)$. Nevertheless, β could be considered as a measure of the full width at half maximum (FWHM) of $P_\beta(s)$.

Sometimes, time-domain relaxation function is not available, whereas frequency-domain physical quantity, e.g., susceptibility, could be measured. Therefore, one needs to find the Fourier transform of the Kohlraush function. Let us define the Fourier transform of the stretched exponential function as follows:

$$k_\beta(\omega) = 2\int_0^\infty \exp[-(t/T^*)^\beta]\cos(\omega t)dt. \tag{158}$$

For small values of ω, one can express $k_\beta(\omega)$ in the form of the following sum [72]:

$$k_\beta(\omega) = \frac{2T^*}{\beta}\sum_{k=0}^{\infty}(-1)^k \frac{\Gamma\left((k+1)/\beta\right)}{\Gamma(k+1)}(\omega T^*)^{2k}, \tag{159}$$

whereas for large values of ω one can write

$$k_\beta(\omega) = 2T^*\sum_{k=1}^{\infty}(-1)^{k-1}\sin(k\beta\pi/2)\frac{\Gamma(k\beta+1)}{\Gamma(k+1)}(\omega T^*)^{-1-k\beta}. \tag{160}$$

Similar to Eq. 151, one can introduce a *correlation* (not relaxation) *time probability density function* $p(\tau_c;\alpha,\beta,...)$ and define an averaged spectral density $\langle j(\omega;\alpha,\beta,...)\rangle$ as follows:

$$\langle j(\omega;\alpha,\beta,...)\rangle = \int_0^\infty p(\tau_c;\alpha,\beta,...)\frac{2\tau_c}{1+\omega^2\tau_c^2}d\tau_c, \tag{161}$$

where we assumed that each correlation time characterizes an exponential correlation function $g(\tau) = \exp(-|\tau|/\tau_c)$. Note that $p(\tau_c;\alpha,\beta,...)$ cannot depend on ω; it is a property of the molecular system under study, not of the measuring apparatus [73].

Since the Fourier transform is a linear operation, $p(\tau_c;\alpha,\beta,...)$ also gives the reduced correlation function as a distribution of exponential correlation functions:

$$\left\langle g(\tau;\alpha,\beta,...)\right\rangle = \int_0^\infty p(\tau_c;\alpha,\beta,...)e^{-|\tau|/\tau_c}d\tau_c, \tag{162}$$

which could often be described by the Kohlraush function. Functions given by Eqs. 151 and 162 should not be confused: the first one correspond to the *macroscopic* process characterizing by the effective relaxation time T^*, whereas the second one describes the time evolution of the correlation function, which is the characteristic function of the *microscopic* processes occurring in solid. Here, we shall focus on spectral densities, taking into account that corresponding correlation functions could be found via Eq. 162.

Many different spectral densities were suggested to analyze nuclear spin relaxation rates in solids. Most of them have their origin in dielectric relaxation experiments. One of the most successful spectral densities used to interpret nuclear spin relaxation experiments in solids is so-called *Cole-Davidson function* $j_{\mathrm{CD}}(\omega,\beta)$, which is defined as follows:

$$j_{\mathrm{CD}}(\omega;\beta) = -\frac{2}{\omega}\mathrm{Im}\left\{\frac{1}{\left(1+i\omega\tau_c\right)^\beta}\right\} = \frac{2}{\omega}\frac{\sin\left[\beta\arctan(\omega\tau_c)\right]}{\left(1+\omega^2\tau_c^2\right)^{\beta/2}}. \tag{163}$$

It easy to show that at $\omega_L\tau_c << 1$

$$j_{\mathrm{CD}}(\omega;\beta) = 2\beta\tau_c, \tag{164}$$

whereas at $\omega_L\tau_c >> 1$

$$j_{\mathrm{CD}}(\omega;\beta) = 2\sin(\beta\pi/2)\tau_c^{-\beta}\omega^{-(1+\beta)}. \tag{165}$$

It is interesting to note that the same behavior has the following function:

$$j_\beta(\omega) = \frac{2\tau_c}{1+\left(\omega^2\tau_c^2\right)^{\frac{1}{2}(\beta+1)}}, \tag{166}$$

namely, at $\omega_L\tau_c << 1$

$$j_\beta(\omega) = 2\tau_c, \tag{167}$$

and at $\omega_L\tau_c >> 1$

$$j_\beta(\omega) = 2\tau_c^{-\beta}\omega^{-(1+\beta)}. \tag{168}$$

Taking into account that $0 < \beta \le 1$ and comparing Eqs. 164 and 165 with Eqs. 167 and 168, one can write the following approximate equality:

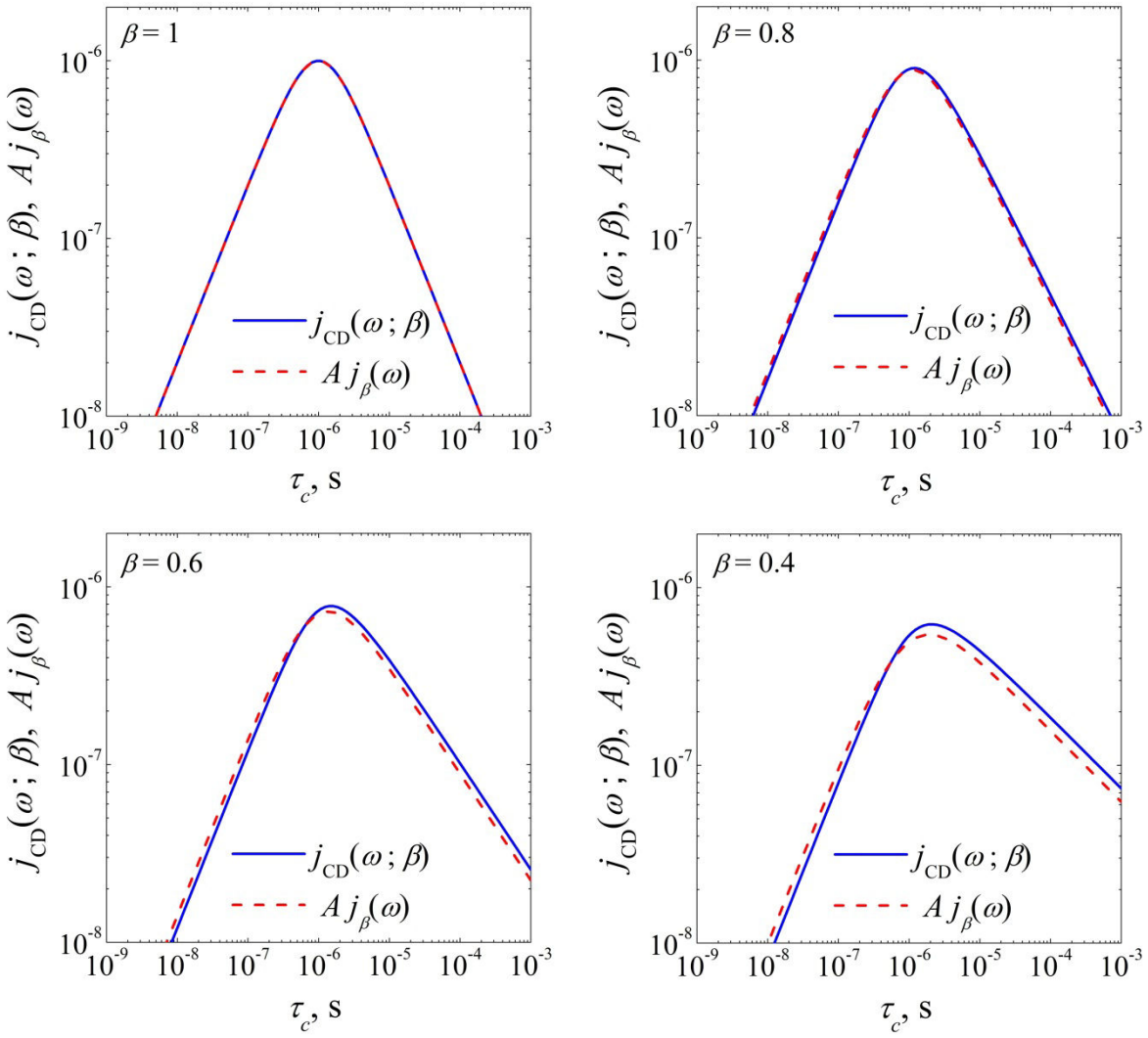

Fig. 10. Comparison of the Cole-Davidson function $j_{CD}(\omega;\beta)$ and the function $A j_\beta(\omega)$ (see Eqs. 166 and 171) at different values of β.

$$\frac{2}{\omega}\frac{\sin\left[\beta\arctan(\omega\tau_c)\right]}{\left(1+\omega^2\tau_c^2\right)^{\beta/2}} \approx \frac{1}{2}\left[\beta+\sin(\beta\pi/2)\right]\frac{2\tau_c}{1+\left(\omega^2\tau_c^2\right)^{\frac{1}{2}(\beta+1)}} \tag{169}$$

or

$$j_{CD}(\omega;\beta) \approx A\, j_\beta(\omega), \tag{170}$$

where

$$A = \frac{1}{2}\left[\beta+\sin(\beta\pi/2)\right] \tag{171}$$

and $j_\beta(\omega)$ is defined by Eq. 166. One can see form Fig. 10 that Eq. 169 is satisfied with a good accuracy if β is not far from unity. Thus, for fitting the temperature dependences of the

spin lattice relaxation rates $1/T_1$ and $1/T_{1\rho}$ (see Eqs. 145 and 150, respectively) one can use either Eq. 163 or Eq. 166; both of these functions could also be used for NMR linewidth analysis.

One can see from Fig. 10 that enhancement of β increases asymmetry of the log-log plot of the spectral density. Assuming the Arrhenius behavior of the correlation time, $\tau_c = \tau_0 \exp(E_a/kT)$, where E_a is an activation energy of the process, one can find from Eqs. 167 and 168 that the slope of the high-temperature ($\omega_L \tau_c << 1$) side of $j(\omega)$ is $E^{high} = E_a$, whereas the slope of the low-temperature side ($\omega_L \tau_c >> 1$) of the spectral density is $E^{low} = \beta E_a$ (without taking into account the sign of the slope). Therefore, one can write

$$E^{low} = \beta E^{high}. \tag{172}$$

Hitherto, we assumed that non-exponential relaxation is the consequence of the fact that the relaxing macroscopic system consists of the appropriate number of subsystems, each of which relaxes exponentially with its own relaxation time. This assumption could have a real physical meaning only when one deals with disordering systems such as glasses, polymers, etc., albeit even in this case one cannot get rid of some contradictions. Such approach, however, cannot be used for regular crystalline structures, where non-exponential relaxation also takes place quite often. The reason of this phenomenon one usually associates with a non-Markovian type of the dynamical process in a solid [74]. In this case, parameters β and R^* considered above have other physical interpretation. Thus, if the generalize relaxation model is applicable to the system, and relaxation could be considered as a self-similar process, then the parameter β in Eq. 163 is a dimension of the fractal set, at which interaction times between system's components are distributed [75].

Chapter 2. Theory and measurement of diffusion in solids

2.1 Diffusion and ionic conductivity in crystals

2.1.1 Bonding in solids and types of conductivity

There exist two types of conductivity: 1) electronic conductivity, which takes place in metals and semiconductors and 2) ionic conductivity, which usually occurs in electrolytic solutions, typical ionic crystals at high temperature, and in different types of solid electrolytes (fast ionic conductors). In case of the electronic conductivity, the transfer of matter does not occur, whereas in the second case the flow of the electric current takes place due to the motion of ionized atoms or molecules, i.e. due to the transference of matter.

In solids, the type of the conductivity depends mainly on the nature of chemical bonds. In case of *covalent bonds*, electron pairs are trapped in very stable and directional orbitals and it is difficult to detach an electron from the atom without gaining a lot of energy. The energy, which is necessary to break the chemical bond and to detach the electron from its atom, is referred to as a band gap. Covalent crystals with the band gap being less than 1–1.5 eV are usually referred to as semiconductors, whereas solids with a higher value of the band gap are referred to as insulators.

If elements of a solid have few electrons in the valence shell, they lower the energy by sharing a sea of valence electrons with all atoms in the structure forming a *metallic bonding*. The deficiency of electrons makes available many unoccupied orbital states. As a result, high electronic conductivity takes place in metals. Along with the transport of electrons the transport of ions could also occur in metals, when the electric current flows. This is so-called effect of *electromigration*, which is caused by the momentum transfer between conducting electrons and diffusing metal ions. Electromigration occurs when some of the momentum of a moving electron is transferred to a nearby activated ion. This causes the ion to move from its original position. Over time this force (so-called “electron wind”) knocks a significant number of atoms far from their original positions. This effect is important in applications where high direct current densities are used, such as in microelectronics and related structures. As the structure size in electronics such as integrated circuits decreases, the practical significance of this effect increases.

Finally, if the different elements of a solid have very different electronegativities, the most electronegative atom will affectively take valence electrons of the less electronegative one. Thus, in sodium chloride, Na will easily lose its valence electron to Cl, which thereby fills its valence shell. Both are stabilized together as Na^+ and Cl^- ions forming a packed structure with an *ionic bonding*. It should be noted that the bond between the two ions would be weak, since there is no overlap of electrons. Nevertheless, if many such pairs are packed with alternating cation and anion side by side in three-dimensional structure, there is a total electrostatic energy gain. The packing of ions is rigid and the materials are in general hard and brittle. The electrons have no possibilities to leave the anions, and the materials are generally insulators. However, at high temperatures (around several hundred kelvins below the melting point), ions can leave their normal crystallographic positions and travel (diffuse) through the crystal.

2.1.2 Point defects

Ionic conductivity and diffusion in crystalline solids takes place because of the presence of different types of imperfections (defects) in crystal. If the imperfection is limited to one lattice site and its immediate vicinity (vacancy or interstitial atom), it is a zero-dimensional imperfection and is termed as a point defect. Dislocations, which are characterized by displacements in the structure in certain directions, correspond to one-dimensional or linear defects. The plane defects or two-dimensional defects comprise stacking faults, grain boundaries, internal interfaces, and external surfaces. Point defects are responsible for lattice diffusion, whereas along plane defects and dislocations one can observe surface diffusion and dislocation diffusion, respectively. Solid-state diffusion determines or strongly influences a number of properties and processes such as mass transport in solids, solid state reactions, sintering, high-temperature creep, etc. Hereinafter, we shall focus on lattice diffusion and, consequently, on properties of point defects.

Formation of the point defects – vacancies and interstitial atoms – can be different. Thus, a vacancy could arise due to the “incomplete evaporation” of the near-surface atom, i.e. due to the shift of the atom from the frontier atomic layer directly to the surface of the crystal. The atom of the neighboring atomic layer could occupy the site of this atom in the course of time and consequently the vacancy will migrate inside the crystal. Such imperfections are termed Schottky defects. Formation of Schottky defects can only occur at surfaces or other extended defects (e.g., dislocations, grain boundaries) since the atoms in the vacated sites must escape. The defects then diffuse into the crystal until equilibrium is reached.

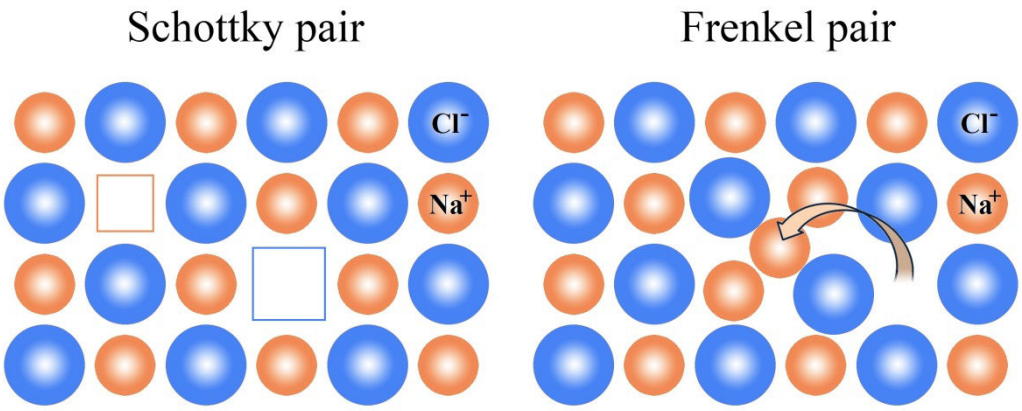

Fig. 11. An example of point defects in a binary ionic crystal (NaCl).

In the ionic solids, any point defect usually possesses an electric charge; therefore, the appearance of only one vacancy (e.g. the cationic vacancy) leads to the violation of the electroneutrality of the crystal. To conserve the electroneutrality of the stoichiometric crystal, a complementary point defect with opposite effective charge must be formed. Note that this requirement is valid only for stoichiometric crystals, since in nonstoichiometric compounds the electroneutrality is conserved through the formation of point defects and charge compensating electronic defects. The balance of populations of cation and anion vacancies could be achieved by the creation of different amount of defects depending of the stoichiometry of the compound. For example, if the crystal has a formula *MX*, then the number of cation vacancies will be equal to the number of anion vacancies. It is necessary to remember that the number of Schottky defects in a crystal of formula *MX* is equal to one-half of the total number of vacancies. In crystals of more complex formula, such as titanium dioxide, TiO_2, there will be twice as many anion vacancies as cation vacancies in a Schottky disorder. This is because we need the absence of two O^{2-} ions to electrically counterbalance the loss of the one Ti^{4+} ion from the crystal. This ratio of two anion vacancies per one cation vacancy will hold in all compounds of formula MX_2. In crystals like Al_2O_3, two Al^{3+} vacancies will be balanced by three O^{2-} vacancies. Thus, in crystals with a formula M_2X_3, a Schottky defect will consist of two vacancies on the cation sub-lattice and three vacancies on the anion sub-lattice. It should be noted that these vacancies are not necessarily clustered together and only the relative numbers are needed to keep the crystals electrically neutral.

The defect formation could happen also inside the crystal by means of the shift of the cation from its site in the crystalline lattice to the interstice – under this jump the pair vacancy-interstitial atom appears. Such paired impurities are termed Frenkel defects. Frenkel pairs, which consist of *an*ion vacancies and *an*ion interstitials, are called *an*ion-Frenkel pairs

or sometimes anti-Frenkel pairs. Frenkel disorder usually occurs in the cationic sub-lattice and it is less common to observe anti-Frenkel disorder. This is the consequence of the fact that anions are commonly larger than cations. An important exception to this generalization lies in the occurrence of anti-Frenkel disorder in fluorite-structured compounds, like alkaline earth halides (CaF_2, SrF_2, $SrCl_2$, BaF_2), lead fluoride (PbF_2), and thorium, uranium, and zirconium oxides (ThO_2, UO_2, ZrO_2) [76]. One reason for this is that the anions have a lower electrical charge than the cations, while the other reason lies in the nature of the open structure of the fluorite lattice. It should be noted that under the formation of Frenkel defects the electroneutrality is conserved automatically, since the formation of the positively charged interstitials and negatively charged vacancies occurs simultaneously. Moreover, the relative number of vacancies is not connected to the formula of the compound.

Although Schottky and Frenkel disorder may be simultaneously presented in stoichiometric compounds, one type of disorder usually predominates. Schottky disorder is favored where the cations and anions are of the comparable size, while Frenkel disorder predominates when the sizes of the cations and anions are appreciably different. Another factor is that Schottky disorder tends to dominate when the structure is very effectively packed so that the interstitials that are part of Frenkel pairs are hard to form.

2.1.3 Thermodynamics of point defects

As it was mentioned above, formation of point defects requires considerable energy consumption; nevertheless, at relatively high temperature, an existence of point defects is expected to be energy-advantageous. The fact is that the appearance of the defects increases the internal energy $\mathcal{E}$ of the crystal and its entropy $\mathcal{S}$ as well. Thus, for given value of pressure P and temperature T the part of the Gibbs potential of the crystal, $\mathcal{G} = \mathcal{E} + PV - T\mathcal{S} = \mathcal{H} - T\mathcal{S}$, caused by the presence of the interstitial atoms has a minimum at certain defect concentration. The equilibrium concentration is determined by the balance between the enthalpy ($\mathcal{H}$) and entropy ($\mathcal{S}$).

The change of the entropy due to the appearance of the defects (such entropy is called *configurational entropy*) can be determined as follows

$$\mathcal{S}^{conf} = k \ln Z, \tag{173}$$

where k is the Boltzmann constant and Z is a statistical weight of the system at given temperature or more exactly the part of the statistical weight, which is connected with the placing of the defects in the crystal.

Suppose that all interstitial atoms were "born" inside the crystal, i.e. they arise via Frenkel mechanism. The defect concentration, i.e. the number of Frenkel pairs in the unit volume, we shall designate as N assuming the equality of interstitial atoms and vacancies at any temperature. The number of ways to place N atoms into the N' interstices could be found using the following formula of combinatorial analysis:

$$Z' = \frac{N'!}{N!(N'-N)!}. \tag{174}$$

Analogously, one can find the number of ways to place N vacancies into N_0 nodes of a given sub-lattice:

$$Z'' = \frac{N_0!}{N!(N_0-N)!}. \tag{175}$$

Using Stirling's formula

$$\ln x! \approx x(\ln x - 1), \tag{176}$$

which is valid when x is big, and taking into account that $Z = Z'Z''$ we can write for the configurational entropy

$$\begin{aligned} \mathcal{S}^{conf} &= k\left[\ln\frac{N'!}{N!(N'-N)!} + \ln\frac{N_0!}{N!(N_0-N)!}\right] \approx \\ &\approx k\left[N_0\ln N_0 - (N_0-N)\ln(N_0-N) - N\ln N\right] + \\ &+ k\left[N'\ln N' - (N'-N)\ln(N'-N) - N\ln N\right]. \end{aligned} \tag{177}$$

If the formation of one Frenkel defect requires the energy U_F^f, then the enhancement of the internal energy of the crystal due to the formation of N defects equals to NU_F^f. Hereby, the expression for the free energy takes the form

$$\mathcal{F} = NU_F^f - T\mathcal{S}^{conf}, \tag{178}$$

where $\mathcal{S}^{conf}$ is defined by Eq. 177. At thermal equilibrium, the free energy has a minimum relative to the change of N, i.e.

$$\left(\frac{\partial\mathcal{F}}{\partial N}\right)_T = 0. \tag{179}$$

After the minimization of the function $\mathcal{F}$ (Eq. 178) and subsequent transformations one can obtain for the defect concentration

$$N = \sqrt{(N_0-N)(N'-N)}\exp\left(-\frac{U_F^f}{2kT}\right), \tag{180}$$

or taking into account that $N << N_0$ and $N << N'$

$$N = \sqrt{N_0 N'} \exp\left(-\frac{U_F^f}{2kT}\right). \tag{181}$$

Factor $1/2$ in exponent of Eq. 181 appears because of the assumption that the numbers of vacancies and interstitial atoms are equal.

Deriving Eq. 181 we did not take into account that a vibrational motion of the atom in the interstice slightly differs from the vibrational motion in the lattice site. One can consider this fact by means of adding a supplementary component to the free energy (Eq. 178):

$$\mathcal{F} = NU_F^f - T\mathcal{S}_{Sc}^{conf} + \Delta\mathcal{F}^{vib}, \tag{182}$$

where $\Delta\mathcal{F}^{vib}$ is a change of vibrational free energy of the crystal under the formation of N interstitial atoms. Minimization of function $\mathcal{F}$ now gives

$$\begin{aligned}\left(\frac{\partial\mathcal{F}}{\partial N}\right)_T &= U_F^f - T\frac{\partial\mathcal{S}_{Sc}^{conf}}{\partial N} + \left(\frac{\partial\Delta\mathcal{F}^{vib}}{\partial N}\right)_T \\ &= U_F^f - kT\ln\frac{(N_0 - N)(N' - N)}{N^2} + \left(\frac{\partial\Delta\mathcal{F}^{vib}}{\partial N}\right)_T = 0,\end{aligned} \tag{183}$$

whence, assuming again that $N \ll N_0$ and $N \ll N'$ we have

$$N = \sqrt{N_0 N'} \exp\left(-\frac{U_F^f}{2kT}\right)\exp\left(-\frac{1}{2kT}\left(\frac{\partial\Delta\mathcal{F}^{vib}}{\partial N}\right)_T\right). \tag{184}$$

One can estimate $\Delta\mathcal{F}^{vib}$ considering the vibrating atom as an isotropic three-dimensional oscillator. For the Helmholtz energy of linear oscillator we can write

$$F^{vib} = -kT\ln Z, \tag{185}$$

where

$$Z = \int e^{-\frac{U}{kT}} d\Omega \tag{186}$$

is a statistical integral, U is potential energy of the oscillator, and Ω designates phase space of the oscillator (in case of linear oscillator, Ω coincides with complete number scale). If f is a force constant of the linear oscillator, then the force acting on it equals to $f\xi$, where ξ is a deviation from the equilibrium position. Thus, statistical integral equals to

$$Z = \int_{-\infty}^{+\infty} e^{-\frac{1}{2}\frac{f\xi^2}{kT}} d\xi = \sqrt{\frac{2\pi kT}{f}}. \tag{187}$$

For the atom in the lattice site we have

$$F^{vib} = -\frac{3}{2}kT \ln \frac{2\pi kT}{f}. \tag{188}$$

The atom will have other force constant f' in the interstice; thereby, after the formation of N interstitial atoms the Helmholtz energy changes by the value

$$\Delta\mathcal{F}_1^{vib} = -\frac{3}{2}NkT \ln \frac{f}{f'} = -NkT \ln \left(\frac{v}{v'}\right)^3, \tag{189}$$

where $2\pi v = \sqrt{f/m}$ and $2\pi v' = \sqrt{f'/m}$ are vibrational frequencies of atoms in the lattice sites and in the interstices, respectively. If to take into account that atoms surrounding interstitial ions and vacancies also change their vibrational frequency, then we have to take into account an additional contribution to the free energy, which will have the following form:

$$\Delta\mathcal{F}_2^{vib} = -NkT \left[\ln \left(\frac{v}{v''}\right)^{3z''} + \ln \left(\frac{v}{v'''}\right)^{3z'''} \right], \tag{190}$$

where z'' and z''' are numbers of atoms, surrounding interstitials and vacancies, respectively, while v'' and v''' are their frequencies.

Since the dependence of vibrational frequencies of atoms on temperature is quite weak, one can write:

$$\Delta\mathcal{S}^{vib} = -\left(\frac{\partial \Delta\mathcal{F}^{vib}}{\partial T}\right)_V = -\frac{1}{T}\left(\Delta\mathcal{F}_1^{vib} + \Delta\mathcal{F}_2^{vib}\right) = -\frac{1}{T}\Delta\mathcal{F}^{vib}. \tag{191}$$

Then Eq. 184 takes the form

$$N = \sqrt{N_0 N'} \exp\left(-\frac{U_F^f}{2kT}\right) \exp\left(\frac{1}{2k}\left(\frac{\partial \Delta\mathcal{S}^{vib}}{\partial N}\right)_T\right). \tag{192}$$

A quantity $\left(\partial \Delta\mathcal{S}^{vib}/\partial N\right)_T$ is an entropy change related to the alteration of vibrational frequency of the atom under its transition from the lattice site to the interstice, i.e. $\left(\partial \Delta\mathcal{S}^{vib}/\partial N\right)_T = \Delta S^{vib}$. Therefore,

$$N = \sqrt{N_0 N'} \exp\left(-\frac{U_F^f - T\Delta S^{vib}}{2kT}\right). \tag{193}$$

In fact, processes mentioned above do not give full list of phenomena, which are associated with formation of defects in crystal; therefore, we can write ΔS_F^f instead of ΔS^{vib}, implying under this designation the entropy change which occurs under all possible processes, but taking into account that the main contribution to ΔS_F^f is caused by the vibrational entropy. Then the expression for Frenkel pair concentration will have the form

$$N = \sqrt{N_0 N'} \exp\left(-\frac{U_F^f - T\Delta S_F^f}{2kT} \right) = \sqrt{N_0 N'} \exp\left(-\frac{\Delta F_F^f}{2kT} \right), \tag{194}$$

where ΔF_F^f is a free energy change under the formation of one Frenkel pair. To determine the dependence of the defect concentration on the external pressure, one has to use the Gibbs potential instead of the free energy:

$$\Delta \mathcal{G} = \Delta \mathcal{F} + P\Delta V = \Delta \mathcal{H} - T\Delta \mathcal{S}. \tag{195}$$

Then, the concentration of Frenkel pairs could be written in following general form:

$$N = \sqrt{N_0 N'} \exp\left(\frac{\Delta S_F^f}{2k} \right) \exp\left(-\frac{\Delta H_F^f}{2kT} \right), \tag{196}$$

where ΔH_F^f is the formation enthalpy of one Frenkel pair.

Consideration of the Schottky defect concentration depends on the composition of the compound, since, as it was noted above, Shottky disorder could comprise different amount of vacancies depending on chemical formula of the compound. For binary ionic crystal, such as NaCl, the equilibrium concentration of vacancies of both cations and anions is

$$N = N_0 \exp\left(-\frac{\Delta G_{Sc}^f}{2kT} \right), \tag{197}$$

where N_0 is the concentration of cations (or anions) in the crystal, and ΔG_{Sc}^f is the formation Gibbs energy of one Schottky pair.

2.1.4 Basics of diffusion

The equations governing diffusion processes are Fick's laws. These laws represent a continuum description and are purely phenomenological. The Fick's first law relates the concentration gradient of a given species ∇n with its flux J; for an isotropic medium, the Fick's first law can be written as follows:

$$J = -D\nabla n. \tag{198}$$

The negative sign in Eq. 198 indicates opposite directions of diffusion flux and concentration gradient. Diffusion is a process which leads to an equalization of concentration. The factor of proportionality, D, is referred to as the *diffusion coefficient* or *diffusivity* of the species considered. The diffusion coefficient has the dimension of *length*^{2} *per time* and bears the units $[\mathrm{cm^2 s^{-1}}]$ or $[\mathrm{m^2 s^{-1}}]$.

If the number of diffusing particles is conserved in the diffusion process, then the flux J has to obey an equation of continuity:

$$\frac{\partial n}{\partial t} = -\nabla \cdot J, \tag{199}$$

where $\nabla\cdot$ denotes the vector operation divergence. Fick's first law (Eq. 198) and the equation of continuity (Eq. 199) can be combined to give an equation, which is called Fick's second law or *diffusion equation*:

$$\frac{\partial n}{\partial t} = \nabla \cdot (D \nabla n), \tag{200}$$

which for concentration-independent diffusivity D in isotropic medium simplifies to

$$\frac{\partial n}{\partial t} = D \Delta n, \tag{201}$$

where $\Delta = \nabla \cdot \nabla$ denotes the Laplace operator.

Let us consider one of the solutions of Eq. 201 in a one-dimensional case. If the diffusing species (diffusant) is deposited at the plane $x = 0$, i.e. the initial condition is the following:

$$n(x,0) = n_s \delta(x), \tag{202}$$

where n_s denotes the number of diffusing particles per unit area, and $\delta(x)$ is the Dirac delta function, then the solution of Eq. 201 is [77]

$$n(x,t) = \frac{n_s}{\sqrt{\pi D t}} \exp\left(-\frac{x^2}{4Dt}\right). \tag{203}$$

The initial condition given by Eq. 202 is often called *instantaneous planar source*. This solution is also referred to as Gaussian solution. The quantity $l = \sqrt{4Dt}$ is a characteristic diffusion length, which occurs frequently in diffusion problems.

Other solution occurs, if the source of diffusant is constant. This situation takes place, when the free end of the semi-infinite medium is continuously exposed to a fixed concentration, e.g., when atoms from the constant source bombard the surface of the quite thick plate. In this case, the concentration distribution is defined as follows [77]:

$$n(x,t) = n_s \left[1 - \operatorname{erf}\left(\frac{x}{\sqrt{4Dt}}\right)\right], \tag{204}$$

where

$$\operatorname{erf}(z) = \frac{2}{\sqrt{\pi}} \int_0^z e^{-\gamma^2} d\gamma. \tag{205}$$

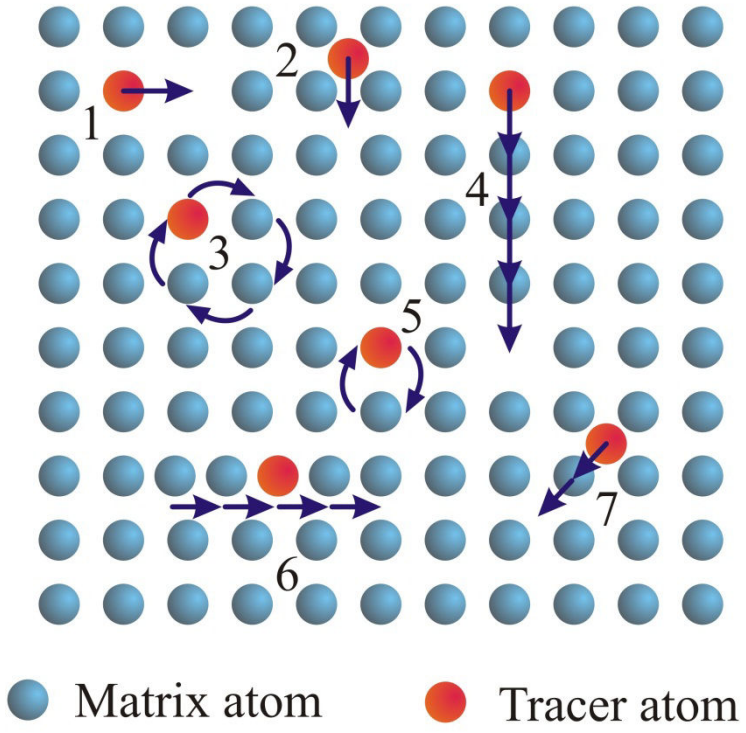

Fig. 12. Diffusion mechanisms: 1 – vacancy mechanism, 2 – interstitial mechanism, 3 – ring diffusion mechanism, 4 – caterpillar mechanism, 5 – direct exchange, 6 – crowdian mechanism, 7 – interstitialcy mechanism.

From a microscopic point of view, diffusion occurs by Brownian motion of atoms or molecules. In gases, diffusion occurs by free flights of atoms and molecules between their collisions. Here, a mean free path λ, corresponding to the average distance traveled by a moving particle between successive collisions, could be defined. The individual path lengths of fights are distributed around λ. Diffusion in liquids can be described as randomly directed shuffles, each much smaller than the average spacing of atoms in a liquid. Finally, in crystalline solids, diffusion occurs by atomic jumps in a lattice. The most important point is that a separation of time scales exists between the elementary jump process of particles between neighboring lattice sites and the succession of steps that lead to macroscopic diffusion [78]. In solids, the average distance between lattice sites δ (or between interstices) could take the role of the mean free path λ, and some formula derived for gases could be used for solids just substituting λ by δ.

The diffusion process (and the self-diffusion process as well) in a crystal can be implemented by several mechanisms [79-85]. If an atom in the node of the crystalline lattice could move jumping into an adjacent unoccupied lattice site (vacancy), then the diffusion is said to take place by *vacancy mechanism* (Fig. 12). This type of diffusion is quite general for

different solids and plays a decisive role in metals with packed structures. If an atom on an interstitial site moves to one of the neighboring interstitial sites, the diffusion occurs by an *interstitial mechanism* (Fig. 12). Such a movement or jump of the interstitial atom involves a considerable distortion of the lattice, and this mechanism is probable when the interstitial atom is smaller than the atoms of the normal lattice positions. Diffusion of interstitially dissolved light atoms, e.g. H, C, N, and O in metals provides the best-known examples of this mechanism.

If the distortion becomes too large to make the interstitial mechanism probable, interstitial atoms can move via an *interstitialcy mechanism*. In the interstitialcy mechanism, an interstitial atom pushes one of its nearest neighbors on a normal lattice site into another interstitial position and itself occupies the lattice site of the displaced atom (Fig. 12).

The diffusion of substitutional solutes and of solvent atoms themselves requires a mechanism different from interstitial diffusion [78]. Thus, self- and substitutional solute diffusion in metals could occur by a *direct echange* of neighboring atoms (Fig. 12), in which two atoms move simultaneously. If three or more atoms are involved in exchange mechanism, then the diffusion is said to occur through *ring diffusion mechanism*, which could be represented as a rotation of atoms as a group by one atom distance (Fig. 12). It should be noted that ring versions of atomic exchanges have lower activation energies but increase the amount of collective atomic motion, which makes this more complex mechanism unlikely for most crystalline substances.

In elemental solids, other variants of the interstitial mechanism have also been proposed. Thus, if several ions within some volume are displaced from their normal lattice positions to allow the placement of an additional ion along a line within the volume, the diffusion is said to occur by *crowdion mechanism*. The energy to move a "crowdion" may be small, but it can only move along the line or along equivalent directions. Finally, Yokota [86] proposed a so-called "*caterpillar mechanism*" for fast diffusion in Ag_2S. In this mechanism, it is assumed that an ion can jump not only into a nearest neighboring vacant site, but also into a site already occupied, with the result that the latter ion performs a similar jump in the same direction. This process continues until one of the ions ends the sequence by jumping into a vacancy.

Let us consider the case of unidirectional diffusion of interstitials in a simple cubic crystal. We assume for the sake of simplicity that the diffusing atoms are dissolved in low concentrations and that they move by jumping from an interstitial site to a neighboring one

with a jump length δ. Let us find the net flux J_x of diffusing particles between two planes, 1 and 2, at a distance of the jump length. We suppose a concentration gradient along the *x*-direction and introduce the following quantities: the jump rate Γ (number of jumps per unit time) from one plane to the neighboring one; number of interstitials n_{s1} per unit area in plane 1; number of interstitials n_{s2} per unit area in plane 2. Without a driving force, forward and backward hops occur with the same jump rate and the net flux J_x from plane 1 to 2 is

$$J_x = \frac{1}{2}\left(\Gamma n_{s1} - \Gamma n_{s2}\right). \tag{206}$$

The factor $1/2$ is introduced due to the fact that particles in both planes can jump in opposite directions, i.e. the number of particles jumping from plane 1 to 2 is $1/2\,\Gamma n_{s1}$, and the number of particles jumping from unit area of plane 2 to plane 1 is given by $1/2\,\Gamma n_{s2}$.

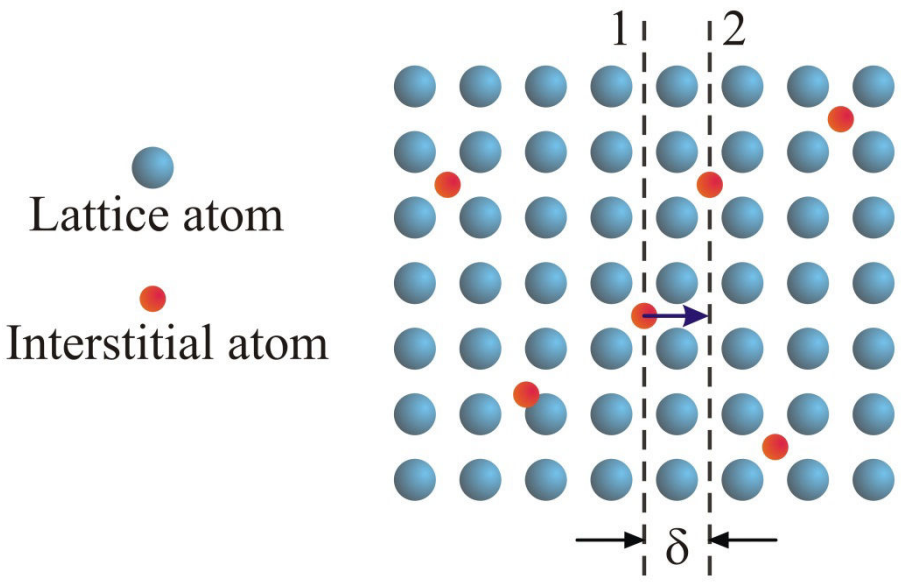

Fig. 13. Schematic representation of unidirectional diffusion of atoms in a lattice.

The quantities n_{s1} and n_{s2} are related to the volume concentrations of diffusing atoms via

$$n_1 = \frac{n_{s1}}{\delta}, \quad n_2 = \frac{n_{s2}}{\delta}. \tag{207}$$

Usually, in diffusion studies the concentration field, $n(x,t)$, changes slowly as a function of the distance variable x in terms of interatomic distances. From a Taylor expansion of the concentration-distance function, keeping only the first term, we get

$$n_1 - n_2 = -\delta \frac{\partial n}{\partial x}. \tag{208}$$

Inserting Eqs. 207 and 208 into Eq. 206 we have

$$J_x = -\frac{1}{2}\delta^2 \Gamma \frac{\partial n}{\partial x}. \tag{209}$$

If diffusion can take place in three orthogonal directions, only one third of the particles jump along positive direction of the *x*-axis. Therefore, in three-dimensional case

$$J_x = -\frac{1}{6}\delta^2 \Gamma \frac{\partial n}{\partial x}. \tag{210}$$

By comparison with Fick's first law (Eq. 198) we obtain for the diffusion coefficient

$$D = \frac{1}{6}\delta^2 \Gamma. \tag{211}$$

This equation shows that the diffusion coefficient is essentially determined by the product of the jump rate and the jump distance squared.

2.1.5 Diffusion as an activation process

Now let us consider in detail the movement of the interstitial atoms dissolved in low concentration in a simple cubic crystal. Such movement is associated with the transition of a given impurity atom to one of the neighboring interstices. The transition could be described in terms of usual double-well potential (for simplicity we shall believe that potential barrier and wells have a rectangular form). Barrier height adds up to the energy, which the atom has to possess to move to new interstice. The probability P_1 that the atom occupies the potential well depends on the width δ_1 of the well and on the energy U_1 of its "bottom". According to the Boltzmann distribution,

$$P_1 = \delta_1 \exp\left(-\frac{U_1}{kT}\right). \tag{212}$$

The probability P_2 to find the atom on the top of the barrier is defined by its width δ_2 and by the energy of the top U_2 via the similar expression. The ratio of these probabilities equals to

$$\frac{P_2}{P_1} = \frac{\delta_2}{\delta_1} \exp\left(-\frac{\Delta U}{kT}\right), \tag{213}$$

where $\Delta U = U_2 - U_1$ is the barrier height (Fig. 14).

The probability to find the atom in some state is proportional to the "lifetime" of the atom in this state, therefore P_2 / P_1 equals to the ratio of corresponding time intervals t_2 / t_1. Hereby,

$$\frac{t_2}{t_1} = \frac{\delta_2}{\delta_1} \exp\left(-\frac{\Delta U}{kT} \right). \tag{214}$$

It is easy to understand the meaning of time t_1: it is a "lifetime" of the atom in the potential well. The meaning of time t_2 is not so clear. It would seem that one can identify t_2 with a hopping time from one potential well to another, but such simplification is not quit accurate. In fact, this consideration does not take into account a dumping of energy which has to occur when the atom gets to a new well. If there is no such dumping, then after the hopping to the neighboring well the atom comes back to the old one; moreover, one can expect that the atom will jump hither and thither repeatedly if the redundant energy is not dumped. Thus, it is necessary to include into consideration some mechanism of energy dumping caused by the interaction of given atom with its surrounding. Then the "lifetime" of the atom on the top of the barrier t_2 is equivalent to the time of energy dumping, i.e. to the time to return to the equilibrium state. Hereinafter we shall imply that such dumping is taken into account.

At room temperature one can apply Maxwellian distribution for the atoms of crystalline lattice. It means that average kinetic energy at one degree of freedom equals to $kT / 2$, consequently, average velocity of atom in the potential well equals to $\sqrt{kT / m}$. At the same velocity (in order of magnitude) the jump to the neighboring well occurs. Hereby, for time t_2 we can write

$$t_2 = \frac{\delta_2}{\sqrt{kT / m}}. \tag{215}$$

Then for time t_1 we have

$$t_1 = t_2 \frac{\delta_1}{\delta_2} \exp\left(\frac{\Delta U}{kT} \right) = \frac{\delta_1}{\sqrt{kT / m}} \exp\left(\frac{\Delta U}{kT} \right). \tag{216}$$

The ratio $\frac{\delta_1}{\sqrt{kT / m}}$ equals to motion time of the atom from one wall of the potential well to another, i.e. equals to the vibration period of the atom in the interstice. So, replacing t_1 by τ one can write:

$$\tau = \tau_0 \exp\left(\frac{\Delta U}{kT} \right), \tag{217}$$

or in terms of a jump frequency

$$\nu = \nu_0 \exp\left(-\frac{\Delta U}{kT}\right), \tag{218}$$

where ν_0 is referred to as *attempt frequency*. Taking into account that the rate frequency is proportional to the number of adjacent sites (interstices) Z, i.e. $\Gamma = \nu Z$, one can write for the diffusion coefficient of the impurity

$$D = \frac{1}{6} Z\delta^2 \nu_0 \exp\left(-\frac{\Delta U}{kT}\right). \tag{219}$$

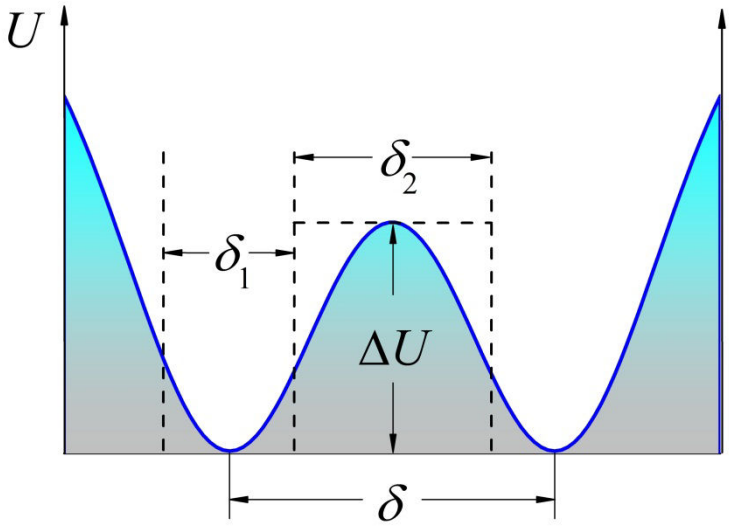

Fig. 14. Double-well potential describing the change of the atom energy during the duffusing jump.

Equation 219 has to be specified. The fact is that this formula was obtained with the assumption that the movement of the interstitial atom occurs regardless of the motion of other atoms, i.e. it is supposed that neighboring atoms persist in their equilibrium positions. Actually, under the shift of interstitial atom to another interstice, surrounding atoms have to "move aside". To take into account such process it is not enough to redefine the energy of the potential barrier ΔU. In fact, *one cannot consider thermal motion of a given atom irrespective of the motion of its neighbors; in other words, it is necessary to consider a complex composed of a given atom and its neighboring atoms or even, strictly speaking, the crystal in whole*. From this point of view the transition of the atom over the barrier can be considered as a specific fluctuation; the probability of such fluctuation is determined by the increase of Helmholtz energy ΔF at constant temperature and by the increase of Gibbs energy $\Delta G = \Delta H^m - T\Delta S^m$ at constant pressure, where ΔH^m is an enthalpy needed to carry

the defect from an initial equilibrium position to a saddle point (sometimes referred to as migration enthalpy) and ΔS^m is a corresponding entropy change.

Substituting ΔU by ΔG in Eq. 217 we shall obtain the following expression:

$$\tau = \tau_0 \exp\left(-\frac{\Delta S^m}{k}\right)\exp\left(\frac{\Delta H^m}{kT}\right), \tag{220}$$

whence for the diffusion coefficient we have

$$D = \frac{1}{6} Z\delta^2 v_0 \exp\left(\frac{\Delta S^m}{k}\right)\exp\left(-\frac{\Delta H^m}{kT}\right). \tag{221}$$

It should be noted that Eq. 221 is valid only for interstitial diffusion in dilute solid solutions, e.g., diffusion of protons by the free transport mechanism in metal oxides with simple cubic structure. The diffusivity of a host constituents (i.e. self-diffusion) by an interstitial mechanism is not only proportional to the probability that the interstitial defect jumps, but also to the probability that a constituent ion is interstitial. It means that the jump frequency will be now proportional to the concentration of the Frenkel pairs

$$\Gamma = vZ\, N/N_0, \tag{222}$$

where N and N_0 are the concentration of the Frenkel pairs and the full concentration of ions, respectively. Thereby, taking into account Eqs. 211 and 222 we shall obtain for the *self*-diffusion coefficient

$$D = D_0 \exp\left(-\frac{\Delta H^m + \Delta H_F^f/2}{kT}\right), \tag{223}$$

where

$$D_0 = \frac{1}{6} Z\sqrt{N'/N_0}\,\delta^2 v_0 \exp\left(\frac{\Delta S^m + \Delta S_F^f/2}{k}\right). \tag{224}$$

From the mathematical point of view, vacancy mechanism of self-diffusion is similar to diffusion of interstitials. However, it is impossible to measure directly in a real experiment the diffusion coefficient of holes (vacancies), since it is impossible to observe the motion of emptiness. In fact, one can measure a self-diffusion coefficient of the crystal, i.e. observe the motion of atoms (ions). If ions move due to the vacancy mechanism, then they can travel only when there is a hole at the neighboring site. Taking into account that the concentration of vacancies even at high temperatures is much less than the concentration of ions, one can expect the self-diffusion coefficient be also much less than the diffusion coefficient of vacancies. The relationship between them is determined as:

$$D = \frac{N}{N_0} D_v,$$

where N is the concentration of vacancies and D_v is their diffusion coefficient; N_0 is the concentration of lattice sites. For binary ionic solids, N is determined by the Eq. 197, while the diffusion coefficient of vacancies is determined by Eq. 221, where ΔH^m is referred to the "activation enthalpy" of vacancy migration.

2.1.6 Pre-exponential factor

Let us consider in detail the pre-exponential factor (or prefactor) D_0 in Eq. 223

$$D_0 = \alpha \delta^2 \nu_0 \exp\left(\frac{\Delta S^m + \Delta S_F^f / 2}{k} \right), \tag{225}$$

where $\alpha = \left(Z\sqrt{N/N_0} \right) / 6$. While the activation energy of the ion's jump is defined by the barrier "height", the pre-exponential factor is related to the number of atoms participating in this jump, or to the number of possible ways of jumping from a given position [80]. As one can see, D_0 depends on the value of the migration entropy ΔS^m as well as by the value of the defect formation entropy ΔS_F^f. These quantities should be distinguished. The latter is caused mainly by the change of the vibrational state of the crystal due to the shift of one atom from its normal position to the interstice. Migration entropy, in turn, is caused by the change of the vibrational state of the crystal due to the movement of the diffusing atom from its equilibrium position (the bottom of the potential well) to the saddle point, i.e. on the top of the potential barrier. It is usually assumed that $\Delta S^m \gg \Delta S_F^f$, and then the entropy part of the prefactor could be written as follows [87]:

$$\nu_0 \exp\left(\frac{\Delta S^m}{k} \right) = \frac{\prod_{j=1}^{\mathcal{N}} \nu_j}{\prod_{j=1}^{\mathcal{N}-1} \nu_j'}, \tag{226}$$

where ν_j is a j-th normal mode of the crystal at the starting point of the transition, and ν_j' is the value of a j-th normal frequency, when the diffusing atom oscillates near the saddle point; $\mathcal{N} = 3N_0$ is the number of degrees of freedom. Eq. 226 was first deduced by Vineyard and bears his name. This formula could be considered as a generalization of Eq. 189, where we considered all atoms of the crystal as independent three-dimensional oscillators. (It should be

noted that Eq. 189 was derived for the formation entropy ΔS_F^f, and v' had the sense of the vibrational frequency of an atom in an interstice. However, similar approach could be used for derivation of Eq. 226, but with v' having the sense of the frequency of the atomic oscillations in the saddle point.)

Let us now find the link between these quantities and thermodynamic properties of the crystal. According to the definition, entropy can be expressed as

$$S = -\left(\frac{\partial G}{\partial T}\right)_P. \tag{227}$$

One can write for the entropy change under the jump of the atom

$$\Delta S^m = -\Delta G_0 \left(\frac{\partial\left(\Delta G^m / \Delta G_0\right)}{\partial T}\right)_P, \tag{228}$$

where ΔG_0 is the Gibbs energy change under the movement of the atom at temperature $T = 0$. As $TS = 0$ at absolute zero, then ΔG_0 coincides with activation enthalpy ΔH^m of the process. If to assume that the Gibbs energy change under the ion's jump coincides with a work of lattice deformation, then the temperature dependence of ΔG^m is determined by the temperature dependence of shear modulus

$$\mu = \mu_0 + T\frac{d\mu}{dT}. \tag{229}$$

Consequently,

$$\frac{\partial\left(\Delta G^m / \Delta G_0\right)}{\partial T} = \frac{d\left(\mu / \mu_0\right)}{dT}, \tag{230}$$

whence

$$\Delta S^m = -\Delta H^m \frac{d\left(\mu / \mu_0\right)}{dT}. \tag{231}$$

For metals the following formula is valid [80]:

$$\frac{d\mu}{dT} \approx \frac{1}{T_m}, \tag{232}$$

where T_m is a melting temperature. Introducing coefficient

$$\lambda = \frac{d\left(\mu / \mu_0\right)}{d\left(T / T_m\right)}, \tag{233}$$

one can obtain

$$\Delta S^m = \lambda \frac{\Delta H^m}{T_m}. \tag{234}$$

(Note that the superscript *m* comes from the word "migration", whereas the subscript *m* comes from "melting".)

Most metals have $\lambda = 0.25 - 0.45$ [80]. For the pre-exponential factor we now have

$$D_0 = \alpha\delta^2 \exp\left(\frac{\lambda \Delta H^m}{kT_m}\right)\exp\left(\frac{\Delta S_F^f/2}{k}\right). \tag{235}$$

Unfortunately, estimation of entropy ΔS_F^f cannot be done so easy; however, the following rough generalization could be made

$$D_0 = \alpha\delta^2 \exp\left(\frac{\beta\lambda \Delta H^m}{kT_m}\right), \tag{236}$$

where the parameter β is of the order of unity [80].

It has to be noted that Eq. 236 is approximate formulae and coefficients λ and β do not have real physical sense. In addition, application of these formulae is limited by fcc and bcc metals, but sometimes they are used for the description of diffusion in ionic crystals [11, 88, 89]. In fast ionic conductors, where the phase transition is accompanied by a considerable disordering of the lattice, melting temperature T_m has to be substituted by temperature of the phase transition to the superionic state T_{tr}.

In most solids, the prefactor has the value in the range $D_0 = 10^0 - 10^{-3}\ \mathrm{cm^2/s}$; however, in case of surface diffusion or other types of "facilitated" diffusion, D_0 has lower value. Much less often, the pre-exponential factor surpasses 1 $\mathrm{cm^2/s}$. From the physical point of view, such case could be realized due to cooperative nature of diffusion, i.e. when a group of atoms is involved into a jump [80].

2.1.7 Correlation effects

Everywhere above it was assumed that each subsequent jump of the ion in the lattice occurs independently on the previous jumps. Such a jump sequence is usually termed *uncorrelated random walk* or a Markov sequence (memory free walk). The set of *n* individual ion jumps of a particle could be characterized by the mean square value of the net displacement

$$\left\langle \mathbf{R}^2 \right\rangle = \sum_{i=1}^{n} \left\langle \mathbf{r}_i^2 \right\rangle + 2\sum_{i=1}^{n-1} \sum_{j=i+1}^{n} \left\langle \mathbf{r}_i \mathbf{r}_j \right\rangle, \tag{237}$$

where $\mathbf{r}_i$ denotes a displacement vector under the *i*-th jump. In Eq. 237, the first term contains squares of the individual jump lengths only, whereas the second term contains $n(n-1)/2$ average values of the products $\mathbf{r}_i\mathbf{r}_j$, which define correlation (memory) effects. For a Markov sequence, these average values are zero, as for every pair $\mathbf{r}_i\mathbf{r}_j$ one can find for another particle of the ensemble a pair $\mathbf{r}_i\mathbf{r}_j$ equal and opposite in sign. Thus, for a random walk without correlation we have

$$\left\langle \mathbf{R}^2_{\text{random}} \right\rangle = \sum_{i=1}^{n} \left\langle \mathbf{r}_i^2 \right\rangle. \tag{238}$$

Several atomic mechanisms of diffusion in crystals entail diffusive motions of atoms, which are not free of memory effects. For example, correlation effects are involved by the vacancy mechanism. Thus, upon exchange, vacancy and "tagged" atom (tracer) move in opposite directions. Immediately after the exchange, the vacancy is for a while available next to the tracer atom, thus increasing the probability for a reverse jump of the tracer. Consequently, the tracer atom does not diffuse as far as expected for a complete random series of jumps. This reduces the efficiency of the tracer walk in the presence of positional memory effects with respect to an uncorrelated random walk.

Correlation effects could be accounted for by introducing the correlation factor f [78]

$$f = \lim_{n\to\infty} \frac{\left\langle \mathbf{R}^2 \right\rangle}{\left\langle \mathbf{R}^2_{\text{random}} \right\rangle} = 1 + 2\lim_{n\to\infty} \frac{\sum_{i=1}^{n-1} \sum_{j=i+1}^{n} \left\langle \mathbf{r}_i\mathbf{r}_j \right\rangle}{\sum_{i=1}^{n} \left\langle \mathbf{r}_i^2 \right\rangle}, \tag{239}$$

where unity (the leading term) is associated with uncorrelated (Markovian) jump sequences and double summation contains the correlation between jumps. Correlation factor may be also defined as the ration of the diffusivity of tagged atoms, D^*, and a hypothetical diffusivity arising from uncorrelated jump sequences, D_{random}, via

$$f = \frac{D^*}{D_{\text{random}}}. \tag{240}$$

Thereby, for the (self-)diffusion coefficient (Eq. 211) in the cubic lattice we now have to write

$$D \equiv D^* = \frac{1}{6} f\delta^2\Gamma. \tag{241}$$

Correlation effects are important in solid-state diffusion of crystalline materials, whenever diffusion is mediated by a diffusion vehicle. Examples for diffusion vehicles are

vacancies, vacancy pairs, self-interstitials, etc. There must be at least three identifiable "species" involved in the diffusion process. For example, during tracer diffusion via vacancies in pure crystals, the three participating "species" are vacancies, host atoms, and tracer atoms. Interstitial diffusion in a dilute interstitial solution is uncorrelated, because no diffusion vehicle is involved.

Under vacancy mechanism, successive jumps occur with higher probability in the reverse direction; therefore, the contribution of the double sum in Eq. 239 is negative. Consequently, if the diffusion vehicle is involved, i.e. when non-Markovian jumps occur, $f < 1$. For the Markovian jump sequence, the correlation factor equals to unity, $f = 1$. For example, in the face-centered cubic lattice the vacancy mechanism involves correlations with the factor $f = 0.7815$, whereas in the lattice with the diamond structure $f = 1/2$ [78]. Interstitial self-diffusion in any lattice is not accompanied with correlation effects, and $f = 1$.

2.1.8 Ionic conductivity and self-diffusion. Haven ratio

As it was mentioned above, external electric field applied to the crystal puts the irregular ionic motion in order and an electric current emerges. Current density governed by the drift of the ions of certain type is defined as

$$j = nev_d, \tag{242}$$

where e is a charge of ions, n is their concentration, and v_d is a drift velocity. At relatively low electric field E, the drift velocity is proportional to E:

$$v_d = uE = qeE; \tag{243}$$

coefficient of proportionality u is called ionic *mobility*. (A quantity $q = u/e$ is the mobility related to the value of the ionic charge, i.e. q is the coefficient of proportionality between the drift velocity and the force, $F = eE$, acting on the ion.) Substituting given expression for v_d into the equation for j, we shall obtain

$$j = ne^2qE = \sigma E, \tag{244}$$

where

$$\sigma = ne^2q \tag{245}$$

is an ionic conductivity of the crystal.

The mobility q is related to the diffusion coefficient by the relationship

$$q = \frac{\tilde{D}}{kT}, \tag{246}$$

which was introduced by Einstein and Smolukhovsky into the theory of Brownian motion, but is applicable also to particles of any type, if they move stochastically and follow the Maxwellian-Boltzmann statistics. Substituting Einstein-Smolukhovsky expression for q into the formula for conductivity σ, we shall obtain

$$\sigma = \frac{ne^2\tilde{D}}{kT}. \tag{247}$$

Equation 247 is usually referred to as *Nernst-Einstein relation*. It should be noted that $\tilde{D}$ does not correspond to the tracer diffusion coefficient D^*, which was considered above, but has to be related to *chemical diffusion* (therefore we use tilde above it). This is the consequence of the fact that Eq. 246 is deduced under the assumption that the concentration of diffusing particles obeys the Boltzmann distribution,

$$n(x) = A\exp\left(-\frac{U}{kT}\right), \tag{248}$$

where U is the potential energy of the particle in the external field. It means that diffusing species are considered as non-interacting particles. More generally, interactions are present between them. For this case, Murch [82] showed that the general form of the Nernst-Einstein relation is

$$\sigma = \frac{ne^2\tilde{D}}{kT}\left(\frac{\partial \ln(N/N_0)}{\partial \mu}\right), \tag{249}$$

where μ is the chemical potential of the particles and N/N_0 is their site fraction.

When the distribution of particles is completely ideal (no interactions, not even site blocking effects), the thermodynamic factor is unity and Eq. 249 reduces to Eq. 247. In this special case, the diffusion coefficient $\tilde{D}$ equals to the tracer diffusion coefficient D^*, so that

$$\sigma = \frac{ne^2D^*}{kT}. \tag{250}$$

When particles are ideally distributed but subject to site blocking effects, Eq. 249 can be written as [78]

$$\sigma = \frac{ne^2D^*}{fkT}, \tag{251}$$

where f is the tracer correlation factor considered above. It should be noted that Eq. 251 is appropriate to very dilute solution. Ionic crystals having a virtually perfect lattice of ions fall into this category.

In solid-state diffusion literature, Eq. 247 is often used to calculate another "diffusion coefficient" called the *charge diffusion coefficient* via

$$D_\sigma = \frac{k\sigma T}{ne^2}. \tag{252}$$

D_σ has the dimension of a diffusion coefficient; however, it does not correspond to any diffusion coefficient that can be measured by way of Fick's laws. Equation 252 is just used as a means of changing the d. c. conductivity to a quantity that has the dimensions of a diffusion coefficient. Note that the identification of D_σ with a diffusion coefficient is only adequate for non-interacting particles.

The ratio of the tracer diffusion coefficient, D^*, and the charge diffusion coefficient, D_σ, is called *Haven ratio*:

$$H_R = \frac{D^*}{D_\sigma}. \tag{253}$$

Strictly speaking, there is no a straightforward physical meaning of the Haven ratio; moreover, a general theory of H_R is not yet available. However, one can show that if the lattice of charge carriers is almost full or empty, then the interpretation of the Haven ratio is straightforward. Such case occurs, e.g., when the vacancy mechanism takes place. Then the Haven ratio simply equals the tracer correlation factor:

$$H_R \approx f. \tag{254}$$

In such a case, from a measurement of the Haven ratio the correlation factor and then the mechanism of diffusion could be exposed.

Finally, let us note that Eq. 247 defines the temperature evolution of the d. c. conductivity of ionic crystals:

$$\sigma T = \sigma_0 \exp\left(-\frac{\Delta H_\sigma}{kT}\right), \tag{255}$$

where $\Delta H_\sigma = \Delta H^m + \Delta H_F^f/2$. Thus, the activation energy of the conductivity has to be equal to the activation energy of the diffusion process. This fact could be used for validation of the conductivity/diffusion measurements. Note also that the linear temperature dependence of σ is sometimes ignored in view of its exponential dependence and the following formula is used:

$$\sigma' = \sigma_0 \exp\left(-\frac{\Delta H'_\sigma}{kT}\right), \tag{256}$$

where $\Delta H'_\sigma = \Delta H_\sigma + k\overline{T}$ and $\overline{T}$ is a mean temperature of a measuring interval.

2.2 Measurement of the self-diffusion coefficient in solids

2.2.1 Methods of diffusion measurement in solids

Various techniques were developed to measure diffusion coefficients in solids. One can group them into two major categories: direct and indirect methods.

Direct methods are based on the Fick's laws and phenomenological definition of the diffusion coefficient therein. They are sensitive to long-range diffusion and, in this sense, they are macroscopic. Among direct methods, the following techniques could be listed: tracer diffusion, chemical diffusion, nuclear reaction analysis, pulsed field gradient NMR, etc.

Contrary, indirect methods are not directly based on the laws of Fick. They usually study phenomena which are influenced by the diffusion jumps of atoms. Some of these methods are sensitive to one or a few atomic jumps only. Quantities such as relaxation times or line widths are measured and the mean residence time of the diffusing atoms, $\overline{\tau}$, is deduced therefrom. A microscopic model of the atomic jump process is needed to deduce the diffusivity. In the simple case, the diffusion coefficient is given by

$$D = \frac{\delta^2}{6\overline{\tau}}, \tag{257}$$

where δ denotes the length of the atomic jump. The following indirect techniques could be listed: mechanical spectroscopy (internal friction, Gorski effect), NMR line shape analysis, spin-lattice relaxation measurements, Mössbauer spectroscopy, etc.

One of the most widespread methods for measuring the self-diffusion coefficient is the method of radioactive isotopes (tracer diffusion) [78]. Different techniques could be applied within this method; the widely used one is the concentration profile analysis. The concentration could be measured directly by chemical, spectroscopic, radiometric methods, by x-ray and electron diffraction, or by different indirect methods, such as measurements of microhardness, electrical conductivity, thermal e.m.f., etc. These methods are usually destructive, but they are very informative, especially when studying heterogeneous media.

Two different types of boundary conditions are usually used in the method of radioactive isotopes: 1) diffusion from a constant source, when the constant flow of the diffusant is created on the boundary of the sample, e.g., by ion bombardment, or 2) thin source diffusion. In the second case, the sample is coated by a thin layer of radioactive substance followed by a high temperature annealing; usually, the annealing temperature is above $0.7T_m$ (T_m is a melting temperature). The concentration distribution $C(x)$ could be

determined by destructive methods, e.g., by beveling method, by method of layers removal, etc., or by nondestructive methods, such as nuclear spectroscopy, absorption of ionizing radiation, etc.

Other powerful tool for diffusion measurement is *pulsed field gradient* (PFG) NMR. In the PFG method, the attenuation of a spin echo signal resulting from the dephasing of the nuclear spins due to the combination of the translational motion of the spins and the imposition of spatially well-defined gradient pulses is used to measure motion. This method is widely used for measuring diffusion in solids as well as in liquids and is a unique tool for studying molecular dynamics in chemical and biological systems.

We used this method for measuring cationic diffusion in sulfates; therefore, it is expedient to write about PFG NMR in more detail.

2.2.2 Magnetic gradients and diffusion

To understand the principle of diffusion measurements using magnetic gradients, one has to generalize the following formula:

$$\omega_L = \gamma B_0, \tag{258}$$

where ω_L is a Larmor frequency, γ is a gyromagnetic ratio, and B_0 is an external magnetic field. (As above, we assume that $\mathbf{B}_0$ is oriented along the *z*-axis.) It is assumed implicitly in Eq. 258 that the magnetic field has the same value in any small part of the sample. If the gradient **g** of the magnetic field,

$$\mathbf{g} \equiv \nabla \mathbf{B} = \frac{\partial \mathbf{B}_z}{\partial x}\mathbf{i} + \frac{\partial \mathbf{B}_z}{\partial y}\mathbf{j} + \frac{\partial \mathbf{B}_z}{\partial z}\mathbf{k}, \tag{259}$$

exists, then the Larmor frequency will have different values in different points of the sample. Thereby, Eq. 258 has to be written as follows:

$$\omega_{eff}(\mathbf{r}) = \gamma\left(B_0 + \mathbf{gr}\right) = \omega_L + \gamma\mathbf{gr}. \tag{260}$$

In normal NMR spectrometers, it is more common to measure diffusion with the gradient oriented along the *z*-axis (i.e. parallel to $\mathbf{B}_0$). In this case, **g** depends only on *z* coordinate; therefore, we shall denote it as *g*. During time *t*, an individual spin will be turned through the angle

$$\varphi(t) = \underbrace{\gamma B_0 t}_{\text{static field}} + \underbrace{\gamma \int_0^t g(t')z(t')dt'}_{\text{applied gradient}}, \tag{261}$$

where the first term corresponds to the phase accumulated due to the constant external field, and the second term corresponds to the phase shift, caused by the field gradient. It is taken into account in Eq. 261 that the field gradient may depend on time. Time dependence of the spin coordinate $z(t)$ implies that the spin can diffuse.

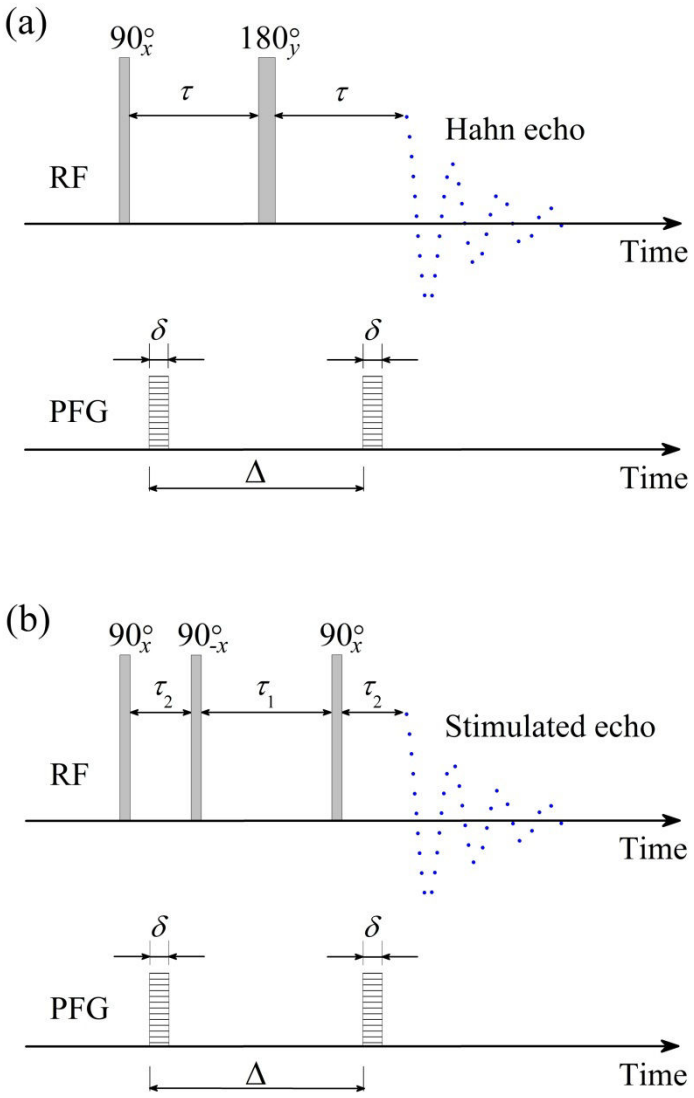

Fig. 15. Pulse sequences for the PFG NMR method: (a) Hahn echo and (b) STE sequences. The PFGs of the strength g and duration δ are applied at a tim interval of Δ. In the STE pulse sequence, three 90° radiofrequency pulses (RF) are applied; the interval τ_2 between the first and the secon RF pulses and between the third pulse and FID acquisition is related to T_2 process and the interval τ_1 between the second and the third RF pulses is related to the T_1 process. Detailed description of the Hahn echo pulse sequence see in the main text.

If the field gradient g is known, then it follows from Eq. 260 that one can label the position of a spin inside the sample (albeit indirectly, through the Larmor frequency). In addition, one can follow the motion of the spin through the sample (at least, along the z-axis), since the frequency of its precession will vary with the change of z coordinate. This provides the basis for measuring diffusion.

The most common approach is to use a simple modification [90, 91] of the Hahn spin-echo pulse sequence [92, 93], in which equal rectangular gradient pulses of duration δ are inserted into each τ period (the "Stejskal and Tanner sequence" or "PFG sequence") (Fig. 15a). We will now explain how this method works.

Let the equilibrium spin system exist and the PFG sequence is applied to it. $(90°)_x$-pulse rotates all the spins by 90°, placing them along the $-y$ axis of the rotating frame. During the first τ-period at time t_1, a gradient pulse of duration δ and magnitude g is applied so that at the end of the first τ-period, spin i experiences a phase shift

$$\varphi_i(\tau) = \underbrace{\gamma B_0 \tau}_{\text{static field}} + \underbrace{\gamma g \int_{t_1}^{t_1+\delta} z_i(t)dt}_{\text{applied gradient}}, \tag{262}$$

where we have taken g out of the integral since we are considering a constant amplitude gradient. At the end of the first τ-period, a $(180°)_y$ pulse is applied that has the effect of reversing the sign of the precession (i.e. the sign of the phase angle) or, equivalently, the sign of the applied gradients and static field. At time $t_1 + \Delta$, a second gradient pulse of equal magnitude and duration is applied. Thus, at the end of the echo sequence, the total phase shift of spin i relative to being located at $z = 0$ is given by

$$\begin{aligned} \varphi_i(2\tau) &= \left\{ \gamma B_0 \tau + \gamma g \int_{t_1}^{t_1+\delta} z_i(t)dt \right\} - \left\{ \gamma B_0 \tau + \gamma g \int_{t_1+\Delta}^{t_1+\Delta+\delta} z_i(t')dt' \right\} = \\ &= \gamma g \left\{ \int_{t_1}^{t_1+\delta} z_i(t)dt - \int_{t_1+\Delta}^{t_1+\Delta+\delta} z_i(t)dt' \right\}. \end{aligned} \tag{263}$$

If the spin was not diffusing during the experiment, then the phase shift due to the two gradient pulses would cancel, i.e. $\varphi_i(2\tau) = 0$. In the presence of diffusion, the total phase shift will be nonzero, and it will be determined by the value of a gradient g and a time Δ (Δ is often called a *diffusion time*).

Since in reality we deal with an ensemble of spins, we should talk about the mean value of $\varphi(2\tau)$, which is defined by the phase distribution function $P(2\tau,\varphi)$. The normalized intensity (i.e. an attenuation) of the echo signal, *S*, at $t=2\tau$ is determined by the average value of phase factor $\exp(i\varphi)$, i.e.

$$S(2\tau)=S_{g=0}(2\tau)\int_{-\infty}^{+\infty}P(2\tau,\varphi)\exp(i\varphi)d\varphi, \tag{264}$$

where $S_{g=0}(2\tau)$ is the signal intensity in the absence of gradient. By definition, $P(2\tau,\varphi)$ must be a normalized function, and so

$$\int_{-\infty}^{+\infty}P(2\tau,\varphi)d\varphi=1. \tag{265}$$

Thus, one can see that in the absence of diffusion, i.e. when $\varphi_i(2\tau)=0$ and $\exp(i\varphi)=1$, the signal $S(2\tau)$ will have a maximum value.

It is obvious that at zero gradient (or in the absence of diffusion) the signal attenuation is determined by the spin-spin relaxation time T_2,

$$S_{g=0}(2\tau)=S(0)\exp\left(-\frac{2\tau}{T_2}\right); \tag{266}$$

therefore, to find of the echo signal $S(2\tau)$, one has to determine the function

$$f(\delta,g,\Delta,D)=\int_{-\infty}^{+\infty}P(2\tau,\varphi)\exp(i\varphi)d\varphi, \tag{267}$$

which is determined by the pulse sequence. To solve this problem, one can use a macroscopic approach, which implies consideration of Bloch equations including the effects of diffusion of magnetization.

These equations could be written in the vector form as follows:

$$\frac{\partial\mathbf{M}(r,t)}{\partial t}=\gamma\mathbf{M}\times\mathbf{B}(\mathbf{r},t)-\frac{M_x\mathbf{i}+M_y\mathbf{j}}{T_2}-\frac{\left(M_z-M_0\right)\mathbf{k}}{T_1}+D\nabla^2\mathbf{M}, \tag{268}$$

which is valid for isotropic diffusion. If to assume that both external magnetic field and field gradient are applied along the *z*-axis, then one can write the following equalities:

$$B_x=0,\ B_y=0,\ B_z=B_0+gz. \tag{269}$$

Substituting Eq. 269 into Eq. 268, and taking into account that

$$M\times B=\left(M_yB_z-M_zB_y\right)_x+\left(M_zB_x-M_xB_z\right)_y+\left(M_xB_y-M_yB_x\right)_z, \tag{270}$$

we shall obtain the following equation:

$$\frac{\partial m}{\partial t} = -i\omega_L m - i\gamma g z m - \frac{m}{T_2} + D\nabla^2 m. \tag{271}$$

where

$$m = M_x + iM_y. \tag{272}$$

In the absence of diffusion (i.e. $D = 0$), Eq. 271 is an ordinary differential equation with separable variables. In this case, *m* relaxes exponentially with the time constant T_2:

$$m = \psi \exp\left(-i\omega_{eff} t - \frac{t}{T_2}\right), \tag{273}$$

where ψ represents the amplitude of the precessing magnetization unaffected by the effects of relaxation. Substituting Eq. 273 into Eq. 271 we shall obtain the following equation:

$$\frac{\partial \psi}{\partial t} = -i\gamma g z \psi + D\nabla^2 \psi, \tag{274}$$

whose solution has the following form in the absence of diffusion:

$$\psi(z,t) = S \exp\left(-i\gamma z F\right), \tag{275}$$

where *S* is a constant, and

$$F(t) = \int_0^t g(t')dt'. \tag{276}$$

Now, if we consider the case of the PFG pulse sequence, then evolution of the spin system after the $(90°)_x$-pulse is described by Eq. 275, where *S* corresponds to the value of ψ immediately after the pulse. If during the first τ-period a magnetization vector will be rotated by the angle φ in the *xy*-plane, then after the 180°-pulse it will be rotated by the angle $-\varphi$ relative to the original position (i.e. 180°-pulse will turn the magnetization vector through the angle -2φ). Thus, we have after the $(180°)_y$-pulse:

$$\psi(z,t) = S \exp\left[-i\gamma z \left(F - 2f\right)\right], \tag{277}$$

where $f = F(\tau)$. Equations 275 and 277 can be combined into

$$\psi(z,t) = S \exp\left[-i\gamma z \left(F - 2H(t-\tau) f\right)\right], \tag{278}$$

where $H(t)$ is the Heaviside step function. It should be noted that Eq. 278 was derived for the PFG sequence, and so in the case of other pulse sequence this equation could be invalid.

Now let us take into account the influence of diffusion on the value of the magnetization. To do this, one has to substitute Eq. 278 into Eq. 274; assuming that *S* is a function of time we shall obtain the following equation:

$$\frac{dS(t)}{dt} = -\gamma^2 D\left[F - 2H(t-\tau)f\right]^2 S(t). \tag{279}$$

Integration of Eq. 279 from 0 to 2τ gives

$$\ln\left[\frac{S(2\tau)}{S(0)}\right] = \ln\left[E(2\tau)\right] = -\gamma^2 D\left\{\int_0^{2\tau} F^2 dt - 4f\int_\tau^{2\tau} F dt + 4f^2\tau\right\}, \tag{280}$$

where $E(2\tau)$ is an attenuation of the echo signal caused by spin diffusion in the field gradient. In case of the PFG sequence, the expression in the curly brackets equals to $g^2\delta^2\left(\Delta - \delta/3\right)$ [94]; therefore,

$$E(2\tau) = \exp\left[-\gamma^2 g^2 D\delta^2\left(\Delta - \frac{\delta}{3}\right)\right]. \tag{281}$$

Eq. 281 shows that varying *g*, Δ, or δ one can find diffusion coefficient *D*. Usually, the field gradient *g* is used as a variable, whereas magnitudes Δ and δ are used as parameters.

It should be noted that when measuring the diffusion coefficient in the powder sample, the value of Δ should be chosen carefully. Actually, each powder particle has a border, which sometimes could be impenetrable; therefore, the value of *D* could be determined improperly. The fact is that if the real diffusion coefficient *D* if quite large, then at big values of Δ a diffusing atom could be reflected many times from the "walls" of the crystalline particle being in its volume. Consequently, if the boundary effects are not properly accounted for and we analyze the data using the model of free diffusion, we will measure an apparent diffusion coefficient D_{app} and not the true diffusion coefficient. This effect is called *restricted diffusion*.

Restricted diffusion could be characterized by the dimensionless variable

$$\xi = \frac{D\Delta}{R^2},$$

where *R* is a radius of a powder particle. If $\xi << 1$, then free diffusion occurs, i.e. the diffusing particle does not diffuse far enough to feel the effect of the boundary. In this case, change of Δ does not lead to a change in the measured diffusion coefficient, and $D_{app} = D$. If $\xi \approx 1$, then a certain fraction of the particles will feel the effect of the boundary, and the apparent diffusion coefficient D_{app} will be now dependent on the diffusion time Δ. Finally, if $\xi > 1$, then the maximum distance that the confined particle can travel is limited by the boundaries, and thus the measured mean-squared displacement and diffusion coefficient again becomes independent of Δ and depends only on *R*. Thus, when measuring the diffusion coefficient, one

has to make sure that parameters of the experiment correspond to the case of $\xi < 1$. To do this, one should compare measurements at different values of Δ.

Finally, note that the Stejskal-Tanner sequence has several drawbacks. Since the main events for the magnetization take place in the *xy*-plane, the maximum value of the diffusion time Δ is limited by the spin-spin relaxation time T_2. Actually, at small values of T_2, the NMR signal decays rapidly, and so one cannot use big values of Δ because of the small intensity of the echo signal. One can avoid this difficulty by using a pulse sequence presented in the Fig. 15b (*stimulated echo sequence*) [94]. In this case, after the $(90°)_x$-pulse the gradient pulse is applied followed by another $(90°)_x$-pulse, which returns the magnetization to the *z*-axis. Now, the main events for the magnetization take place in the *xz* plane; therefore, the signal attenuation is determined mainly by the time T_1. Since $T_1 \geq T_2$, the time Δ can be larger than in the case of the Stejskal-Tanner sequence. Note that Eq. 281 is also valid for the STE sequence.

Other difficulty, which occurs both for the Stejskal-Tanner sequence and STE sequence, is the generation of eddy currents in the surrounding conducting surfaces around the gradient coils (e.g., probe housing, cryostat, radiation shields, etc.), which could appear during the rapid rise of the gradient pulses. Eddy currents can have the following effects: (a) phase changes in the observed spectrum and anomalous changes in the attenuation, (b) gradient-induced broadening of the observed spectrum, and (c) time-dependent but spatially invariant B_0 shift effects (which appears as ringing in the spectrum). To decrease the generation of eddy currents, one uses shielded gradient coils and additional field gradient pulses [95].

Chapter 3. High-temperature NMR

3.1 NMR at high temperature

3.1.1 General aspects of high-temperature NMR

The term "high-temperature (HT) NMR" means rather different things for different groups of scientists. Thus, biochemists can use this term already for 320 K, whereas for material scientists the high-temperature NMR range could reach more than 2300 K.[96, 97] The most common commercially available NMR probes allow heating the sample using the heat transfer via a flowing gas stream passing through the heater placed at a distance from the radiofrequency coil. In this case, it is capable to reach only 420-520 K. This technique rapidly becomes inefficient because of low gas heat capacities, but has been used with success to 870-1020 K in both designs for static and MAS probes [96, 98, 99].

Temperatures higher than those available with gas flow heating could be reached, e.g., by means of static probes with relatively large radiofrequency coils surrounding both heater and sample, and kept cool by vacuum dewars or by water cooling system [100]. In this case, resistive heating elements must meet several unusual design criteria. They must be insensitive to the radiofrequency field to prevent distortion of the magnetic field at the sample. A number of geometries have been discussed, including bifilar solenoids, straight wires or rods parallel to the magnetic field, and concentric sheet metal cylinders [101, 102]. In some cases, power supplies have been cycled on and off in synchronization with radiofrequency pulses to eliminate field perturbations.

The highest temperatures can be reached with laser heating system [20, 40, 97, 103], which can eliminate many of difficulties of resistive heating. It should be noted, however, that the laser heating is not widespread, and extremely high temperatures (~2800 K) NMR experiments have been developed in one laboratory (CNRS CEMHTI, Orléans, France), with CO_2 continuous lasers with levitation device to avoid any interaction between the sample and the sample holder.

The experimental setting usually used in CEMHTI for HT NMR measurements with laser heating is presented in Fig. 16. It is made of the following elements: CW CO_2 laser of 250 W (one or two depending on experimental requirements), a visible red lase aligned with the CO_2 laser to provide a visualization of the optical path, and a copper mirror allowing the reflection of the laser beams axially in the center of the cryomagnet shim assembly.

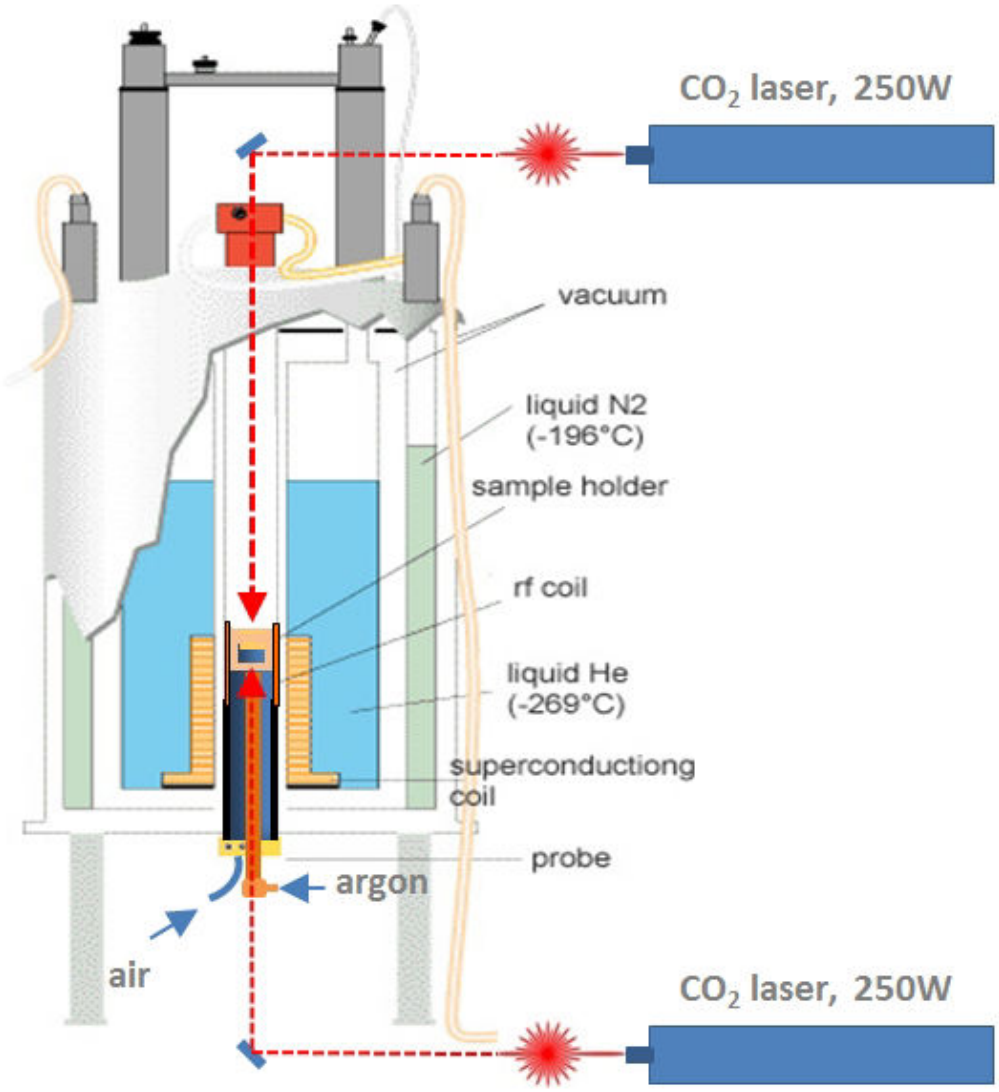

Fig. 16. Schematic representation of the NMR spectrometer equipped with two CO_2 lasers for sample heating (CNRS CEMHTI, Orléans, France).

Different kinds of information become available in HT NMR experiments. Thus, HT solid-state phase transitions could be investigated by this approach. Structural information from NMR line shapes in solids could occasionally be obtained at elevated temperatures, and more applications are coming with the improvement of high-temperature magic-angle spinning (MAS) technology [104-106]. In many materials, such as molten salts, metals and oxides, the liquid phase of interest cannot be quenched to room temperature and the study of these objects could be carried out only *in situ* at high temperatures.

3.1.2 Three main difficulties of high-temperature NMR

A number of technical difficulties are inherent to NMR measurements at elevated temperatures. We shall consider here three of them: 1) the choice of an appropriate container, 2) thermal shielding, 3) measurement and control of the temperature. Nowadays, all of these technical challenges are successfully resolved.

The container

For many materials particularly reactive liquids, the simple task of finding a suitable container often becomes quite difficult at high temperature. Because materials of substantial thickness located between sample and radio frequency coils must be electrically insulating (or at least radio frequency transmitting), the use of metal or graphite sample containers is generally precluded. Solutions to problems of reaction between containers and samples thus can be limited. Silica glass or ceramics have often been used for both solid and liquid metal samples and organic materials. Silica glass tubes have also been used for molten salts, although alkali vapors in particular can cause devitrification and failure at high temperature. Container made of tubular single crystals of sapphire (Al_2O_3) could be used for these purposes. Hexagonal boron nitride, BN, which is characterized by good thermal conductivity, inertness, and high melting temperature (3246 K), has proven to be a satisfying container material for a large range of substances including highly corrosive liquid fluorides [103].

Thermal shielding

The problem of thermal shielding is particularly relevant, if there is little space between the sample and the emission/detection coil. Since the radiofrequency coil is close to the sample, it is thus close to the sample temperature; therefore, the signal-to-noise ratio in the coil wire will be significantly reduced due to thermal noise. Moreover, the electrical resistivity of metals increases substantially with increasing temperature (often by a factor of 4 from 300 to 1500 K), reducing the quality factor Q and thus lowering both the excitation field and the sensitivity to the NMR signal.

The best way to eliminate this problem is to keep the radiofrequency coil at temperatures below 400 K. The laser heating system allows to meet this requirement relatively simply and very effectively. It could be carried out by using several ceramic barriers with an argon flow passing between them. This allows cooling the ceramics preventing the coil from the heating and the crucible from oxidizing as well [20].

The PFG NMR probe, where such thermal shielding is realized, was designed at CEMHTI; its head is presented in Fig. 17. The crucible is inserted into a mullite support, surrounded by an alumina tube. An additional protection in the form of silica glass tube is

placed between the alumina tube and the coil. An argon stream at room temperature flows between the mullite cradle and the alumina tube. The radiofrequency coil is also cooled by an additional nitrogen (or air) stream (see also Fig. 16). An additional water cooling of the gradient coil is also used.

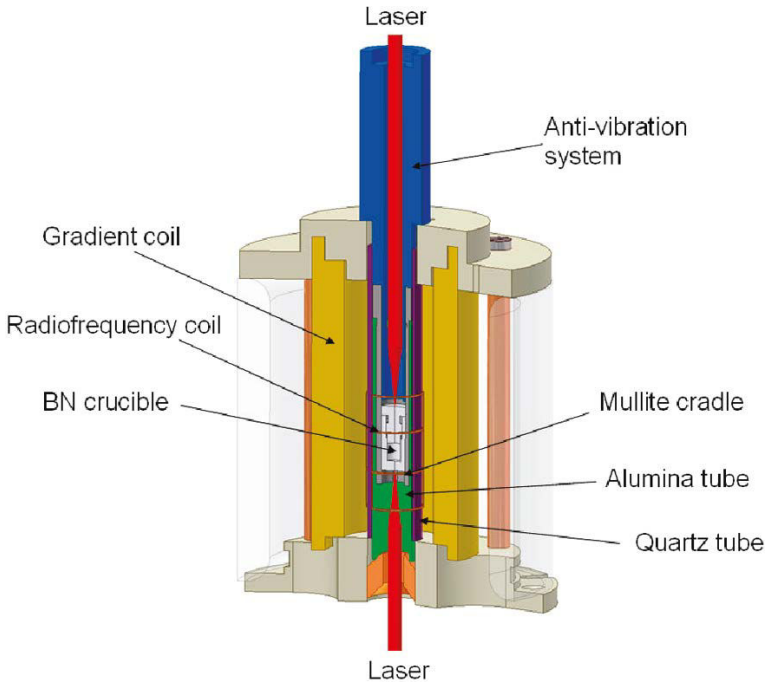

Fig. 17. Schematic drawing of the high temperature PFG NMR probe head [20].

It should be noted that this PFG NMR probe is unique and, at present, is available only at CEMHTI. Main advantage of this technique is that it allows studying ion dynamics and local structure of both liquids and solids at very high temperatures (up to 1500 K).

Temperature control and calibration

Temperature control in HT NMR experiments is complicated by the need to isolate thermocouples from radiofrequency field of excitation pulses, and to prevent the introduction of parasitic signal into the receiver. One of the possibilities to eliminate this problem is the location of the temperature sensor at some distance from the sample; however, this requires the careful calibration of temperature gradients. At sufficiently high temperatures (particularly above 1900 K), optical pyrometry could be used as a useful alternative to thermocouples.

At relatively low temperatures, lead nitrate, $Pb(NO_3)_2$, could be used as an effective NMR thermometer. The idea is that the isotropic chemical shift δ_{iso} of ^{207}Pb nuclei is very sensitive to the change of temperature. An empirical relation between absolute temperature and isotropic chemical shift δ_{iso} of ^{207}Pb was found by Beckmann [107]:

$$T = \left(\delta_{iso} + 3713.9\right)/0.758. \tag{282}$$

The maximum temperature, which could be measured with this "thermometer", is limited by the melting point of the lead nitrate (543 K).

Temperature measurement in the case of laser heating also cannot be applied directly, and an indirect calibration of the temperature is usually used. If only one laser is used for heating [40], and the sample container is heated by the laser beam at its bottom, then the temperature of the crucible could be measured using a thermocouple inserted into the upper part of the crucible. After this calibration, the thermocouple is removed and the crucible with the sample is heated at the same conditions (the same gas pressure, the same position of the laser focalization point on the crucible, etc.). It is obvious that when heating the container only from its one side, temperature gradients occur in the sample. To eliminate (or at least decrease) the value of the temperature gradients, heating by two continuous CO_2 lasers (from top and bottom of the crucible) could be used. The main disadvantage of this geometry is inability to use thermocouple; therefore, the temperature calibration is usually made using several compounds whose melting temperature is well defined. One uses here the fact that at the melting point the NMR signal usually changes greatly.

Let us consicder in detail the temperature calibration of CO_2 laser-heating system in the NMR study. The main goal of our consideration is to find the relation between the laser power W delivered to the crucible and the resuling temperature T of the sample. Moreover, the problem of the cooling rate will be also considered.

It has been already noted earlier [20] that at small CO_2 laser power the temperature increases linearly with power; however, at higher temperatures this dependence is not linear anymore due to the radiation of the crucible. To find a quite general expression for $W(T)$ (or for $P(T)$, where P is a percentage of the maximum available laser power), an equation of the heat transfer through the surface of the crucible has to be considered.

First, note that the most dielectrics have high value of the attenuation coefficient at the CO_2 laser wavelength ($\lambda = 10.6\,\mu\text{m}$), and the radiation is absorbed by a layer of several microns in thickness. This applies also to the boron nitride, but the attenuation length here is quite big: $l = 100\,\mu\text{m}$ [108]; nevertheless, we shall assume hereinafter that the heat source is always a surface. The total heat flow dQ/dt through the surface of the crucible could be written as follows:

$$\frac{dQ}{dt} = \left(\frac{dQ}{dt}\right)_N + \left(\frac{dQ}{dt}\right)_{SB} + W, \tag{283}$$

where the first term determines the heat transfer from the container surface to the surrounding gas flow through a forced convection (so-called Newtonian cooling); the second term corresponds to the energy loss via radiation and is sometimes referred to as Stefan cooling [109]; finally, W is a laser power delivered to the crucible.

Under the forced convection, the heat loss is proportional to the temperature difference between the hot body and the fluid:

$$\left(\frac{dQ}{dt}\right)_N = -Ah(T - T_{gas}), \tag{284}$$

where T_{gas} is the temperature of the surrounding gas, A is the surface area, and h is a heat transfer coefficient, which is assumed to be independent on temperature. Generally, h depends on the kind of the heat transfer agent, type of convection, geometry of the cooling body, etc. Note also that in reality h is not always constant and sometimes depends on temperature difference. For the gas, h could take values in the rage 10-300 $\mathrm{W{\cdot}m^{-2}K^{-1}}$ [110].

The second term in Eq. 283, which corresponds to the Stefan cooling, is

$$\left(\frac{dQ}{dt}\right)_{SB} = -A\sigma(\varepsilon T^4 - \alpha T_{env}^4), \tag{285}$$

where $\sigma = 5.67 \times 10^{-8}\ \mathrm{W{\cdot}m^{-2}K^{-4}}$ is a Stefan-Boltzmann constant, ε and α are emissivity and absorptivity of the crucible, respectively, and T_{env} is the mean temperature of the sources of thermal radiation in the environment of the sample container.

Finally, the power of the laser could be written as follows:

$$W = pW_{max}{\cdot}(P/100), \tag{286}$$

where W_{max} is a maximum available laser power, and P is a percentage of the maximum power controlled by the experimenter. It should be taken into account that a certain fraction of the delivered laser power is spent on reflection and scattering by optical elements (mirrors, optical windows, etc.); therefore, one has to introduce the coefficient p corresponding to the part of the laser power directly used for heating.

Under fixed laser power, the system will increase (or decrease) its temperature until input and output heat flows are equal. At equilibrium, the heat flow equals to zero, $dQ/dt = 0$; therefore, combining Eqs. 283-286, one can write for the temperature dependence of P:

$$P = aT^4 + bT - c, \tag{287}$$

where

$$a = \frac{A\sigma\varepsilon \cdot 100}{pW_{max}}, \quad b = \frac{Ah \cdot 100}{pW_{max}}, \quad c = \frac{A \cdot 100}{pW_{max}}(hT_{gas} + \sigma\alpha T_{env}^4). \tag{288}$$

If at some value of P (let us designate this value as P_1) the system is in equilibrium, then the decrease of the laser power leads to the cooling of the crucible, which could be described by the following equation:

$$C\frac{dT}{dt} = -Ah(T - T_1) - A\sigma\varepsilon(T^4 - T_1^4) - \frac{pW_{max}}{100}\Delta P, \tag{289}$$

where $C = dQ/dT$ is a heat capacity of the container's material, $\Delta P = P_1 - P_2$, and $P_2 < P_1$. There is no prospect to integrate Eq. 289 to obtain an analytical time dependence of temperature; however, at certain conditions, one can simplify this equation. Thus, if the temperature difference is quite small, i.e. $T - T_1 << T_1$, then one can represent $T^4 - T_1^4$ as follows:

$$T^4 - T_1^4 = (T^2 + T_1^2)(T + T_1)(T - T_1) \approx 4T_1^3(T - T_1). \tag{290}$$

Substituting Eq. 290 into Eq. 289, we shall obtain:

$$\frac{dT}{dt} = -\kappa(T - T_1) - w\Delta P, \tag{291}$$

where

$$\kappa = \frac{A}{C}(h + 4\sigma\varepsilon T_1^3), \quad w = \frac{pW_{max}}{C \cdot 100}. \tag{292}$$

Integration of Eq. 291 gives

$$T(t) = T_1 - \frac{w\Delta P}{\kappa}\left(1 - e^{-\kappa t}\right). \tag{293}$$

At small t, i.e. at $\kappa t << 1$, one can simplify Eq. 293 to obtain

$$T(t) = T_1 - w\Delta P t. \tag{294}$$

Finally, one can see that cooling rate at small t is constant and proportional to ΔP:

$$-\left.\frac{dT}{dt}\right|_{\kappa t \ll 1} = w\Delta P. \tag{295}$$

We obtained two important results. First, Eq. 287, which could be used for the temperature calibration, gives a thermometer for the CO_2 laser heating system. Second, Eq. 295, which allows evaluating the cooling rate (without thermocouple!) using ΔP as a measure of this rate.

For NMR measurements, we used a Bruker Avance WB 400 MHz spectrometer (the operating field 9.4 T) equipped with two CO_2 lasers "Coherent Diamond K-250"

($W_{max} = 250\,\mathrm{W}$ for each laser). The used static NMR probe was a new high-temperature probe especially designed by the Bruker company and modified in CEMHTI, Orléans. We used an argon stream preventing the BN from oxidizing at high temperature and providing the convective heat transfer from the crucible; an additional nitrogen stream was also used for cooling the radiofrequency coil. The BN crucible containing the powder and closed with the screw cap was heated symmetrically by the two lasers from top and bottom. For the temperature calibration, four samples with different melting temperatures, T_m, were used: $LiNO_3$ ($T_m = 527\,\mathrm{K}$) [111], $(LiF)_{0.5}$-$(KF)_{0.5}$ ($T_m = 765\,\mathrm{K}$) [112], $LiNaSO_4$ ($T_m = 888\,\mathrm{K}$) [37], and $(YF_3)_{0.2}$-$(LiF)_{0.8}$ ($T_m = 968\,\mathrm{K}$) [113]. Note also that the α-β phase transition in $LiNaSO_4$ ($T_{tr} = 788\,\mathrm{K}$) [10] is also accompanied with a great NMR signal change; therefore, the temperature of its transition could also be used as a reference point. Thus, we have five reference points, all of which lie on the curve defining by Eq. 287 (Fig. 18). Fitting parameters were found to be: $a = 1.96\times10^{-12}\,\mathrm{K}^{-4}$, $b = 4.14\times10^{-3}\,\mathrm{K}^{-1}$, $c = 0.33$.

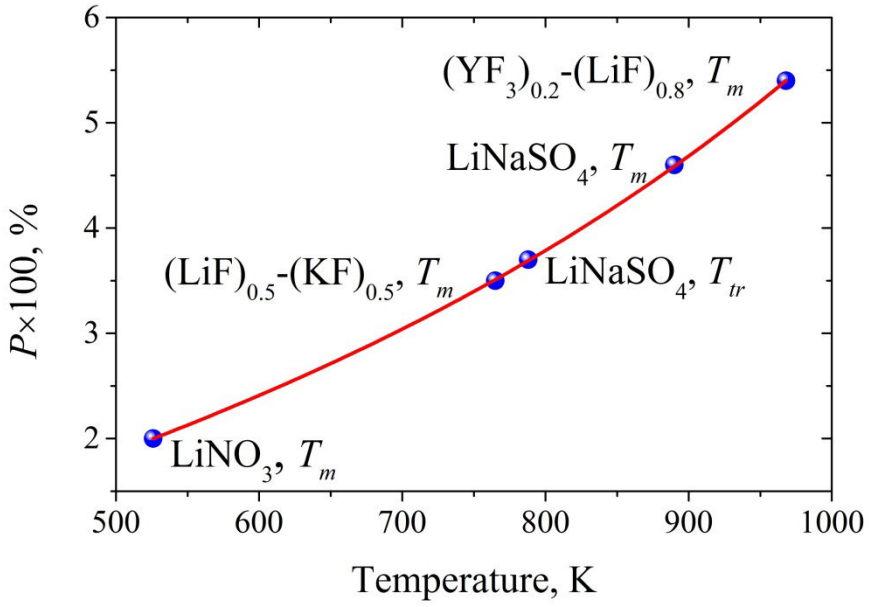

Fig. 18. Percentage of the lasers power (CO_2 250 W) versus sample temperature.

Let us also estimate the cooling rate of the BN crucible using Eq. 295. The value of W_{max} available with two CO_2 lasers is 500 W; assuming that $p = 0.95$ and taking into account that the heat capacity of BN above 700 K is ca. 20 J/(K·mol) [114] one can find that the BN crucible of the weight ca. 1.6 g is cooling with the rate

$$-\left.\frac{dT}{dt}\right|_{\kappa t \ll 1} = r \approx 3.6 \times \Delta P \text{ K/s}. \qquad (296)$$

Note once again that Eq. 296 is valid only at small t, i.e. at the initial stage of the cooling process.

It should be noted that the result given by Eq. 296 is very important, since it gives an opportunity for *kinetic* measurements and thus extends the range of issues of HT NMR.

Chapter 4. Experimental study of alkali sulfates

4.1 Structure and dynamics of lithium-sodium sulfate

4.1.1 Structure of $LiNaSO_4$

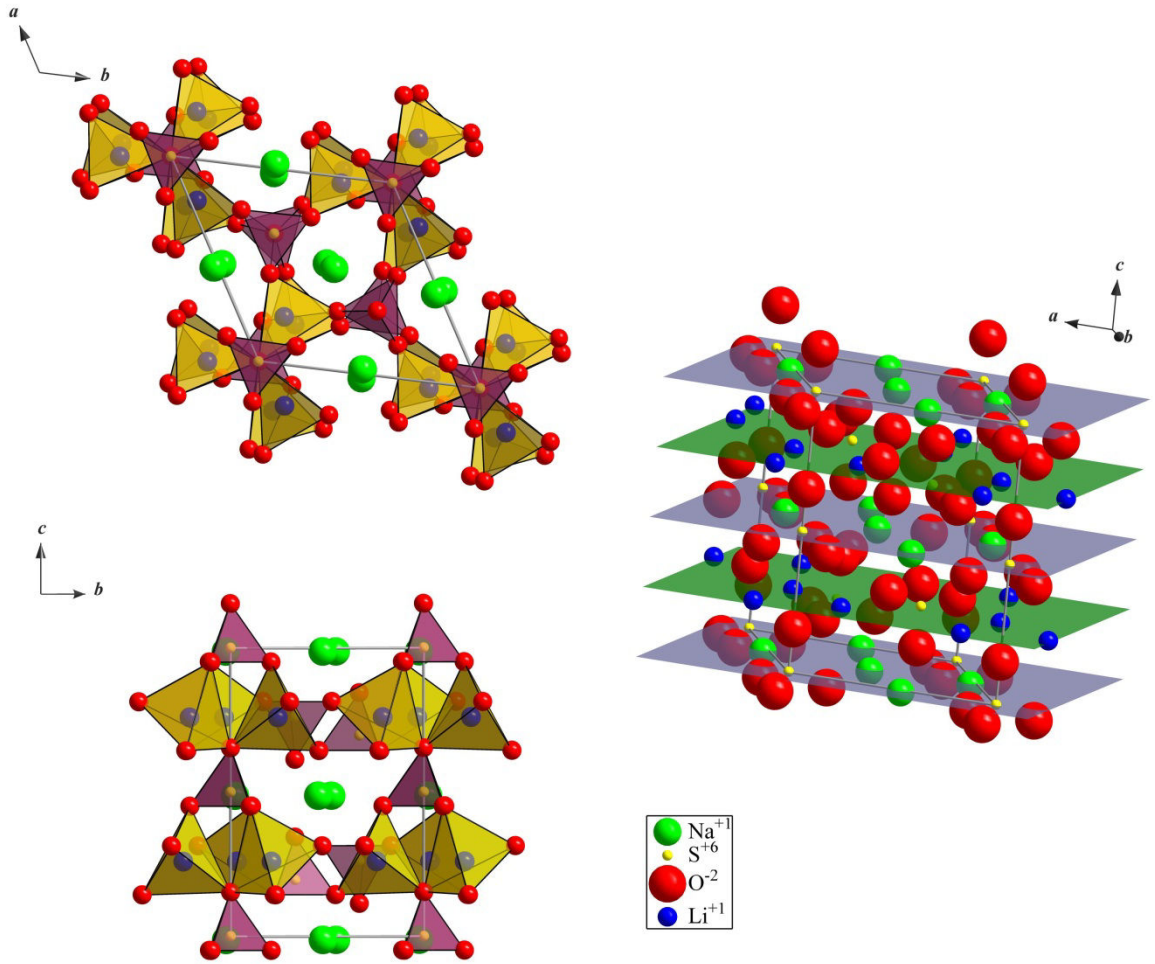

Fig. 19. Projections of β-$LiNaSO_4$ structure along [100] and [001] (on the left) and 3D-structure of β-$LiNaSO_4$ represented as "sandwich" (on the right).

The structure of LNS at room temperature (β-modification) was first deciphered in 1967 by Morosin and Smith [115]. At room temperature, the crystal structure of LNS is trigonal with space group symmetry $P31c$ and six formula units per unit cell. Lattice parameters are $a = 7.6310$ Å and $c = 9.8600$ Å [10]. The unit cell has the form of a right prism whose vertices and centers of the edges, oriented along the c-axes, are occupied by sulfur atoms. Each S^{+6} ion is surrounded by four O^{-2} ions, which form quite regular tetrahedrons. The average $S-O$ separation (1.469 Å) found in LNS is in agreement with

similar values (1.467–1.474 Å) found in other sulfates [115]. Projections of the LNS unit cell along [100] and [001] directions are presented in Fig. 19.

The structure of β-LNS is built up of SO_4 and LiO_4 tetrahedrons adjoined by their vertices (see Fig. 19). Three crystallographically different SO_4-groups are located on the threefold axes in two types of sequences. In the first type along $(0, 0, z)$ all the SO_4 tetrahedrons are oriented pointing up. In the second along $(\frac{1}{3}, \frac{2}{3}, z)$ and $(\frac{2}{3}, \frac{1}{3}, z)$ the tetrahedrons are arranged ordered up and down. The linkage of the SO_4 and LiO_4 tetrahedrons leads to a channel-like structure. The Na^+ ions are located inside these channels surrounded by an irregular arrangement of eight oxygens forming a distorted antiprism [10, 115]. The structure of β-LNS can be also presented as a "sandwich", i.e. stack of alternating planes of two types. Planes of the first type are occupied by Li^+ and S^{+6} ions, whereas other planes are occupied by Na^+ and S^{+6} ions (see Fig. 19). Layers between them are occupied by oxygens as well as sulfur atoms, which belong to SO_4 groups aligned along $(\frac{1}{3}, \frac{2}{3}, z)$ and $(\frac{2}{3}, \frac{1}{3}, z)$. Such presentation of LNS structure could be useful when comparing crystalline lattice of α- and β-modifications, since the orientation of the c-axis coincides with [111] direction in the lattice of α-LNS [10].

In 1958, Förland and Krogh-Moe [28, 29] deciphered the high-temperature structure of LNS. It was shown that above 788 K [10] (α-modification) LNS has a body-centered cubic structure with a high dynamical disorder of cationic (Li^+, Na^+) and oxygen sub-lattices. In fact, Li^+, Na^+, and O^{-2} ions have no fixed coordinates in the structure of α-LNS; therefore, the high-temperature phase of LNS is sometimes treated as *quasi-liquid* state. It was found later by means of reverse Monte Carlo modeling [35] that the highest Na^+ density distribution is in the six octahedral $(\frac{1}{2}, 0, 0)$ sites, while the Li^+ density distribution is far more disordered: Li^+ ions are found everywhere except in the SO_4 sites, even in those Na^+ positions that are not occupied by Na^+ ions. Diffusion of sulfur atoms, in turn, is negligible and they occupy (0,0,0) and $(\frac{1}{2}, \frac{1}{2}, \frac{1}{2})$ sites in the body-centered cubic cell.

In the α-modification, which exists in the temperature range 788-888 K, LNS has very high ionic conductivity (0.92 $Ohm^{-1}cm^{-1}$ at 823 K [116]); just below the melting point (888 K) the conductivity is 1.35 $Ohm^{-1}cm^{-1}$ and it increases by about 10% when the salt melts [37]. Below the phase transition to the β-modification, the ionic conductivity abruptly decreases by at least two orders of magnitude: 0.0010 $Ohm^{-1}cm^{-1}$ at 773 K [117].

4.1.2 Preparation of samples

$LiNaSO_4$ single crystals were grown by slow evaporation method using Na_2SO_4 and $Li_2SO_4 \cdot H_2O$ as precursors. It should be noted that crystals of alkali metal salts are usually grown from water solutions because of several reasons:

- most of the alkali metal salts are highly soluble in water; it allows to grow crystals at relatively low temperature ($50-60°C$) and pressure;
- single crystals grown from the aqueous solution have clearly defined habit that allows determining the directions of the crystallographic axes and the angles between them;
- growing from the aqueous solution does not require special expensive equipment in contrast to the growing of crystals from the melt, where maintenance of high temperature is required.

Methods of the crystal growing from the solution could be classified by ways to create a supersaturation in the solution: 1) method of reducing the temperature, 2) evaporation method, 3) method of a temperature difference. The choice of the growing method depends on the chemical composition of precursors. Thus, if precursors have positive solubility coefficients, i.e. their solubility increases with temperature, then one usually uses the method of reducing the temperature. In this method, the supersaturation necessary for the crystal growth is created by a slow decrease of the temperature. Different variants of this method differ in the initial temperature, in the temperature reduction rate, and in other details.

Some alkali sulfates have negative solubility coefficients [118], so the decrease of the temperature will lead to the decrease of the supersaturation, and crystals will not grow. In this case, the evaporation method is used. The idea of this method is based on the fact that the vapor pressure of the solvent is almost always greater than the vapor pressure of the dissolved substance. Therefore, to create the supersaturation it is enough to allow the vapor go to the environment. Thereby, the supersaturation necessary for the crystal growth could be supported just by the evaporation of the water from the solution. Note that this method requires a high stability of the temperature, since a small increase of the temperature leads to the dissolution of vertices and edges of the crystal. Evaporation of the solution should occur in a sterile environment, i.e. presence of dust particles in the solution should be excluded.

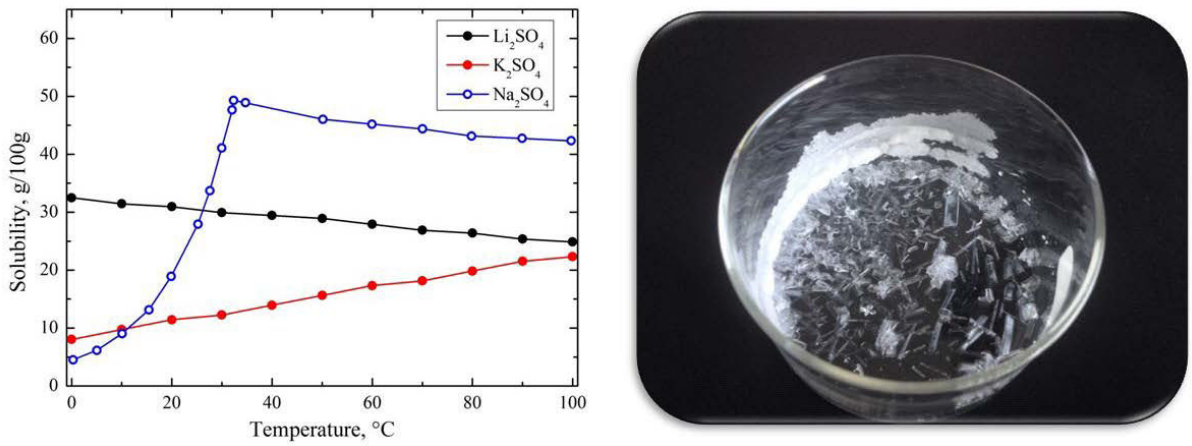

Fig. 20. Solubility curves of some alkali sulfates [118] (on the left) and crystalline aggregates of $LiNaSO_4$ grown by evaporation from the solution (on the right).

Solubilities of sodium sulfate, Na_2SO_4, and lithium sulfate monohydrate, $Li_2SO_4 \cdot H_2O$, are presented in Fig. 20 (left). One can see from this figure that the solubility of lithium sulfate decreases with temperature, whereas the solubility of sodium sulfate initially increases when heating, reaches a maximum at about 30°C, and then slowly decreases with temperature. Such behavior of solubilities does not allow using the method of reducing the temperature, and the slow evaporation method should be used.

Equimolar solution of Na_2SO_4 and $Li_2SO_4 \cdot H_2O$ was prepared at 313 K. After a complete dissolution of the components, the solution was filtered to remove insoluble impurities and small undissolved crystallites. Thereafter, we poured the solution into a glass crystallizer and placed into a thermostat at 333 K. To reduce the rate of the evaporation we covered the crystallizer with the cap from a metal foil with holes ~0.5 mm in a diameter. Crystals with linear sizes 4×2 mm were grown during two weeks. Grown crystals had clearly defined habit – their shape had the form of triangular prism. Some of crystals had an equatorial mark in the form of superficial crack. When crystals reached the desired size, we removed them from the crystallizer and the rest of the solution was evaporated completely to obtain crystalline aggregates of LNS (see Fig. 20 right). Obtained aggregates were immersed into ethanol to remove water from the surface, and then were dried and crumbled under the argon atmosphere in the gloves box. The obtained powder was analyzed by X-ray diffraction showing pure $LiNaSO_4$ X-ray diffraction pattern.

Unannealed powders and annealed samples were studied separately. Annealing of powders was carried out in BN crucibles at atmospheric pressure in a furnace Nabertherm L9/11 with controller P320. Two sets of samples were annealed at temperatures 823 K and

763 K. High-temperature annealing was carried out for 24 hours; the samples were heated at 4.5 K/min and were cooled at 1 K/min.

4.1.3 Experimental details

4.1.2.1 NMR measurements

High-temperature NMR measurements have been carried out using a Bruker Avance WB 400 MHz spectrometer, operating at 9.4 T. The BN crucible containing the powder and closed with the screw cap was heated symmetrically by two CO_2 lasers (detailed descriptions are given in Chapter 3). Two different probes were used for measurements.

Diffusion measurements were carried out using a modified 10 mm axial liquid NMR probe equipped with a gradient coil (5.5 G/(cm A)) coupled with gradient amplifier Great 10A (10A) [20]. The head of this PFG NMR probe is presented in Fig. 17. The maximum value of the magnetic field gradient available with this probe was 1200 G/cm. The 90°-pulse for ^{7}Li magnetization had the RF field strength in the range 15-20 kHz in different experiments. In case of ^{23}Na, the RF field strength was 20 kHz. LiCl and NaCl molar solutions were used as reference for the ^{7}Li and ^{23}Na chemical shift scales, respectively.

Both ^{7}Li and ^{23}Na diffusion phenomena were observed using a stimulated-echo (STE) PFG NMR pulse sequence (Fig. 15b). The stimulated echo attenuation E was fitted by the Stejskal and Tanner equation

$$E = \exp\left[-\gamma^2 g^2 \delta^2 D\left(\Delta - \frac{\delta}{3}\right)\right], \tag{297}$$

where parameters δ and Δ were fixed, and the gradient g was varied in the range from 0 to 1200 G/cm.

Relaxation measurements and kinetic study (see below) have been done using a static NMR probe designed in CEMHTI and manufactured by the Bruker company. The main advantage of this probe is an ability to cool the sample with considerable cooling rate (~100 K/min), since the multilayer ceramic barrier is substituted here by a single-wall thick ZrO_2 tube. Moreover, the space between the sample and the emission/detection coil is slightly increased in this probe due to the use of a powerful coil with a bigger diameter (18 mm compare to 10 mm in case of diffusion probe).

The spin-lattice relaxation time constants of ^{7}Li was found via saturation-recovery pulse sequence, whereas spin-lattice relaxation time of ^{23}Na nuclei was measured using

inversion-recovery technique (see Fig. 7). Recovery of the magnetization $A(\tau)$ in the saturation-recovery experiment was fitted by the function

$$A(\tau) = A(\infty)\left[1 - \exp\left(-\frac{\tau}{T_1}\right)\right], \tag{298}$$

whereas after inversion-recovery pulse-sequence the intensity of the recovering signal was analyzed by

$$A(\tau) = A(\infty)\left[1 - 2\exp\left(-\frac{\tau}{T_1}\right)\right]. \tag{299}$$

To record NMR spectra of the LNS single crystal we used the same high-temperature experimental setup as in case of powder. Since the largest faces of the crystal are parallel to the *c*-axis, we can unambiguously determine the orientation of the crystal. Thus, in the experiment, the crystal was placed on the bottom of the crucible onto one of its three largest faces, i.e. the *c*-axis of the crystal was oriented perpendicular to the magnetic field.

4.1.2.2 X-ray diffraction

In situ high temperature XRD data were collected on a D8 Advance Bruker diffractometer ($\mathrm{Cu\ K}\alpha_{1,2}$ radiation) equipped with a Vantec-1 linear detector and a HTK16 Anton Paar chamber. The powder sample was deposited on a platinum ribbon heating stage. The temperature behavior of this ribbon was previously calibrated using known phase transitions and thermal expansion of a corundum reference. The heating rate in the XRD experiment was 10 K/min, whereas minimum and maximum cooling rates were taken to be 2 K/min ("slow cooling") and 100 K/min ("fast cooling"), respectively. Isothermal data were collected between 15 and 70° (2θ) with a 0.016° step size.

4.1.2.3 DFT calculations

Along with experimental study, we have carried out CASTEP [119] calculations of the principal values of the EFG and tensors of ^{7}Li and ^{23}Na nuclei in β-LNS. To obtain C_Q and η values for, a plane wave basis set energy cut-off of 650 eV and a Monkhorst-Pack [120] grid density in the range 0.05-0.06 Å^{-1} (corresponding to a *k*-point mesh of $4\times2\times2$) were used. The computation of the EFG tensors were performed using the PAW method [121]. For the NMR calculations, we used structures obtained after PBE-DFT atomic position optimization [122]. Atomic positions were optimized by minimizing the residual forces on all atoms below

10 meV $Å^{-1}$ using the Broyden-Fletcher-Goldfarb-Shanno (BFGS) method [123] and keeping symmetry constrains and fixing the cell parameters to the experimentally determined values.

4.1.4 Line width analysis

4.1.4.1 ^{7}Li and ^{23}Na NMR line width narrowing in $LiNaSO_4$

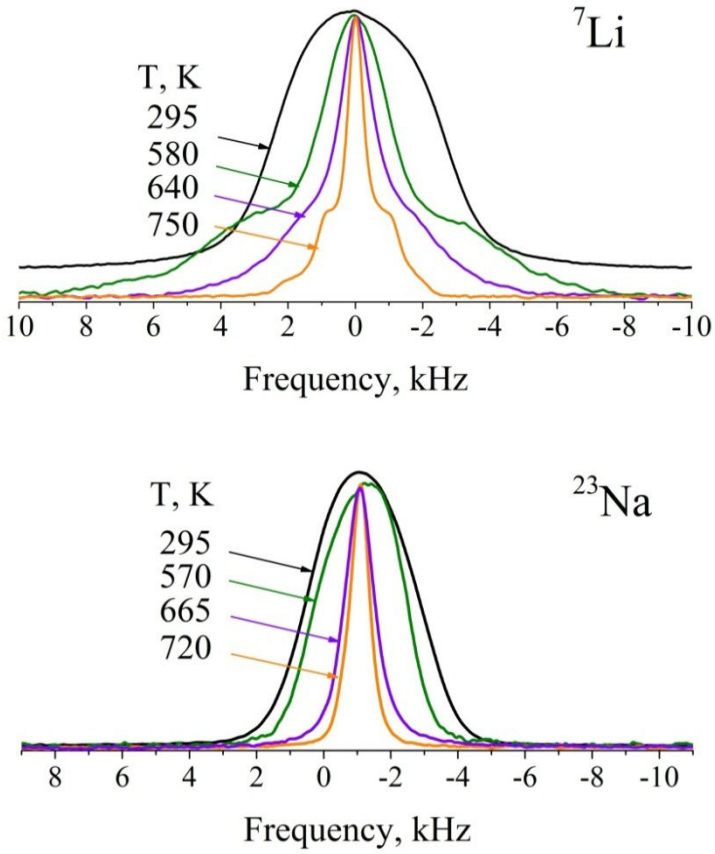

Fig. 21. Temperature dependences of ^{7}Li and ^{23}Na NMR spectra.

It was noted by several authors [11, 13, 40] that even below the phase transition, both Li^{+} and Na^{+} ions can diffuse in LNS. For the first time it was revealed by Massiot *et al*. [40] who carried out ^{7}Li and ^{23}Na NMR line width analysis as well as spin-lattice relaxation measurements in a wide temperature range (295-940 K). Activation energies for Li^{+} and Na^{+} motion below the phase transition were estimated to be 0.86 and 1.54 eV, respectively. Kanashiro *et al*. [11] performed spin-lattice relaxation measurements of ^{7}Li nuclei and revealed that the temperature evolution of the ^{7}Li spin-lattice relaxation rate in LNS single crystal at different magnetic fields could not be described by a single BPP curve, but the spectral density function with at least two correlation times has to be used (Fig. 5),

i.e. diffusivity of both cationic sub-lattices was confirmed. The authors estimated activation

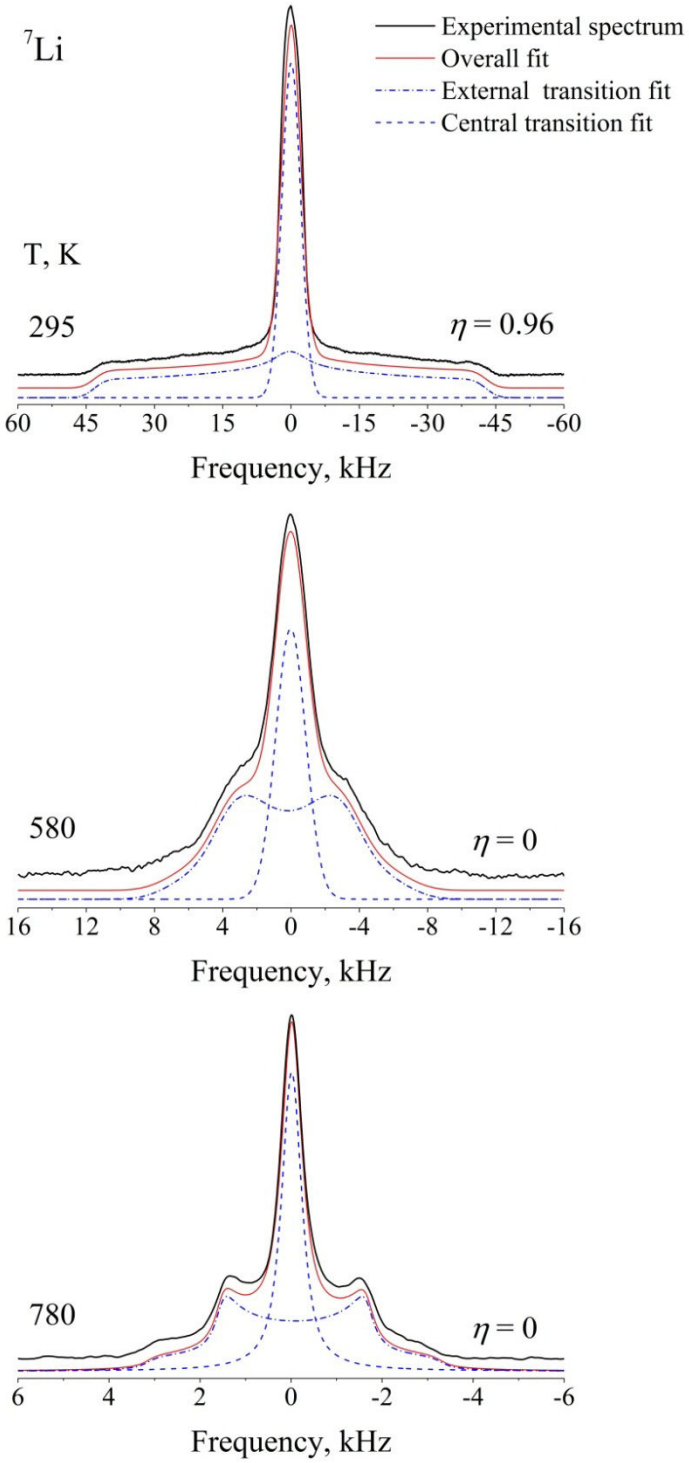

Fig. 22. ^{7}Li NMR powder spectra of $LiNaSO_4$ at different temperatures and their computer fitting. Black solid line corresponds to the experimental spectrum; dashed and dash dotted lines correspond to the central transition and external transition fits, respectively; red solid line corresponds to the overall fit of the spectrum.

energies for Li^+ and Na^+ motion below 788 K to be 0.7 and 1.20 eV, respectively. An additional proof of the Na mobility could be obtained from the temperature analysis of the IR absorption spectra of LNS. Thus, it was noted by Zhang *et al*. [13] that the temperature dependence of Na modes is similar to the behavior of Li modes; namely, both sets of spectral lines exhibit considerable frequency shifts and broadenings when heating. Taking into account that such behavior of lithium modes is caused by the Li^+ diffusion, one can reasonably assume that Na^+ ions can also leave their lattice sites.

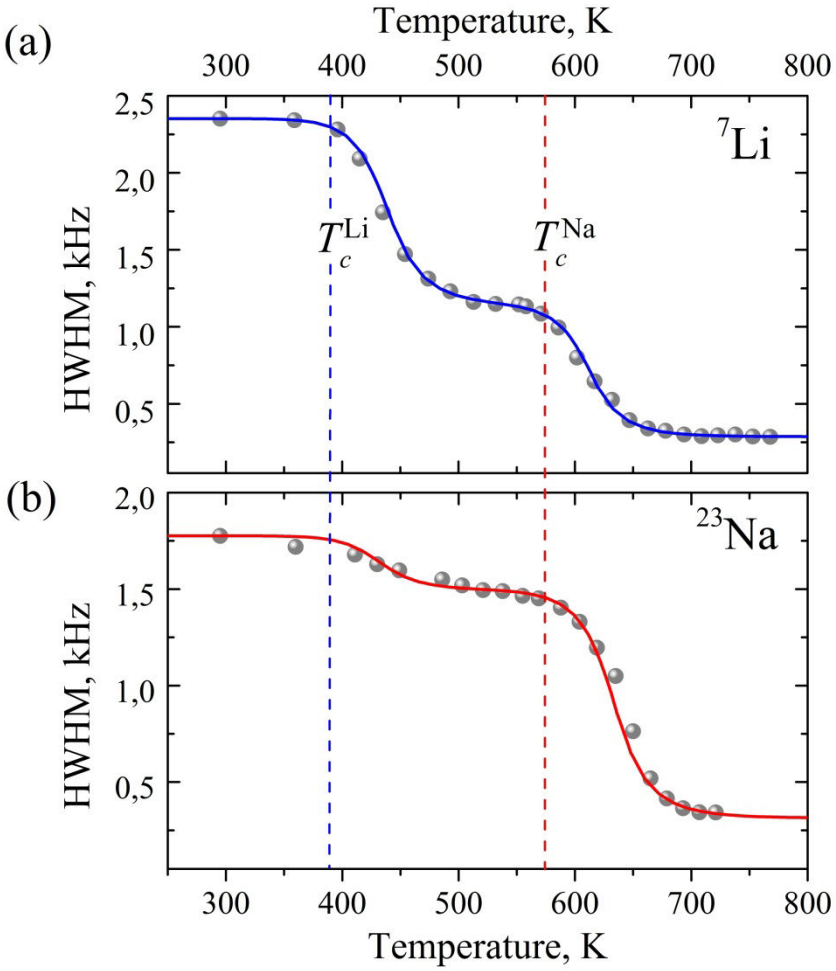

Fig. 23. Temperature dependences of ^{7}Li (a) and ^{23}Na (b) NMR line widths (HWHMs). Dotted vertical lines indicate onset temperatures of the motional narrowing.

Temperature evolutions of ^{7}Li and ^{23}Na NMR spectra of the LNS powder in the temperature range 295-788 K are presented in Fig. 21 (see also Figs. 29 and 34). The values of the NMR line widths were found by fitting of the LNS powder spectra (Fig. 22) with DMfit software [124]. It should be noted that in case of ^{7}Li (Fig. 23a) only the *central* transition line

width was taken into account. Note also that the central transition was fitted by a pseudo-Voigt function $V_p(x)$:

$$V_p(x) = pL + (1-p)G(x), \tag{300}$$

where $G(x)$ is a Gaussian curve, $L(x)$ is a Lorentzian curve, and $0 \le p \le 1$. Parameter p, which defines the relative weight of the Gaussian- and Lorentzian-type contribution to the line width broadening, varies from zero to unity in the course of motional narrowing. In the rigid lattice the spectral line has the Gaussian-type broadening ($p \approx 0$), whereas at high temperature, when cationic mobility is very fast, the narrowed line has the shape close to the Lorentzian curve ($p \approx 1$).

One can see from Fig. 23 that temperature dependences of ^{7}Li and ^{23}Na NMR line widths have the form of a two-step function. It should be taken into account that both ^{7}Li and ^{23}Na are quadrupolar nuclei; therefore, the width of the central line may contain contribution from the quadrupolar interactions. The influence of the quadrupolar Hamiltonian on the central transition depends on the value of the quadrupolar coupling constant and, consequently, it will affect differently ^{7}Li and ^{23}Na spectra. Let us consider this question in more detail.

In solids containing ^{7}Li nuclei, the value of the rigid line width could be usually used as the natural measure of the dipolar interactions. For the LNS, the half-width at half-maximum (HWHM), $\delta\omega_0^{\mathrm{Li}}/2\pi \approx 2.35\times10^3$ Hz, is 37 times smaller than the value of C_Q, which was found to be 8.7×10^4 Hz. (The value of C_Q was determined the fir of the ^{7}Li magic angle spinning spectrum at room temperature; the fit is presented in Fig. 24.) However, the second order of the quadrupolar interactions is negligible: $\chi_Q^2/2\pi\omega_L \approx 10$ Hz (at $\omega_L/2\pi = 155.5\times10^6$ Hz), where $\chi_Q = 3\pi C_Q/I(2I-1)$. Since we study the temperature evolution of only the central transition, the contribution of the external transitions to the central line of the ^{7}Li NMR powder spectrum can be neglected.

It should be also noted that the value of the spin-spin relaxation time could be very small, if quadrupolar interactions are quite big. This may lead to an additional broadening of the NMR line, which could surpass the dipolar broadening of the line. However, this case could be easily identified, since the shape of the NMR line should then differ significantly from the Gaussian. We revealed that the central transition line in the LNS at room temperature can be almost ideally fitted by the Gaussian function; therefore, one can

confidently conclude that its broadening is inhomogeneous, i.e. occurs due to the dipolar interactions of a big amount of spins.

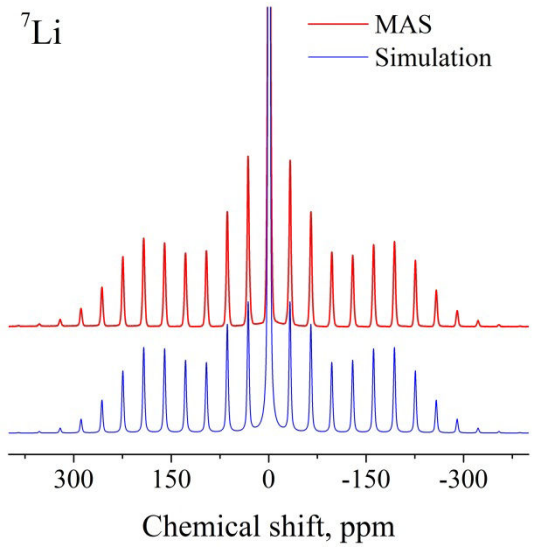

Fig. 24. Room temperature ^{7}Li NMR spectra of $LiNaSO_4$ powder: red line corresponds to the magic angle spinning (MAS) spectrum at rotating frequency 5 kHz, whereas blue line corresponds to the best fit of the MAS spectrum. The fitted value of the quadrupolar coupling constant, C_Q, was 8.7×10^4 Hz.

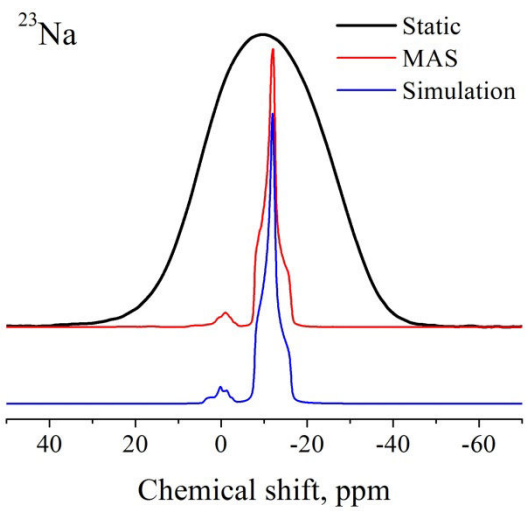

Fig. 25. Room temperature ^{23}Na NMR spectra of $LiNaSO_4$ powder: static spectrum (black line), magic angle spinning (MAS) spectrum at rotating frequency 25 kHz (red line), and the best fit of the MAS spectrum (blue line). The fitted value of the quadrupolar coupling constant, C_Q, was 1.15×10^6 Hz.

Quadrupolar coupling constant C_Q of ^{23}Na nuclei was found to be at least 13 times larger than C_Q of ^{7}Li at room temperature (1.15 MHz to be compared with 87 kHz, respectively); therefore, only central transition is observed in the ^{23}Na static powder spectrum. (Similar to lithium, the value of C_Q for sodium nuclei was found from fitting the ^{23}Na magic angle spinning spectrum at room temperature; the fit is presented in Fig. 25.) Comparatively large value of C_Q for ^{23}Na nuclei gives the following estimation for the second order quadrupolar coupling: $\chi_Q^2/2\pi\omega_L \approx 3\times10^3$ Hz (at $\omega_L/2\pi = 105.8\times10^6$ Hz); this is comparable with the broadening due to dipole-dipole interactions in the rigid lattice. As a result, ^{23}Na powder spectrum at room temperature has a shape of a distorted Gaussian (see Fig. 23d), whose asymmetry is caused generally by the second order quadrupolar interactions.

It follows from the above that temperature evolution of ^{7}Li and ^{23}Na NMR line widths may slightly differ due to the difference in values of C_Q. This distinction should be taken into account when fitting experimental data (see below).

Vertical dashed lines in Figs. 23a,b indicate onset temperatures T_c of the motional narrowing. The lower temperature ($T_c^{\mathrm{Li}} \sim 390\,\mathrm{K}$) corresponds to the onset of the line narrowing due to the Li^+ motion, whereas at the higher temperature ($T_c^{\mathrm{Na}} \sim 570\,\mathrm{K}$) line narrowing occurs due to the Na^+ motion. Onset temperature could be a useful parameter, if the full curve $\delta\omega(T)$ cannot be determined. In such case, the activation energy of the Li^+ hopping process can be estimated by using the empirical expression of Waugh and Fedin [125]:

$$E_a^{\mathrm{WF}} \approx 1.617 \times 10^{-3}\, T_c^{\mathrm{Li}}, \tag{301}$$

where the onset temperature is in kelvins and the activation energy – in electronvolts. Substituting $T_c^{\mathrm{Li}} = 390\,\mathrm{K}$ into Eq. 301 we find $E_a^{\mathrm{WF}} = 0.63\,\mathrm{eV}$.

4.1.4.2 Theoretical treatement of motional narrowing under diffusion of two spin sub-lattices

It is obvious that motions of Na^+ and Li^+ ions should be characterized by different correlation times, τ_c^{Li} and τ_c^{Na}; therefore, the BPP approximation [64, 126] cannot be used for the line width analysis in LNS. Bilski *et al*. obtained expressions, which can be used to analyze temperature dependences of different NMR measured values in case of several correlation times [127]. Using the approach of Bilski *et al*. [127, 128] we found the autocorrelation function for the fluctuations of the dipolar Hamiltonian in the case of diffusion of two spin sub-lattices. We also obtained an expression for the temperature dependence of the NMR line width, which could be used in the fitting procedure. Proposed fitting formula has been extended to the case of a distribution of correlation times.

The enhancement of the mobility of nuclei leads to a line width narrowing. Along with this narrowing, the shape of the line changes: in “rigid” lattice, i.e. in the absence of movement, the line is described by the Gaussian, whereas under the fast relative motion of nuclei the spectral line takes the form of the Lorentzian curve. The reason that the NMR signal in solid has the shape close to the Gaussian curve is purely statistical in nature. Thus, due to the smallness of the Zeeman interaction with respect to the value of *kT* the spin system is a somewhat disordered; hereby, during the time of the order of T_2, each spin could be considered as a source of a constant magnetic field. It is clear that near each spin a nonzero

local magnetic field B_{loc} exists, which is the sum of the magnetic fields produced by all other spins. Since the direction of the magnetic moment of a given spin could be different at different crystallographic sites, the value of the local field could be different at different nuclei. Difference of the local fields causes the difference of the precession frequencies of different nuclear spins; therefore, the net NMR signal of the solid will have the shape and the width determined by the distribution function of the local fields. It should be noted that the direct dipole-dipole coupling exists not only between neighboring nuclei, but, strictly speaking, between all nuclei of the sample. Since the number of nuclei in crystal is usually very high, one can find distribution of the values of the local magnetic field using the central limit theorem. Let B_i designates the field produced by the *i*-th spin in the point under consideration. If the number *n* of spins is very high, then the central limit theorem predicts

$$\frac{S_n}{\sigma\sqrt{n}} \xrightarrow[n\to\infty]{} \frac{1}{\sigma\sqrt{2\pi}} e^{-\frac{B_{loc}^2}{2\sigma^2}}, \tag{302}$$

where $S_n = \sum_{i=1}^{n} B_i$ and $\sigma = \sqrt{\langle B_{loc}^2 \rangle}$ is a standard deviation. (The value of the standard deviation depends on the crystal structure.) Thus, the central limit theorem says that the line shape has to be Gaussian. The half width at half maximum (HWHM) of the line, $\delta\omega_0$, is determined by the standard deviation: $\delta\omega_0 = -\gamma\sqrt{2\ln 2}\sigma$, where γ is the gyromagnetic ratio.

The relative movement of spins could lead to the motional narrowing of the NMR signal. The reason of this narrowing is that local magnetic fields are time-dependent, when spins move relative to each other. Thus, B_{loc} fluctuates under the motion of spins, and is characterized by the correlation time τ_c. If $\delta\omega_0\tau_c >> 1$ ($\delta\omega_0 = -\gamma\sqrt{2\ln 2}\sqrt{\langle B_{loc}^2 \rangle}$ is the line width in the "rigid" lattice), then the width of the NMR signal is not affected by the change of τ_c, and inhomogeneous broadening plays a dominant role defining the Gaussian shape of the line. If $\delta\omega_0\tau_c \sim 1$, then the diminution of τ_c leads to the narrowing of the line. Finally, if the fluctuation frequency $1/\tau_c$ surpasses the "rigid" line width $\delta\omega_0$, then nuclear spins "feel" only average values of fluctuations, which are close to zero. In other words, if $\delta\omega_0\tau_c << 1$, the line width again is not affected by the change of τ_c, and the case of extreme motional narrowing could occur.

The most frequently used formula for the temperature evolution of the NMR line width makes use of the second moment of the line [64, 126]:

$$M_2(T) = \bar{M}_2 + \frac{2}{\pi}(M_2^0 - \bar{M}_2)\arctan(\alpha\,\delta\omega\,\tau_c), \tag{303}$$

where M_2^0 is the second moment in the rigid lattice, $\bar{M}_2$ is the residual second moment in the fast ionic motion limit, τ_c is a correlation time, and $\delta\omega$ is the half-width at half-maximum (HWHM) of the line. The coefficient α in Eq. 303 is of order of unity. Equation 303 is analyzed in detail, e.g., in the book of Abragam [64] and is a consequence of the BPP approximation (with subsequent *ad hoc* introduction of the parameter $\bar{M}_2$, which takes into account inhomogeneous broadening effects [129]).

Strictly speaking, the BPP approximation can be used, if all internal interactions are averaged by an isotropic averaging process similar to the rotational diffusion occurring in molecules. Nevertheless, Eq. 303 works well in many solids, for which ionic diffusion can be described by Markovian jumps, and if τ_c is understood to be an average time between jumps of an atom from one atomic site to another [126, 130].

If two spin sub-lattices, *I* and *S*, exist in a solid, then the secular part of the dipolar Hamiltonian related to spins *I* could be written as follows [64]:

$$\begin{aligned}\mathcal{H}_D^I = \frac{1}{4}\gamma_I^2\hbar\sum_i^{N_I}\sum_j^{N_I}\frac{1-3\cos^2\theta_{ij}^{II}}{(r_{ij}^{II})^3}(3I_{iz}I_{jz} - I_i\cdot I_j) + \\ +\gamma_I\gamma_S\hbar\sum_i^{N_I}\sum_j^{N_S}\frac{1-3\cos^2\theta_{ij}^{IS}}{(r_{ij}^{IS})^3}I_{iz}S_{jz}.\end{aligned} \tag{304}$$

Here the first term corresponds to the interaction energy of spins *I* between themselves, whereas the second term defines interactions of spins *I* with spins *S*. θ_{ij}^{II} and r_{ij}^{II} define the orientation and distance between a pair of *I* spins, whereas θ_{ij}^{IS} and r_{ij}^{IS} determine the orientation and distance between an *IS* pair of unlike spins. Finally, γ_I, γ_S and N_I, N_S are gyromagnetic ratios and numbers of spins *I* and *S*, respectively. The dipolar Hamiltonian $\mathcal{H}_D^S$ related to spins *S* could be deduced from Eq. 304 by interchanging *I* and *S*.

The local dipolar field at the *I* spin has two additive contributions: 1) the field created by the spins of the *I* sub-lattice and 2) the field generated by the spins from the *S* sub-lattice. Consequently, the second moment of the NMR signal of *I* spins, in the rigid lattice, will consist of two components (we omit hereinafter the subscript "0" at the second moments in the rigid lattice, if it does not cause confusion):

$$M_2^I = M_2^{II} + M_2^{IS}, \tag{305}$$

where [64]

$$\begin{aligned} M_2^{II} &= \frac{3}{4}\gamma_I^4\hbar^2\,\frac{I(I+1)}{N_I}\sum_i^{N_I}\sum_j^{N_I}\frac{\left(1-3\cos^2\theta_{ij}^{II}\right)^2}{(r_{ij}^{II})^6} = \Lambda_{II}\sum_i^{N_I}\sum_j^{N_I}\left(b_{ij}^{II}\right)^2, \\ M_2^{IS} &= \frac{1}{3}\gamma_I^2\gamma_S^2\hbar^2\,\frac{S(S+1)}{N_S}\sum_i^{N_I}\sum_j^{N_S}\frac{\left(1-3\cos^2\theta_{ij}^{IS}\right)^2}{(r_{ij}^{IS})^6} = \Lambda_{IS}\sum_i^{N_I}\sum_j^{N_S}\left(b_{ij}^{IS}\right)^2, \end{aligned} \tag{306}$$

and

$$b_{ij}(t) = \frac{1-3\cos^2\theta_{ij}(t)}{r_{ij}^3(t)} \tag{307}$$

(coefficients Λ_{II} and Λ_{IS} are defined by expressions standing before the sums in Eqs. 306).

When the *I* and *S* spin-bearing atoms start to move, functions $b_{ij}^{II}(t)$ and $b_{ij}^{IS}(t)$ become time-dependent and motional narrowing occurs. If one assume that the movements are uncorrelated and can be described by unique correlation times τ_c^I and τ_c^S, it is clear that $b_{ij}^{II}(t)$ depends only on the relative motion of spins *I* and, consequently, depends only on its characteristic time τ_c^I. Function $b_{ij}^{IS}(t)$, however, depends on the motion of spins *I* as well as on the motion of spins *S*; therefore, the autocorrelation function of this mutual motion depends on τ_c^I and τ_c^S as well. From the physical point of view, it means that, in the case of a diffusion of two spin sub-lattices with two distinct activation energies, the motional narrowing occurs in two stages. In the first stage, the NMR line narrowing starts with the motion of the spin carriers with lower activation energy; in the second stage, when spin carriers with the highest activation energy start to move, an additional narrowing occurs. To find the full curve for the temperature evolution of the NMR line width, one has to deduce the autocorrelation function of fluctuations of the dipolar Hamiltonian (Eq. 304) due to the relative motion of two spin sub-lattices.

Now, we assume that ionic motion in solids can be considered as discrete jumps from a given lattice site to *n* neighboring sites R_k, $k = 1, 2, ..., n$, in order to find the part of the autocorrelation function $G_I(\tau)$ characterizing fluctuations of the dipolar Hamiltonian $\mathcal{H}_D^I$ under the motion of spin *I* carriers (let us denote this part of the autocorrelation function as $G_{II}(\tau)$). Assuming that the ionic diffusion is a stationary Markovian process, we can write [128]:

$$G_{II}(\tau) = \Lambda_{II} \sum_{i,j}^{N_I} \sum_{l,m}^{n_I} p_I(R_l) P_I(R_l, R_m, \tau) b_{ij}^{II}(R_l) b_{ij}^{II}(R_m), \tag{308}$$

where the $p_I(R_l)$ function determines the probability that at time $t = 0$ the random function $b_{ij}^{II}(t)$ is equal to $b_{ij}^{II}(R_l)$, while $P_I(R_l, R_m, \tau)$ defines the probability that at time τ the function $b_{ij}^{II}(t)$ is equal to $b_{ij}^{II}(R_m)$, if initially it was equal to $b_{ij}^{II}(R_l)$; n_I is the number of different discrete lattice sites, between which spins *I* can jump. One can show [127] that, for the Markovian jumps, the conditional probability is

$$P_I(R_l, R_m, \tau) = \frac{1}{n_I}\left(1 - e^{-\tau/\tau_c^I}\right) + e^{-\tau/\tau_c^I} \delta_{lm}, \tag{309}$$

where δ_{lm} is a Kronecker delta and where it was assumed that the probability of the random variable $R(t)$ changing from R_l to R_m by one jump is $W_{lm} = 1/\tau_c^I n_I$ (at $l \neq m$). Substituting Eq. 309 into Eq. 308 one can find that the function $G_{II}(\tau)$ is

$$G_{II}(\tau) = \bar{M}_2^{II} + (M_2^{II} - \bar{M}_2^{II}) e^{-|\tau|/\tau_c^I}, \tag{310}$$

where

$$\bar{M}_2^{II} = \Lambda_{II} \sum_{i,j}^{N_I} \left[\frac{1}{n_I} \sum_{m=1}^{n_I} b_{ij}^{II}(R_m) \right]^2 \equiv \Lambda_{II} \sum_{i,j}^{N_I} \left(\bar{b}_{ij}^{II} \right)^2 \tag{311}$$

is a motionally "narrowed" value of the second moment M_2^{II}. It should be noted that Eqs. 309 and 311 implicitly assume equal occupancies of the various sites, i.e. $p_I(R_l) = 1/n_I$.

The part of the autocorrelation function $G_I(\tau)$ characterizing fluctuations of the dipolar Hamiltonian $\mathcal{H}_D^I$ under the motion of spin *S* carriers (let us denote it as $G_{IS}(\tau)$) can be written as follows:

$$G_{IS}(\tau) = \Lambda_{IS} \sum_{i}^{N_I} \sum_{j}^{N_S} \sum_{l,m;l',m'} p_I(R_l) p_S(R_{l'}) P_I(R_l, R_m, \tau) P_S(R_{l'}, R_{m'}, \tau) b_{ij}^{IS}(R_l, R_{l'}) b_{ij}^{IS}(R_m, R_{m'}), \tag{312}$$

where we assumed that diffusing jumps of spins *I* occur independently on jumps of spins *S*. The product $p_I(R_l) p_S(R_{l'})$ determines the probability that at time $t = 0$ the random function $b_{ij}^{IS}(t)$ is equal to $b_{ij}^{IS}(R_l, R_{l'})$, while the product $P_I(R_l, R_m, \tau) P_S(R_{l'}, R_{m'}, \tau)$ defines the probability that at time τ the function $b_{ij}^{IS}(t)$ is equal to $b_{ij}^{IS}(R_m, R_{m'})$, if at initial time it was equal to $b_{ij}^{IS}(R_l, R_{l'})$. Unlike Eq. 308, functions $b_{ij}^{IS}(t)$ in Eq. 312 depend simultaneously on

the position R_m of spins *I* as well as on the position $R_{m'}$ of spin *S*. Since the motion of spins belonging to different sub-lattices is assumed to be independent, corresponding probabilities are multiplied. Conditional probabilities $P_I(R_l, R_m, \tau)$ and $P_S(R_l, R_m, \tau)$ could be defined by Eq. 309 with appropriate indices. Assuming that probabilities $p_I(R_l)$ and $p_S(R_{l'})$ are equal to $1/n_I$ and $1/n_S$, respectively, where n_I and n_S are corresponding numbers of different lattice sites, between which diffusing jumps occur, one can find for $G_{IS}(\tau)$ [127]:

$$\begin{aligned} G_{IS}(\tau) = &\left\langle M_2^{IS} \right\rangle + \left(\bar{\bar{M}}_2^{IS} - \left\langle M_2^{IS} \right\rangle \right) e^{-|\tau|/\tau_c^I} \\ &+ \left(\bar{M}_2^{IS} - \left\langle M_2^{IS} \right\rangle \right) e^{-|\tau|/\tau_c^S} \\ &+ \left(M_2^{IS} + \left\langle M_2^{IS} \right\rangle - \bar{M}_2^{IS} - \bar{\bar{M}}_2^{IS} \right) e^{-|\tau|\left(\frac{1}{\tau_c^I} + \frac{1}{\tau_c^S} \right)}, \end{aligned} \tag{313}$$

where

$$\begin{aligned} \bar{M}_2^{IS} &= \Lambda_{IS} \sum_i^{N_I} \sum_j^{N_S} \left[\frac{1}{n_I} \sum_{l=1}^{n_I} b_{ij}^{IS}(R_l, R_{l'}) \right]^2, \\ \bar{\bar{M}}_2^{IS} &= \Lambda_{IS} \sum_i^{N_I} \sum_j^{N_S} \left[\frac{1}{n_S} \sum_{l'=1}^{n_S} b_{ij}^{IS}(R_l, R_{l'}) \right]^2, \\ \left\langle M_2^{IS} \right\rangle &= \Lambda_{IS} \sum_i^{N_I} \sum_j^{N_S} \left[\frac{1}{n_S} \sum_{l'=1}^{n_S} \frac{1}{n_I} \sum_{l=1}^{n_I} b_{ij}^{IS}(R_l, R_{l'}) \right]^2, \end{aligned} \tag{314}$$

and M_2^{IS} is defined by Eq. 306.

As we assume the motion of spin *I* and *S* carriers to be independent (i.e. uncorrelated), the evolution of terms M_2^{II} and M_2^{IS} also occurs independently. Since their contribution to M_2^I is additive, one can write the following formula for the autocorrelation function $G_I(\tau)$ of dipolar fluctuations caused by simultaneous motion of two sub-lattices:

$$G_I(\tau) = G_{II}(\tau) + G_{IS}(\tau). \tag{315}$$

Substituting Eq. 310 and Eq. 313 into Eq. 315, we obtain

$$\begin{aligned} G_I(\tau) = &\bar{M}_2^{II} + \left\langle M_2^{IS} \right\rangle \\ &+ \left(M_2^{II} + \bar{\bar{M}}_2^{IS} - \bar{M}_2^{II} - \left\langle M_2^{IS} \right\rangle \right) e^{-|\tau|/\tau_c^I} \\ &+ \left(\bar{M}_2^{IS} - \left\langle M_2^{IS} \right\rangle \right) e^{-|\tau|/\tau_c^S} \\ &+ \left(M_2^{IS} + \left\langle M_2^{IS} \right\rangle - \bar{M}_2^{IS} - \bar{\bar{M}}_2^{IS} \right) e^{-|\tau|\left(\frac{1}{\tau_c^I} + \frac{1}{\tau_c^S} \right)}. \end{aligned} \tag{316}$$

If in a given temperature range the condition $1/\tau_c^I >> 1/\tau_c^S$ is valid, then the following simplification can be made:

$$e^{-|\tau|\left(\frac{1}{\tau_c^I}+\frac{1}{\tau_c^S}\right)} \approx e^{-|\tau|/\tau_c^I}. \tag{317}$$

In this case, Eq. 316 could be written as follows:

$$\begin{aligned} G_I(\tau) = \bar{M}_2^{II} + \left\langle M_2^{IS} \right\rangle \\ + \left(M_2^I - \bar{M}_2^{II} - \bar{M}_2^{IS} \right) e^{-|\tau|/\tau_c^I} \\ + \left(\bar{M}_2^{IS} - \left\langle M_2^{IS} \right\rangle \right) e^{-|\tau|/\tau_c^S}, \end{aligned} \tag{318}$$

where, as above, $M_2^I = M_2^{II} + M_2^{IS}$. For a reduced correlation function $g(\tau) = G_I(\tau)/G_I(0)$ (we omit the index *I* at $g(\tau)$ for simplicity) one can write

$$\begin{aligned} g(\tau) = Q_1 + Q_3 + (1 - Q_1 - Q_2) e^{-|\tau|/\tau_c^I} \\ + (Q_2 - Q_3) e^{-|\tau|/\tau_c^S}, \end{aligned} \tag{319}$$

where we introduced three parameters

$$Q_1 = \frac{\bar{M}_2^{II}}{M_2^I},\ Q_2 = \frac{\bar{M}_2^{IS}}{M_2^I},\ Q_3 = \frac{\left\langle M_2^{IS} \right\rangle}{M_2^I}. \tag{320}$$

Physical interpretation of parameters in Eq. 319 is transparent: Q_1 is a measure of the averaging of the dipolar interactions by relative motion of spins *I*; Q_2 characterizes the motion of spins *I* with respect to spins *S* (when spins *S* are immobile); finally, Q_3 characterizes the cumulative effect of simultaneous motion of both sub-lattices on dipolar interactions. Unfortunately, these parameters cannot be found from the experimentally observed correlation function. In fact, they combined in Eq. 319 and cannot be separated. It means that Eq. 319 cannot be used in fitting procedure, and, for practical applications, Eq. 319 is rewritten as follows:

$$g(\tau) = a + (1 - b) e^{-|\tau|/\tau_c^I} + (b - a) e^{-|\tau|/\tau_c^S}, \tag{321}$$

where

$$\begin{aligned} a = Q_1 + Q_3 = \frac{\bar{M}_2^{II} + \left\langle M_2^{IS} \right\rangle}{M_2}, \\ b = Q_1 + Q_2 = \frac{\bar{M}_2^{II} + \bar{M}_2^{IS}}{M_2}. \end{aligned} \tag{322}$$

Now we can deduce a formula for the temperature dependence of the second moment M_2 under diffusion of two spin sub-lattices. It is known that the temperature evolution of the NMR line width is determined by the following equation [64]:

$$M_2(T) = \frac{M_2^0}{2\pi} \int_{-\alpha\delta\omega}^{\alpha\delta\omega} j(\omega) d\omega, \tag{323}$$

where M_2^0, as above, is the "rigid" second moment and the coefficient α is of the order of unity. Spectral density $j(\omega)$ is given as usual:

$$j(\omega) = \int_{-\infty}^{\infty} g(\tau) e^{-i\omega\tau} d\tau, \tag{324}$$

where $g(\tau)$ is a reduced spectral density function. Substituting Eq. 321 into Eq. 323 and taking into account Eq. 324, one can find for the second moment of the NMR line the following formula:

$$\begin{aligned} M_2(T) = aM_2^0 + \frac{2}{\pi}(1-b)M_2^0 \arctan(\alpha\delta\omega\tau_c^I) \\ + \frac{2}{\pi}(b-a)M_2^0 \arctan(\alpha\delta\omega\tau_c^S). \end{aligned} \tag{325}$$

Temperature dependence in Eq. 325 is determined by the correlation time τ_c, which is usually assumed to obey the Arrhenius law: $\tau_c = \tau_0 \exp(E_a/kT)$, where E_a is an activation energy of the dynamical process.

It should be noted that when $\delta\omega\tau_c \le 1$, it is quite difficult (or even meaningless) to determine the second moment of the NMR line [64], since the shape of the NMR signal deviates significantly from the Gaussian line shape. Therefore, it is advisable to use other parameter, which determines the temperature evolution of the resonance line. Usually, the half-width at half-maximum $\delta\omega$ (HWHM) is used as such parameter. Equation 325 will be then rewritten in the form of the following implicit equation:

$$\begin{aligned} \delta\omega^2 = a\delta\omega_0^2 + \frac{2}{\pi}(1-b)\delta\omega_0^2 \arctan(\alpha\delta\omega\tau_c^I) \\ + \frac{2}{\pi}(b-a)\delta\omega_0^2 \arctan(\alpha\delta\omega\tau_c^S). \end{aligned} \tag{326}$$

Equation 326 assumes exponential correlation functions for both sub-lattices, *I* and *S*. In fact, Eq. 326 can be rewritten in the following form

$$\begin{aligned} \delta\omega^2 = a\delta\omega_0^2 + (1-b)\delta\omega_0^2 K^I(\delta\omega) \\ + (b-a)\delta\omega_0^2 K^S(\delta\omega), \end{aligned} \tag{327}$$

where functions $K^I(\delta\omega)$ and $K^S(\delta\omega)$ are

$$K^{I,S}(\delta\omega) = \frac{\int_{-\alpha\delta\omega}^{\alpha\delta\omega} j^{I,S}(\omega)d\omega}{\int_{-\infty}^{\infty} j^{I,S}(\omega)d\omega}, \tag{328}$$

and spectral densities, $j^I(\omega)$ and $j^S(\omega)$, are defined by the BPP model:

$$j^{I,S}(\omega) = \frac{2\tau_c^{I,S}}{1+\left(\omega\tau_c^{I,S}\right)^2}. \tag{329}$$

However, ionic mobility in solids is often accompanied by non-exponential relaxation phenomena [73]. In this case, spectral density functions in the form of Eq. 329 are inadequate, and different empirical spectral densities, which take into account a distribution of correlation times, are usually applied. One of the most successful spectral densities used to interpret experimental data in solids is a *Cole-Davidson function* $j_{\mathrm{CD}}(\omega,\beta)$, which is defined as follows [73]:

$$j_{\mathrm{CD}}(\omega;\beta) = \frac{2}{\omega}\frac{\sin\left[\beta\arctan(\omega\tau_c)\right]}{\left(1+\omega^2\tau_c^2\right)^{\beta/2}}, \tag{330}$$

where $0<\beta<1$. It is easy to show that at $\omega\tau << 1$

$$j_{\mathrm{CD}}(\omega;\beta) \sim \tau_c, \tag{331}$$

whereas at $\omega\tau >> 1$

$$j_{\mathrm{CD}}(\omega;\beta) =\sim \tau_c^{-\beta}\omega^{-(1+\beta)}. \tag{332}$$

An application of Eq. 330 for the analysis of relaxation data is quite simple, whereas the line width analysis is complicated by this approach, since it involves a primitive of the spectral density function. Unfortunately, the primitive of Eq. 330 does not exist, and one cannot find an analytical expression for Eq. 327 similar to Eq. 326. This trouble, however, can be overcome by using an approximate function, whose behavior is close to the Cole-Davidson function and whose primitive could be expressed explicitly (at least in terms of special functions). It is easy to show that the following spectral density,

$$j_\beta(\omega) = \frac{2\tau_c}{1+\left(\omega^2\tau_c^2\right)^{\frac{1}{2}(\beta+1)}}, \tag{333}$$

obeys Eqs. 331-332 and, consequently, could be used instead of Eq. 330. In contrast to the Cole-Davidson function, one can find an integral of Eq. 333 in terms of well-known

hypergeometric function, ${}_2F_1(a,b;c;z)$ [131]. Thus, $K^{I,S}(\delta\omega)$ functions can be written as follows (we omit superscripts *I* and *S* for simplicity):

$$K(\delta\omega) = A_\beta \tau_c 2\alpha\,\delta\omega\ {}_2F_1\left(1,\frac{1}{\beta};1+\frac{1}{\beta};-\left(\alpha\,\delta\omega\,\tau_c\right)^\beta\right), \tag{334}$$

where a normalization factor,

$$A_\beta = \left[\int_{-\infty}^{\infty} j_\beta(\omega)d\omega\right]^{-1}, \tag{335}$$

can be found numerically. Substituting then Eq. 334 into Eq. 327, we shall obtain a fitting function (in the analytical form!) to describe the two-step narrowing of the NMR lines observed in the case of a distribution of correlation times and/or activation energies. It should be noted that if the distribution of correlation times really takes place, then the *I* and *S* sub-lattices should be characterized by two different parameters: β^I and β^S.

Table 4.

Fitting parameters of Eq. 327 for ^{7}Li and ^{23}Na line widths in $LiNaSO_4$

	Spectral density		
	Eq. 329	Eq. 333	Eq. 329
	^{7}Li		^{23}Na
E_a^{Li}, eV	0.70 ± 0.05	2.1^*	0.7^*
τ_0^{Li}, s	$(3.5\pm0.3)\times10^{-12}$	$(7.9\pm2.5)\times10^{-28}$	$3.5\times10^{-12*}$
E_a^{Na}, eV	1.33 ± 0.05	4.2^*	1.33^*
τ_0^{Na}, s	$(1.0\pm0.3)\times10^{-14}$	$(6.3\pm2.5)\times10^{-38}$	$1.0\times10^{-14*}$
a	0.015	0.015	0.031
b	0.235	0.235	0.323
α	1^*	1^*	1.6±0.1
β^{Li}	-	0.34 ± 0.01	-
β^{Na}	-	0.30 ± 0.01	-

Comment: Parameters marked with an asterisk were fixed when fitting.

It was shown above that narrowing of the ^{7}Li NMR line in the LNS is caused predominantly by the fluctuations of the dipolar Hamiltonian, i.e. by modulations of the

dipole-dipole couplings due to the motion of spins. In other words, the dipolar correlation function (Eq. 321) and consequently the derived fitting function (Eq. 325) could be adequately used for the analysis of the temperature evolution of the ^{7}Li NMR line width. Solid line in Fig. 23a corresponds to the best fit of Eq. 325; fitted parameters are listed in Table **4**.

Despite of a distortion of the ^{23}Na central transition due to quadrupolar interaction, we used Eq. 325 just to see whether it is possible to obtain satisfactory fit of $\delta\omega^{\mathrm{Na}}(T)$ with the same parameters as in case of ^{7}Li. Solid line in Fig. 23b corresponds to the best fit of Eq. 325 (values of activation energies and preexponential factors were fixed); fitted parameters are listed in Table **4**. It should be also noted that in spite of inadequacy of the used model for ^{23}Na, temperature evolution of its line width contains two steps similar to the case of ^{7}Li and, moreover, could be even rather well approximated with the same values of correlation times τ_c^{Li} and τ_c^{Na}. It means that the temperature evolution of the ^{23}Na line width is substantially caused by the fluctuations of the dipolar Hamiltonian. In fact, using the nutation curve technique we revealed that the quadrupolar coupling constant (i.e. its averaged value) of ^{23}Na nuclei is almost unchanged when heating the LNS powder (see Fig. 34); therefore, the contribution of the second order quadrupolar interactions is approximately the same at different temperatures and, consequently, do not affect strongly the temperature dependence of the ^{23}Na HWHM.

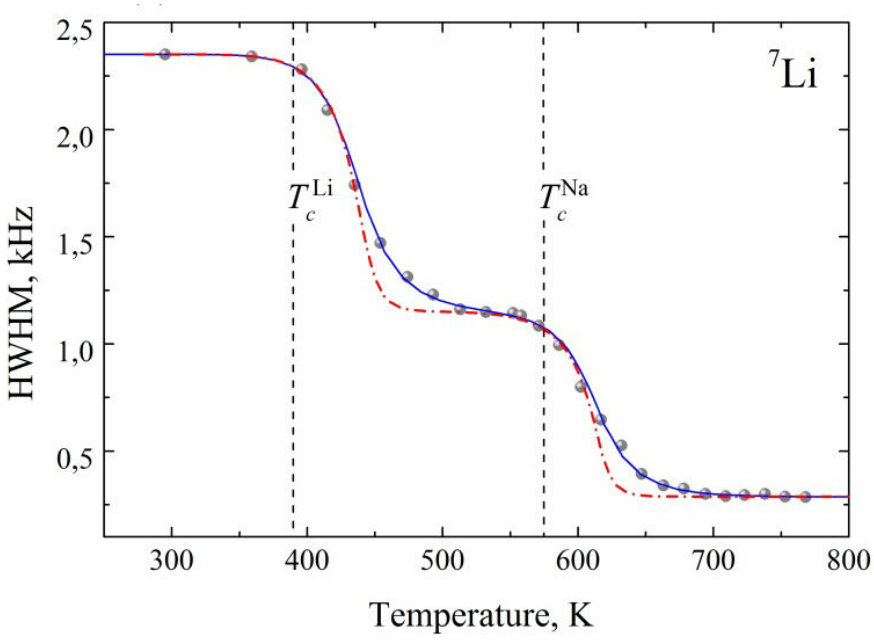

Fig. 26. Computer fittings of temperature dependence of ^{7}Li NMR line width using different spectral densities: blue solid line – Eq. 329; red dash-dotted line – Eq. 333.

To give a conclusion, let us note once again that Eq. 325 gives a good fit for the evolution of ^{7}Li NMR line width. For ^{23}Na nuclei, this model also works quite well. Parameter α was found to be equal to unity in the case of ^{7}Li, whereas it differs from unity in the case of ^{23}Na. It is quite difficult to determine a clear physical sense of the parameter α in the case of ^{23}Na; one can only say that it reflects the fact that the measured values of the ^{23}Na NMR line widths are affected not only by the non-averaged dipole-dipole coupling, but also by quadrupolar coupling.

It should be noted that the value of the activation energy of Li^{+} jumps found due to Eq. (326) is very small when compared with ionic conductivity measurements [4, 11]. In fact, Mellander *et al*. [4] found that the d.c. ionic conductivity of the LNS single crystal had an activation energy 2.15 eV, which is three times larger than the value obtained by NMR study (0.70 eV). This discrepancy is well known from line-shape studies on solid electrolytes with a single mobile ion species [132-134]. In principle, it could be attributed 1) to an inadequacy of the assumption of an exponential correlation function and 2) to local motion of lithium ions.

To examine the first assumption, we have fitted experimental data using Eq. (333) as a spectral density function for both ionic species and fixing the values of the activation energies as follows: $E_a^{\mathrm{Li}} = 2.1\,\mathrm{eV}$ and $E_a^{\mathrm{Na}} = 4.2\,\mathrm{eV}$. Resulting fit is presented in Fig. 1a (dash-dotted line). Corresponding fitting parameters are listed in Table 1. One can see that this model does not work quite well (one can clearly see the two main discrepancies between the fit and experimental points at the bottom of the steps). Moreover, the values of the pre-exponential factors were found to be incredibly small and parameters β^{Li} and β^{Na} also had rather low values (see Table 1). This indicates the first assumption to be unjustified.

Thereby, the local motion of lithium ions seems to be more reasonable explanation of the distinction between energy values obtained by different techniques. The simplest model explaining mentioned difference is based on the assumption that there exist potential barriers of various heights. Since the d.c. conductivity involves ionic migration over long distances, only ions with sufficient energy to surmount the highest barriers will contribute to the conductivity process. However, other ions may overcome lower potential barriers and move shorter distances within a local cavities, whose boundaries are defined by the highest potential barriers. Although such local motions do not contribute to the long-range charge transfer, they can narrow the NMR spectra.

4.1.5 Spin-lattice relaxation

It is easy to show that two-time correlation function leads also to the appearance of two maxima in the temperature dependence of the spin-lattice relaxation rate $1/T_1$ [127]. This fact is a consequence of the well-known formula (see Eq. 146):

$$1/T_1 \propto j(\omega_L) + 4j(2\omega_L), \tag{336}$$

where $j(\omega)$ is a spectral density of the correlation function given by Eq. 321. This result implicitly assumes that spin-lattice relaxation is defined by the fluctuations of the dipolar Hamiltonian. In case of quadrupolar nuclei, relaxation is usually caused by the fluctuations of the quadrupolar interactions; therefore, instead of the dipolar correlation function (Eq. 321) one has to use a "quadrupolar" correlation function. The latter could be defined also by Eq. 321, but with redefined parameters *a* and *b*.

It is important to note that Eq. 321 is valid for quadrupolar relaxation only if ^{23}Na and ^{7}Li nuclei "see" exclusively the fluctuations of the electric field gradient (EFG) due to the local motions of Li^+ and Na^+ ions (or vacancies). However, ^{23}Na and ^{7}Li nuclei could also "see" the fluctuations of the EFG due to the motions of other neighboring molecular groups, whose dynamics may be "invisible" for the dipolar Hamiltonian. It means that dipolar and quadrupolar correlation functions could be defined by different motional processes and, consequently, could be different.

It is known that reorientations of sulfate groups as well as translational diffusion of cations take place in the *β*-LNS [13, 43]. Since natural abundance of ^{33}S and ^{17}O nuclei is very low and nuclear spins of other stable isotopes of these elements are zero, one can neglect the dipole-dipole interactions between Li and S,O as well as between Na and S,O. Therefore, dipolar Hamiltonian is insensitive to the quasi-rotations of SO_4 anions. (It is valid, if quasi-rotations of sulfate groups are uncorrelated with the translational motion of cations; for the *α*-LNS this condition is not satisfied, but for the *β*-LNS it is apparently true.) Contrary, EFG tensors of ^{7}Li and ^{23}Na nuclei will "see" such reorientations; therefore, correlation function describing fluctuations of the quadrupolar Hamiltonian in LNS will differ (may be not very much) from Eq. 321.

Temperature dependences of the spin-lattice relaxation rates of ^{7}Li and ^{23}Na nuclei are presented in Fig. 27. One can see that the ^{7}Li spin-lattice relaxation rate has an Arrhenius behavior on the low-temperature side of its temperature dependence. The activation energy was found to be in excellent agreement with the result of the line width analysis: $E_a = 0.71 \pm 0.03\,\mathrm{eV}$. Around 715 K, one clearly observes a maximum of the $1/T_1$ curve. The

^{23}Na spin-lattice relaxation rate shows similar temperature behavior. The low-temperature shoulder has the slope with $E_a = 0.68 \pm 0.04\,\text{eV}$, which is in a good agreement with the ^{7}Li relaxation data. In fact, this indicates that motion of only one type of nuclei governs relaxation of both ^{7}Li and ^{23}Na nuclear spins in the low-temperature side of the $1/T_1$ curves. Namely, the motion of lithium ions leads to the fluctuations of the electric field gradient (EFG) not only around ^{7}Li nuclei, but also around ^{23}Na.

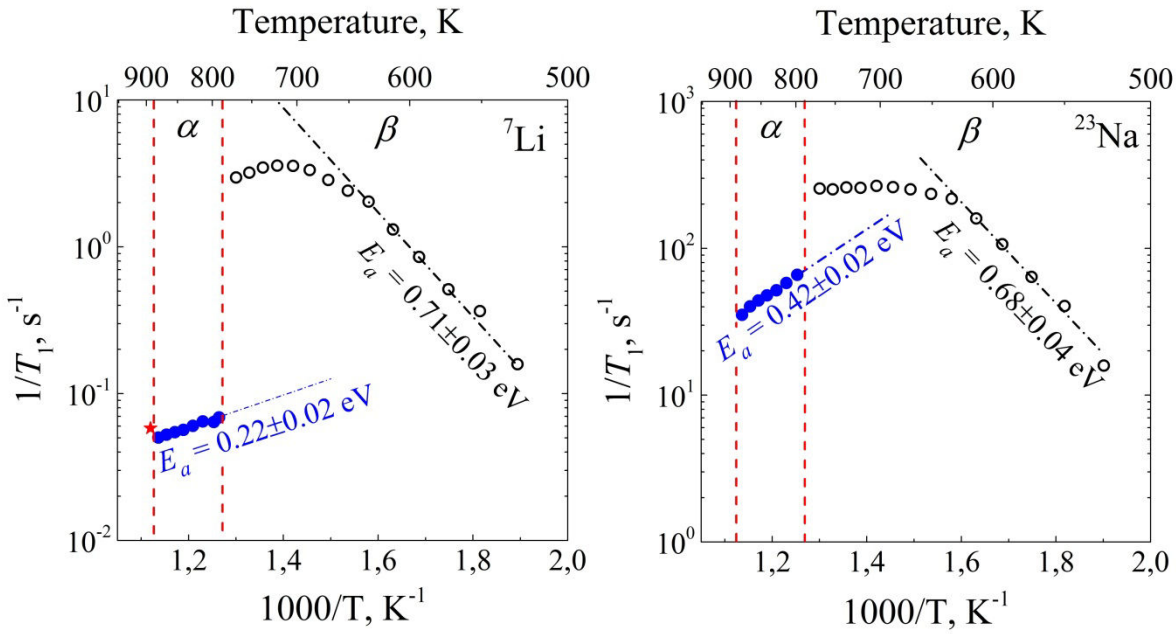

Fig. 27. Temperature evolution of the spin-lattice relaxation rate of ^{7}Li (on the left) and ^{23}Na (on the right) nuclei. Vertical dashed lines indicate phase boundaries: the *α*-*β* phase transition and melting at 788 K and 888 K, respectively. Measurements were carried out at 9.4 T.

Unfortunately, it is impossible to observe two maxima of the ^{7}Li $1/T_1$ curve in the field of 9.4 T, since the first maximum occurs close to the *α*-*β* phase transition, and the second one could be reached only at higher temperature, where the *α*-phase is already stable. However, in case of ^{23}Na, the second maximum probably starts to appear near the phase transition; therefore, a broad plateau appears at the high-temperature part of the ^{23}Na $1/T_1$ curve. Note, that using low magnetic fields Kanashiro *et al.* [11] really observed two maxima on the $1/T_1$ curve of ^{7}Li nuclei. However, clearly observed peaks were obtained only at very low frequency ($\omega_L^{\text{Li}}/2\pi = 6\times10^{6}$ Hz), whereas at higher frequencies mentioned maxima were weakly distinguishable.

The value of the activation energy for Li^+ was found to be $E_a = 0.70 \pm 0.02\,eV$, and the activation energy of Na^+ jumps in turn was $E_a = 1.20 \pm 0.02\,eV$; this result is in excellent agreement with the values obtained here.

The fact that at higher Larmor frequencies Kanashiro *et al*. did not observe two separate maxima of the relaxation rate, but revealed only considerable asymmetry of the $1/T_1$ curve, could be explained by the influence of the reorientations of sulfate groups on the quadrupolar relaxation of ^{7}Li nuclei.

In the α-phase, the ^{7}Li relaxation rate is abruptly decreased around 40 times (see Fig. 27); $1/T_1$ shows again the Arrhenius behavior with $E_a = 0.22 \pm 0.02\,eV$. After melting, the relaxation rate changes quite weakly. The ^{23}Na spin-lattice relaxation rate is decreased only 4 times after the α-β phase transition. The temperature evolution of ^{23}Na relaxation rate in α-phase obeys the Arrhenius law with an activation energy $E_a = 0.42 \pm 0.02\,eV$ that is almost two times higher than the corresponding value for the ^{7}Li spin-lattice relaxation, but is quite close to the activation energy of the diffusion process in the α-phase (see below).

4.1.6 ^{7}Li and ^{23}Na self-diffusion measurements

As it was shown above, the spin-lattice relaxation time of ^{23}Na is around two orders of magnitude smaller than that of ^{7}Li at corresponding temperatures. This makes the measurements of the ^{23}Na self-diffusion coefficient impossible below the phase transition. In fact, for the PFG STE measurements of ^{23}Na below 788 K, the maximum value of the diffusion time Δ, which could be taken without significant loss of the signal-to-noise ratio, is around 20 ms; it is too small to measure the value of $D < 10^{-12}$ m^2s^{-1}. In contrast, diffusion of the ^{7}Li nuclei could be measured below the α-β phase transition in quite wide temperature range: 720-788 K. One can see (Fig. 28) that the temperature dependence of the ^{7}Li diffusion has an Arrhenius behavior with an activation energy $E_a = 2.07 \pm 0.03\,eV$. This value is in a quite good agreement with the ionic conductivity measurements carried out by Mellander *et al*. [4] ($E_a = 2.15\,eV$) and Kanashiro *et al.* [11] ($E_a = 2.23\,eV$).

Above the phase transition, both nuclei have almost the same value of the self-diffusion coefficient; moreover, the activation energies for both cations are equal and have the value $E_a = 0.51 \pm 0.01\,eV$. It is an excellent confirmation of the paddle-wheel mechanism, due to which the radii of cations are of little importance for their diffusion rates. However, such value of E_a is in a worse agreement with the conductivity data. Thus, Secco [32]

showed that the activation energy of the conductivity in the rotator phase of LNS was around 0.44 eV.

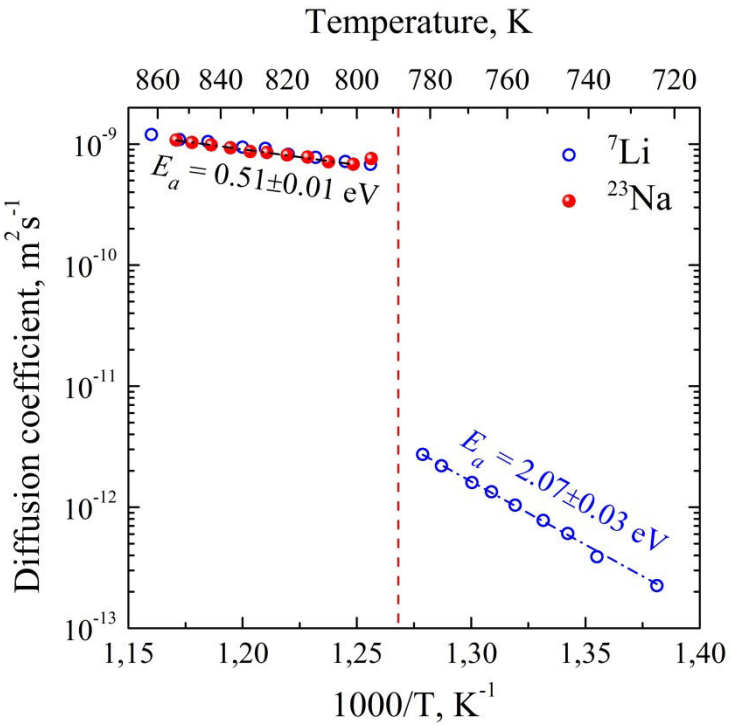

Fig. 28. Temperature evolution of of ^{7}Li and ^{23}Na self-diffusion coefficients. Dashed line indicates the α-β phase transition temperature.

One can see that the activation energy of Li motion in β-phase found from relaxation measurements is almost three times smaller than the value obtained in diffusion experiment. This is the consequence of the difference between microscopic nature of relaxation process and the macroscopic nature of the direct diffusion measurements. It means that there exist some local motions of Li^+ ions, which affect the relaxation process, but which cannot be seen by PFG NMR.

In terms of energy landscape, it means that there exist at least two types of potential barriers of different heights: 1) low barriers separating local sites, the jumps between which could be seen by means of relaxation measurements, and 2) high barriers separating distant sites, the jumps between which cause the macroscopic movements of atoms.

It should be noted that the value of the activation energy of Li^+ jumps found from the line width analysis is very small when compared with ionic conductivity [4, 11] and self-diffusion measurements. Such discrepancy is usually attributed to local motion of lithium ions [132-134]. The simplest model explaining mentioned distinction of the activation energies is based on an assumption that there exist potential barriers of various heights. Since the d.c. conductivity involves ionic migration over long distances, only ions with sufficient energy to

surmount the highest barriers will contribute to the conductivity process. However, other ions may overcome lower potential barriers and move shorter distances within a local cavities, whose boundaries are defined by the highest potential barriers. Although such local motions do not contribute to the long-range charge transfer, they could narrow the NMR spectra and even could govern the magnetic relaxation process.

4.1.7 NMR study of sulfate reorientations

We have already noted above that along with high cationic mobility, a rotational disorder of sulfate groups takes place in the LNS. In the α-modification, reorientations of anions are correlated with the translational motion of cations. This coupling between cationic diffusion and anions' rotation, first revealed in Li_2SO_4, led to the term "cogwheel mechanism" or "paddle-wheel mechanism" [135], which carried the additional implication that the cationic diffusion was enhanced by the sulfate ion reorientational jumps (Fig. 3).

It is interesting to note that the SO_4 orientational disorder as well as cationic mobility occurs also well below the α-β phase transition [12, 13]. However, the low-temperature reorientations have only weak effect on the behavior of the Li^+ ions [13], i.e. there is no strong coupling between the cationic diffusion and the SO_4 reorientational jumps in the β-phase.

Rotational disorder of the SO_4 anions in the LNS has been studied by inelastic and quasi-elastic neutron scattering [46], and by optical (IR and Raman) spectroscopy [12, 13, 43]. Raman (and IR) spectroscopy gives information about rotational, vibrational or stretching modes of sulfates, whose analysis makes it possible to infer the features (timescale, activation energy, etc.) of rotational dynamics. Neutron techniques, in turn, could provide information about inelastic scattering by oxygens of sulfate groups, and one can determine, e.g., timescale of reorientations. Thereby, both neutron and light scattering allow probing the dynamics of the sulfate anions directly.

NMR can be also be used for this purpose. However, isotopes of sulfur and oxygen nuclei with nonzero spins (^{33}S and ^{17}O) have very low natural abundance. Therefore, in unenriched samples, one can measure the effect of the SO_4 reorientations on neighboring nuclei. In this sense, NMR can be considered as an indirect probe to study the sulfate dynamics. The problem, however, is that the effect of the reorientational jumps of the sulfate groups on the ^7Li and ^{23}Na relaxation in the LNS is, apparently, quite weak, while the relaxation process is mainly governed by the diffusion of Li^+ and Na^+ ions themselves [11,

39]. Linewidth analysis is either inapplicable to study sulfate dynamics because of an insensitivity of Li-Li, Na-Na and Li-Na dipolar interactions to the SO_4 reorientations [136].

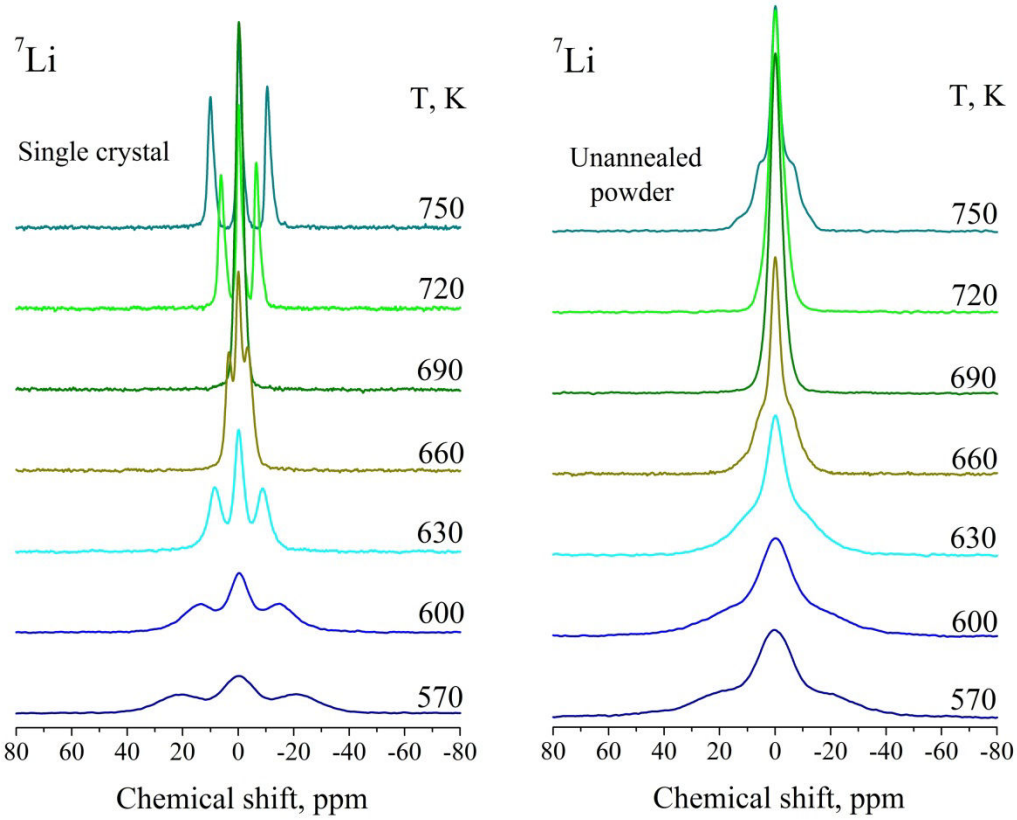

Fig. 29. Temperature evolution of the ^{7}Li NMR spectrum of the $LiNaSO_4$ single crystal with the *c*-axis oriented perpendicular to the magnetic field (on left) and "green" powder (on the right).

It is known from the crystallographic data [10, 115] that the unit cell of the *β*-LNS contains six Li^+ ions, each in a general position 6c. Electric field gradient (EFG) tensors at Li sites have the same principal values, but differ in their orientation with respect to crystallographic axes. Since ^{7}Li is a quadrupolar nucleus with spin $I = 3/2$, each of the six nuclei in the cell has to give the NMR signal consisting of three lines: central transition line and two symmetrical satellites (external transitions), whose integral intensities are related as 3:4:3 [56, 64].

In fact, below 550 K the NMR spectrum of the LNS single crystal represents a multicomponent pattern, whose lines are broadened due to non-averaged dipolar interactions. Above 550 K, the ^{7}Li NMR spectrum of the LNS single crystal contains only three lines, whose intensities obey the rule 3:4:3 (see Fig. 29). We attributed this phenomenon to the lithium mobility, i.e. to the averaging of the EFG tensors due to an exchange (i.e. jumps) between different Li sites. The distance between the satellites, which we referred to as *NMR*

splitting, ν_Q, is determined by an exchange matrix and by the orientation of the EFG tensors relative to the magnetic field. Obviously, observed value of ν_Q should be considered as motionally averaged value of the NMR splitting, $\langle \nu_Q \rangle$ (we omit the angle brackets hereinafter for simplicity).

One can show [137, 138] that the exchange of quadrupolar nuclei between different sites leads to a gradual smearing of the NMR multicomponent pattern when increasing a hopping frequency. At a certain value of the frequency of atomic jumps, which depends on the values of the EFG tensors' elements, only three lines remain in the spectrum of the $I = 3/2$ nuclei. However, further increase of the hopping frequency will not affect the shape of the NMR spectrum [137, 138], if principal values of the EFG tensor at a given site are unchangeable and if we do not take into account other interactions, e.g., fluctuations of the dipolar Hamiltonian.

As for LNS, the six EFG tensors at the Li sites in the single crystal are averaged above 550 K. Therefore, according to just mentioned arguments, the value of ν_Q should not change when further heating. However, the observed value of motionally averaged NMR splitting changes when heating above 550 K: it decreases down to zero at around 690 K, and then starts to increase (Fig. 1). Similar behavior was also observed in the LNS powder. In principle, it could be attributed 1) to a strong temperature dependence of principle values of the ^{7}Li EFG tensors 2) to an influence of neighboring molecular groups, or 3) to both of these effects. Let us show that namely the reorientation of sulfate anions is responsible for the observed temperature evolution.

Generally, the value of the quadrupolar splitting in solids is a function of pressure *P*, volume *V*, and temperature *T*, $\nu_Q(P,V,T)$. Therefore, the following equality takes place at constant pressure:

$$\left(\frac{d\nu_Q}{dT}\right)_P = \left(\frac{\partial \nu_Q}{\partial T}\right)_V + \left(\frac{\partial \nu_Q}{\partial V}\right)_T \frac{dV}{dT}, \tag{337}$$

where ν_Q, in turn, is defined as follows ($I = 3/2$) [64]:

$$\nu_Q = \frac{1}{2} C_Q \left(3\cos^2\theta - 1 + \eta \sin^2\theta \cos 2\varphi\right), \tag{338}$$

where $C_Q = e^2 qQ/h$ is a quadrupolar coupling constant, η is an asymmetry parameter, $q = V_{ZZ}/e$, where V_{ZZ} is the principal value of the EFG tensor; finally, Euler angles θ and φ

define the orientation of the EFG tensor with respect to the magnetic field. A theory of the temperature dependence of the quadrupolar splitting was studied in detail for nuclear quadrupole resonance (NQR) problems by Bayer [139] and Kushida [140]. Thus, it was shown that in usual ionic crystals the first term in the right side of Eq. 337 (so-called Bayer's term) is caused by lattice vibrations, under the influence of which the elements of the EFG tensor oscillate, i.e. magnitudes $C_Q(t)$ and $\eta(t)$ become functions of time. Since the lattice vibration frequency is usually much higher than ν_Q, the nucleus "feels" only average values: $\langle C_Q(t) \rangle$ and $\langle \eta(t) \rangle$.

According to the Bayer's theory, which considers the bending motion of the EFG tensor around an axis perpendicular to the direction of *q,* quadrupolar splitting has to decrease when heating, since the value of the quadrupolar coupling constant decreases with increasing temperature owing to the thermal averaging of the orientation of the EFG tensor. (A detailed description of this effect is given in the Appendix). If the Bayer's theory is valid, then the change of the NMR (or NQR) splitting with temperature is comparatively weak: the magnitude $\nu_Q^{-1}\left(d\nu_Q/dT\right)$ is usually of the order $10^{-4}-10^{-5}$ deg^{-1} [141].

If the evolution of $\langle C_Q(t) \rangle$ is governed mainly by the stretching normal modes involving a periodic change of V_{ZZ}, then the Bayer's term, $\left(\partial\nu_Q/\partial T\right)_V$, could be positive. This fact is a consequence of the sign ambiguity of the second derivative of *q* with respect to normal coordinates (Eq. A.9). It should be noted that the positive temperature dependence of the quadrupolar splitting, which is usually referred to as anomalous temperature dependence, is treated in literature to be an influence of the lattice expansion or the consequence of other effects, which are not directly related to lattice vibrations [141, 142]. This stereotype originates from the pioneering work of Kushida *et al*. [140], where authors have paid particular attention to the second term in the right side of Eq. 337 (it is now sometimes referred to as Kushida's term), but do not indicating explicitly that their approach redefines also the Bayer's term allowing it to be positive at certain conditions.

Kushida's term, in turn, defines the change of the quadrupolar splitting due to thermal expansion of the crystalline lattice. This term can be written as [141]

$$\left(\frac{\partial\nu_Q}{\partial V}\right)_{P,T}\left(\frac{\partial V}{\partial T}\right)_P = -\frac{\alpha}{\chi}\left(\frac{\partial\nu_Q}{\partial P}\right)_{V,T}, \tag{339}$$

where α stands for the thermal expansion coefficient and χ is the isothermal compressibility. Both α and χ are normally positive; therefore, when $\left(\partial v_Q/\partial P\right)_{V,T}$ is negative, then observed quadrupolar splitting could increase with increasing temperature.

In crystals, containing complex ions or molecules, the temperature dependence of v_Q often deviates from the Bayer-Kushida theory. In such case, the influence of a reorientational motion of molecular groups (particularly, at elevated temperatures) has to be taken into account. For the first time, this effect was observed in ammonium salts [143], where the change of the quadrupolar splitting was found to be caused by the ammonium ion reorientations. Negita *et al*. [143] developed the so-called "fly-by" model [144] to describe the temperature dependence of the quadrupolar splitting of the nuclei located in the neighborhood of the NH_4^+ ions. Later, this model was also used to explain the influence of 180° flips of the water molecules on the temperature behavior of the water containing compounds [145].

As we know, Negita's model has not been applied to study reorientational motions in sulfates; however, we do not see any physical limitations to do this. In terms of sulfate reorientational jumps, the "fly-by" model could be described as follows.

Let the SO_4^{-2} ion be static during the time period τ_r and the observed quadrupolar splitting of the neighboring nucleus be v_r. By definition, τ_r corresponds to the correlation time of the ion reorientation, i.e. is understood as a mean time between instantaneous reorientational jumps. It is assumed that during a reorientational jump, whose duration equals τ_f, oxygens "fly-by" the neighboring nucleus and the splitting equals v_f during τ_f. Naturally, we expect $\tau_f < \tau_r$. If the condition $\tau_f, \tau_r << 1/v_Q$ is fulfilled, then the average quadrupolar splitting could be written in the following form [146]:

$$v_Q = v_Q^0(T) + v_r + (v_f - v_r)\left(1 + \frac{\tau_r}{\tau_f}\right)^{-1}. \qquad (340)$$

where $v_Q^0(T)$ is the unperturbed splitting, i.e. the value of v_Q in the absence of the sulfate reorientations, including the Bayer temperature dependence if appropriate. Since the Bayer's contribution to the temperature evolution of v_Q is usually much weaker than the reorientational effect, the term $v_Q^0(T)$ is often considered to be a constant. Usually, τ_f is

assumed to be temperature-independent, whereas τ_r is chosen in the Arrhenius form, $\tau_r = \tau_0 \exp(E_a/kT)$.

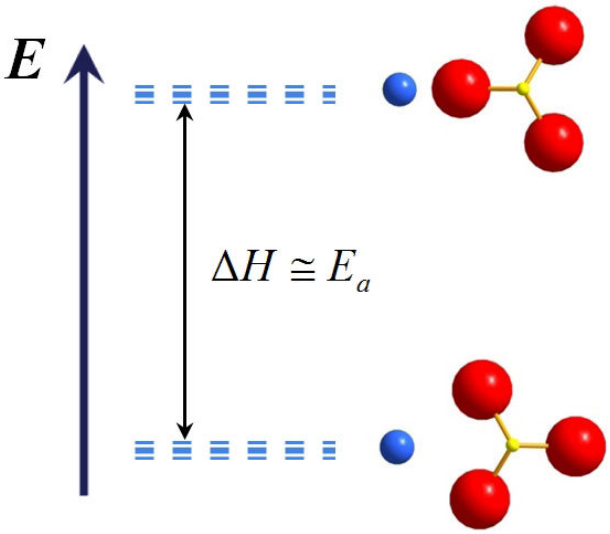

Fig. 30. Jump reorientational model as a two-state model. $\Delta H \cong E_a$ corresponds to the activation energy of the reorientational jump.

It should be noted that the jump reorientational model is a "two-state" model: the sulfate ion is either at rest or rotating. If these two states are associated with single energy levels, then their relative populations must be related by a Boltzmann factor: $n_f/n_r = \exp(-\Delta E/kT)$, where ΔE is the energy difference between the two states.

Since the populations of each of the two levels are proportional to the lifetimes of the anion in the two states, one can write: $n_f/n_r = \tau_f/\tau_r$. Therefore, at high temperatures τ_r cannot be shorter than τ_f. However, a more satisfactory approach assumes that each of the two states is associated with a complex of energy levels so that the ratio of populations is

$$\frac{n_f}{n_r} = \frac{\tau_f}{\tau_r} \equiv K(T) = \exp\left(-\frac{\Delta G}{kT}\right), \tag{341}$$

where $K(T)$ is an equilibrium constant and ΔG is a Gibbs energy difference. In the high-temperature limit, the ratio of lifetimes is governed by the factor $\exp(\Delta S/k)$, which determines the difference between densities of the two states, and, generally, can exceed unity.

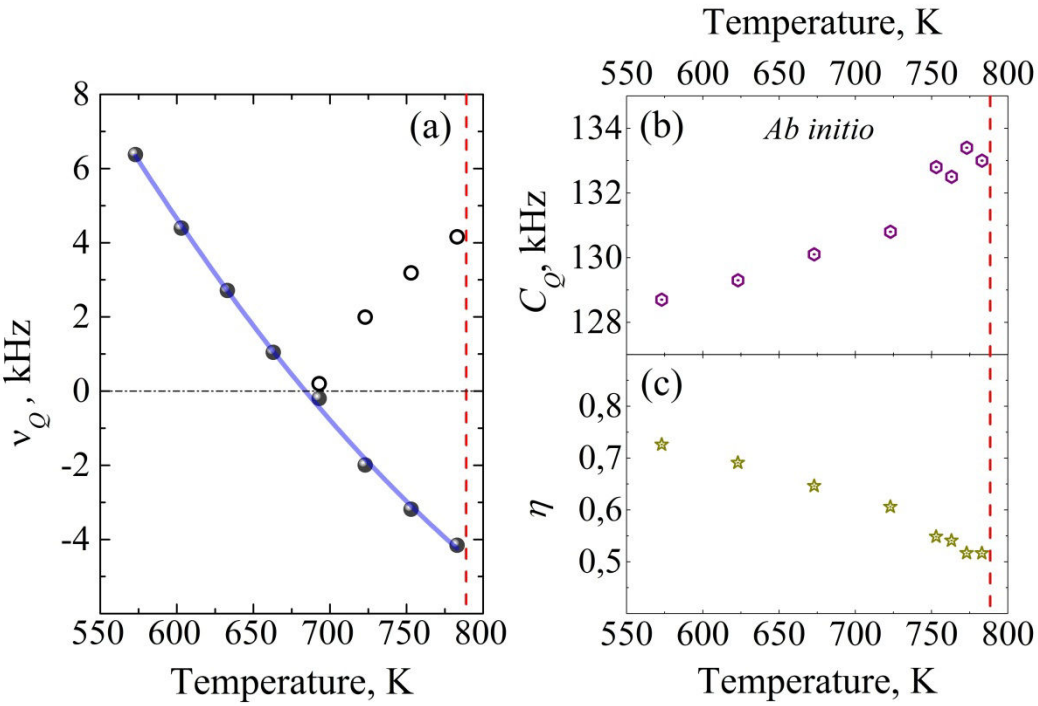

Fig. 31. (a) Temperature dependence of splitting, ν_Q, between the satellites in the ^{7}Li NMR spectrum of the $LiNaSO_4$ single crystal with the *c*-axis oriented perpendicular to the magnetic field. Blue solid line denotes the best fit of Eq. 340, whereas red dashed line denotes the boundary of the β-phase (788 K). (b) Calculated values of the ^{7}Li quadrupolar coupling constant in the "frozen" lattice and (c) corresponding calculated values of the ^{7}Li asymmetry parameter.

Temperature evolution of the ^{7}Li quadrupolar splitting in the LNS single crystal is presented in Fig. 31a. First of all, it should be noted that NMR experiment does not allow determining the sign of the quadrupolar splitting, and only the absolute value of ν_Q could be measured. Therefore, it is assumed in Fig. 31a that above 690 K real values of ν_Q could have positive as well as negative sign. The jump reorientational model, however, predicts monotonic behavior of ν_Q; therefore, if the quadrupolar splitting is positive above 690 K (empty dots in Fig. 31a), this should be caused by other effect. The most plausible explanation of this possible non-monotonic temperature dependence of ν_Q is an abrupt increase of $\langle q(t) \rangle$ around 690 K due to the effect of stretching motions of the EFG tensor mentioned above (Eq. A.9). One can show, however, that such increase should be accompanied also by the growth of the spin-lattice relaxation rate above 690 K, which has not been observed [11]. Finally, taking into account that no phase transitions were found in the LNS near 690 K we should consider the monotonic behavior of $\nu_Q(T)$ to be more preferable.

One can see from Fig. 31a that $\nu_Q = 0$ at around 690 K. Well away from this point, the magnitude $\nu_Q^{-1}\left(d\nu_Q/dT\right)$ was found to be of the order of 10^{-2} deg^{-1}, what is much higher than the value predicted by the Bayer's theory ($10^{-4} - 10^{-5}$ deg^{-1}). Therefore, the first term in the right side of Eq. 337 does not give significant contribution to the temperature evolution of ν_Q and could be considered as a constant in the temperature range under consideration.

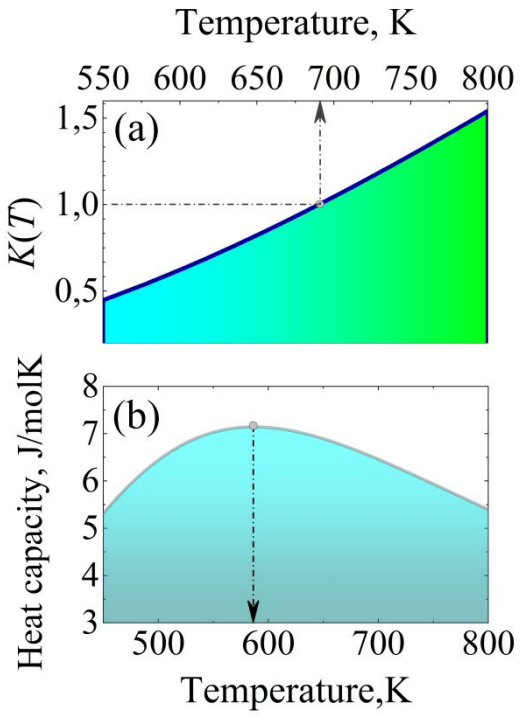

Fig. 32. (a) Temperature dependence of the equilibrium constant, $K(T) \equiv \tau_f / \tau_r$. (b) Temperature dependence of the heat capacity of $LiNaSO_4$ according to Eq. 342**.**

The contribution of the Kushida's term, i.e. the influence of the lattice expansion on the NMR splitting, can be calculated by *ab initio* methods. For this, we have carried out CASTEP [119] calculations of the principal values of the EFG tensors for each Li site at different temperatures. It should be noted that NMR-CASTEP calculations give values of the EFG tensors in the "frozen" lattice, i.e. neither lattice vibrations nor diffusion of ions are taken into account, and the temperature of the system is assumed to be 0 K. However, the temperature could be introduced indirectly using the data on the temperature evolution of the lattice parameters [10]. In this sense, one can built the "temperature dependences" of the calculated ^{7}Li NMR parameters, which are presented in Figs. 31b,c. One can see that the ^{7}Li quadrupolar coupling constant of the "frozen" lattice slightly grows when increasing temperature, whereas the asymmetry parameter monotonically decreases. The only feature in

Figs. 31b,c is a small jump of C_Q above 750 K. This behavior could be explained by the strongly anisotropic thermal expansion of the crystalline lattice of the LNS above this temperature [10].

Obviously, weak positive temperature dependence of C_Q (Fig. 31b) could not govern the strong negative temperature dependence of ν_Q above 550 K (Fig. 31a). In addition, weak evolution of the asymmetry parameter in the frozen lattice (Fig. 31c) either could not give a significant contribution to the temperature evolution of ν_Q. Thereby, the temperature dependence of the ^{7}Li quadrupolar splitting in the LNS single crystal above 550 K cannot be governed by thermal expansion of the crystalline lattice. We believe that the main contribution to the temperature evolution of $\Delta\nu_Q$ is associated with the reorientational effect.

The best fit of the Negita's model (Eq. 340) to our experimental data is presented in Fig. 31a (blue line). The activation energy (or rather enthalpy, ΔH) for the SO_4 reorientational jumps was found to be $0.19 \pm 0.02\,\text{eV}$; the term $\Delta\nu_Q^0 + \Delta\nu_r$, in turn, had the value 21±2 kHz, whereas $\Delta\nu_f - \Delta\nu_r$ was found to be $-42.6 \pm 0.9\,\text{kHz}$. We assumed the term $\Delta\nu_Q^0$ to be temperature-independent. It is interesting to note that $\tau_f/\tau_r \equiv K(T) = 1$ at around 690 K and even exceeds unity upon further heating (Fig. 2d). Such behavior of the lifetimes ratio, τ_f/τ_r, indicates that the orientational disorder of the sulfate groups occurs well below the *α*-*β* phase transition temperature (788 K).

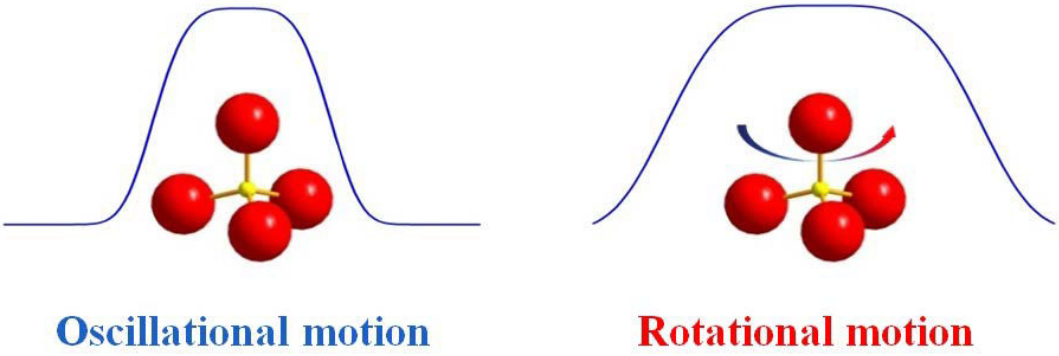

Fig. 33.Schematic representation of the probability function $|\psi|^2$ of the SO_4^{-2} ion under oscillational and rotational motions.

Takahashi *et al*. [147] estimated that the potential energy barrier to rotation of SO_4 groups should be not less than 0.3 eV in alkali-metal sulfate crystals. We obtained an underestimated value; however, such low activation energy is reasonable, since the effect of

reorientations is already observable at comparatively low temperatures. It should be noted that the value of the activation energy found by Teeters and Frech [43] was even much less: 0.09 ± 0.01 eV.

The transition from oscillational to rotational motion of sulfate ions should be accompanied by thermal phenomena. In fact, when the amplitudes of SO_4 external vibrations are small, i.e. when a vibrational quantum number *n* is quite low, eigenfunctions of oscillators corresponding to librations of the SO_4 groups, $\psi(\Theta,\Phi)$, change only slightly as *n* is increased (Θ and Φ stand for the Euler angles determining the orientation of the SO_4^{-2} ion). The probability function, $|\psi|^2$, has maxima in the neighborhood of the equilibrium values of Θ and Φ, and falls off rapidly from these maxima. Increase in *n* causes only some spread, corresponding to larger amplitudes of oscillations. However, when *n* starts to exceed some critical value, the eigenfunctions change completely in nature, becoming much more nearly constant [148]. This change increases the repulsive forces between the molecular groups, and tends to spread the crystal lattice. Such expansion of the lattice decreases the potential barriers for reorientations, so that more SO_4 groups can rotate. This transition is accompanied by an anomaly of a heat capacity, C_p, which can be defined as follows [146]:

$$C_p = kN_A \frac{K}{(K+1)^2}\left(\frac{\Delta H}{kT}\right)^2, \tag{342}$$

where *k* is the Boltzmann constant, N_A is the Avogadro constant, and ΔH is the activation enthalpy for the SO_4 reorientational jump. Substituting the equilibrium constant, $K(T)$, and the enthalpy, ΔH, found from the Negita's model, into Eq. 342, we obtained a small – 7.1 J/(mol·K) – anomaly of the heat capacity with the maximum occurring at 587 K (Fig. 31e). Such anomaly was really observed experimentally at around 600 K [10]. It was assumed that the small maximum of C_p is associated with successive phase transition; however, as we have just shown, it corresponds to the transition from oscillational to rotational motion of sulfate ions, and is not accompanied to an essential change in the structure of the crystal.

Since EFG tensors near ^{7}Li nuclei are affected by the reorientational motion of SO_4 groups, similar effect should be observed also on the EFG tensors near ^{23}Na nuclei. In Fig. 34a, temperature evolution of the ^{23}Na NMR powder spectrum is presented. One can see that at around 600 K the line starts to narrow due to the motion of Na^+ ions; at 690 K its width is minimal, but when further heating the signal starts to broaden slightly and the asymmetry of its shape increases (Fig. 34b). The asymmetry of the line is caused by the contribution of the

second order quadrupolar interactions; therefore, the hardly detectable growth of the ^{23}Na line width above 690 K corresponds to the growth of the quadrupolar splitting. Such behavior of ^{23}Na NMR spectrum provides additional grounds to assume that namely reorientational motion of SO_4 groups causes temperature dependences of quadrupolar interactions considered above.

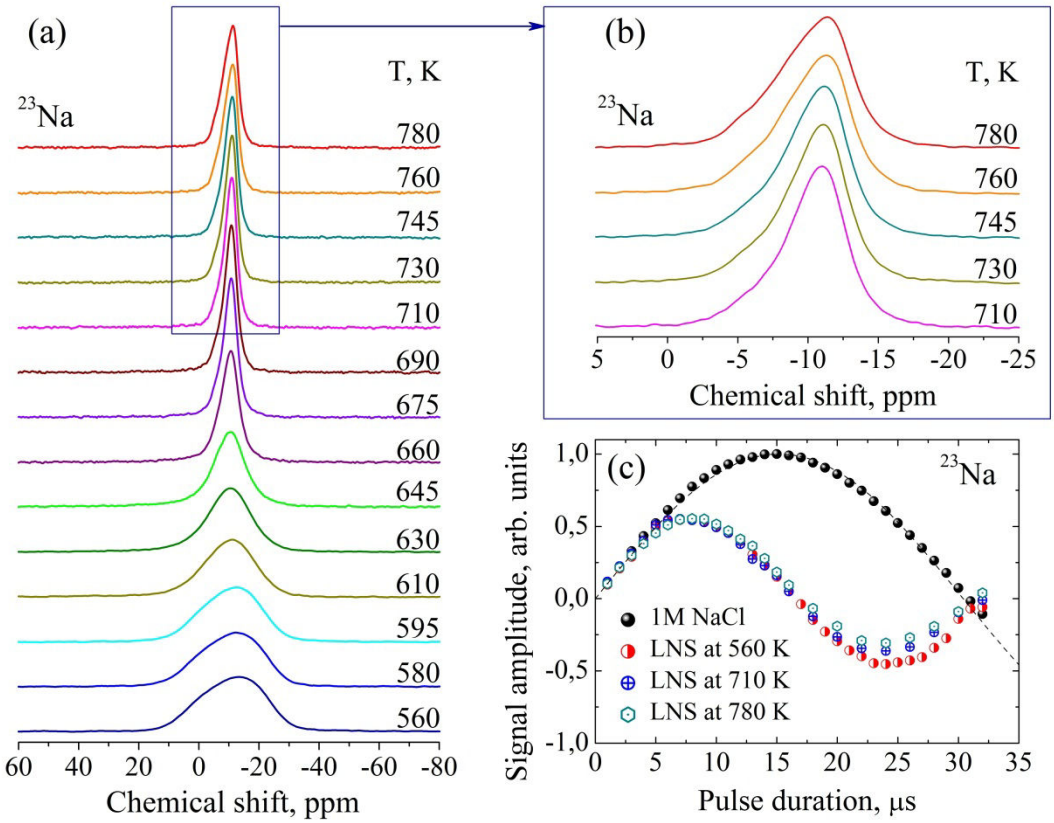

Fig. 34. (a)-(b): Temperature dependences of ^{23}Na spectrum of $LiNaSO_4$ powder. (c): ^{23}Na nutation curves of $LiNaSO_4$ at different temperatures compared to nutation in 1M NaCl water solution.

Finally, it should be noted that the averaging of the dipolar interactions above 690 K (in the spectra of both ^{7}Li and ^{23}Na nuclei) does not correspond to the extreme motional narrowing, albeit the lines reach their minimal widths. According to the definition, the extreme motional narrowing occurs when *all* interactions are averaged down to zero. However, the quadrupolar splitting of both ^{7}Li and ^{23}Na nuclei grows (in absolute value) above 690 K, i.e. it is averaged towards higher values of $|\Delta\nu_Q|$. The good way to see the motional narrowing effect is to compare nutation curves at different temperatures. ^{23}Na nutation curves are presented in Fig. 34c. Dashed line (together with black filled dots) corresponds to the ^{23}Na nutation curve in 1M NaCl and determines the nutation frequency – 16.5 kHz. 23Na nutation curves of LNS recorded at three other temperatures and shown in

Fig. 34c indicate that quadrupolar interactions are much higher than the nutation frequency, $\omega_Q^{(1)} >> \omega_{nut}$, consequently, an extreme motional regime does not take place in LNS even just below the α-β phase transition.

4.1.8 Kinetics of the α-β phase transition

Kinetics of the first-order phase transition in solids could be investigated by a number of techniques [149, 150]. The most natural techniques for studying structural phase transitions (including their kinetics) are scattering experiments: XRD and neutron scattering. Comparing the peak intensities of characteristic diffraction patterns of both the phases, the amount of an appearing phase $x(t)$ as a function of time can be obtained. The main disadvantage of the scattering methods is the limited time resolution due to the comparatively long period needed for measurement. The time resolution could be improved by using the high intensity of synchrotron radiation; however, this method is still not applicable to fast transitions.

In metals and semiconductors, electrical conductivity is a valuable tool for studying phase transformations. In the transition region, the measured conductivity $\sigma(t)$ is an averaged quantity depending on the percentage of the two phases. This method is not limited in its time resolution; therefore, it could be used for studying fast transition kinetics. However, the averaged conductivity depends on the distribution of both phases in the sample and an appropriate model has to be used to calculate $x(t)$ from $\sigma(t)$.

Kinetic parameters could be also measured by differential thermal analysis (DTA). There are several possible ways in which DTA might be used [151]. Thus, one could involve analysis of partially transformed material by measuring peak areas corresponding to the phase transition. From these data and with the aid of calibration curves, the percentage transformation could be determined. In addition to this static (isothermal) analysis, dynamic (non-isothermal) methods, which allow measuring activation energy and mechanism of crystallization, could be used. Parameters of the phase transition kinetics can be obtained by experimental DTA results using proper equations proposed to interpret non-isothermal data [152, 153].

Finally, transition kinetics could be often measured by means of NMR. Similar to all mentioned techniques, NMR tools are also based on the changes of measurable property sensitive to the presence of one of the phases. Thus, the difference of the NMR line shape in different phases could be used as such measurable property. Other type of experiments could be based on the difference of relaxation times. For a good review on NMR approach to the

kinetics measurement see papers of Feio and Cohen-Addad [154, 155], where authors make an analysis of three different types of isotherms: normalized spectrum area, half-width at half-maximum, and spin-lattice relaxation time T_1 isotherms.

It should be noted that if spin-lattice relaxation time is used as a measureable parameter, only slow kinetics could be usually studied, since T_1 measurement takes significant time. However, the difference between T_1 values in different phases could be used also for the study of quite fast kinetics. For this purpose, we developed a very easy technique, which is based on the difference of spin-lattice relaxation times in the two phases, but which does not evolve the direct measurement of T_1.

Let us assume that two phases under consideration, α and β, are characterized by different spin-lattice relaxation times $T_{1\alpha}$ and $T_{1\beta}$, respectively. Strictly speaking, it is not valid, if quadrupolar nuclei are considered, since non-exponential relaxation could occur in this case and more than one relaxation time constants exist for each phase. However, even in the case of quadrupolar nuclei, the non-exponentiality can be neglected and an effective single relaxation time could be introduced. In a single-pulse experiment, the spin system has to be allowed to relax after each 90°-pulse, i.e. a relaxation delay $d \approx 5T_1$ has to be waited before the following pulse. If the delay d does not obey this relation (i.e. smaller than $5T_1$), then the saturation effect occurs. Assuming that the characteristic time of the free induction decay, i.e. T_2^*, is quite short, so that $T_2^* << d$, one can write for the amplitude of the signal after the n-th pulse ($n > 1$):

$$M_x = M_z^0 \left[1 - \exp\left(-\frac{d}{T_1} \right) \right], \tag{343}$$

where M_z^0 is an equilibrium value of the magnetization.

During the α-β phase transition, the energy transfer mechanism between the spin system and its physical environment steadily changes, so that the part of spin system starts to relax faster or slower than before the phase transition. Taking into account Eq. 343 one can write for the magnetization in the transition region

$$M_x = M_z^0 \left\{ x_\alpha(t) \left[1 - \exp\left(-\frac{d}{T_{1\alpha}} \right) \right] + x_\beta(t) \left[1 - \exp\left(-\frac{d}{T_{1\beta}} \right) \right] \right\}, \tag{344}$$

where $x_\alpha(t)$ and $x_\beta(t)$ are relative amounts of phases α and β, respectively, and $t = nd$. The normalized NMR signal amplitude in the transition region could be written as follows:

$$I = \frac{M_x}{M_z^0} = C_\alpha - (C_\alpha - C_\beta)x_\beta(t), \tag{345}$$

where

$$C_\alpha = \left[1 - \exp\left(-\frac{d}{T_{1\alpha}}\right)\right], \quad C_\beta = \left[1 - \exp\left(-\frac{d}{T_{1\beta}}\right)\right], \tag{346}$$

and where it was taken into account that $x_\alpha(t) + x_\beta(t) = 1$. Equation 345 gives a tool to study the kinetics of the phase transition, since, as one can see, time evolution of the amplitude of the NMR signal is just proportional to the amount of appearing β-phase.

The procedure of the kinetics experiment could be as follows. Before starting an acquisition, the system is stabilized at the temperature exceeding a few degrees the α-β phase transition point. Then the laser power is reduced abruptly by the value ΔP, and the operator runs the acquisition recording each transient in a pseudo-2D NMR data array (similar to T_1 experiment). After completion of the phase transition, the system could be again heated above the phase transition, and the experiment could be reiterated. The experiment has to be repeated several times for each value of ΔP to avoid casual errors.

As it follows from Eq. 345, the time dependence of the NMR signal intensity in the kinetics experiments is determined by $x_\beta(t)$, i.e. by the time evolution of the amount of appearing β-phase. Generally, the time evolution of the volume fraction $x(t)$ of the appearing phase depends on different factors: geometry of nuclei (germs), nucleation rate, crystallization rate, crystallization mode (interface- or diffusion-controlled growth), presence of impurities, cooling/heating rate, etc.

The function describing the time evolution of the global crystallization process, i.e. $x(t)$, was first found by A.N. Kolmogorov [156], who solved the problem of the solidification of a melt assuming that emergence of crystallization nuclei in a parent phase is random and that the growth rate of these nuclei is linear. Two years later, Avrami [157, 158] introduced the so-called "expanded volume fraction" $x_\beta^e = V_\beta^e / V_0$, where V_β^e is the volume occupied by nuclei of the new phase β if they can grow without being hindered by the presence of other nuclei; V_0 is the total volume of the phases. It was shown that the real volume fraction $x_\beta = V_\beta / V_0$ is related to x_β^e as follows:

$$x_\beta = 1 - \exp(-x_\beta^e). \tag{347}$$

Equation 347 is referred to as Avrami equation. One can find [159] that in the case of a constant nucleation rate v the expanded volume fraction is $x_\beta^e = Kt^4$; the rate constant is $K = (\pi/3)c^3 v$, where c is the linear growth rate of the spherical nucleus and v is the nucleation rate (the number of nuclei appearing in the unit volume of the parent phase per one second).

When all nuclei emerge simultaneously at the initial stage of the crystallization, then $x_\beta^e = K't^3$, where $K' = (4\pi/3)c^3 N_{av}$, where N_{av} is the average number of germs per unit volume.

If the nucleation rate is a function of time, $v = const \cdot t^\alpha$, than the more general type of equation has to be written:

$$x_\beta = 1 - \exp\left[-(kt)^b\right], \tag{348}$$

where the constant k is the function of temperature and of the geometry of germs (sometimes it is referred to the rate constant of the crystallization); the exponent b is a function of the type of nucleation. Parameters k and b are usually referred to as Avrami parameters, and Eq. 348 is referred to as Kolmogorov-Johnson-Mehl-Avrami (KJMA) equation [156-158, 160].

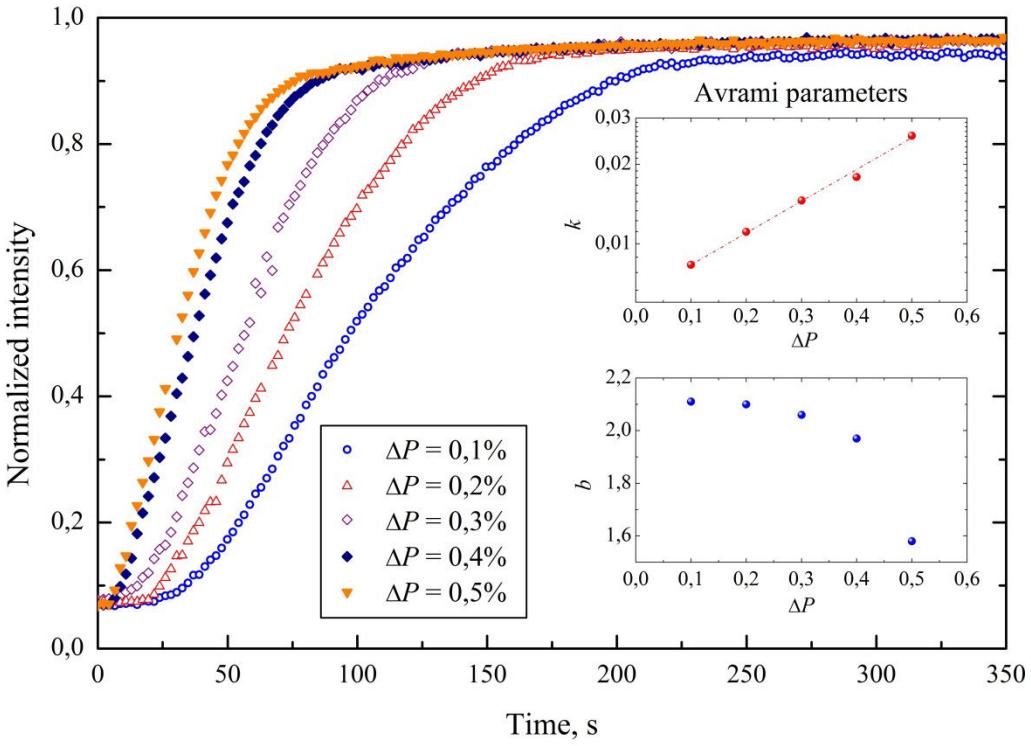

Fig. 35. Time evolution of the amount of the β phase during the α-β phase transition in $LiNaSO_4$. The dependence of Avrami parameters on the cooling rate (more precisely, on ΔP) is shown in the inserts.

If Avrami parameters are found, then one can make assumptions concerning the crystallization mode and the type of nucleation. Thus, in the case of interfaced-controlled growth of spherical germs: 1) $b = 4$ for the constant nucleation rate, and 2) $b = 3$ for rapidly exhausted nucleation. In the case of diffusion-controlled growth of spherical germs: 1) $b = 5/2$ for the constant rate, and 2) $b = 3/2$ for rapidly exhausted nucleation [159].

It should be noted that KJMA equation was derived for isothermal crystallization and, strictly speaking, cannot be used for the non-isothermal case. Under non-isothermal behavior, other models, e.g., Ozawa equation [161], has to be applied. Nonetheless, KJMA equation has also been used by some authors [162-165] to describe the non-isothermal crystallization of semi-crystalline polymers. We also shall use this approach for the crystallization kinetics of the LNS.

Table 5.

Avrami parameters at different values of ΔP. Second column contains approximate values of the cooling rate.

ΔP	r, K/min	b	$k \times 10^{-3}$
0.1	21	2.11	8.3
0.2	43	2.10	11.1
0.3	64	2.06	14.6
0.4	86	1.97	17.9
0.5	107	1.58	25.7

As it was explained above, the kinetics of the *α-β* phase transition in LNS was measured via cooling of the powder sample, which was preliminarily stabilized at the temperature exceeding a few degrees the *α-β* phase transition point. The cooling rate was controlled by the change of the laser power, which is given by the value of ΔP (see Eq. 295 and Eq. 296). It was noted in Chapter 3 that the cooling rate r is proportional to ΔP only at the initial stage of the cooling process, and the overall process is exponential: $r = w\Delta P \exp(-\kappa t)$. However, it was revealed that LNS has anomalously narrow thermal hysteresis (around 4 K) [10]; therefore, the onset of the phase transition occurs at the initial stage of cooling and we can assume that the cooling rate in our experiment is constant at

given ΔP. Note that under the cooling rate we understand here the rate, at which the temperature changes near the phase transition point.

The time evolution of the normalized NMR intensity I (Eq. 345) at different values of ΔP is presented in Fig. 35. One can see that for all cooling rates the experimental curves have a characteristic S-shape (so-called sigmoidal curve). As it was expected, the crystallization process is completed faster at higher cooling rates, i.e. crystallization curves become steeper when increasing ΔP. All curves were fitted by Eq. 345 with $x_\beta(t)$ given by KJMA relation (Eq. 348). Corresponding Avrami parameters were plotted against ΔP, and are presented in the insets of Fig. 35. Values of the Avrami parameters are also listed in Table **5**.

One can see that the rate constant k increases with the growth of ΔP showing an Arrhenius behavior. Contrary, the Avrami exponent b decreases with temperature from the value 2.11 down to 1.58. This indicates that: 1) the phase transition occurs due to the diffusion-controlled growth of germs, since $2.5 < b < 1.5$, and 2) when increasing the cooling rate, nucleation centers tend to appear simultaneously at the initial stage of cooling.

Freiheit *et al*. [10] showed that the transformation of the LNS lattice under the *α-β* phase transition can be considered as a minor displacement of S^{6+} ions. Thereforeit was assumed that the transition occurs via diffusionless mechanism [10, 38], i.e. could be referred to martensitic transitions. However, very high mobility of the cationic sub-lattice (and of the oxygen sub-lattice as well) does not allow attributing this phase transition to the pure martensitic transformation. Moreover, small values of the Avrami exponent b indicate that the diffusion-controlled growth of germs takes place. It means that the limiting stage of the transition kinetics is related to the diffusion of the cations, but not to the transformation of the sulfur sub-lattice.

4.1.9 Rearrangement of powder particles under cooling through the α-β phase transition

The ^{7}Li NMR spectrum of the LNS single crystal at 750 K with the *c*-axis oriented perpendicular to the magnetic field is presented in Fig. 36 (lower spectrum). As it was explained above, this spectrum is a result of averaging of the EFG tensors due to an exchange (i.e. jumps) between different Li sites. The distance between the satellites in the spectrum of the crystal depends on the orientation of the crystallographic axes with respect to the magnetic field.

The powder is an ensemble of crystallites randomly oriented in the space, and each crystallite in the powder will give its own spectrum. In the case of $I = 3/2$, the summation (or rather integration) over the orientations of all crystallites gives a powder pattern that has the form presented in Fig. 36 (upper spectrum), where the ^{7}Li NMR spectrum of unannealed powder of $LiNaSO_4$ recorded at 750 K is presented.

In order to study the effect of rearrangement of powder particles we recorded spectra at 750 K. At this temperature, the motion of lithium ions is fast enough to suppress the dipolar broadening and the signal to noise ratio is much better. The quadrupolar coupling decreases almost to zero on heating up to 690K and increases again on further heating. At 750K, the quadrupolar coupling is quite high and allows abserving the individual lines in the case of single crystal.

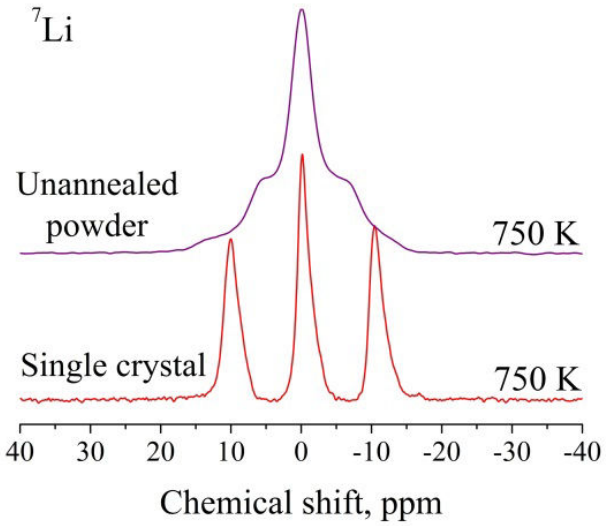

Fig. 36. ^{7}Li NMR spectra of $LiNaSO_4$ at 750 K recorded in single crystal and unannealed powder.

Above 788 K, both ^{7}Li and ^{23}Na spectra of LNS powder contain only single line; this reflects its quasi-liquid structure. After subsequent cooling below the phase transition, the ^{7}Li powder spectrum differs substantially from the usual $I = 3/2$ powder pattern presented in Fig. 36.

After different cycling of heating and cooling through the phase transition, different patterns have been obtained. Figure 37a presents one of such patterns obtained after slow cooling (~20-50 K/min) from 800 K to 750 K. One can see that the ^{7}Li powder spectrum in Fig. 37a consists of three lines, typical of the spectrum of the LNS single crystal at this temperature (Fig. 36) with the central, $-1/2 \leftrightarrow +1/2$, and external, $\pm 3/2 \leftrightarrow \pm 1/2$, transitions. It

means that some new arrangement of crystallites takes place in the powder after cooling through the phase transition.

Different spectral patterns have been obtained when repeating this experiment keeping the same conditions. However, all spectra observed after slow cooling are quite different from the usual $I = 3/2$ powder pattern, whereas after quenching to room temperature, the NMR spectrum of the reheated sample (Fig. 37b) is again similar to the $I = 3/2$ powder pattern, but with a complex shape.

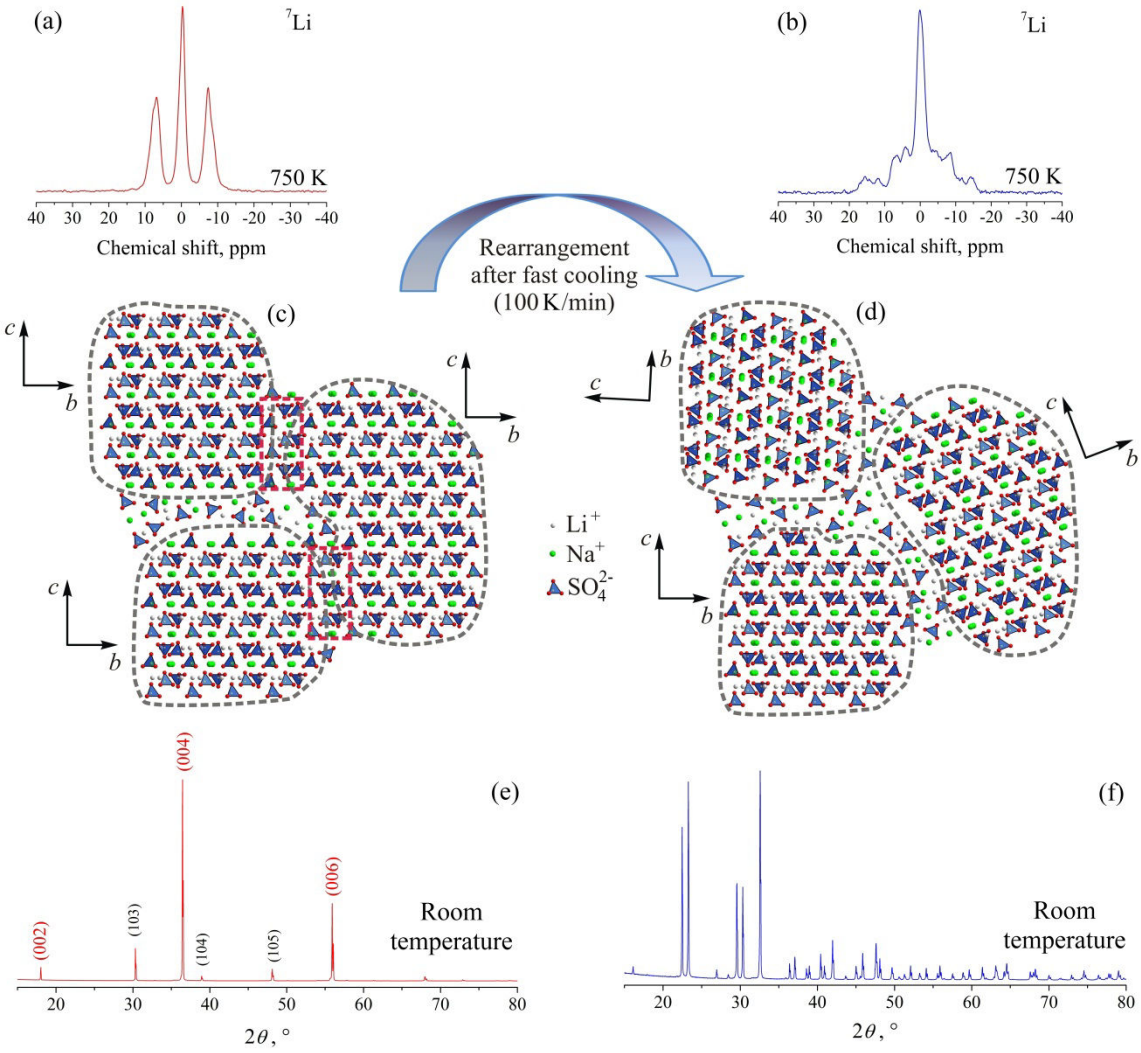

Fig. 37. (a)-(b): ^{7}Li NMR spectra of the $LiNaSO_4$ powder after slow (a) and fast (b) cooling. (c)-(d): Schematic representation of the $LiNaSO_4$ crystallites' arrangement after slow (c) and fast (d) cooling; dashed rectangles outline the "necks" between powder particles. (e)-(f): XRD powder patterns of the $LiNaSO_4$ after slow (e) and fast (f) cooling. At each experiment, the cooling passes through the α-β phase transition.

The rearrangement of the crystallites in the LNS powder after slow cooling through the phase transition is confirmed also by the XRD data. The room-temperature XRD pattern of the LNS powder heated up to 823 K and subsequently cooled at ~1 K/min is presented in Fig. 37e. Figure 37f contains the XRD pattern of the same sample after quenching, that would rather correspond to a random distribution of the powder crystallites in the sample after fast cooling.

Effect of the rearrangement of crystallites in the LNS powder was observed also in the annealed samples. Similar regularities were observed when cooling annealed samples through the phase transition. Thus, under slow cooling, the crystalline lattices of grains were tended to be oriented in the same direction, whereas fast cooling destroyed this type of ordering.

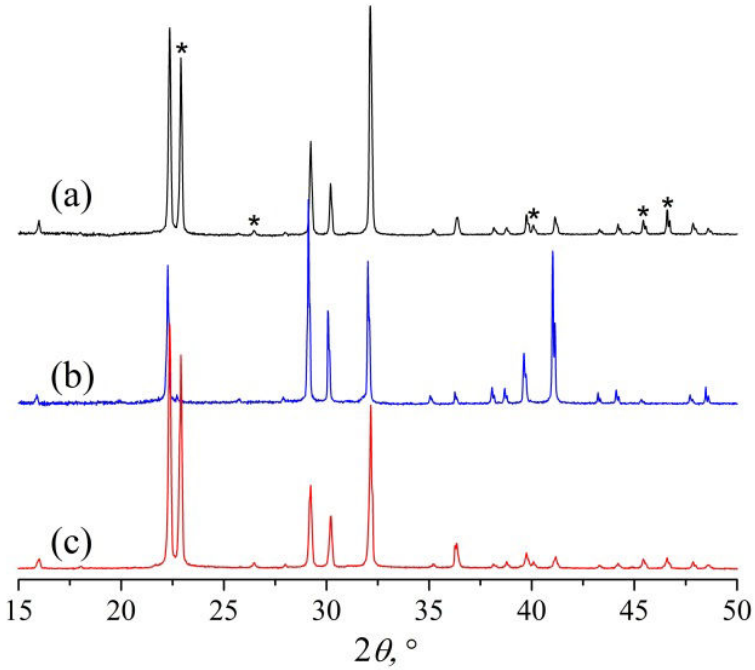

Fig. 38. XRD patterns of $LiNaSO_4$ powder at 753 K: (a) before annealing; (b) after annealing at 823 K and subsequent cooling with the cooling rate 2 K/min; (c) after annealing at 823 K and subsequent cooling with the cooling rate 100 K/min.

Observed phenomenon can be explained quite easy. Remembering that any phase transition is a stochastic process and taking into account the existence of inevitable temperature gradients in the sample, one can confidently assert that the phase transition in some crystallites occurs earlier than in other ones. If the cooling rate is quite small, then emerging trigonal phase intergrowths into neighboring crystallites through the common borders. The powder particles, in which the phase transition occurs earlier, could be

considered as “macroscopic nucleation centers”, which determine the orientation of the crystallographic axes in other crystallites of the powder sample.

To provide the intergrowth of the trigonal phase into neighboring crystallites, a set of conditions have to be fulfilled.

1) The crystallites must have necks between its neighbors, i.e. rigid coupling between powder particles has to exist.

2) The borders between crystallites must be “transparent” for the moving cations, since the kinetics of the phase transition was found to be determined by the diffusion.

3) Mechanical stresses have to exist on the borders, because the structural interrelationship between crystalline lattices of α- and β-modifications should be destroyed. Let us show that all of these conditions are satisfied.

Generally, real necks emerge between neighboring powder particles under sintering. It is interesting to note the effect of the rearrangement of crystallites in the LNS powder we originally observed in the annealed samples, and only later, the same effect was reproduced in the unannealed LNS powders. Since the diffusion rate in α-LNS is very high (), the processes of sintering should occur very quickly; therefore, common necks, which are formed at the initial stage of sintering [166, 167], could appear almost immediately after the heating above the phase transition. Thus, the first condition, i.e. the existence of the necks, is fulfilled.

In the diffusion experiment, we varied the diffusion time Δ to determine the effect of the borders on the value of the self-diffusion coefficient; however, evidence of restricted diffusion was not revealed neither in the β-LNS, nor, what is more important, in the α-LNS. This result indicates that (at least) in α-LNS diffusing cations “do not feel” the crystalline borders and can easily cross them getting into neighboring powder particles. Apparently, such transparency of borders enables the trigonal phase to germinate from a given crystallite to the neighboring ones. Thus, the second condition is also satisfied.

It has been already shown that the α-β phase transition in the LNS is ferroelastic in its nature [38], i.e. the sulfur sub-lattice of the α-LNS is very malleable near the phase transition, and could be easily deformed under the influence of external mechanical forces [168]. It also means that sulfur ions can move quite far during the phase transition, and they apparently do this, if there are external forces acting on the crystal. Such plasticity may cause the violation of the structural relationship between α- and β-phases. It was shown by Freiheit *et al*. [10] that a significant shrinkage of the crystalline lattice occurs under the phase transition (the volume of the unit cell is decreased at ~6% under the transformation of the lattice from cubic to trigonal). (Note that the term “shrinkage” is related here to the decrease of the interatomic

distances under the phase transition, but not to the shrinkage of the powder sample after sintering.) Due to the presence of the common borders, the phase transition occurring inside of one of the neighboring crystallites may lead to the emergence of mechanical stresses on these borders, i.e. the clamping of the crystalline lattice could take place. Such clamping may act as the external force required to the destruction of structural interrelationship between crystalline lattices of α- and β-modifications. Thus, the third condition is also satisfied.

In summary, we would suggest the following mechanism for the discussed phenomenon. Let some crystallite of the LNS powder undergo the structural α-β phase transition. This transformation changes not only the volume structure of the crystallite, but also the structure of its boundary. Since this border is common for at least two powder particles, its crystallization corresponds to the creation of a germ of the β-phase for the neighboring crystallite. This germ governs the phase transition, providing the direction of the crystallographic axes of the β-modification. Thus, the trigonal phase expands into the volume of the powder sample, using necks (borders) between distinct powder crystallites as channels of growth. The most important thing here is that the orientation of the crystallographic axes in all powder crystallites is determined by the orientation of the lattice in the first powder particle, which could be considered as a macroscopic germ.

It should be noted that crystallites tend to orient their lattices in the same manner only at small cooling rate r. It could be explained by assuming that the nucleation rate is very low at small r, whereas the growth rate is very high. In other words, few (or even only one) germs are assumed to appear in the sample during the overall phase transition process at small r, and these germs grow quickly into the remaining volume. On the other hand, we revealed that the Avrami exponent b is decreased when increasing the cooling rate (see inset in Fig. 35). This indicates that the nucleation rate is very high at "fast cooling" (b tends to 3/2), and big amount of germs appears in the sample at the same time. As a result, formation of the trigonal phase occurs simultaneously over the entire volume of the sample, and powder particles change its crystalline structure from cubic to trigonal independently of the others. In fact, one can see from Fig. 37b that the NMR spectrum of the powder sample after quenching resembles the spin $I = 3/2$ powder pattern with an incomplete averaging over different orientations of the crystallites.

Going to other sulfates…

Before going to other representatives of double alkali sulfates it should be noted that we did not have a possibility (because of limitations in time) to pay as much attention to these compounds as to lithium sodium sulfate. However, it is very important to compare different members of $LiMSO_4$ family in order to find common features and distinguish their individual characteristics. Thus, it is interesting to follow the dependence of Li mobility on the size of the second cation. Moreover, crystalline structures in different phases of given compouns should be compared to give more reasonable justification for joining these sulfates into the same family. Without this comparison, the whole picture will not be complete.

First, we consider Li dynamics of each compound, and then we make comparative description of the whole family.

4.2 Structure and dynamics of lithium-potassium sulfate

4.2.1 Structure of $LiKSO_4$

Lithium potassium sulfate, $LiKSO_4$ (LKS), has been investigated in detail for over more than a century [47, 48], and a large variety of physical phenomena have been found in its different crystalline phases (pyroelectricity, ferroelectricity, ferroelasticity, fast-ionic conductivity, and structure modulation). LKS undergoes over ten phase transitions in the 20-1000 K temperature range. At least two phase transitions take place in LKS above room temperature: at 708 K and 943 K. The complexity and richness of its phase diagram is unusual for an inorganic crystal with such a simple chemical formula.

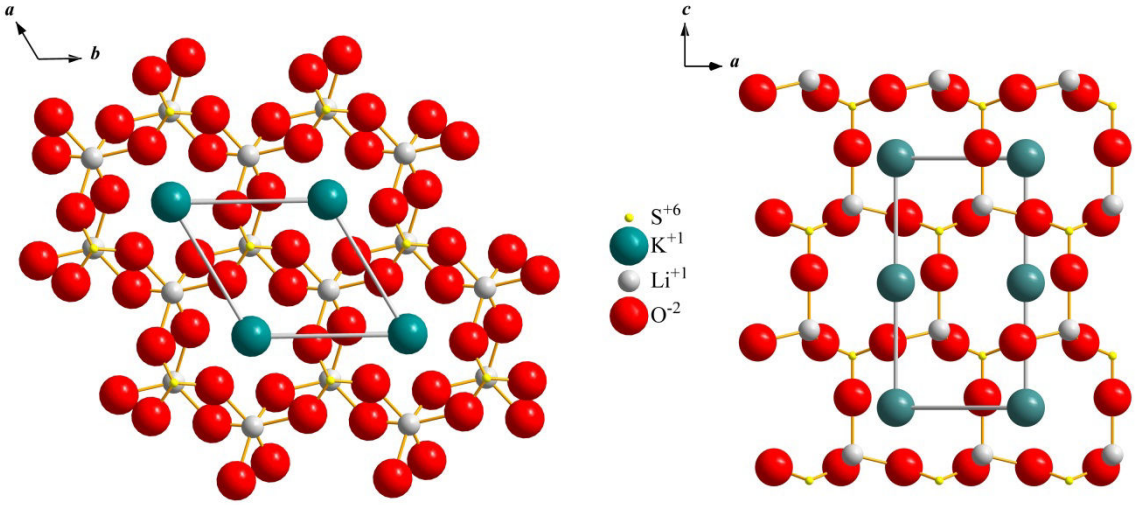

Fig. 39. Structure of $LiKSO_4$ at room temperature ($P6_3$, $Z = 2$) projected on the basal plane (on the left) and perpendicular to it (on the right).

Only the structures of two phases are now well established: the high-temperature phase (phase *I*, $T > 943$ K) and the room temperature phase (phase *III*, $203\ \text{K} < T < 708\ \text{K}$). Crystal structure refinements at room temperature have been carried out by Karppinen *et al*. [169] and Bhakay-Tamhane *et al*. [170] for a twinned crystal. It was shown that at ambient temperature LKS belongs to the space group $P6_3$ with two formula units per unit cell (Fig. 39). The SO_4 and LiO_4 tetrahedra form an ordered three-dimensional framework structure characterized by six-membered rings of three LiO_4 and SO_4 tetrahedra. The apices of the three LiO_4 tetrahedra point in the opposite direction to those of the three SO_4 tetrahedra [171]. The K^+ ions occupy positions on the hexagonal *c*-axis and are coordinated by nine oxygens. The structure is very compact in the basal plane (the Li^+ ions are tightly closed into a tetrahedral

cage of oxygen) if compared with the perpendicular direction. In fact, SO_4 librations around axes parallel to *c* are submitted to restoring forces more important due to stronger chemical bonds in the basal plane with respect to the other directions [172].

The high-temperature phase (phase *I*) belongs to the space group $P6_3/mmc$ with two formula units per unit cell [55, 173, 174]. The structure can be described as a hexagonal close packing of sulfate tetrahedra, with the K^+ ions occupying the octahedral sites (every K^+ ion is surrounded by six sulfate ions) and the Li^+ ions occupying the tetrahedral sites (Fig. 40). This produces a framework of corner-shared LiO_4 and SO_4 tetrahedra with K^+ filling the cavities within the framework. The K^+ ion displays a tricapped trigonal prism coordination with respect to oxygen atoms. It should be noted that the symmetry elements of the $P6_3/mmc$ group, absent in the $P6_3$ group, are due to the orientational disorder of the sulfate groups and, moreover, that in this structure two equivalent positions are available for each lithium ion, a necessary condition for a good ionic conductivity.

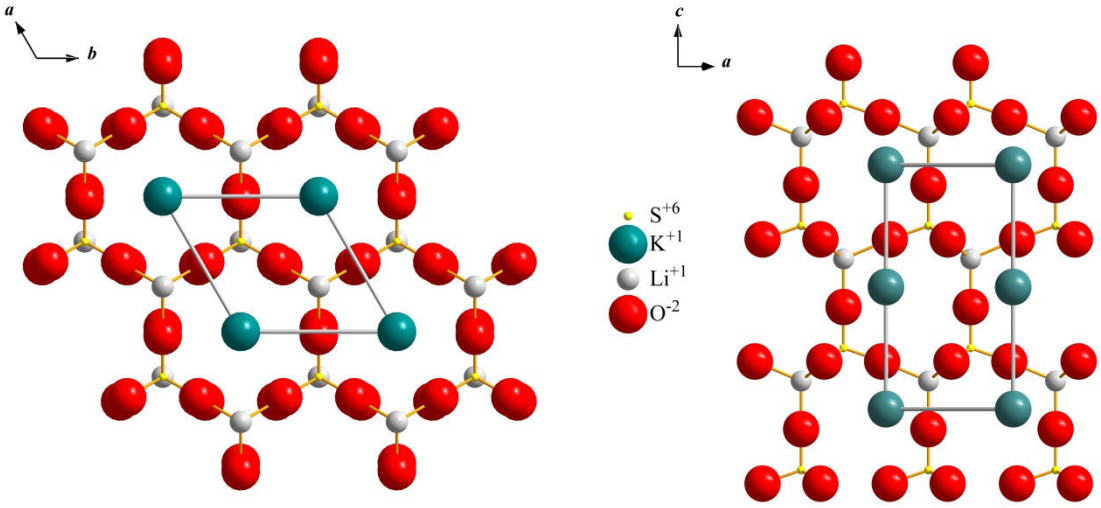

Fig. 40. Structure of $LiKSO_4$ above 943 K ($P6_3/mmc$, $Z = 2$) projected on the basal plane (on the left) and perpendicular to it (on the right).

The structure of the intermediate phase (phase *II*, $708 < T < 943$) is more controversial: some authors proposed the existence of a fourfould superstructure ($Z = 8$) above 708 K with symmetry $P6_3$ and a possible modulated incommensurate phase between 743 and 943 K [173], while others stated that the experimental results could be interpreted assuming a model of twinned orthorhombic domains with symmetry *Pmcn* and $Z = 4$ [175]. Using X-ray powder diffraction Pietraszko [174] confirmed the symmetry *Pmcn* in the temperature range 743–935 K (phase *II*), as well as the hexagonal symmetry $P6_3/mmc$ of the phase *I*. Scherf *et al*. [176] using polarization microscopy on thin LKS single-crystal plates,

studied the domain structure growth during the $III \rightarrow II$ transition and confirmed the orthorhombic character of the phase *II*. According to the structural studies carried out by Pinheiro *et al*. [177] phase *II* consists of three types of orthorhombic twinned domains with *Pmcn* symmetry oriented at 120° to each other.

4.2.2 Experimental details

The procedure of the preparation of the LKS powder was analogous to the preparation of the $LiNaSO_4$ samples (see section 4.1.2). Namely, LKS powder was obtained by grinding of the LKS single crystals grown by a slow evaporation technique using equimolar solution of K_2SO_4 and $Li_2SO_4 \cdot H_2O$ as precursors. NMR measurements have been carried out using a static NMR probe designed by the Bruker company and modified in CEMHTI, Orléans. Spin-lattice relaxation measurements have been carried out via saturation-recovery pulse sequence. Data on the spin-lattice relaxation in the rotating frame have been obtained using a standard spin-locking technique (see section 1.2.). The 90°-pulse for ^7Li magnetization had the duration, corresponding to a RF field strength of 17.8 kHz. The strength of the locking field was 41.5 kHz. LiCl molar solution was used as reference for the ^7Li chemical shift scale.

4.2.3 Lithium mobility in $LiKSO_4$

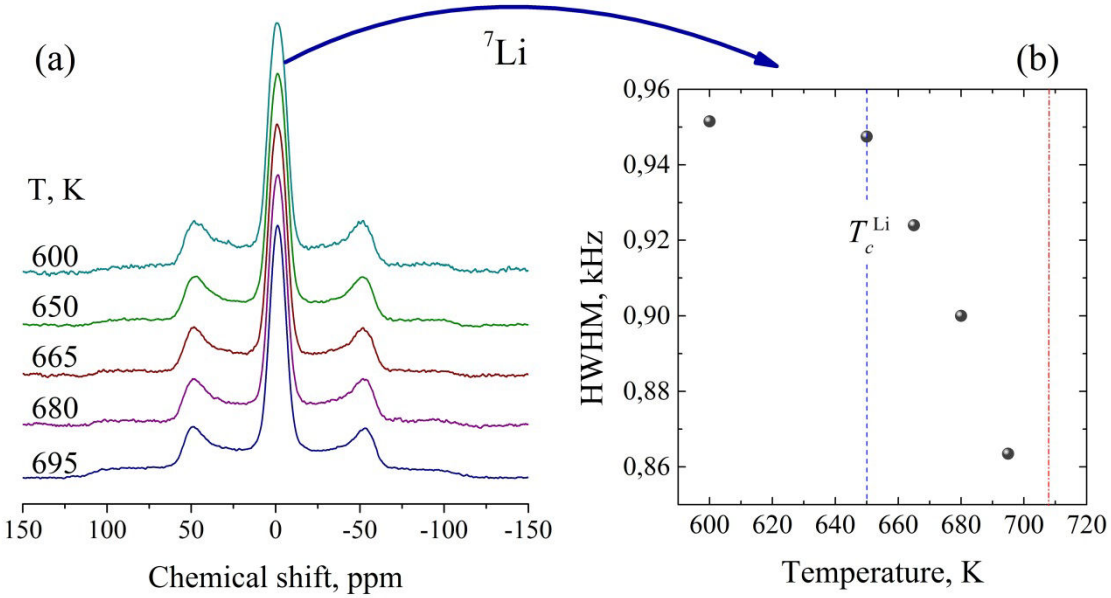

Fig. 41. (a) Temperature dependence of ^7Li NMR powder spectrum in $LiKSO_4$. (b) Temperature evolution of a central transition width. Dashed line indicates the onset temperature of a motional narrowing. Vertical dash-dotted line indicates a boundary of the *III* phase.

Despite of a vast bibliography on LKS [178], only several papers were devoted to the ionic mobility in this compound [6, 51, 179]. The most extensive study on lithium conductivity was carried out by Pimenta *et al*. [6, 172] Authors stated that a rotation of a sulfate group around an axis in the basal plane permits a Li^+ ion to reach position, which is normally forbidden, since lithium ions are closed into a tetrahedral cage formed by oxygen, each one belonging to a different sulfate group. To minimize the energy in this new local configuration associated with the displacement, the other three sulfate groups linked to this particular lithium ion will rotate and, consequently, provoke the displacement of the other lithium ions out of their sites, and so on. The lithium-ion mobility is, therefore, coupled with the rotation movements of the sulfate groups by a "paddle-wheel" mechanism similar to $LiNaSO_4$.

It was shown [6] that below 653 K and above 708 K the ionic conductivity of the LKS single crystal (along the *c*-axis) obeyed an Arrhenius law with activation energies 1.8 and 1.65 eV in phases *III* and *II*, respectively. Between 653 and 708 K, the slope of the experimental curve (in the logarithmic scale) was not constant and increased steadily up to transition temperature. This result was attributed to the decrease of the activation energy in this temperature range. The decrease in energy, in turn, was considered as a consequence of the increasing disorder of sulfate ions below the phase transition. Above 708 K, the value of the conductivity (~0.1 $Ohm^{-1}cm^{-1}$) was found to be only one order of magnitude inferior to the accepted hallmarks of superionic phases [6]. At the $III \rightarrow II$ phase transition, the conductivity increased suddenly by a factor of 20, whereas the jump of the ionic conductivity at the $II \rightarrow I$ transition (943 K) is markedly smaller. It was shown that the phase transition at 943 K is also preceded by a decrease of the activation energy due to an additional increase of the orientational disorder [6].

In present research, we studied lithium mobility in LKS by means of NMR. Below 708 K, the line width analysis was applied to find the activation energy of Li^+ jumps, whereas above the phase transition (i.e. in phase *II*), T_1 and $T_{1\rho}$ measurements were carried out to understand ionic motion.

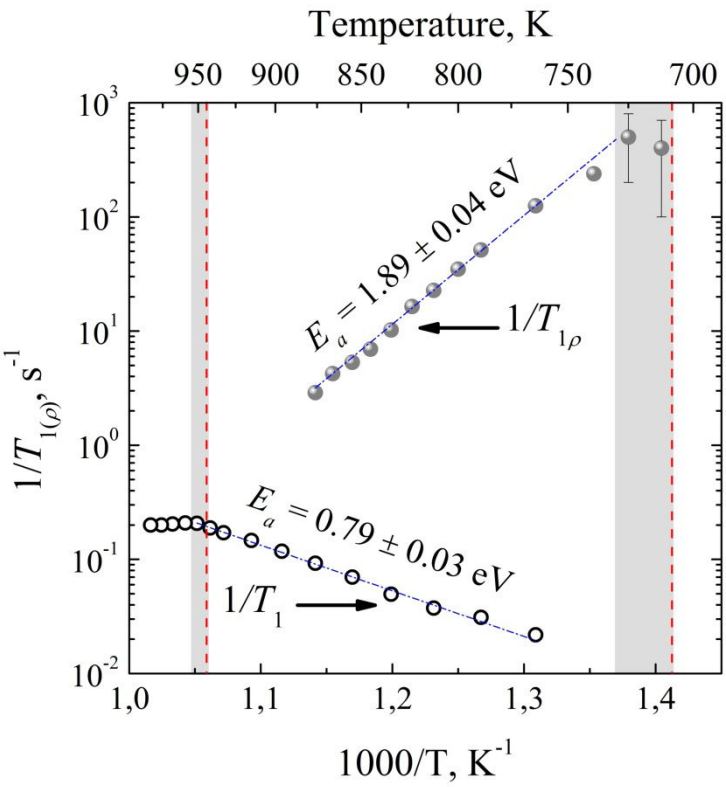

Fig. 42. Temperature dependences of $1/T_1$ (open circles) and $1/T_{1\rho}$ (filled circles) relaxation rates. Dash-dotted lines correspond to Arrhenius fits to the experimental data. Blackout regions indicate temperature ranges, where the coexistence of the two phases was observed. Vertical dashed lines indicate the boundaries of the *II* phase.

Temperature dependence of a ^{7}Li NMR powder spectrum of LKS is presented in Fig. 41a. To obtain the values of the central transition widths, each spectrum was fitted with DMfit software [124]. Corresponding temperature evolution of the central transition width is presented in Fig. 41b. Due to the phase transition, which occurs at 708 K, an abrupt jump of the ionic mobility accompanied by a sudden decrease of the line width takes place at this temperature. Therefore, the full $\delta\omega(T)$ curve is not available and to evaluate an activation energy of Li^+ jumps an empirical relation of Waugh and Fedin [125] should be used. Using the value of the onset temperature of $T_c^{Li} = 650\,K$, we obtain $E_a^{WF} = 1.05\,eV$. Similar to $LiNaSO_4$, a considerable discrepancy takes place between the NMR (Waugh-Fedin) value of the activation energy and the value obtained from d.c. conductivity measurements, 1.80 eV [6]. It should be noted that obtained discrepancy is not such big as in the case of $LiNaSO_4$; however, the same explanation, namely, the existence of potential barriers of various heights could be applied. On the other hand, one should remember that the Waugh-Fedin approach is a quite rough estimation. This can also explain the mentioned difference.

Figure 42 contains the temperature dependences of two different relaxation rates: $1/T_1$ and $1/T_{1\rho}$. Blackout regions indicate temperature ranges, where the coexistence of the two phases was observed. One can see that in the $708 < T < 943$ range one cannot obtain the whole curves of the relaxation rates, and only a "low-temperature shoulder" of the $1/T_1$ curve and a "high-temperature shoulder" of the $1/T_{1\rho}$ dependence can be measured. It was revealed, that both temperature dependences obey the Arrhenius law and the values of the activation energies were found to be $E_a^{low} = 0.79\,\mathrm{eV}$ and $E_a^{high} = 1.89\,\mathrm{eV}$. This discrepancy indicates that there exists a distribution of correlation times describing the mobility of Li^+ ions. The stretching parameter, $\beta = E_a^{low} / E_a^{high}$, in turn, was found to be quite far from unity, $\beta \approx 0.42$, indicating a considerable deviation of the correlation function from the exponent (see section 1.2.).

4.3 Structure and dynamics of lithium-rubidium sulfate

4.3.1 Structure of $LiRbSO_4$

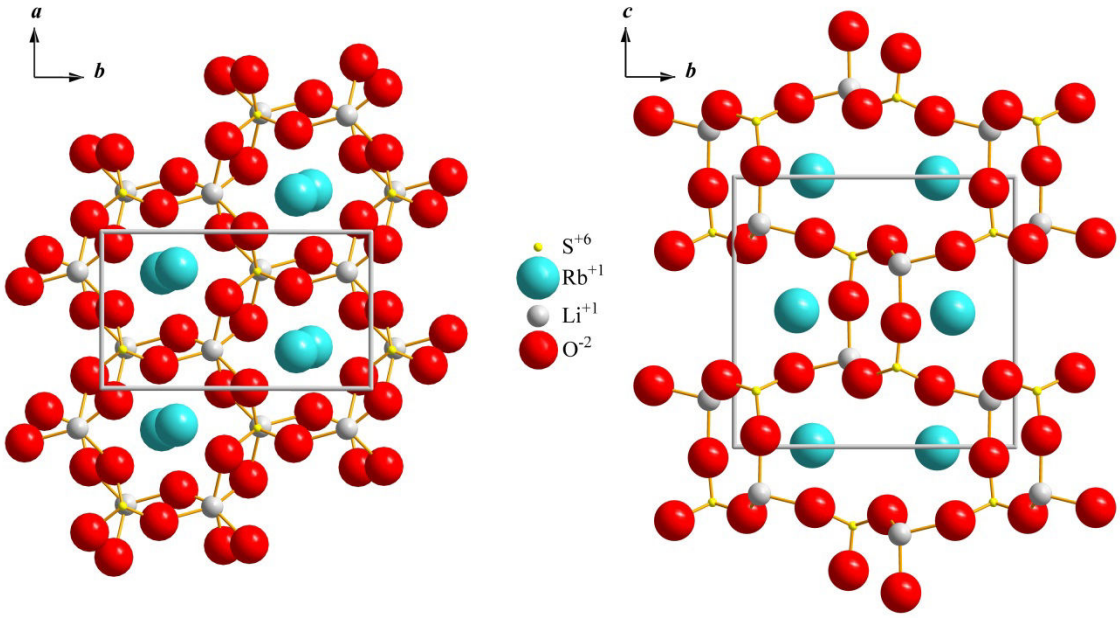

Fig. 43. Structure of $LiRbSO_4$ at room temperature (phase *V*, $P112_1/n, Z = 4$) projected on different planes.

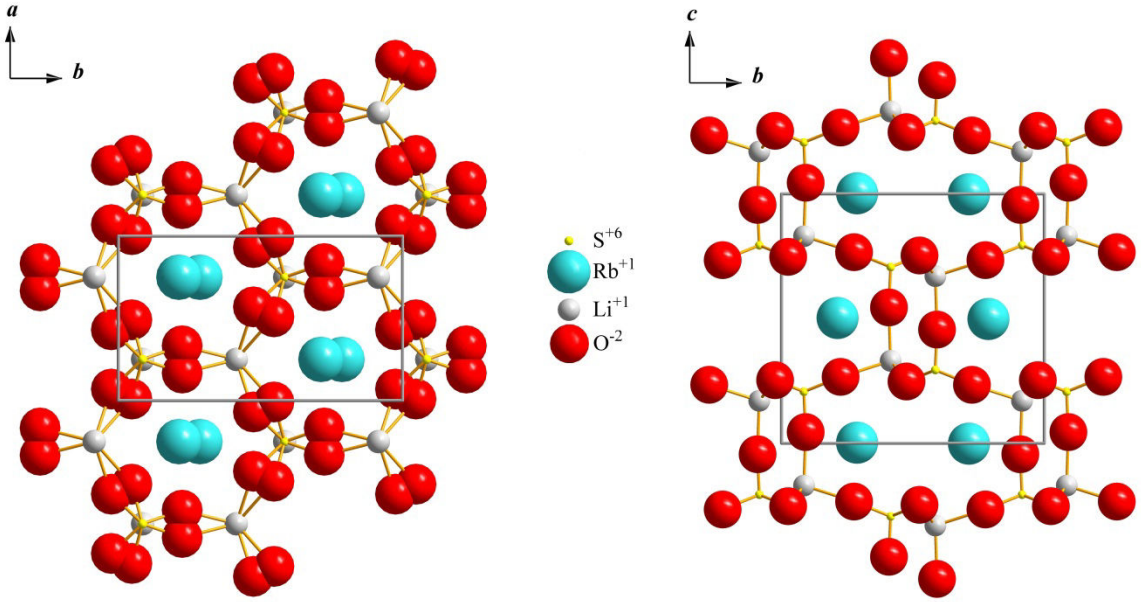

Fig. 44. Structure of $LiRbSO_4$ above 477 K (phase *I*, *Pmcn*, $Z = 4$) projected on different planes.

$LiRbSO_4$, lithium rubidium sulfate (hereinafter LRS), undergoes successive structural phase transitions at temperatures between 439 and 477 K: paraelectric (phase *I*)($T_{tr1} = 477\,\mathrm{K}$)

→ incommensurate (phase *II*) ($T_{tr2} = 475\,\mathrm{K}$) → ferroelastic (phase *III*) ($T_{tr3} = 458\,\mathrm{K}$) → ferroelectric (phase *IV*) ($T_{tr4} = 439\,\mathrm{K}$) → paraelectric (phase *V*) [14]. At all temperatures, LRS has a framework structure make up of alternating LiO_4 and SO_4 tetrahedra forming six-membered rings, inside which Rb^+ cations are located [15]. The phase transition is approximately described as arising from changes of the orientations of tetrahedral SO_4-groups.

LRS belongs to the monoclinic point group ($P112_1/n$, $Z = 4$) at room temperature (phase *V*) and is orthorhombic (*Pmcn*, $Z = 4$) above 477 K (phase *I*). Phases *IV* ($439 < T < 458$) and *III* ($458 < T < 475$) are known to be monoclinic (respectively $P11n$, $Z = 20$ and $P2_1/c11$, $Z = 8$) and phase *II* exhibits incommensurate modulations [15, 16]. The melting point is around $T_m = 1010\,\mathrm{K}$ [17]. Even in the monoclinic phases, the distortion of the lattice from the orthorhombic structure is small since the monoclinic angles are very close to 90° [16]. Moreover, the b/a ratio of the lattice parameters is about 1.73 in all phases, i.e. the Bravais lattice is almost hexagonal. Therefore, LRS has been described by some authors as a pseudo-hexagonal network of six-membered rings of SO_4 and LiO_4 tetrahedra [15] (Fig. 43).

High-temperature orthorhombic phase is also referred to as disordered phase since SO_4 ions occupy with an equal probability two positions related by the mirror of the *Pmcn* structure [15, 180]. Two configurations of the SO_4 tetrahedron can be reached by ±16.8° rotation from the mirror plane about an axis nearly oriented to the *c*-axis (Fig. 44). Farhi and Coudin [181] showed that from the Raman point of view the LRS crystal behaves as if it was orthorhombic above 439 K. Nevertheless, a monoclinic ordering exists in the temperature range $439 < T < 477\,\mathrm{K}$ and it is expressed through residual Raman lines. The microscopic nature of this ordering was related to the rotation of the SO_4 tetrahedra about the *c*-axis.

4.3.2 Experimental details

LRS powder was obtained by grinding of the LRS single crystals grown by a slow evaporation technique using equimolar solution of Rb_2SO_4 and $Li_2SO_4{\cdot}H_2O$ as precursors. Details of the NMR measurements are identical to $LiKSO_4$ study.

4.3.3 Lithium mobility in $LiRbSO_4$

Until nowadays, Li^+ mobility in LRS has not been considered at all, since its high-temperature phase has very low ionic conductivity. It should be noted that phase transitions

considered above are not accompanied by an increase of the ionic mobility, whereas a dynamical disorder of a lithium sub-lattice, seemingly, takes place only above ~600 K.

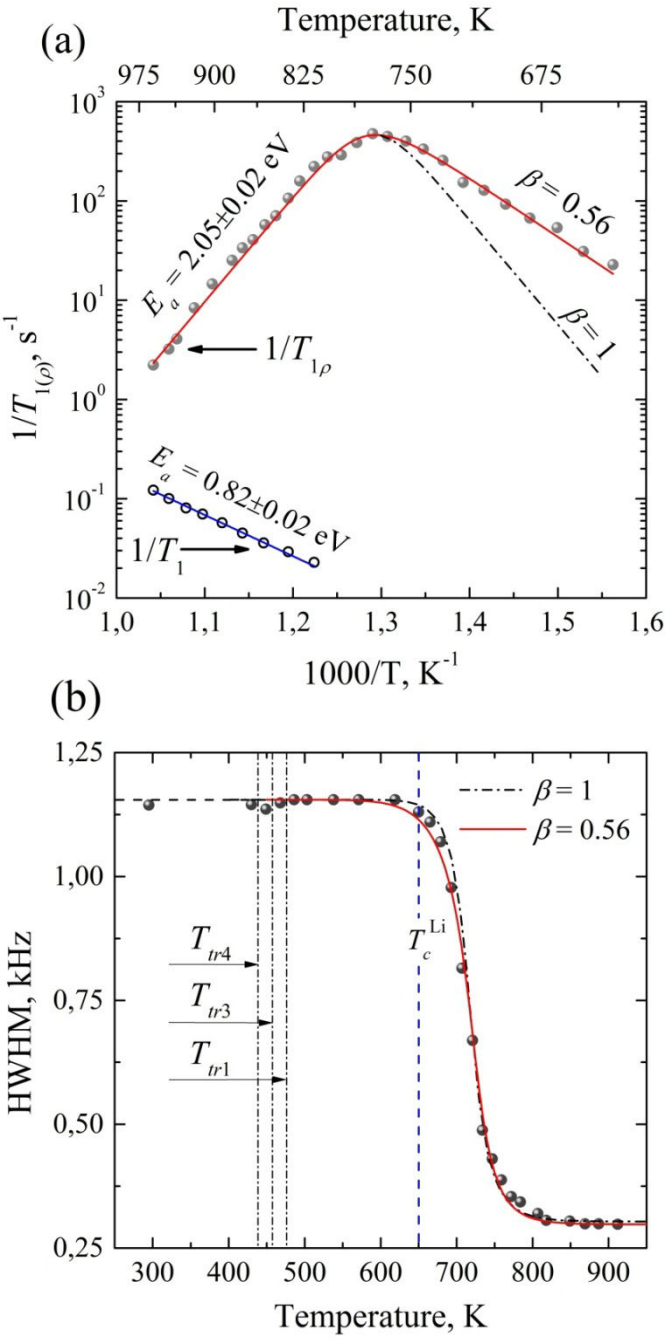

Fig. 45. (a) ^{7}Li NMR spin-lattice relaxation rates of $LiRbSO_4$ in both the laboratory (open circles) and the rotating (filled circles) frame of reference. (b) Central transition width of the ^{7}Li NMR powder spectra of $LiRbSO_4$ as a function of temperature. Both types of experimental data were fitted with the BPP model, $\beta = 1$, (black dash-dotted line) as well as with the model assuming a distribution of correlation times, $\beta < 1$, (red solid line). Vertical dash-dotted lines in figure (b) indicate the phase transition temperatures; whereas the vertical dashed line indicates the onset temperature of the line narrowing.

To understand the motion of Li^+ ions in LRS, we have carried out high-temperature NMR measurements. Activation energy and correlation times of Li^+ jumps were determined by means of line width analysis and relaxation measurements.

Figure 45a contains the temperature dependences of two different relaxation rates: $1/T_1$ and $1/T_{1\rho}$. Temperature evolution of the spin-lattice relaxation rate in the rotating frame, $1/T_{1\rho}$, was obtained between 640 and 960 K, whereas $1/T_1$ dependence was measured only above 810 K. Below 810 K, relaxation time constant T_1 was found to exceed one minute that makes the corresponding measurements to be time-consuming. One can see that $1/T_1$ has an Arrhenius behavior in the temperature range under consideration. An activation energy was found to be $E_a = 0.82 \pm 0.02\,\text{eV}$.

It is clearly seen from Fig. 45a that the $1/T_{1\rho}$ logarithmic plot is asymmetric. The BPP model is thus and to fit the experimental data, we used a spectral density function given by Eq. 166. (It was shown in section 1.2.9 that this approach is equivalent to the Cole-Davidson model.) Red solid line in Fig. 45a corresponds to the best fit obtained. The activation energy was found to be $E_a = 2.05 \pm 0.02\,\text{eV}$, whereas the parameter β was found to deviate significantly from unity: $\beta = 0.56$. Such stretching parameter gives the following value for the slope of the low-temperature shoulder of the $1/T_{1\rho}$ curve: $E_a^{low} = 1.15\,\text{eV}$. This value exceeds slightly the activation energy found from the $1/T_1$ slope; however, this can be explained by the assumption that the distribution of correlation times varies with temperature.

Temperature evolution of the central transition line width of the ^7Li NMR powder spectra is presented in Fig. 45b. Experimental data were fitted with the BPP model (dash-dotted curve) as well as with the model assuming a distribution of correlation times (solid line). In the second case, the parameter β was fixed to be 0.56, as it was found from relaxation measurements. It is interesting to note that both models (BPP and Cole-Davidson) give a satisfactory fit and, moreover, give the same value of the activation energy for Li^+ jumps: $E_a = 2.05 \pm 0.05\,\text{eV}$. The only minor difference is in preexponential factors: $\tau_0^{\text{BPP}} = (1.6 \pm 0.2) \times 10^{-18}\,\text{s}$ and $\tau_0^{\text{CD}} = (2.5 \pm 0.3) \times 10^{-18}\,\text{s}$. Finally, it should be noted that the onset temperature of a motional narrowing was rather low, $T_c^{\text{Li}} = 650\,\text{K}$, and gives rather low value of the activation energy: $E_a^{\text{WF}} = 1.05\,\text{eV}$. This indicates that the Waugh-Fedin relation [125] can involve large error, particularly, in case of distribution of correlation times.

4.4 Structure and dynamics of lithium-cesium sulfate

4.4.1 Structure of $LiCsSO_4$

At ambient temperature, $LiCsSO_4$ (CLS) has an orthorhombic structure (space group *Pmcn*) with four molecular units per unit cell [18, 19]. Figure 46 shows the projections of the atomic positions in the *Pmcn* phase on two different planes. The four Li and Cs atoms in a unit cell are crystallographically equivalent. The oxygen coordination around each Cs is 11-fold, and the Li^+ ion has a tetrahedral coordination. Each SO_4 tetrahedron in the network of CLS is surrounded by four LiO_4 tetrahedra via common corners and vice versa. The framework contains channels, in which the Cs^+ cations are incorporated. The alternating LiO_4 and SO_4 tetrahedra are positioned on mirror planes perpendicular to [010]. In the actual structure, the SO_4 groups are disordered between two orientations symmetric with respect to the mirror plane.

Below room temperature, LCS undergoes a phase transition at about 202 K to a ferroelastic phase with monoclinic structure (space group $P2_1/n$) without undergoing a change in the number of atoms in the unit cell. Above room temperature, only one phase transition was found to be at 1013 K from electrical conductivity measurements [182].

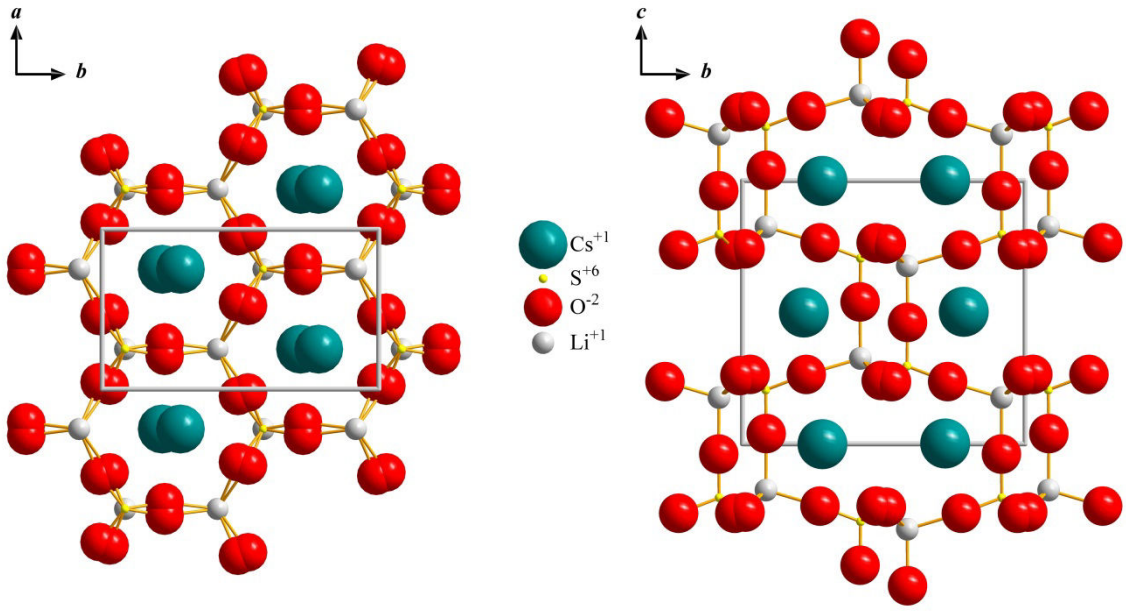

Fig. 46. Structure of $LiCsSO_4$ at room temperature projected on different planes.

4.4.2 Experimental details

LRS powder was obtained by grinding of the LCS single crystals grown by a slow evaporation technique using equimolar solution of Cs_2SO_4 and $Li_2SO_4 \cdot H_2O$ as precursors. For other experimental details see sections 4.1.2 and 4.2.2.

4.4.3 Lithium mobility in $LiCsSO_4$

Similar to $LiRbSO_4$, the ionic conductivity of LCS is rather low; therefore, there is a lack of bibliography concerning the lithium mobility in this compound. To understand the ionic motion, we have carried out the measurements of spin lattice relaxation rate in the rotating frame, $1/T_{1\rho}$, in the 750-1000 K temperature range. Along with relaxation study, the line width analysis has been also carried out in the 500-1000 K range.

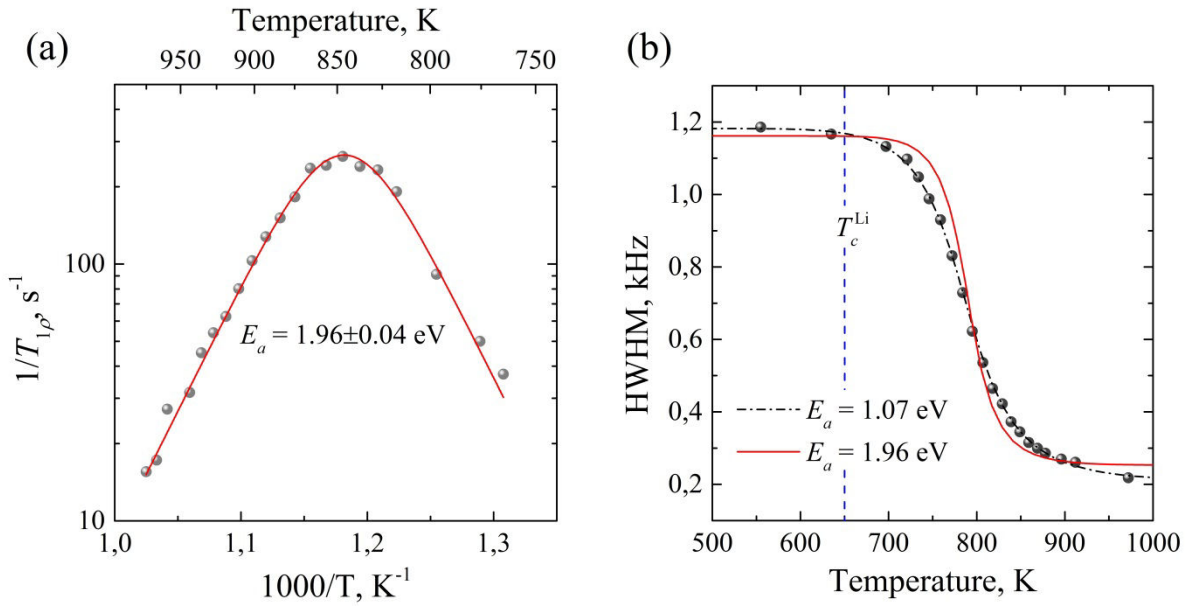

Fig. 47. (a) ^{7}Li NMR spin-lattice relaxation rate of $LiCsSO_4$ in the rotating frame of reference. (b) Central transition width of the ^{7}Li NMR powder spectra of $LiCsSO_4$ as a function of temperature. Vertical dashed line indicates the onset temperature of the line narrowing.

Temperature evolution of $1/T_{1\rho}$ is shown in Fig. 47a. One can see that the logarithmic plot of $1/T_{1\rho}$ is symmetric; therefore, we have applied the BPP model to fit experimental data (solid line in Fig. 47a). An activation energy of Li^+ jumps was found to be 1.96 eV. However, the data on the ^{7}Li central transition width (Fig. 47b) deviate significantly from the relaxation data. In fact, the best fit to the temperature dependence of the ^{7}Li line width (dash-dotted line in Fig. 47b) gives the value of the activation energy of 1.07 eV, whereas keeping $E_a = 1.96\,\text{eV}$, we obtain unsatisfactory fit (red solid line in Fig. 47b). The Waugh-Fedin

approach [125] with $T_c^{\mathrm{Li}} = 650\,\mathrm{K}$ again gives underestimated value: $E_a^{\mathrm{WF}} = 1.05\,\mathrm{eV}$. The obtained discrepancy is very strange and has not been observed for compounds considered above. For the present, we cannot find a reasonable explanation of this fact.

4.5 Discussion: comparison of transport properties in alkali sulfates

Temperature dependences of the ionic conductivity of three related superionic conductors are presented in Fig. 48. One can see that conductivities of Li_2SO_4 and $LiKSO_4$ have almost the same activation energies below 850 K: $E_a \approx 1.7\,\text{eV}$. $LiNaSO_4$, in turn, exhibits much higher potential barrier; nevertheless, due to the phase transition at 788 K, an absolute value of the $LiNaSO_4$ ionic conductivity is the highest among other sulfates in the 788-888 temperature range. It should be noted, however, that despite of the same slope of experimental curves, lithium sulfate and lithium potassium sulfate exhibit different temperature behavior near the phase transition point. In fact, Li_2SO_4 exhibits the sharp phase transition, and the temperature dependence of the conductivity is not deviated considerably from the straight line on a "log" plot. Contrary, $LiKSO_4$ exhibits considerable "non-linearity" (deviation from the Arrhenius law), which was assumed to be the consequence of the decrease of the activation energy when heating above 870 K [6].

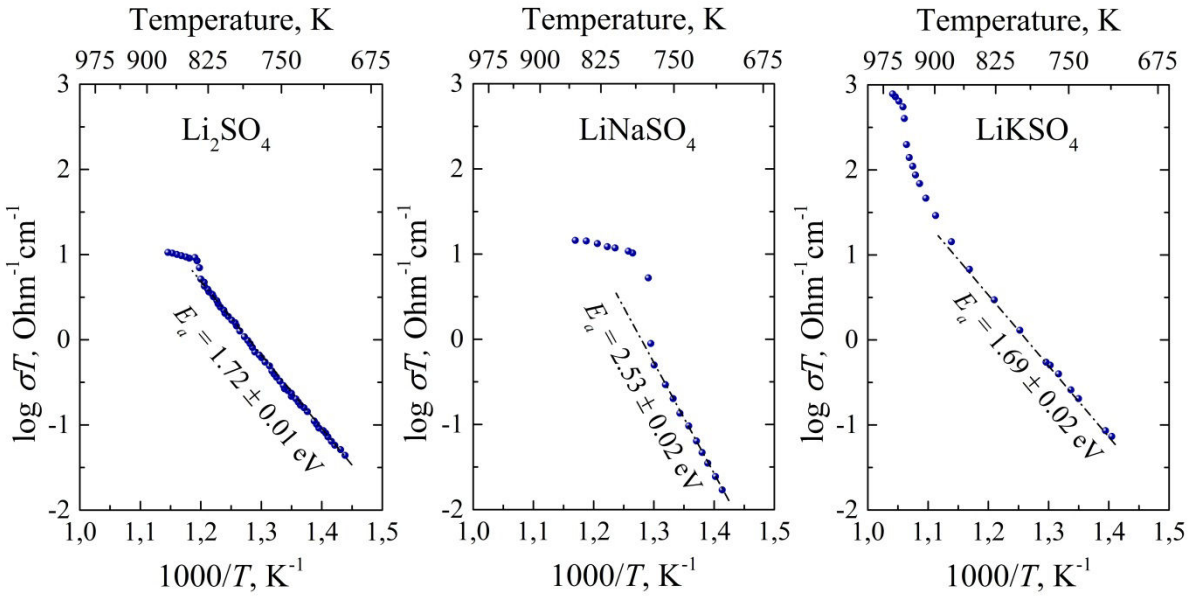

Fig. 48. Temperature dependences of the ionic conductivity in different sulfate superionic conductors [5, 6]. Values of the activation energy, E_a, are shown near the corresponding data.

One can see from Fig. 48 that similar to Li_2SO_4 lithium sodium sulfate exhibits quite sharp phase transition; moreover, both Li_2SO_4 and $LiNaSO_4$ have almost the same absolute values of the conductivity in the high-temperature phase. Obviously, concentration of Li^+ ions in lithium sulfate exceeds approximately twice the concentration of these ions in lithium

sodium sulfate; therefore, one should assume that 1) both Li^+ and Na^+ ions transfer the charge in $LiNaSO_4$ above the phase transition, and 2) the diffusivity of Na^+ is not less than the diffusivity of Li^+.

As we have mentioned above that this really takes place in α-$LiNaSO_4$ (Fig. 28) due to the paddle-wheel mechanism of the ionic motion. It was also shown above that Na starts to move well below the phase transition; however, its diffusivity in β-$LiNaSO_4$ is much lower than the diffusivity of Li (Fig. 23). This can be used to explain an abrupt increase of the $LiNaSO_4$ ionic conductivity after the phase transition. In fact, a contribution of Na^+ motion into ionic conductivity below the phase transition is comparatively small, and the charge transfer is governed mainly by Li motion. Just above the phase transition, the diffusivity of Na is abruptly increased due to the onset of SO_4 reorientations giving rise to the sharp increase of the net conductivity.

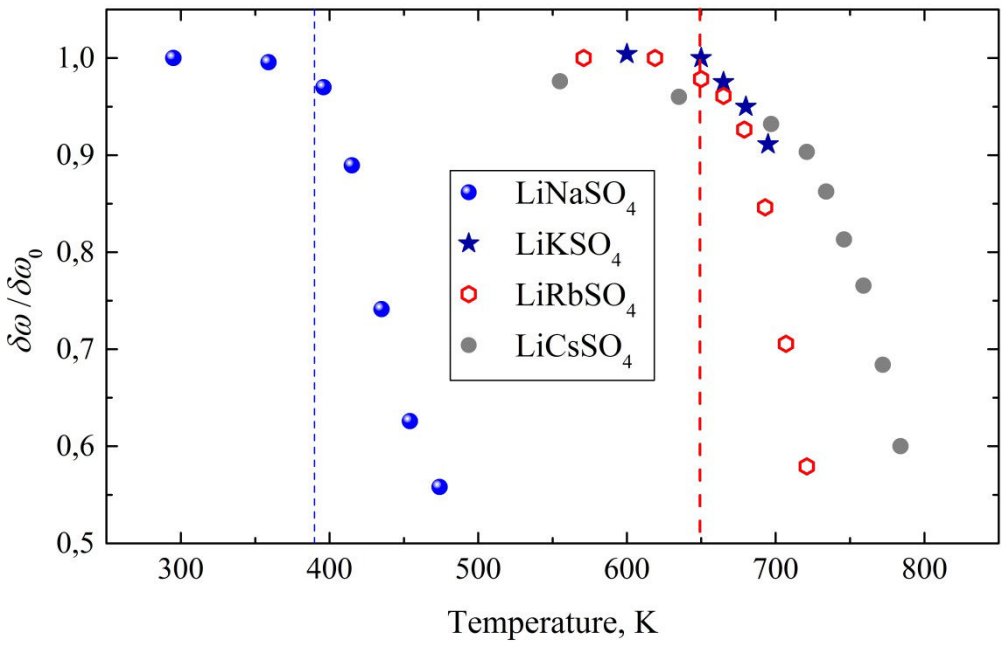

Fig. 49. Temperature dependences of relative NMR line width, $\delta\omega/\delta\omega_0$, in four alkali sulfates.

It is interesting to follow the influence of the M^+ cation size on Li mobility in $LiMSO_4$ compounds. First, it should be noted that the two-step motional narrowing occurs only in $LiNaSO_4$, whereas in other compounds such behavior of the NMR line width has not been observed. This indicates that cations of a big radius (bigger than Na^+) cannot diffuse in a crystal and form a second "skeleton" sub-lattice in addition to sulfur ions.

It is reasonable to assume that the size of cations forming immobile sub-lattice should influence the mobility of lithium. In fact, one can see from Fig. 49 that the onset temperature

of Li motion in $LiNaSO_4$ (blue dashed line) is much lower than in other sulfates. Thereby, the increase of the radius of the second cation hinders Li mobility. However, the onset temperature of Li mobility in alkali sulfates with big cations (K^+, Rb^+, and Cs^+) is almost the same (red dased line in Fig. 49). In other words, the hindering is most effective when going from Na^+ to K^+, whereas the further increase of the cation's radius does not give any significant effect on the onset temperature. Using an approach of Waugh and Fedin (WF) [125] we found an activation energy of Li jumps to be approximately 0.63 and 1.05 eV in $LiNaSO_4$ and in other compounds, respectively.

Table 6. Activation energies of Li jumps in double alkali sulfates determined by different techniques: Waugh-Fedin astimation, E_a^{WF}; $\delta\omega(T)$ curve fitting, $E_a^{\delta\omega}$; T_1 measurements, $E_a^{T_1}$; $T_{1\rho}$ measurements, $E_a^{T_{1\rho}}$.

Sulfate	E_a^{WF}, eV	$E_a^{\delta\omega}$, eV	$E_a^{T_1}$, eV	$E_a^{T_{1\rho}}$, eV
$LiNaSO_4$ (β-phase)	0.63	0.71	0.71	-
$LiKSO_4$ (phase *II*)	1.05	-	0.79	1.89
$LiRbSO_4$ (phase *I*)	1.05	2.05	0.82	2.05
$LiCsSO_4$	1.05	1.07	-	1.96

It should be noted that the WF estimation is quite rough and other techniques can give different values of the potential barrier. In Table **6**, we listed values of activation energy for Li jumps determined by four different methods. One can see that values obtained for $LiNaSO_4$ are in a quite good agreement, whereas for other compounds obtained results are contradictory. Thus, $LiRbSO_4$ exhibits the highest discrepancy between the WF approach and the full $\delta\omega(T)$ curve fitting. Probably, this discrepancy is caused by the distribution of correlation times observed in $LiRbSO_4$. Non-exponential relaxation (i.e. the distribution of τ_c) was also assumed to exist in $LiKSO_4$; however, it's impossible to compare E_a^{WF} and $E_a^{\delta\omega}$ for this compound, since the full $\delta\omega(T)$ is not available due to the phase transition occurring at

708 K. In contrast, E_a^{WF} was found to be almost equal to $E_a^{\delta\omega}$ in $LiCsSO_4$, where relaxation was found to be exponential.

It is interesting to note that both $LiKSO_4$ and $LiRbSO_4$ have rich phase diagrams along with non-exponentiality of Li relaxation. In contrast, in $LiNaSO_4$ and $LiCsSO_4$, where the non-exponentiality has not been observed, only one phase transition occurs above room temperature. Probably, these facts are somehow interrelated.

Other feature, which has to be noted here, is that both Li_2SO_4 and $LiNaSO_4$ have cubic structure in the high-temperature phase in contrast to other alkali sulfates under consideration. Thus, the α-phase of $LiNaSO_4$ ($T > 788$ K) is body-centered cubic, whereas the phase *I* of $LiKSO_4$ ($T > 943$ K) is hexagonal. This difference was reflected also by NMR measurements: while the ^{7}Li NMR spectrum of a $LiNaSO_4$ powder above 788 K contained only a single line indicating the cubic symmetry, the spectrum of $LiKSO_4$ above 943 K represented a clearly observed $I = 3/2$ powder pattern. It is easy to show that the bcc lattice of the α-$LiNaSO_4$ cannot be obtained directly from the trigonal lattice of the β-phase. In other words, the transformation to the superionic phase is reconstructive in its nature, i.e. a group-sugroup relationship between the symmetry of the phases is absent. (The same is valid for Li_2SO_4.) Different nature of phase transitions in, e.g., $LiNaSO_4$ and $LiKSO_4$, should have some impacts. Thus, the effect of rearrangement of powder crystallites, which was revealed in $LiNaSO_4$ when cooling through the phase transition, has not been observed in $LiKSO_4$. It does not seem to be possible to explain in detail this discrepancy at current stage of study; however, we believe that this is a consequence of the different nature of phase transitions in these two compounds.

The symmetry of the high-temperature phase should affect also the symmetry of reorientational motion of sulfate groups. Thus, in α-$LiNaSO_4$ (bcc lattice) oxygens were found to be distributed in an octahedrally distorted spherical shell with six preferential sites around each sulfur atoms [35], i.e. SO_4 rotational motion was found to be almost isotropic. Quasi-rotations of sulfates in $LiKSO_4$ (phase *I*, hexagonal lattice), in turn, were found to occur along the *c*-axis, i.e. in the basal plane [172]. Nevertheless, both compounds exhibit strong correlations between rotational jumps of SO_4 groups and translational motion of cations, i.e. the paddle-wheel mechanism takes place.

Dynamical disorder of sulfate groups was found to exist in both $LiNaSO_4$ and $LiKSO_4$ even below the superionic phase transition. It was noted by Pimenta *et al*. [6] that in $LiKSO_4$ paddle-wheel coupling still takes place in the phase *II*. Thus, it was assumed that this coupling

leads to the decrease of the activation energy of the conductivity, which results in the deviation of $\sigma(T)$ from the Arrhenius law. In contrast, Zhang *et al*. [13] revealed that sulfate reorientations have only weak effect on the behavior of the Li^+ ions in β-$LiNaSO_4$, i.e. there is no strong coupling between the cationic diffusion and the SO_4 reorientational jumps in the β-phase. This is confimed also by conductivity measurements in lithium sodium sulfate, where the deviation from the Arrhenius law has not been observed.

It is reasonable to assume that reorientational jumps of SO_4 groups occur also in two other compounds ($LiRbSO_4$ and $LiCsSO_4$) at elevated temperatures. However, a detailed study of this problem has not been yet carried out.

Main conclusions and perspectives

A short review of an accomplished work

The main goal of the present research was a detailed study of ionic transfer in double sulfates belonging to the $LiMSO_4$ family, where M = Na, K, Rb, Cs. The most attention has been paid to $LiNaSO_4$ as to the most interesting (in terms of the ion dynamics) compound among other double sulfates. The interest to $LiNaSO_4$ is, first, due to the highest (among other members of the $LiMSO_4$ family under consideration) ionic conductivity in the 600-850 K temperature range. Albeit the conductivity of $LiKSO_4$ exceeds the highest value of σ in $LiNaSO_4$ above 850 K (Fig. 2), these temperatures are too high for the most possible applications, particularly, for batteries. We also had shown that single crystals of lithium sodium sulfate are the most unpretentious to the growing conditions. In fact, crystals with well-defined habit and good optical properties were obtained under different temperatures, pH levels, and rates of evaporation. Other compounds, in turn, had some disadvantages, e.g., $LiKSO_4$ was found to form almost spherical (albeit faceted) crystals under elevated evaporation rates.

It was shown by the present study as well as by some previous works that ions of the two types (Li^+ and Na^+) transfer the charge in $LiNaSO_4$. This leads to interesting effects, such as the existence of two minima in the temperature evolution of the spin-lattice relaxation time at low magnetic field. We also observed a two-step motional narrowing, which has not been previously observed and which was found to be caused also by simultaneous diffusion of two spin (cationic) sub-lattices. It should be noted that these phenomenona are clearly observed experimentally because of a considerable difference between characteristic times of Li and Na motions. In fact, due to significant difference, a contribution of the slowest motion (Na in the present case) is visible only at elevated temperatures, whereas motion with the shortest τ_c can be probed at lower temperatures. Moreover, inequality $\tau_c^{Li} << \tau_c^{Na}$ allows applying quite simple mathematical models for the analysis of experimental data.

For the first time, we have carried out PGF NMR measurements of ^7Li and ^{23}Na self-diffusion coefficients in $LiNaSO_4$: lithium diffusion was measured in the 720-860 K range, whereas the self-diffusion coefficient of sodium was measured in the 790-860 K range. Diffusion coefficients of Li^+ and Na^+ ions at 823 K were found to be approximately the same and equal to $D \approx 10^{-9}\ m^2/s$. This is an excellent confirmation of the paddle-wheel mechanism, due to which the radii of cations are of little importance for their diffusion rates.

Unfortunately, attempts to study correlation effects comparing diffusion and conductivity measurements failed because of a large spread of experimental data on the ionic conductivity in $LiNaSO_4$ and, as a consequence, inability to determine the Haven ratio. Nevertheless, both conductivity and diffusion activation energies were found to be in a good agreement.

For the first time, we have measured the phase transition kinetics in $LiNaSO_4$. The measurements have been carried non-isothermally, i.e. at non-zero cooling rate. In fact, the kinetics of the α-β phase transition was measured via cooling of the $LiNaSO_4$ powder sample, which was preliminarily stabilized at the temperature exceeding a few degrees the phase transition point. Kolmogorov-Johnson-Mehl-Avrami (KJMA) equation was found to be an appropriate model for the analysis of the time evolution of the appearing β-phase during the α-β phase transition. It was shown that the phase transition occurs due to the diffusion-controlled growth of germs, and the nucleation was found to be rapidly exhausted at high cooling rates.

We also found that after slow cooling through the α-β phase transition, powder crystallites are *not* randomly oriented in space, but a new arrangement of crystallites takes place in the sample. This phenomenon was treated as the intergrowth of the trigonal phase through the common borders of powder crystallites. We assumed that the trigonal phase expands into the volume of the powder sample using necks (borders) between distinct powder crystallites as channels of growth. The most important thing here is that the orientation of the crystallographic axes in all powder crystallites was assumed to be determined by the orientation of the lattice in the first powder particle, which could be considered as a macroscopic germ. It has been also revealed that crystallites tend to orient their lattices in the same manner only at small cooling rate. This feature is in agreement with kinetics measurements and can be explained by the fact that the nucleation rate is very low at small cooling rates, whereas the growth rate, in turn, is very high.

We have carried out an NMR study of the sulfate ion reorientations in the low-temperature modification of LiNaSO4. The influence of the SO_4 reorientational jumps on the quadrupolar interactions of ^7Li nuclei was investigated by a jump reorientational model, which has not previously been applied to sulfates. The activation energy required for the SO_4 reorientations was found to be 0.19 eV. It was also revealed that the SO_4 reorientational disorder should be associated with a small anomaly of a heat capacity at around 600 K, which was previously observed experimentally.

High-temperature NMR study of $LiKSO_4$ has been also carried out for the first time. This compound has two phase transitions above room temperature: at 708 K and 943 K. Below 708 K, the line width analysis has been applied to find an activation energy of Li^+

jumps, whereas above the phase transition (i.e. in phase *II*), T_1 and $T_{1\rho}$ measurements have been carried out to understand ionic motion. It was found that T_1 measurements give quite close values of activation energies for Li^+ jumps in $LiNaSO_4$ and $LiKSO_4$: 0.7 (in β-phase) and 0.79 eV (in phase *II*), respectively. However, a considerable deviation of a correlation function from the exponent was revealed in $LiKSO_4$. This non-exponentiality causes the difference between the slopes of relaxation data. In fact, the $1/T_{1\rho}$ slope (or rather the slope of its high-temperature shoulder) gives a value around 1.9 eV for the activation energy. Therefore, a comparison of potential barriers for Li^+ jumps in $LiNaSO_4$ and $LiKSO_4$ found from the relaxation data is meaningless, whereas one should compare conductivity (or diffusion) data. Activation energies of the ionic conductivity were found to be 2.15 and 1.65 eV for $LiNaSO_4$ and $LiKSO_4$, respectively. This indicates that below 788 K $LiKSO_4$ should be a better conductor (Fig. 2).

Finally, we have carried out high-temperature NMR study with line width analysis and $T_{1\rho}$ measurements of two other compounds with larger ions: $LiRbSO_4$ and $LiCsSO_4$. Lithium mobility has been studied in these compounds for the first time. It was shown that the correlation function describing Li^+ jumps in $LiRbSO_4$ deviates significantly from exponent, whereas for $LiCsSO_4$ such deviation has not been observed and BPP model was found to be applicable for ^7Li relaxation data in $LiCsSO_4$.

Things to be proud of

Attempts to understand behavior of $LiNaSO_4$ in different experiments led to the development of a set of techniques, which could be useful, in perspective, for the NMR study of other solids. Thus, we have shown that an orientational disorder of sulfate groups affects significantly the quadrupolar interactions of ^7Li nuclei. It provides an NMR probe to study reorientational jumps of SO_4 groups. We applied the Negita's model (reorientational jump model) to find the activation energy of the SO_4 reorientational jumps and to reveal the onset temperature of quasi-rotations of sulfate groups.

The proposed method is a "low-cost" technique, since it does not require ^{17}O enriched sample and dispenses with time-consuming ^{33}S NMR. Other advantage of the given method is the possibility to probe reorientational motions without NMR relaxation measurements. This is particularly relevant for $LiNaSO_4$, since both ^{23}Na and ^7Li relaxation are almost insensitive to the dynamics of sulfate groups.

An expression for the dipolar correlation function characterizing the fluctuations of the Hamiltonian under uncorrelated diffusion of two cationic sub-lattices in a solid has been obtained. The corresponding formula, which could be used for fitting the two-step temperature dependencies of the NMR line width, has been deduced. The obtained function has been also extended to the case of correlation times distribution. The advantage of this approach is that even in the case of τ_c distribution the fitting function could be expressed in the analytical form.

To measure the kinetics of the α-β phase transition in $LiNaSO_4$, we developed a very easy technique, which is based on the difference of spin-lattice relaxation times in the two phases, but which does not involve the direct measurement of T_1. The technique allows measuring time evolution of the volume of the appearing phase at controlled cooling rates. Applying the KJMA equation for fitting experimental curves, one can extract Avrami parameters – the principal quantities determining the crystallization mode and the type of nucleation. The main advantage of this method is that it can be used to study quite fast kinetics.

Appendix

A.1 Temperature dependence of the quadrupolar splitting: the Bayer-Kushida theory

If the asymmetry parameter, η (or rather $\langle\eta(t)\rangle$) is close to zero, then the influence of lattice vibrations on the value of ν_Q is determined by the change of the principal value of the EFG tensor, i.e. is governed by the function $\langle C_Q(t)\rangle$, where angular brackets denote a time averaging. The latter could be written in the following form [139]:

$$\langle C_Q(t)\rangle = \frac{e^2Q}{h}\langle q(t)\rangle\left[1-\frac{3}{2}\langle\vartheta^2(t)\rangle\right], \tag{A.1}$$

where the angle $\vartheta(t)$ defines the bending motion of the EFG tensor around an axis perpendicular to the direction of q. Time dependence of q, in turn, is governed by the stretching normal modes involving a periodic change of V_{ZZ}. Angles ϑ and θ should not be confused: the former determines a periodic deviation of the principal axis of the EFG tensor from its equilibrium orientation due to vibrations, whereas the latter defines the orientation of the EFG tensor with respect to the external magnetic field.

Taking into account that amplitudes of the vibrations are usually very small, one can put $\vartheta << 1$ (this assumption was used in Eq. (A.1)), whereas the Euler angle θ can take any value.

H. Bayer [139] considered the evolution of the quadrupolar splitting under the bending motion of the EFG tensor assuming the principal value to be unchanged, i.e. $\langle q(t)\rangle = q_0$. Assuming further that N normal modes contribute to this bending motion one can represent $\vartheta(t)$ as a superposition of these modes:

$$\vartheta(t) = \sum_{i=1}^{N}\alpha_i\xi_i, \tag{A.2}$$

where ξ_i stands for the i-th normal coordinate. Taking into account that the mean square displacement of the quantum oscillator is [183]

$$\langle\xi_i^2\rangle = \frac{\hbar}{2\omega_i}\coth\left(\frac{\hbar\omega_i}{2kT}\right), \tag{A.3}$$

where ω_i is a frequency of the i-th normal mode, we have

$$\left\langle C_Q(t)\right\rangle = C_Q^0\left[1-\frac{3\hbar}{4}\sum_{i=1}^{N}\alpha_i^2\omega_i^{-1}\coth\left(\frac{\hbar\omega_i}{2kT}\right)\right]. \tag{A.4}$$

Assuming that we can use the following expansion:

$$\coth(x) = \frac{1}{x}+\frac{x}{3}+O(x^3), \tag{A.5}$$

we obtain

$$\left\langle C_Q(t)\right\rangle = C_Q^0\left(1+a_\vartheta T+b_\vartheta/T\right), \tag{A.6}$$

where

$$a_\vartheta = -\frac{3}{2}k\sum_{i=1}^{N}\frac{\alpha_i^2}{\omega_i^2}, \quad b_\vartheta = -\frac{\hbar^2}{8kT}\sum_{i=1}^{N}\alpha_i^2. \tag{A.7}$$

One can see from Eq. (A.7) that $a_\vartheta, b_\vartheta < 0$; moreover, it is easy to show that since $\omega \sim 10^{12}-10^{13}\ \mathrm{s}^{-1}$, the ratio of fitting parameters is $b_\vartheta/a_\vartheta \sim 10^3-10^5\ \mathrm{K}^2$. Thereby, Eq. (A.6) determines the *negative* temperature dependence of the quadrupolar coupling constant, which is linear at elevated temperatures, but deviates from the straight line when the temperature decreases.

Weak negative temperature dependence of the quadrupolar splitting observed in a vast majority of solid substances is usually referred to as normal (Bayer's type) temperature dependence. In this case, parameters a_ϑ, b_ϑ are assumed to be temperature-independent. In reality, however, these parameters are functions of the volume [140] and, consequently, they can be expected to change in the constant pressure measurements accompanying by thermal expansion. This circumstance was first pointed by T. Kushida *et al*. [140]; therefore, the second term in the right side of Eq. (337) (see the main text) is sometimes referred to as Kushida's term.

Let us now assume that $\left\langle C_Q(t)\right\rangle$ is governed mainly by the stretching normal modes involving a periodic change of V_{ZZ}. Following Eq. (A.2), we can expand $q(t)$ into a series with respect to normal coordinates ξ_i:

$$q(t) = q_0+\sum_{i=1}^{N}\frac{\partial q}{\partial\xi_i}\xi_i+\sum_{i=1}^{N}\frac{\partial^2 q}{\partial\xi_i\partial\xi_j}\xi_i\xi_j+\ldots \tag{A.8}$$

Taking into account that $\left\langle\xi_i\right\rangle = 0$ we obtain

$$\left\langle q(t)\right\rangle = q_0+\frac{\hbar}{2}\sum_{i=1}^{N}\frac{\partial^2 q}{\partial\xi_i^2}\omega_i^{-1}\coth\left(\frac{\hbar\omega_i}{2kT}\right). \tag{A.9}$$

In contrast to Eq. (A.4), where coefficients α_i^2 are always positive, second derivatives $\partial^2 q/\partial \xi_i^2$ could have any sign resulting in positive or negative temperature dependence of ν_Q (regardless of the influence of thermal expansion). It is easy to show that Eq. (A.9) governs the linear temperature dependence of the quadrupolar coupling constant at elevated temperatures, whereas at lower temperatures $\langle q(t) \rangle$ does not depend against *T*.

An increase (or decrease) of $\langle q(t) \rangle$ leads also to an anomaly of the relaxation rate. In fact, the temperature dependence of the relaxation rate constant could be defined as follows [69, 184]:

$$T_1^{-1} = K(I) \langle q^2(t) \rangle \left[J(\omega_L) + 4J(2\omega_L) \right], \tag{A.10}$$

where $J(\omega)$ is a spectral density function, ω_L is the Larmor frequency, and $K(I)$ is a coefficient depending on the spin quantum number. One can find using Eq. (A.8) that

$$\langle q^2(t) \rangle = q_0^2 + \frac{\hbar}{2} \sum_{i=1}^{N} A_i \omega_i^{-1} \coth\left(\frac{\hbar \omega_i}{2kT} \right), \tag{A.11}$$

where

$$A_i = \left(\frac{\partial q}{\partial \xi_i} \right)^2 + \frac{\partial^2 q}{\partial \xi_i^2}. \tag{A.12}$$

It is obvious that if the second derivatives are positive, then Eq. (A.11) governs an increase of the relaxation rate above $\Theta_E/2$, where Θ_E is the Einstein temperature of a given solid.

References

[1] A. Despotuli, A. Andreeva // Modern Electronics **5**, 10 (2006).
[2] A.D. Robertson, A.R. West, A.G. Ritchie // Solid State Ionics **104**, 1 (1997).
[3] A.G. Ritchie, N.E. Bagshaw // Philos. T. Roy. Soc. A **354**, 1643 (1996).
[4] B.E. Mellander, B. Granéli, J. Roos // Solid State Ionics **40–41, Part 1**, 162 (1990).
[5] U.M. Gundusharma, C. MacLean, E.A. Secco // Solid State Commun. **57**, 479 (1986).
[6] M.A. Pimenta, P. Echegut, F. Gervais, P. Abélard // Solid State Ionics **28–30, Part 1**, 224 (1988).
[7] A. Lundén // Solid State Commun. **65**, 1237 (1988).
[8] A. Lundén // Solid State Ionics **68**, 77 (1994).
[9] N.H. Andersen, P.W.S.K. Bandaranayake, M.A. Careem, M.A.K.L. Dissanayake, C.N. Wijayasekera, R. Kaber, A. Lundén, B.E. Mellander, L. Nilsson, J.O. Thomas // Solid State Ionics **57**, 203 (1992).
[10] H.C. Freiheit, H. Kroll, A. Putnis // Z. Kristallogr. **213**, 575 (1998).
[11] T. Kanashiro, T. Yamanishi, Y. Kishimoto, T. Ohno, Y. Michihiro, K. Nobugai // J. Phys. Soc. Jpn. **63**, 3488 (1994).
[12] L. Börjesson, L.M. Torell // Phys. Rev. B **32**, 2471 (1985).
[13] M. Zhang, A. Putnis, E.K.H. Salje // Solid State Ionics **177**, 37 (2006).
[14] Y. Shiroishi, A. Nakata, S. Sawada // J. Phys. Soc. Jpn. **40**, 911 (1976).
[15] A. Kunishige, H. Mashiyama // J. Phys. Soc. Jpn. **56**, 3189 (1987).
[16] H. Mashiyama, K. Hasebe, S. Tanisaki, Y. Shiroishi, S. Sawada // J. Phys. Soc. Jpn. **47**, 1198 (1979).
[17] S.V. Mel'nikova, M.V. Gorev, V.A. Grankina // Phys. Solid State **40**, 1219 (1998).
[18] A.I. Kruglik, M.A. Simonov, E.P. Zhelezin // Phys. Dokl. **24**, 596 (1979).
[19] A. Niwata, K. Itoh // J. Phys. Soc. Jpn. **64**, 4733 (1995).
[20] A.-L. Rollet, V. Sarou-Kanian, C. Bessada // Inorg. Chem. **48**, 10972 (2009).
[21] A.K. Ivanov-Shitz, I.V. Murin, Ionika tverdogo tela [Solid-state ionics], Saint Petersburg University, Saint Petersburg, 2000.
[22] M. Faraday // Philos. T. Roy. Soc. Lond. **23**, 507 (1833).
[23] S. Geller, Solid Electrolytes, Springer Berlin Heidelberg, New York, 1977.
[24] M. O'Keeffe, B.G. Hyde // Philos. Mag. **33**, 219 (1976).
[25] A.L. Despotuli, A.V. Andreeva, B. Rambabu // Ionics **11**, 306 (2005).
[26] I. Riess // Solid State Ionics **157**, 1 (2003).
[27] A. Benrath, K. Drehkopf // Zeitschrift für Physikalische Chemie **99**, 57 (1921).
[28] T. Förland, J. Krogh-Moe // Acta Chem. Scand. **11**, 565 (1957).
[29] T. Förland, J. Krogh-Moe // Acta Crystallogr. **11**, 224 (1958).
[30] A. Lundén // Solid State Ionics **28–30, Part 1**, 163 (1988).
[31] Y. Feng, J.L. Luo, K.T. Chuang // J. Electrochem. Soc. **153**, A1049 (2006).
[32] E.A. Secco // J. Solid State Chem. **96**, 366 (1992).
[33] E.A. Secco, M.G. Usha // Solid State Ionics **68**, 213 (1994).
[34] E.A. Secco // Solid State Ionics **60**, 233 (1993).
[35] L. Karlsson, R.L. McGreevy // Solid State Ionics **76**, 301 (1995).
[36] R. Tärneberg, A. Lundén // Solid State Ionics **90**, 209 (1996).
[37] A. Lundén, L. Nilsson // J. Mater. Sci. Lett. **5**, 645 (1986).
[38] H.C. Freiheit // Solid State Commun. **119**, 539 (2001).
[39] K.D. Junke, M. Mali, J. Roos, D. Brinkmann, A. Lundén, B. Granéli // Solid State Ionics **28–30**, 1287 (1988).

[40] D. Massiot, C. Bessada, P. Echegut, J.P. Coutures, F. Taullele // Solid State Ionics **37**, 223 (1990).
[41] D. Teeters, R. Frech // J. Chem. Phys. **76**, 799 (1982).
[42] D. Teeters, R. Frech // Phys. Rev. B **26**, 4132 (1982).
[43] D. Teeters, R. Frech // Phys. Rev. B **26**, 5897 (1982).
[44] M.A. Pimenta, P. Echegut, G. Hauret, F. Gervais // Phase Transit. **9**, 185 (1987).
[45] R.H. Chen, C.-M. Tseng, C.S. Shern, T. Fukami // Solid State Ionics **181**, 877 (2010).
[46] D. Wilmer, H. Feldmann, J. Combet, R.E. Lechner // Physica B **301**, 99 (2001).
[47] G. Wyrouboff // Bull. Soc. Fr. Mineral Crystallogr. **13**, 215 (1890).
[48] R. Nacken // Neues Jahrb. Mineral. Beil. **24**, 42 (1907).
[49] H. Blittersdorf // Z. Kristallogr. **71**, 141 (1929).
[50] I.N. Lepeshkov, N.V. Bodaleva, L.T. Kotova // Russ. J. Inorg. Chem. **6**, 864 (1961).
[51] R. Ando // J. Phys. Soc. Jpn. **17**, 937 (1962).
[52] H.F. Fischmeister, A. Rönnquist // Arkiv. Kemi. **15**, 393 (1960).
[53] T.R. Prasad, Y.C. Venudhar, L. Iyengar, K.V.K. Rao // Pramana **11**, 81 (1978).
[54] M.L. Bansal, S.K. Deb, A.P. Roy, V.C. Sahni // J. Phys. Colloques **42**, 902 (1981).
[55] X. Solans, M. Teresa Calvet, M. Luisa Martínez-Sarrión, L. Mestres, A. Bakkali, E. Bocanegra, J. Mata, M. Herraiz // J. Solid State Chem. **148**, 316 (1999).
[56] M.H. Levitt, Spin Dynamics: Basics of Nuclear Magnetic Resonance, 2nd Edition, John Wiley & Sons Ltd2008.
[57] C.P. Slichter, Principles of Magnetic Resonance, Springer-Verlag Berlin Heidelberg, New York, 1980.
[58] D.A. Varshalovich, A.N. Moskalev, V.K. Khersonskii, Quantum Theory of Angular Momentum, World Scientific, London, 1988.
[59] S. Chandra Shekar, A. Jerschow, Tensors in NMR, Encyclopedia of Magnetic Resonance, John Wiley & Sons, 2007.
[60] G.J. Bowden, W.D. Hutchison // J. Magn. Reson. **67**, 403 (1986).
[61] L.D. Landau, E.M. Lifshitz, Quantum mechanics: non-relativistic theory, Pergamon Press Oxford, 1977.
[62] V.M. Mikushev, A.M. Ulyashev, E.V. Charnaya, A. Chandoul // Phys. Solid State **44**, 1044 (2002).
[63] K. Blum, Density Matrix Theory and Applications, Springer-Verlag Berlin Heidelberg, New York, 2012.
[64] A. Abragam, The Principles of Nuclear Magnetism, Clarendon Press, Oxford, 1961.
[65] D. Petit, J.P. Korb // Phys. Rev. B **37**, 5761 (1988).
[66] G. Jaccard, S. Wimperis, G. Bodenhausen // J. Chem. Phys. **85**, 6282 (1986).
[67] M.H. Cohen, F. Reif, Quadrupole Effects in Nuclear Magnetic Resonance Studies of Solids, in: F. Seitz, D. Turnbull (Eds.) Solid State Physics1957, pp. 321.
[68] G. Lipari, A. Szabo // J. Am. Chem. Soc. **104**, 4546 (1982).
[69] A.A. Vashman, I.S. Pronin, Yadernaya magnitnaya relaksatsionnaya spektroskopiya [Nuclear magnetic relaxation spectroscopy], Energoatomizdat, Moscow, 1986.
[70] J. Trzmiel, K. Weron, J. Janczura, E. Placzek-Popko // J. Phys. - Condens. Mat. **21**, 345801 (2009).
[71] D.C. Johnston // Phys. Rev. B **74**, 184430 (2006).
[72] J. Wuttke // Algorithms **5**, 604 (2012).
[73] P.A. Beckmann // Phys. Rep. **171**, 85 (1988).
[74] A.A. Khamzin, R.R. Nigmatullin, I.I. Popov // Fract. Calc. Appl. Anal. **17**, 247 (2014).
[75] R.R. Nigmatullin, Y.E. Ryabov // Phys. Solid State **39**, 87 (1997).
[76] R.J.D. Tilley, Principles and Applications of Chemical Defects, Stanley Thornes Ltd., Cheltenham, 1998.

[77] J. Crank, The Mathematics of Diffusion, Oxford University Press, London, 1980.
[78] H. Mehrer, Diffusion in Solids: Fundamentals, Methods, Materials, Diffusion-Controlled Processes, Springer Berlin Heidelberg, New York, 2007.
[79] J. Frenkel, Kinetic theory of liquids, Oxford University Press, London, 1947.
[80] B.S. Bokshteyn, S.Z. Bokshteyn, A.A. Zhukhovitskiy, Termodinamika i kinetika diffuzii v tverdykh telakh [Thermodynamics and kinetics of diffusion in solid bodies], Metallurgiya Moscow, 1974.
[81] G.E. Murch // Solid State Ionics **7**, 177 (1982).
[82] G.E. Murch, Diffusion Kinetics in Solids, in: G. Kostorz (Ed.) Phase Transformations in Materials, Wiley-VCH Verlag GmbH, Weinheim, 2005.
[83] P. Kofstad, Nonstoichiometry, diffusion, and electrical conductivity in binary metal oxides, John Wiley & Sons, New York, 1972.
[84] J.R. Manning, Non-Random Diffusion in Ionic Crystals, in: A.R. Cooper, A.H. Heuer (Eds.) Mass Transport Phenomena in Ceramics, Plenum Press,, New York, 1975, pp. 1.
[85] A.D. Le Claire, Correlation Effects in Ionic Transport Processes, in: A.R. Cooper, A.H. Heuer (Eds.) Mass Transport Phenomena in Ceramics, Plenum Press, New York, 1975, pp. 17.
[86] I. Yokota // J. Phys. Soc. Jpn. **21**, 420 (1966).
[87] G.H. Vineyard // J. Phys. Chem. Solids **3**, 121 (1957).
[88] K.D. Junke, University of Zürich, Zürich, 1989.
[89] D.P. Almond, A.R. West // Solid State Ionics **11**, 57 (1983).
[90] E.O. Stejskal, J.E. Tanner // J. Chem. Phys. **42**, 288 (1965).
[91] E.O. Stejskal // J. Chem. Phys. **43**, 3597 (1965).
[92] E.L. Hahn // Phys. Rev. **80**, 580 (1950).
[93] H.Y. Carr, E.M. Purcell // Phys. Rev. **94**, 630 (1954).
[94] W.S. Price // Concept. Magnetic. Res. **9**, 299 (1997).
[95] W.S. Price // Concept. Magnetic. Res. **10**, 197 (1998).
[96] J.F. Stebbins // Chem. Rev. **91**, 1353 (1991).
[97] F. Taulelle, J.P. Coutures, D. Massiot, J.P. Rifflet // Bull. Magn. Reson. **11**, 318 (1989).
[98] L.D. Clark // Rev. Sci. Instrum. **40**, 1498 (1969).
[99] D.S. Schreiber // Rev. Sci. Instrum. **35**, 1582 (1964).
[100] S.B. Adler, J.N. Michaels, J.A. Reimer // Rev. Sci. Instrum. **61**, 3368 (1990).
[101] T.S. Aurora, S.M. Day // Rev. Sci. Instrum. **53**, 1152 (1982).
[102] D. Ploumbidis // Rev. Sci. Instrum. **50**, 1133 (1979).
[103] V. Lacassagne, C. Bessada, B. Ollivier, D. Massiot, P. Florian, J.-P. Coutures // C. R. Acad. Sci. Paris Series II b **325**, 91 (1997).
[104] R.C. Crosby, J.F. Haw, D.H. Lewis // Anal. Chem. **60**, 2695 (1988).
[105] J.F. Haw, G.C. Campbell, R.C. Crosby // Anal. Chem. **58**, 3172 (1986).
[106] J.F. Haw // Anal. Chem. **60**, 559A (1988).
[107] P.A. Beckmann, C. Dybowski // J. Magn. Reson. **146**, 379 (2000).
[108] T. Laude, Boron Nitride Nanotubes Grown by Non-Ablative Laser Heating: Synthesis, Characterization and Growth Processes, University of Tsukuba, 2001, pp. 180.
[109] C.T. O'Sullivan // Am. J. Phys. **58**, 956 (1990).
[110] M. Massoud, Engineering Thermofluids: Thermodynamics, Fluid Mechanics, and Heat Transfer, Springer Berlin Heidelberg, New York, 2005.
[111] X. Zhang, K. Xu, Y. Gao // Thermochim. Acta **385**, 81 (2002).
[112] J. Sangster, A.D. Pelton // J. Phys. Chem. Ref. Data **16**, 509 (1987).
[113] I.A. dos Santos, D. Klimm, S.L. Baldochi, I.M. Ranieri // J. Cryst. Growth **360**, 172 (2012).

[114] Boron nitride (BN), Debye temperature, heat capacity, density a. rel. parameters, hex. modification, in: O. Madelung, U. Rössler, M. Schulz (Eds.) Group IV Elements, IV-IV and III-V Compounds. Part b - Electronic, Transport, Optical and Other Properties, Springer Berlin Heidelberg2002, pp. 1.
[115] B. Morosin, D.L. Smith // Acta Crystallogr. **22**, 906 (1967).
[116] A.F. Polishcuk, T.M. Shurzhal // Electrokhimiya **9**, 838 (1979).
[117] K. Singh, V.K. Deshpande // Solid State Ionics **13**, 157 (1984).
[118] IUPAC-NIST Solubility Database, http://srdata.nist.gov/solubility/index.aspx.
[119] J. Clark Stewart, D. Segall Matthew, J. Pickard Chris, J. Hasnip Phil, I.J. Probert Matt, K. Refson, C. Payne Mike, First principles methods using CASTEP, Z. Kristallogr., 2005, pp. 567.
[120] H.J. Monkhorst, J.D. Pack // Phys. Rev. B **13**, 5188 (1976).
[121] P.E. Blöchl // Phys. Rev. B **50**, 17953 (1994).
[122] J.P. Perdew, K. Burke, M. Ernzerhof // Phys. Rev. Lett. **77**, 3865 (1996).
[123] B.G. Pfrommer, M. Côté, S.G. Louie, M.L. Cohen // J. Comput. Phys. **131**, 233 (1997).
[124] D. Massiot, F. Fayon, M. Capron, I. King, S. Le Calvé, B. Alonso, J.-O. Durand, B. Bujoli, Z. Gan, G. Hoatson // Magn. Reson. Chem. **40**, 70 (2002).
[125] J. Waugh, E. Fedin // Phys. Solid State **4**, 1633 (1963).
[126] H.S. Gutowsky, G.E. Pake // J. Chem. Phys. **18**, 162 (1950).
[127] P. Bilski, M. Olszewski, N.A. Sergeev, J. Wąsicki // Solid State Nucl. Mag. **25**, 15 (2004).
[128] P. Bilski, N.A. Sergeev, J. Wąsicki // Appl. Magn. Reson. **18**, 115 (2000).
[129] S.G. Bishop, P.J. Ring, P.J. Bray // J. Chem. Phys. **45**, 1525 (1966).
[130] H.S. Gutowsky, B.R. McGarvey // J. Chem. Phys. **20**, 1472 (1952).
[131] M. Abramowitz, I.A. Stegun, Handbook of Mathematical Functions, Dover Publications, Inc., New York, 1965.
[132] S.G. Bishop, P.J. Bray // J. Chem. Phys. **48**, 1709 (1968).
[133] J.R. Hendrickson, P.J. Bray // J. Magn. Reson. **9**, 341 (1973).
[134] S.W. Martin // Mater. Chem. Phys. **23**, 225 (1989).
[135] L. Nilsson, J.O. Thomas, B.C. Tofield // J. Phys. C Solid State **13**, 6441 (1980).
[136] R.A. Shakhovoy, M. Deschamps, A. Rakhmatullin, V. Sarou-Kanian, P. Florian, C. Bessada // submitted to Solid State Nuclear Magnetic Resonance DOI.
[137] R. Böhmer, K.R. Jeffrey, M. Vogel // Prog. Nucl. Mag. Res. Sp. **50**, 87 (2007).
[138] T.M. Barbara, M.S. Greenfield, R.L. Vold, R.R. Vold // J. Magn. Reson. **69**, 311 (1986).
[139] H. Bayer // Z. Physik **130**, 227 (1951).
[140] T. Kushida, G.B. Benedek, N. Bloembergen // Phys. Rev. **104**, 1364 (1956).
[141] D. Nakamura, R. Ikeda, M. Kubo // Coordin. Chem. Rev. **17**, 281 (1975).
[142] P.K. Burkert, D.G. Klobasa // Z. Naturforsch. A **40**, 274 (1985).
[143] K. Negita, N. Nakamura, H. Chihara // Chem. Phys. Lett. **63**, 187 (1979).
[144] A. Birczyński, C. Dimitropoulos, Z.T. Lalowicz // Physica B **339**, 182 (2003).
[145] M. Mackowiak, R.J.C. Brown // J. Mol. Struct. **111**, 233 (1983).
[146] R.J.C. Brown // Z. Naturforsch. A **45**, 449 (1990).
[147] H. Takahashi, S. Meshitsuka, K. Higasi // Spectrochim. Acta A-M. **31**, 1617 (1975).
[148] L. Pauling // Phys. Rev. **36**, 430 (1930).
[149] B. Lorenz // High Pressure Res. **9**, 107 (1992).
[150] N.V. Chandra Shekar, K. Govinda Rajan // B. Mater. Sci. **24**, 1 (2001).
[151] M.E. Villafuerte-Castrejon, A.R. West // J. Chem. Soc. Faraday Trans. 1 **75**, 374 (1979).
[152] H.E. Kissinger // J. Res. Nat. Bur. Stand. **57**, 217 (1956).

[153] K. Matusita, S. Sakka // J. Non-Cryst. Solids **38–39, Part 2**, 741 (1980).
[154] G. Feio, J.P. Cohen-Addad // J. Polym. Sci. Pol. Phys. **26**, 389 (1988).
[155] G. Feio, G. Buntinx, J.P. Cohen-Addad // J. Polym. Sci. Pol. Phys. **27**, 1 (1989).
[156] A.N. Kolmogorov // Izvestiya Akademii Nauk SSSR, Seriya Matem **1**, 335 (1937).
[157] M. Avrami // J. Chem. Phys. **7**, 1103 (1939).
[158] M. Avrami // J. Chem. Phys. **8**, 212 (1940).
[159] P. Papon, J. Leblond, P.H.E. Meijer, The Physics of Phase Transitions: Concepts and Applications, Springer-Verlag Berlin Heidelberg2006.
[160] W.A. Johnson, R.F. Mehl // Trans. Am. Min. Met. Eng. **135**, 416 (1939).
[161] T. Ozawa // Polymer **12**, 150 (1971).
[162] P. Supaphol, N. Dangseeyun, P. Srimoaon, M. Nithitanakul // Thermochim. Acta **406**, 207 (2003).
[163] P. Supaphol // J. Appl. Polym Sci. **78**, 338 (2000).
[164] Q. Zhang, Z. Zhang, H. Zhang, Z. Mo // J. Polym. Sci. Pol. Phys. **40**, 1784 (2002).
[165] N. Apiwanthanakorn, P. Supaphol, M. Nithitanakul // Polym. Test. **23**, 817 (2004).
[166] Y.E. Geguzin, Fizika spekaniya [Physics of sintering], Nauka, Moscow, 1984.
[167] L.C. De Jonghe, M.N. Rahaman, Chapter 4 - 4.1 Sintering of Ceramics, in: M. Kaneno, K. Koumoto, K. Uchino, R.M. Spriggs, N. Claussen, F. Aldinger, S. Sōmiya (Eds.) Handbook of Advanced Ceramics, Academic Press, Oxford, 2003, pp. 187.
[168] E.K.H. Salje, Phase transitions in ferroelastic and co-elastic crystals, student edition, Cambridge University Press, Cambridge, 1993.
[169] M. Karppinen, J.O. Lundgren, R. Liminga // Acta Crystallogr. C **39**, 34 (1983).
[170] S. Bhakay-Tamhane, A. Sequiera, R. Chidambaram // Acta Crystallogr. C **40**, 1648 (1984).
[171] H. Schulz, U. Zucker, R. Frech // Acta Crystallogr. B **41**, 21 (1985).
[172] M.A. Pimenta, P. Echegut, Y. Luspin, G. Hauret, F. Gervais, P. Abélard // Phys. Rev. B **39**, 3361 (1989).
[173] Y.Y. Li // Solid State Commun. **51**, 355 (1984).
[174] A. Pietraszko // Ferroelectrics **79**, 121 (1988).
[175] H. Sankaran, S.M. Sharma, S.K. Sikka // Solid State Commun. **66**, 7 (1988).
[176] C. Scherf, T. Hahn, G. Heger, R.A. Becker, W. Wunderlich, H. Klapper // Ferroelectrics **191**, 171 (1997).
[177] C.B. Pinheiro, M.A. Pimenta, G. Chapuis, N.L. Speziali // Acta Crystallogr. B **56**, 607 (2000).
[178] P.E. Tomaszewski // J. Solid State Chem. **156**, 253 (2001).
[179] M.M. Ahmad, M.A. Hefnia // Z. Naturforsch. A **56**, 677 (2001).
[180] W. Steurer, H. Wittmann, H. Jagodzinski, A. Pietraszko // Acta Crystallogr. B **42**, 11 (1986).
[181] R. Farhi, F. Coudin // J. Phys. - Condens. Mat. **1**, 6951 (1989).
[182] K. Schroeder, A. Kvist, H. Ljungmark // Z. Naturforsch. A **27**, 1252 (1972).
[183] L.D. Landau, E.M. Lifshitz, Statistical Physics. Part 1, Pergamon Press Ltd., Oxford, 1980.
[184] P.S. Hubbard // J. Chem. Phys. **53**, 985 (1970).

Principales conclusions et perspectives

L'objectif principal de ce travail a porté sur l'étude détaillée du transfert ionique dans les sulfates d'alcalins de la famille $LiMSO_4$, où M = Na, K, Rb, Cs. La plus grande attention a été accordée à $LiNaSO_4$, le composé le plus intéressant en termes de dynamique ionique, avec une conductivité ionique très élevée entre 600 et 850 K. Bien que la conductivité de LiKSO4 dépasse encore la valeur la plus élevée de σ dans LiNaSO4-dessus de 850 K (Fig. 2), ces températures sont pour le moment trop élevées pour les applications potentielles, en particulier, pour les batteries mais ces systèmes sont toutefois intéressants pour mieux comprendre le type de mécanismes de transport impliqués dans les électrolytes solides.

Nous avons également montré qu'il était très facile d'obtenir des monocristaux de sulfate de sodium et de lithium avec des conditions de croissance bien maitrisées, et reproductibles en fonction des conditions de température, pH, et des taux d'évaporation, alors que pour les autres composés comme pour $LiKSO_4$, la croissance est plus délicate .

En accord avec des travaux antérieurs nous avons confirmé que dans $LiNaSO_4$, les deux types de cations Li^+ et Na^+ transportent les charges. Cela conduit à des effets intéressants, tels que l'existence de deux minima dans l'évolution du T_1 avec la température à bas champs magnétiques. Nous avons également observé pour la première fois un rétrécissement de la raie RMN en deux étapes, qui a été expliqué par la diffusion simultanée de deux sous-réseaux cationiques. Il convient de noter que ces phénomènes sont clairement observés expérimentalement du fait de la différence importante entre les temps caractéristiques des mouvements de Li et Na. En fait, en raison de cette différence significative, une contribution du mouvement lent (Na dans le cas présent) est visible uniquement à des températures élevées, alors que le mouvement avec le τ_c plus court peut être sondé à des températures inférieures. En outre, cette différence $\tau_c^{Li} << \tau_c^{Na}$ permet d'appliquer des modèles mathématiques très simples pour l'analyse des données expérimentales.

Nous avons effectué des mesures des coefficients d'autodiffusion de ^7Li et ^{23}Na, par RMN à gradients de champs dans $LiNaSO_4$ entre 720 et 860K. Les valeurs des coefficients de diffusion des ions Li^+ et Na^+ mesurées à 823 K sont quasiment identiques ($D \approx 10^{-9}\ m^2/s$). Ceci confirme le mécanisme d'engrenage proposé pour « libérer » la diffusion des cations, où la valeur du rayon des cations a peu d'influence sur leur vitesse de diffusion.

Nous avons mesuré la cinétique de transition de phase α-β dans $LiNaSO_4$. Les mesures ont été effectuées en conditions non-isothermes au cours du refroidissement de la poudre de

$LiNaSO_4$ préalablement stabilisée quelques degrés au-dessus de la température de transition de phase. L'équation Kolmogorov-Johnson-Mehl-Avrami (KJMA) a été utilisée comme modèle approprié pour l'analyse au cours du temps de l'apparition de la phase à la transition de phase α-β. Il a été montré que la transition de phase se produit par la croissance de germes par diffusion contrôlée et que la nucléation s'arrête rapidement pour des vitesses de refroidissement élevées.

Nous avons également constaté que nous ne retrouvions plus un spectre de poudre après un refroidissement « à travers » la transition de phase, du fait d'un nouvel agencement des cristallites. Nous avons supposé que ce phénomène était lié à une croissance de la phase rhomboédrique au travers des bords des cristallites de la poudre. La phase se développerait ainsi dans tout le volume de l'échantillon de poudre à partir des frontières entre les cristallites qui jouent ainsi le rôle de canaux de croissance.

L'orientation des axes cristallographiques dans toutes les cristallites est déterminée par l'orientation initiale dans la première particule de poudre, que l'on peut alors considérer comme un germe macroscopique. Nous avons aussi observé qu'à faible vitesse de refroidissement, les cristallites ont tendance à orienter leurs réseaux de la même manière en accord avec les mesures cinétiques. Le taux de nucléation est très faible à faibles vitesses de refroidissement, tandis que le taux de croissance, lui, est très élevé.

Nous avons mené en parallèle par RMN l'étude des réorientations des ions sulfate dans la phase basse température de $LiNaSO_4$, en mesurant leur influence sur les interactions quadripolaires du ^7Li à partir d'un modèle de sauts, qui n'a pas encore été appliquée à des sulfates. L'énergie d'activation nécessaire pour la réorientation de SO_4 a été estimée à 0,19 eV. Le désordre de réorientation des SO_4^{2-} est associé à une très faible capacité thermique à 600 K, ce qui a été précédemment observé expérimentalement.

L'étude de $LiKSO_4$ par RMN haute température a été menée par l'étude de la largeur de raie au-dessous de 708K dans la phase I, pour déterminer l'énergie d'activation des sauts du Li+, et au-dessus dans la phase II, par des mesures de T_1 et de $T_{1\rho}$ pour comprendre la dynamique ionique. Des valeurs assez proches des énergies d'activation ont été obtenues pour les sauts du lithium dans les deux systèmes LNS et LKS, de 0.7 dans la phase β et de 0.79eV dans la phase II respectivement. L'énergie d'activation déduite de la pente de l'évolution de $1/T_{1\rho}$, 1.89eV est à rapprocher des données de conductivité estimée à 2,15 et 1,65 eV pour $LiNaSO_4$ et $LiKSO_4$, respectivement. Ce qui indique qu'au-dessous de 788 K $LiKSO_4$ serait un meilleur conducteur (Fig. 2).Enfin, nous étudié la mobilité dans les systèmes $LiRbSO_4$ et $LiCsSO_4$, en augmentant la taille du deuxième cation. Nous avons montré que la fonction de

corrélation décrivant les sauts du Li^+ n'est pas une simple exponentielle dans LiRbSO4 alors qu'une telle déviation n'a pas été observée dans $LiCsSO_4$ et les données de relaxation ont été facilement modélisable par un simple modèle BPP.

Things to be proud of...

Afin de mieux comprendre la dynamique ionique dans les sulfates d'alcalins et plus particulièrement dans $LiNaSO_4$, nous avons pu exploiter l'évolution en température de différents paramètres RMN « sensibles » à la dynamique et développer un ensemble de modèles adaptés pour rendre compte des évolutions observées. Nous avons montré qu'un désordre d'orientation des groupements sulfates affectait de manière significative les interactions quadripolaires des noyaux ^7Li et pu ainsi exploiter cet effet pour sonder les sauts réorientationnels des groupes SO_4^{2-}, en déterminer l'énergie d'activation ainsi que la température d'apparition. La méthode proposée est une technique "à faible coût", car elle permet d'éviter l'enrichissement en ^{17}O de l'échantillon ou des expériences très longues en RMN du souffre 33. Elle permet aussi de sonder ces mouvements sans avoir recours aux mesures de temps de relaxation. Ceci est particulièrement pertinent pour $LiNaSO_4$, puisque les relaxations des deux cations ^{23}Na et ^7Li sont quasi insensibles à la dynamique de groupes sulfates.

Une expression de la fonction de corrélation dipolaire caractérisant les fluctuations de l'Hamiltonien en présence de diffusion non corrélée de deux sous-réseaux cationiques dans un solide a été obtenue. Une formule correspondante pour le fit de l'évolution en température de la largeur de raie RMN en deux étapes comme observée dans le LNS, a été déduite. La fonction obtenue a été également étendue au cas d'une distribution de temps de corrélation. L'avantage de cette approche est que, même dans le cas d'une distribution de τ_c la fonction d'ajustement peut être exprimée sous une forme analytique.

Pour mesurer la cinétique de la transition de phase α-β dans $LiNaSO_4$, nous avons développé une technique très simple, qui est basée sur la différence des temps de relaxation spin-réseau dans les deux phases, mais qui ne nécessite pas la mesure directe de T1. Cette méthode permet de mesurer l'évolution dans le temps du volume de la phase apparaissant à des vitesses de refroidissement contrôlées. A partir de l'application de l'équation KJMA pour fitter les courbes expérimentales, on peut extraire les paramètres d'Avrami, les principales grandeurs qui déterminent le mode de cristallisation et le type de nucléation. Le principal avantage de cette méthode est de pouvoir être utilisée pour étudier les cinétiques très rapides.

Roman SHAKHOVOY

Propriétés structurales et dynamiques des sulfates d'alcalins

Le sujet de cette thèse est principalement ciblé sur l'étude du transport ionique dans les sulfates d'alcalins de la famille LIMSO$_4$, où M =Na, K, Rb, Cs. Une attention particulière est portée sur l'étude du système LiNaSO$_4$, le plus intéressant en termes de dynamique ionique, par RMN en fonction de la température.

Dans le cadre de cette étude, nous avons effectué des mesures de temps de relaxation et de largeurs de raie pour toute la série de composés. Des mesures de coefficients d'autodiffusion du ^{7}li et du ^{23}Na, ont été menées depuis l'ambiante jusqu'à la température de fusion. Pour la première fois, nous avons pu mesurer la cinétique de transition de phase dans LiNaSO$_4$, à partir d'une nouvelle méthode basée sur la différence de temps de relaxation dans les deux phases de part et d'autre de la transition, mais sans mesurer forcément le T_1. Cette technique élaborée dans le cadre de ce travail permet de mesurer l'évolution au cours du temps du volume de la phase qui apparait pour des vitesses de refroidissement contrôlées.

Nous avons aussi mené une étude par RMN des réorientations des groupements sulfates dans la phase basse température. L'influence des réorientations des SO_4^{2-} sur les couplages quadripolaires au noyau 7li, a été étudiée par un modèle de réorientation par sauts, qui n'avait encore jamais été utilisé pour les sulfates. La méthode proposée est une méthode à « bas couts » car elle permet d'atteindre l'information sur la dynamique des groupements sulfates sans enrichir l'échantillon en ^{17}O ou de mener des expériences très longues pour le ^{33}S, ou sans passer par les mesures de temps de relaxation.

Afin d'analyser le rétrécissement par le mouvement (motional narrowing) en fonction de la température dans les solides avec deux sous réseaux cationiques diffusant comme dans le cas du LiNaSO$_4$, nous avons élaboré un modèle permettant de fitter l'évolution observée à deux marches de la largeur de raie RMN avec la température. La fonction analytique obtenue a été étendue au cas de distributions de temps de corrélation

Mots clés : Sulfates d'alcalins, RMN, relaxation, diffusion, cinétique des transitions de phases…

Structural Properties and Dynamics of Alkali Sulfates

The main goal of a present research is a detailed study of ionic transfer in double sulfates belonging to the LiMSO$_4$ family, where M = Na, K, Rb, Cs. The most attention has been paid to LiNaSO$_4$ as to the most interesting (in terms of the ion dynamics) compound among other double sulfates.

We have carried out magnetic relaxation measurements and line width analysis for all compounds under consideration. Moreover, PGF NMR measurements of ^{7}Li and ^{23}Na self-diffusion coefficients in LiNaSO$_4$ have been carried out. For the first time, we have measured the phase transition kinetics in LiNaSO$_4$. For this purpose, we developed a new technique, which is based on the difference of spin-lattice relaxation times in the two phases, but which does not involve the direct measurement of T_1. Elaborated technique allows measuring time evolution of the volume of the appearing phase at controlled cooling rates.

We have carried out NMR study of the sulfate ion reorientations in the low-temperature modification of LiNaSO$_4$. The influence of the SO$_4$ reorientational jumps on the quadrupolar interactions of ^{7}Li nuclei was investigated by a jump reorientational model, which has not previously been applied to sulfates. The proposed method is a "low-cost" technique, since it does not require an ^{17}O enriched sample and dispenses with time-consuming ^{33}S NMR. Other advantage of a given method is a possibility to probe reorientational motions without NMR relaxation measurements.

To analyze motional narrowing in solids with two diffusing spin sublattices (such case occurs, e.g., in LiNaSO$_4$) we deduced a formula, which can be used for fitting of the two-step temperature dependencies of the NMR line width. The obtained function has been also extended to the case, when a distribution of correlation times takes place. The advantage of this approach is that even in the case of distribution of correlation times, the fitting function could be expressed in the analytical form.

Keywords: alkali sulfates, NMR, relaxation, diffusion, phase transition kinetics...

CEMHTI-CNRS UPR3079
Conditions Extrêmes et Matériaux:
Haute Température et Irradiation
1D, avenue de la Recherche Scientifique 45071 Orléans Cedex 2